



**The University of Sydney**

School of Civil Engineering  
Sydney NSW 2006  
AUSTRALIA

<http://www.civil.usyd.edu.au/>

Centre for Advanced Structural Engineering

**Compression Tests of High Strength  
Cold-Formed Cross-Shaped Steel  
Columns**

**Research Report No R869**

**Derrick C Y Yap BE**

**Gregory J Hancock BSc BE PhD DEng**

**April 2006**

ISSN 1833-2781



The University of Sydney

School of Civil Engineering  
Centre for Advanced Structural Engineering  
<http://www.civil.usyd.edu.au/>

## Compression Tests of High Strength Cold-Formed Cross-Shaped Steel Columns

Research Report No R869

Derrick C Y Yap, BE  
Gregory J Hancock, BSc, BE, PhD, DEng

April 2006

### Abstract:

This report describes the experimental investigation of a series of compressive tests on a stiffened-cross shaped section fabricated from cold-formed high strength steel of thickness 0.42 mm and nominal yield stress of 550 MPa. The complex shape has been chosen so that it has a local buckling mode, two distinct distortional buckling modes and a flexural-torsional mode. The first distortional buckling mode has a shorter buckle half-wavelength and hence classified as a *short half-wavelength distortional buckling mode*, while the other distortional mode has a much longer buckle half-wavelength and is classified as a *long half-wavelength distortional buckling mode*. The compression tests were carried out in a 300 kN capacity SINTEC testing machine over a range of lengths with fixed-ended conditions. The varying lengths were chosen so as to observe the buckling modes and the possibility of interaction between them. The experimental results are then compared with design methods in the existing design standards. The methods include the Direct Strength Method (DSM) recently incorporated in the North American Specification and the Australian Cold-Formed Steel Structures Standard AS/NZS 4600. When compared to the existing methods, the test results indicated that at intermediate and longer specimen lengths, the interaction of local and distortional buckling modes has a significant effect on the strength of the section.

This report presents the procedures taken to design the complex shape and the experiments carried out to obtain the geometric imperfections and material properties of the specimens and the test results. New design methods are proposed for the local buckling Direct Strength Method curve as well as for the distortional buckling strength curves so as to account for the effects of interaction of local and distortional buckling modes.

### Keywords:

Cold-formed; High strength steel; Local buckling; Distortional buckling; Interaction buckling; Intermediately-stiffened elements

## Copyright Notice

### School of Civil Engineering, Research Report R869

### Compression Tests of High Strength Cold-Formed Cross-Shaped Steel Columns

© 2006 Derrick C. Y. Yap & Gregory J. Hancock

Email: [D.Yap@civil.usyd.edu.au](mailto:D.Yap@civil.usyd.edu.au)  
[hancock@eng.usyd.edu.au](mailto:hancock@eng.usyd.edu.au)

ISSN 1833-2781

This publication may be redistributed freely in its entirety and in its original form without the consent of the copyright owner.

Use of material contained in this publication in any other published works must be appropriately referenced, and, if necessary, permission sought from the author.

Published by:  
School of Civil Engineering  
The University of Sydney  
Sydney NSW 2006  
AUSTRALIA

April 2006

This report and other Research Reports published by The School of Civil Engineering are available on the Internet:

<http://www.civil.usyd.edu.au>

# TABLE OF CONTENTS

<b>TABLE OF CONTENTS</b> .....	<b>3</b>
<b>1 INTRODUCTION</b> .....	<b>5</b>
<b>2 PREVIOUS TESTS ON THIN-WALLED HIGH STRENGTH SECTIONS</b> .....	<b>6</b>
<b>3 TEST SPECIMEN</b> .....	<b>6</b>
3.1 DESIGN OF OPEN-SECTION SHAPE COLUMN .....	6
3.1.1 <i>Semi-analytical finite strip method (SAFSM)</i> .....	7
3.1.2 <i>Spline finite strip method</i> .....	7
3.2 LENGTH OF COLUMN .....	8
3.3 MATERIAL PROPERTIES .....	8
3.3.1 <i>Material thickness</i> .....	9
3.3.2 <i>Tensile coupons and testing results</i> .....	9
3.4 LABELLING .....	10
3.5 GEOMETRIC IMPERFECTION MEASUREMENTS .....	10
<b>4 COLUMN TESTS</b> .....	<b>11</b>
4.1 GENERAL .....	11
4.2 COLUMN TESTS .....	11
4.3 RESULTS OF COMPRESSION TESTS AND OBSERVATIONS .....	11
4.3.1 <i>Effect of inward and outward deflection cases on section strength</i> .....	13
<b>5 DESIGN METHODS COMPARED WITH TEST RESULTS</b> .....	<b>14</b>
5.1 GENERAL .....	14
5.2 NOMINAL MEMBER CAPACITY $N_c$ TO CLAUSE 3.4 (EFFECTIVE WIDTH METHOD) .....	15
5.2.1 <i>Local and overall buckling <math>N_c</math> (EWM)</i> .....	15
5.2.2 <i>Distortional buckling <math>N_{cd}</math> (EWM)</i> .....	15
5.3 NOMINAL MEMBER CAPACITY $N_c$ TO CLAUSE 7 (DIRECT STRENGTH METHOD) .....	16
5.3.1 <i>Local and overall buckling <math>N_{cl}</math> (DSM)</i> .....	16
5.3.2 <i>Distortional buckling <math>N_{cd}</math> (DSM)</i> .....	17
<b>6 PROPOSED DESIGN METHODS TO DIRECT STRENGTH METHOD</b> .....	<b>18</b>
6.1 PROPOSED METHOD FOR LOCAL BUCKLING .....	18
6.2 PROPOSED METHOD FOR DISTORTIONAL BUCKLING .....	18
6.2.1 <i>Method 1</i> .....	19
6.2.2 <i>Method 2</i> .....	19
6.2.3 <i>Method 3</i> .....	19
<b>7 CONCLUSIONS</b> .....	<b>20</b>
<b>ACKNOWLEDGEMENTS</b> .....	<b>21</b>
<b>REFERENCES</b> .....	<b>22</b>
<b>NOTATIONS</b> .....	<b>24</b>
<b>FIGURES</b> .....	<b>25</b>
<b>TABLES</b> .....	<b>44</b>
<b>APPENDIX A</b> .....	<b>47</b>
GEOMETRIC AND IMPERFECTION MEASUREMENTS .....	47
<b>APPENDIX B</b> .....	<b>84</b>
EXPERIMENTAL GRAPHS .....	84



# 1 INTRODUCTION

Cold-formed steel structures are steel structures that are made by bending flat sheets of steel at ambient temperature into shapes, while hot-rolled steel sections are shaped at elevated temperatures (Hancock, 2003). Cold-formed sections are usually bent by either roll-forming or brake pressing. Davies (2000) highlighted some of the developments of cold-formed steel sections including higher strength steels, evolution of complex section shapes and improved rolling and forming technology.

With ever-advancing technology, cold-formed members are being fabricated with higher yield stress materials. With the use of higher strength steels comes a reduction in thickness, which leads to the development of highly stiffened sections with more folds and stiffeners (Rondal, 2000). In fact with this development, there are numerous applications for cold-formed steel members. Pekoz (1999) noted that there would be a strong interest for the application of cold-formed framing systems in residential and low-rise buildings. These framing systems can have sections that are as thin as 0.42mm with a high yield stress of 550 MPa (Rogers, Yang and Hancock, 2003). These sections can also be used as structural members for plane and space trusses, purlins for roof systems and steel decking (Hancock, 1998). With the design of complex sections, structural instabilities will inevitably be introduced when such steel columns are subjected to compression. Generally, in compression, most columns will exhibit 3 main buckling modes, namely local buckling, distortional buckling and flexural/flexural-torsional buckling as shown in Fig 1. A finite strip buckling analysis (Papangelis and Hancock, 1995) was used to compute the buckling modes and buckling stresses given in Fig. 1 at increasing half wavelengths for the given section.

As defined in the Australian Standard for Cold-formed Steel Structures AS/NZS 4600 (Standards Australia, 2005), local buckling can be defined as the buckling of individual plate elements at relatively short half wavelengths. Distortional buckling consists of the membrane and flexural deformation of the cross section at intermediate half wavelengths. Flexural-torsional buckling is the lateral and torsional deformation of the section without change of cross-sectional shape. The Australian Standard contains design rules for local, distortional and flexural-torsional buckling and allows for the interaction of local and flexural-torsional buckling, but not local and distortional buckling.

For the cross-shaped section in Fig 1, it can be seen that local buckling occurred mainly in the edge-stiffened plate elements including the lips. Distortional buckling, in this case, consists of rotations of the flanges and lips about the uppermost flange-web junctions and includes some transverse bending of the side plate elements. It occurs at a half-wavelength between local and flexural-torsional modes but closer to the flexural-torsional mode. At long half-wavelengths, the flexural-torsional mode rotates about a line parallel with the column axis above the top plate element. The test shape used in this paper is similar to that in Fig 1 except that an intermediate stiffener is included in the rear flange to allow it to be wider and permit manufacture of the section.

In this report, the main objective is to perform tests on thin-walled high strength steel sections which have coincident local, distortional and possibly flexural-torsional buckling modes, including multiple distortional modes at different half-wavelengths. The tests are compared with design rules in the 2005 Australian Standard and the 2001 North American Specification (NAS, 2001) and its 2004 supplement (NAS, 2004), which includes the Direct Strength Method. Proposals to account for the interaction of local and distortional buckling are given.

## 2 PREVIOUS TESTS ON THIN-WALLED HIGH STRENGTH SECTIONS

Tests were conducted by Yang and Hancock (2004) on intermediate stiffened lipped channels, brake-pressed from high strength aluminium/zinc-coated Grade G550 structural steel to Australia Standard AS 1397 (1993) with thickness 0.42 mm and a nominal yield stress of 550 MPa. The length of the columns ranged from 360 mm to 2000 mm. The tests showed the interaction of local and distortional buckling modes for very thin sections. They noted that at intermediate column lengths, the interaction of local and distortional modes induced a premature failure of the intermediately stiffened channel shape as shown in Fig 2. Failure occurred at loads lower than the predicted distortional buckling strength, which was itself lower than the local buckling strength as shown in Fig. 2. Hence the aim of the experiments in this report was to design a new open-section cross-shaped column and to test and observe any possible interaction of buckling modes. The main objective here is to verify the interactions observed by Yang and Hancock (2004) for a different shaped section, and to verify and enhance the proposed design equations.

Narayanan and Mahendran (2003) carried out tests on a series of innovative cold-formed steel columns to investigate the distortional buckling behaviour under axial compression. The tests consisted of G550 steel with thicknesses of 0.8 mm and 0.95 mm, and G250 steel with thicknesses of 0.96 mm and 1.14 mm. The buckling and ultimate strength behaviours of the columns were investigated using finite strip and finite element programs, and the results were compared with experimental results to the Australian cold-formed steel standard.

## 3 TEST SPECIMEN

### 3.1 Design of open-section shape column

The initial open section shape was based on the innovative cold-formed steel column described by Narayanan and Mahendran (2003). The semi-analytical finite strip buckling analysis software THINWALL (Papangelis and Hancock, 1995) was used to optimise an open section shape, similar to Fig 1, so as to achieve local and multiple distortional buckling at similar stresses as shown in Fig 3. However as it was deemed difficult to fabricate the section, the open section shape was made wider with an intermediate stiffener added longitudinally along the rear flange as shown in Fig. 4 to facilitate fabrication. Two different finite strip methods were used to analyse the buckling half-wavelengths and corresponding buckling stresses of the new intermediately stiffened section. These methods are the semi-analytical finite strip method (SAFSM), which assumes simply supported ends, as described in detail in Section 3.1.1 and the spline finite strip method (SFSM) as described in detail in Section 3.1.2.

As it was desired to have similar local and distortional buckling stresses for the designed section, the lip length and lip angle had to be determined. A series of sections with different lip lengths and lip angles was analysed using THINWALL. Lip lengths of 4.24, 5.66, 7.07 and 8.49 mm with lip angles of 90°, 120° and 135° were analysed and the results are shown in Table 1. All sections can be observed to have multiple distortional modes as shown in Figs. 3 and 4 with some sections having up to three distortional modes although two are normally dominant as shown in Figs. 3 and 4. The multiple modes are discussed later in the report. The local and distortional buckling stresses increase with lip size and angle except at

a lip length of 8.49 mm where the local buckling stress decreases. From Table 1, it can be seen that at lip lengths of 7.07 and 8.49 mm the sections have three distortional buckling modes, with one of the modes significantly higher than the local buckling stress. Hence it was not found desirable to analyse these sections further. At a lip length of 4.24 mm, the distortional buckling stresses are less than the associated local buckling stresses however it is preferable to have the stresses closer. At a lip length of 5.66 mm, the sections with 90° and 120° have distortional buckling stresses higher than the local buckling stresses and were not further analysed. Therefore the section with a lip length of 5.66 mm and a lip angle of 135° was chosen for this research as the shorter half-wavelength distortional buckling stress is similar to the local buckling stress. This distortional buckling stress was found to increase slightly with the effect of fixed ended conditions and presents an opportunity to investigate the interaction of local and distortional buckling modes.

### 3.1.1 Semi-analytical finite strip method (SAFSM)

The semi-analytical finite strip method of buckling analysis of thin-walled sections (Cheung, 1976) is a very efficient tool for investigating the buckling behaviour of cold-formed members in compression and bending. SAFSM assumes thin-walled sections buckle with simple supported ends free to warp but with section distortion prevented at the ends. The buckling stress for each buckling mode is plotted along the buckle half-wavelength and is shown as the solid line in Fig 4. It can be observed that local buckling occurred at very short half wavelengths of approximately 30 mm and it can be noted that local buckling occurs in all plate elements.

Multiple distortional buckling modes are also observed for the section at different half-wavelengths. The first distortional mode is observed to occur at short half-wavelengths of approximately 230 mm. This is considered relatively short when compared to the full length of a column. In contrast, the second distortional mode occurs at a longer half-wavelength of approximately 1800 mm. For this particular section, the first distortional mode can be classified as a *short half-wavelength distortional mode*, and displays flange and lip distortions. The second distortional mode is classified as a *long half-wavelength distortional mode* and has rotations of the sides about the uppermost flange-web junction.

From Figs 3 and 4, both sections, with and without the intermediate stiffeners, have relatively similar local buckling stresses of 149.2 MPa and 154.9 MPa respectively. The short half-wavelength distortional mode has a buckling stress of 145.9 MPa for both sections and is relatively similar to the local buckling stress, allowing for the possibility of interaction between the two modes at intermediate lengths. The similarity in buckling stresses between the two sections is observed in the long half-wavelength distortional mode as well. With the inclusion of the intermediate stiffener in the rear flange, there is negligible difference in the buckling stresses and buckle half-wavelengths for the different modes, hence the intermediately-stiffened section was adopted as the final test section for this research. The elastic local and distortional buckling stresses are summarised in Table 2.

### 3.1.2 Spline finite strip method

The SFSM (Lau and Hancock, 1986) buckling analysis, defined by the circle and dashed line in Fig. 4, assumes fixed-ended boundary conditions. This method is more powerful than the SAFSM as it is able to account for different boundary conditions other than simply supported (Cheung, 1976). The SAFSM analysis gives the elastic local and distortional buckling stresses at a given half-wavelength, whereas the SFSM determines the buckling mode and stress at a given length between two fixed ends. The section was constructed with 29 nodal

strips and 30 spline sections longitudinally as shown in Fig. 5. At long half-wavelengths of 3000 mm, the section displayed only flexural-torsional buckling modes. It can be observed from Fig. 4 that the buckling stresses of the long half-wavelength distortional mode at a column length of 2700 mm and the flexural-torsional mode at a column length 3000 mm onwards have increased significantly due to the effect of fixed-ended boundary conditions.

Local buckling from the SFSM analysis occurs at column lengths 30 mm to 1000 mm and is associated with increasing numbers of local buckle half-waves, as shown in Fig. 6a. It has a similar buckle half-wavelength (30 mm) and buckling stress (154 MPa) as the SAFSM analysis. However, at a column length of 600 mm, local and short half-wavelength distortional buckling modes appeared simultaneously as shown in Fig. 6b. Note that Figs. 6b, 6c and 6d have been shortened longitudinally producing different horizontal and vertical scales.

The short half-wavelength distortional mode can be seen to occur alone in Fig. 6c at approximately 1200 mm with five buckle half-waves. The corresponding buckling stress (152 MPa) is slightly higher than the short half-wavelength buckling minima (145 MPa) of the SAFSM analysis due to the effect of end conditions. Therefore, interaction of local and short half-wavelength distortional buckling modes may occur at intermediate lengths.

The long half-wavelength distortional mode as shown in Fig. 6d occurs at approximately 2700 mm with one buckle half-wave. The buckling stress (150 MPa) is much higher than the long half-wavelength buckling minima (95 MPa) of the SAFSM analysis due to the fixed ends. With the effect of fixed ends, the local, short half-wavelength distortional and long half-wavelength distortional buckling modes have relatively similar buckling stresses along a column length up to approximately 2700 mm. Therefore interaction of local and short and long half-wavelength distortional buckling modes may occur at longer lengths since all modes have similar buckling stresses for the fixed-ended section. The elastic buckling stress and corresponding buckling mode for the chosen specimen lengths are summarised in Table 2.

## 3.2 Length of column

The objective of the test program was to investigate the interaction of local and multiple distortional buckling modes. Analysis of the section was performed to determine the distortional buckling stresses and buckle half-wavelengths using the above-mentioned methods, SAFSM and SFSM. A short column length of 110 mm was chosen to test the section undergoing local buckling only. A series of intermediate lengths were chosen to investigate distortional buckling. The chosen lengths were 600, 1200, 1600 and 2000 mm. The length of 2000 mm was chosen to be the longest as it was at the maximum range of the test machine.

## 3.3 Material properties

The steel sheets were produced using a process called cold reduction, whereby the material's strength and hardness is increased. This method also allows the material's thickness to be formed accurately. Initially the sheet steels are rolled to size in a hot strip mill with finishing and coiling temperatures of 940 °C and 670 °C respectively. The hot worked coil of steel, typically 2.5 mm thickness with a minimum specified 300 MPa yield stress, is uncoiled and cleaned in an acid solution to remove surface oxides and scale. The uncoiled steel is then trimmed to size and fed into a cold reduction mill, which may contain up to six sets of stands.

High compressive force in the stands and strip tension systematically reduce the thickness of the steel sheet until the desired dimension is reached.

The milling process causes the grain structure of cold reduced steels to elongate in the rolling direction, whereby there is an increase in material strength and a decrease in material ductility. The effects of cold working are cumulative, i.e. grain distortion increases with further cold working, however it is possible to change the distorted grain structure and control the steel properties through heat treatment. Various types of heat treatment exist and are used for different steel products. G550 sheet steels are stress relief annealed, whereby recrystallisation does not occur. Stress relief annealing involves heating the steel to below the recrystallisation temperature, holding the temperature until the temperature is constant throughout the thickness and then cooling slowly. Mild sheet steels of similar thicknesses are annealed to a greater extent in comparison with G550 sheet steels, and hence recover their ductile behaviour. Annealing is carried out in the hot dip coating line prior to application of either zinc or aluminium/zinc coating. Upon cooling the sheet steel may be further processed through a tension levelling mill, e.g. 0.35% extension, to improve the finish quality and flatness of the coil (BHP, 1992). The G550 sheet steels must be differentiated from other sheet steels whose high yield stress and ultimate strength values are obtained by means of an alloying process, i.e. high strength low alloy (HSLA) steels.

The material property requirements for G550 or Grade E sheet steels are specified in Australia by AS 1397 (1993) and in North America by the following ASTM standards, A653 (2000), A792 (1999), A875 (1999) and A1039 (2004). The steels used for this research were from two different coils, one of which was the same coil used by Yang and Hancock (2004) and the other a new coil from BlueScope Steel.

### 3.3.1 Material thickness

The thickness of the steel sheet has to be accurately measured in order to determine the buckling stress of the section. A layer of corrosion protection coating was applied to the steel sheet during the manufacturing process. Since the thickness of the steel sheet is very thin, this coating may allow the steel to carry more load, hence the base metal thickness of the virgin material had to be determined.

This coating was removed to expose the virgin (base) material by acid etching. The base metal thickness was measured using a digital vernier calliper. The average thickness for the steel sheet is 0.40 mm.

### 3.3.2 Tensile coupons and testing results

Tensile coupons were used to determine the material properties. The test specimens were fabricated out of two different rolls of steel sheet. The original roll, from which 14 of the 15 specimens were fabricated, spare material was taken to fabricate the coupons. A new roll of steel sheet was used to fabricate the last specimen and its remaining material was used to fabricate the coupons.

The coupon dimensions conformed to the Standards Australia AS 1391 (1991) for the tensile testing of metals using 12.5 mm wide coupons with gauge length 50 mm. Rogers and Hancock (1996) noted that a larger radius (55 mm) was required to have a gradual change of cross section from the constant gauge width to the grip in order for the coupon to fail in the middle portion of the constant gauge width. Five tensile coupons were tested for each of the

two different steel sheets with the labels B1\_1 and so forth for the first roll of steel and B2\_1 for the other roll of steel.

The tests were carried out using the Sintech/MTS-300 kN testing machine. The coupons were secured in a pair of vices and an extensometer was used to record the elongation. The yield stress  $F_y$  was obtained using the 0.2 % nominal proof stress. The stress was the load measured divided by the initial cross-sectional area of the coupon. The measured 0.2 % proof stress is shown in Table 3 and ranged from 651 MPa to 694 MPa. The 0.2% proof stress for the second roll of steel (B2) was unable to be determined as the coupon necked and eventually fractured outside the range of the extensometer. The position of the fracture explains why the strain at the ultimate was measured at 0.3 % elongation for all the B2 coupons. The calculated mean value of  $F_y$  is approximately 673 MPa.

The Young's modulus of elasticity ( $E$ ) was also calculated from the stress-strain curves. The calculated mean value of the Young's modulus of elasticity was 228.06 GPa and is shown in Table 3. As these values are based on an extensometer and not strain gauges, then the high values of Young's modulus of elasticity measured may be partly due to the measuring technique. Tests by Yang and Hancock, where strain gauges were used, gave values of approximately 220 GPa.

### 3.4 Labelling

The test specimens were labelled such that the end conditions, type of test, nominal length of specimen and specimen number were expressed by the label.

For example, the label "SCR110\_1" defines the following specimen:

- "SCR" indicates that the section is a stiffened-cross
- "110" indicates the nominal length of the column was 110 mm
- "\_1" indicates the specimen number at a specific length (alternatively "\_2" and "\_3")

### 3.5 Geometric imperfection measurements

Geometric imperfections were measured for all of the test specimens, except specimens SCR110\_1, SCR110-2 and SCR110\_3, with lasers attached to a guide to measure the readings along the specimen length. For the flanges measured, the readings were taken along the centreline between the corners as shown in Fig. 7, indicated as 'L' for laser positions. The main components included consisted of a guide frame, three laser sensors, a Datataker data logger and a synchronous motor. The lasers were attached to individual movable seats, so that they can be adjusted onto the flanges' centreline. The seats are drawn by a synchronous motor in order to keep the sensor moving smoothly and at a constant rate. Each specimen was positioned horizontally across the lasers and was clamped to ensure stability during the testing. The readings were recorded at a rate of 0.5 mm/sec along the specimen length. In addition to the laser measurements, the flanges and the lips were also measured as indicated in Fig. 7 with labels 'F' and 'S' respectively. The full set of measurements is given in Appendix A. The maximum imperfections are summarised in Table 4 and were computed relative to a straight line between the ends.

## 4 COLUMN TESTS

### 4.1 General

A total of 15 specimens was tested at various lengths of 110 mm, 600 mm, 1200 mm, 1600 mm and 2000 mm. The test rig consisted of the SINTECH/MTS-300kN testing machine with fixed-ended bearings as shown in Fig. 8. The bottom bearing was adjustable so that it could orientate the specimens vertically with the ends flat on the plates before the bearing was secured for testing. Specially designed end plates were filled with pattern stone as shown in Fig. 8 to ensure a fixed end boundary condition. The plates also ensured uniform compression and prevented the top and bottom edges from localized failure (Yang and Hancock, 2002). Load and axial shortening was recorded using the SINTECH data acquisition system at a compressive deformation rate of 0.05 mm/min.

Lateral deflections were measured using three LVDT transducers positioned at fixed locations around the specimen (T1, T2 and T3) and located at both edge-stiffened flanges and on the stiffener at the rear flange as shown in Fig. 9. This was carried out at fixed locations along the length of each specimen at the quarter, mid and three-quarter height positions. For some of the test specimens, two additional transducers (T4 and T5) were employed to measure the deflection of the side flanges, indicated by the dashed arrows in Fig. 9. A transducer was positioned to measure the axial deflection (stroke) of the crosshead to minimise errors with the elasticity of the testing machine. The transducers were measured by connecting to a Vishay System 5000 data acquisition system.

### 4.2 Column tests

The results of the compression tests for the stiffened-cross sections are shown in Table 5 and all but one specimen (SCR600\_3) was carried out. The specimen SCR600\_3 was not tested and was used to produce the tensile coupons. In addition, the results for specimen SCR110\_3 are ignored as the boundary condition applied was locally pinned and globally fixed whereas all other specimens had fixed end conditions.

The average ultimate test strengths were approximately 46.8 kN, 38.6 kN, 34.7 kN, 31.4 kN and 29.3 kN respectively for specimen lengths 110 mm, 600 mm, 1200 mm, 1600 mm and 2000 mm as shown in Table 5. The theoretical squash load was calculated to be 105.3 kN and the average ultimate load of the specimens were approximately 44 %, 37 %, 33 %, 30 % and 28 % of the theoretical squash load for the 110 mm, 600 mm, 1200 mm, 1600 mm and 2000 mm specimen lengths respectively. The ultimate loads were noted to be significantly higher than the theoretical local buckling load of 24.2 kN and both the theoretical short half-wavelength and long half-wavelength distortional buckling loads of approximately 23.8 kN respectively for all specimen lengths accounting for the fixed end boundary conditions. This indicated that the columns had high post-local buckling reserve strength and were well into the post-distortional buckling regions prior to failure.

### 4.3 Results of compression tests and observations

All compression test results including the load versus axis shortening and the load versus LVDT measurements are given in Appendix B. The combined results for all test specimens are shown in Figs. 10a and 10b to allow comparison. Some of the early tests (e.g. SCR600\_1) used a coarse range data measurement and showed a stepped output. Later results used more accurate LVDT transducers.

For the test specimens of column lengths 110 mm, the failure modes are observed to be purely local buckling as shown in Fig. 11 and with failure occurring in all flanges. The failure modes are similar to the local buckling for short columns as seen in Fig. 6a using SFSM analysis.

For specimens with column length 600 mm, the failure modes are shown in Figs. 12a and 12b. Specimens SCR600\_1 and SCR600\_2 failed with inelastic local buckling occurring in the rear flanges, however the lips were also inelastically locally buckled prior to failure with the edge-stiffened flanges deforming in a short half-wavelength distortional mode. The failure loads were approximately 38 kN and were much higher than the elastic local buckling load of approximately 24 kN. When the applied load surpassed the elastic local buckling load, elastic local buckling was observed all around the column, at the same time, a short half-wavelength elastic distortional buckling mode with one buckle half-wave was observed to have formed on the edge-stiffened flanges as shown in Fig. 12c, interacting with the local buckles. This interaction of local and short half-wavelength buckling modes is similar to the SFSM analysis seen in Fig. 6b. This short half-wavelength distortional buckling mode “pulled” the edge-stiffened elements laterally in and out, and when combined with the local buckling occurring on the lips, local lip failure occurred. However, the column continued to carry load until ultimate failure occurred in the rear flanges. The points of these initial lip failures and ultimate rear flange failure can be observed in Fig. 10a on the SCR600\_2 curve.

For specimens with column length 1200 mm, specimen SCR1200\_1 failed with one flange deflecting inwards while the other deflected outwards (I-O) as seen in Fig. 13a. Specimens SCR1200\_2 and SCR1200\_3 both failed with flanges deflecting inwards (I-I) as seen in Figs. 13b and 13c. From Table 5, it can be noted that SCR1200\_1 had a slightly higher ultimate load, 36.3 kN, which most likely is due to the difference in failure modes. For all three specimens, elastic local buckling was observed around the column and the elastic short half-wavelength distortional mode with three buckle half-waves was observed to have a slight effect on both edge-stiffened flanges. For specimen SCR1200\_1, the short half-wavelength distortional buckling caused one edge-stiffened flange to deflect inwards and the other outwards. This behaviour was most likely due to either the effects of the imperfections on the specimen or that the specimen's end plates were not fully flushed prior to testing. The failure occurred when the outward deflecting edge-stiffened flange precipitated failure at the junction with the adjacent flange as seen in Fig 13d. The inward deflection at the centre of the short half-wavelength distortional buckles on specimens SCR1200\_2 and SCR1200\_3 was more dominant than the outward deflection at the ends, causing the whole length of the edge-stiffened flanges to deflect inwards at the midsection as seen in Figs. 13b and 13c. This inward deflection of the short half-wavelength distortional mode interacted with the local buckling on the side flanges, causing the side flange to fail locally, as shown in Fig. 13e. Although both SCR1200\_2 and SCR1200\_3 have similar failure modes, the ultimate failure loads were different, 33.4 kN and 34.3 kN respectively, with SCR1200\_2 having a slightly lower failure load due to an initial lip failure on the edge-stiffened flange.

For specimens with column length 1600 mm, the failure modes for SCR1600\_1, SCR1600\_2 and SCR1600\_3 are shown in Figs. 14a, 14b and 14c respectively. The elastic short half-wavelength distortional buckling mode was observed on both edge-stiffened flanges of SCR1600\_1 at a relatively low load of 7 kN with the right edge-stiffened flange noted to deflect outwards slightly at the midsection of the column while the left edge-stiffened flange deflected inwards, as shown in Figs. 14d and 14e respectively. It is interesting to note that at approximately 18 kN, the right edge-stiffened flange switched buckled shape and deflected inwards. At the same time, the inward deflection of the left edge-stiffened flange was the most dominant and hence “pulled” the whole flange inwards. This inward deflection at the

midsection of the edge-stiffened flange caused the left side flange to deflect inwards, resembling a single buckle half-wave of a long-distortional buckling mode. The column had elastic local buckling interacting with the elastic long half-wavelength distortional buckling mode, resulting in an inelastic local failure along the side flange as seen in Fig. 14a.

Similar failure mode behaviour was also observed for specimen SCR1600\_2, with the right edge-stiffened flange remaining relatively straight while the left edge-stiffened flange was deflecting inwards at the midsection of the column, as shown in Figs. 14f and 14g. Similar to the previous specimen, the elastic short half-wavelength distortional buckling mode was initially observed for the left edge-stiffened flange and deflected to resemble an elastic long half-wavelength distortional buckling mode at approximately 15 kN. The column had elastic local buckling interacting with the elastic long half-wavelength distortional buckling mode, resulting in an inelastic local failure along the side flange as seen in Fig. 14b. Both SCR1600\_1 and SCR1600\_2 failed locally on the side flanges with both edge-stiffened flanges deflected inwards (I-I) and had similar failure load of 31.6 kN.

Specimen SCR1600\_3 failed with both edge-stiffened flanges deflecting outwards (O-O) as shown in Fig. 14c. At approximately 15 kN, the outward deflection at the centre was more dominant and the right edge-stiffened flange was noted to deflect outwards at the midsection of the column while the left edge-stiffened flange deflected inwards slightly, as shown in Figs. 14h and 14i respectively. After elastic local buckling was observed on the specimen, the left edge-stiffened flange switched mode and began to deflect outwards, resembling a long half-wavelength distortional buckling mode with a single buckle half-wave. The failure was an inelastic buckle that occurred at the junction of the rear and adjacent side flanges and the failure load was slightly lower than the previous two specimens with 31.1 kN.

For specimens with column length 2000 mm, both specimens SCR2000\_1 and SCR2000\_2 failed with the edge-stiffened flanges deflecting inwards (I-I) as shown in Figs. 15a and 15b respectively. Similar to the inward deflecting specimens of SCR1600\_1 and SCR1600\_2, elastic local buckling was observed around the specimens, while the edge-stiffened flanges deflected inwards at the centre deforming to resemble the elastic long half-wavelength distortional mode with one buckle half-wave. The specimens had local buckling interacting with the long half-wavelength distortional buckling, resulting in inelastic failures at the side flanges. Both SCR2000\_1 and SCR2000\_2 failed locally at the side flanges with both edge-stiffened flanges deflecting inwards (I-I) and both had a similar failure load of 28.4 kN.

Specimen SCR2000\_3 failed with both edge-stiffened flanges deflecting outwards (O-O) as shown in Fig. 15c. The outward deflections at the midsections of the edge-stiffened flanges were more dominant and hence resembled an elastic long half-wavelength distortional buckling mode with one buckle half-wave. Elastic local buckles were observed around the column and the interaction of the local and long half-wavelength distortional buckling modes is shown in Fig. 15d. This interaction caused a loss in column stiffness at approximately 28 kN as observed, with a pointer, as a change in gradient on the SCR2000\_3 curve in Fig. 10b. The column continued to carry load to ultimate failure where inelastic buckling occurred in the junction of the rear flanges and the adjacent side flanges. The ultimate failure load 31.1 kN was higher than the failure loads (28.4 kN, 28.4 kN) of the two inward deflecting specimens as seen in Table 5.

### 4.3.1 Effect of inward and outward deflection cases on section strength

Specimens with column length 1200 mm had two failure modes where the edge-stiffened flanges deflected inward (I-I) and one failure mode with inward and outward (I-O) deflections of the edge-stiffened flanges. The specimen with the (I-O) deflection had a

higher ultimate failure mode. Specimens with column lengths 1600 mm and 2000 mm had two failure modes where the edge-stiffened flanges deflected inward (I-I) and one failure mode with outward (O-O) deflections of the edge-stiffened flanges. The 1600 mm specimen with (O-O) deflections had a slightly lower ultimate failure mode when compared to the specimens with (I-I) deflections. The 2000 mm specimen with (O-O) deflections had a higher ultimate failure load when compared to the specimens with (I-I) deflections. With the exception of the 1600 mm specimen, specimens that have an outward deflection tend to have a higher ultimate load. This can be explained using both the inward (SCR1600\_1 and SCR2000\_1) and outward (SCR1600\_3 and SCR2000\_3) deflecting specimens and comparing the deflections of the edge-stiffened flanges as shown in Fig. 16.

It can be seen in Fig. 16 that specimens SCR1600\_1 and SCR2000\_1 had one edge-stiffened flange deflecting inwards beginning at very low loads of approximately 10 kN. With such significant inward deflections, the edge-stiffened flanges would not be able to carry much load, and would have to distribute the increasing loads to the side flanges as it continued to deflect inwards. This would cause a concentration of loads at the side flanges, resulting in an inelastic local failure at the side flanges usually at the midsection of the column.

For the outward deflecting specimens, SCR1600\_3 and SCR2000\_3, the edge-stiffened flanges remained relatively straight up to approximately 23 kN. This allowed the column to be more rigid and to carry more loads. When the specimens began to deflect outwards, the side flanges also deflected outwards, and the loads from the edge-stiffened flanges were distributed to the junction of the rear and adjacent flanges. Therefore at ultimate load, the failure mode was an inelastic distortional buckling along the rear flange usually at the midsection of the column. This explains why the 1200 mm I-O deflecting specimen has a higher ultimate load than the I-I specimens. Since the SCR1600\_3 specimen has slightly more outward deflection of the edge-stiffened flange, most likely due to imperfections, than the SCR2000\_3 specimen, it was unable to carry more load and hence failed at a slightly lower load than the inward deflecting specimen (SCR1600\_1).

## 5 DESIGN METHODS COMPARED WITH TEST RESULTS

### 5.1 General

Two design methods can be used to predict the member compression capacity: the Effective Width Method (EWM) and the Direct Strength Method (DSM). The EWM accounts for postbuckling of plate elements by using the effective width at the design stress (Von Karman, Sechler and Donnell, 1932). However as sections are designed with more complex shapes, the calculation of effective widths becomes more complicated and may be less accurate. The DSM was developed by Schafer and Pekoz (1998) to overcome this problem by using elastic buckling stress for a whole section rather than individual plate elements. Both methods were used to predict the nominal member capacity of this open-section column and the strength curves are compared in this paper.

The Standard AS/NZS 4600:2005 Cold-formed Steel Structures was used to predict the strength curves as the DSM was included in the revised standard along with minor amendments to the EWM of AS/NZS 4600:1996. The test results are plotted against the effective length of the column and are compared to the design strength curves as detailed in Sections 5.2 and 5.3.

## 5.2 Nominal member capacity $N_c$ to Clause 3.4 (Effective Width Method)

### 5.2.1 Local and overall buckling $N_c$ (EWM)

The nominal member capacity  $N_c$  (EWM) is based on Eq. 3.4.1 (2) of AS/NZS 4600:2005 and uses the effective width formula and conventional column design curve. It allows for interaction of local and overall buckling only. It is the same in the new standard as in AS/NZS 4600:1996 and is represented by ( $\Delta$ ) in Fig. 17. It intersects the vertical axis of an effective length of zero at a section capacity,  $N_s$ , which is shown by a solid line (—) in Fig. 17. The DSM design curves can be compared with these reference lines.

The section capacity  $N_s$  was obtained using the EWM and was approximately 43.5 kN, which was slightly lower than the average ultimate test strength of 46.7 kN for the specimens with column length 110 mm. The strength curves and test results have been plotted against an effective length,  $l_e$ , which is half of the column length to allow for the fixed ends. Other than the 110 mm specimens, the test results showed that the average ultimate test strengths for all longer length specimens were much lower than the predicted member capacity. The reason for the unconservative results at longer lengths is believed to be the interaction of local and distortional buckling.

### 5.2.2 Distortional buckling $N_{cd}$ (EWM)

Two values are shown for this strength curve, which is based on the Cl 3.4.6 of AS 4600. The equations are shown below.

$N_{cd}$  (EWM):

$$\text{For } f_{od} > \frac{f_y}{2}: \quad N_{cd} = Af_y \left( 1 - \frac{f_y}{4f_{od}} \right) \quad (1)$$

$$\text{For } \frac{f_y}{13} \leq f_{od} \leq \frac{f_y}{2}: \quad N_{cd} = Af_y \left[ 0.055 \left( \sqrt{\frac{f_y}{f_{od}}} - 3.6 \right)^2 + 0.237 \right] \quad (2)$$

These are for short (SWD) and long (LWD) half-wavelength distortional buckling. They are shown by ( $\circ$ ) and ( $\star$ ) respectively in Fig. 17 and form a cutoff at lower slenderness for  $N_c$  (EWM). The elastic distortional buckling stresses ( $f_{od}$ ) used in these calculations are based on the SAFSM values as seen in Table 2 for SWD and LWD.

The strength curve for the short half-wavelength distortional buckling was slightly conservative for specimens with column length 600 mm at approximately 38 kN. However the short half-wavelength distortional strength curve was unconservative having higher values of approximately 7.2 % for the specimens with column lengths 1200 mm, which were seen to fail in the short half-wavelength distortional buckling mode. This is most likely due to the interaction of local and short half-wavelength distortional buckling modes not being accounted for.

Specimens with column lengths 1600 mm and 2000 mm were theoretically analysed to fail with short half-wavelength distortional buckling mode with five and six buckle half-waves

respectively as shown in Table 2. Comparing with the short half-wavelength distortional strength curve, it can be seen to be unconservative with the strength curve predicting approximately 15 % and 10.8 % higher respectively. However, during the tests, the buckled shapes for specimens at 1600 mm and 2000 mm were observed to resemble a long half-wavelength distortional buckling mode, as previously detailed in Section 4.3. Therefore if the long half-wavelength distortional strength curve was used to predict and compare with the test results, it can be seen from Fig. 17 that specimens with column length 1600 mm are predicted to be conservative, while specimens with column length 2000 mm are just slightly unconservative. This strength curve appears to predict the longer length specimens more accurately, but the interaction of local and long half-wavelength distortional buckling modes have not been accounted for in Eqs. 1 and 2.

## 5.3 Nominal member capacity $N_c$ to Clause 7 (Direct Strength Method)

### 5.3.1 Local and overall buckling $N_{cl}$ (DSM)

The equation to predict  $N_{cl}$  (DSM) is based on Cl 7.2.1.3 of AS/NZS 4600:2005. It requires  $N_{ce}$  (DSM), which is based on Cl 7.2.1.2 of AS/NZS 4600:2005. The equations are as shown below.

$N_{ce}$  (DSM):

$$\text{For } \lambda_c \leq 1.5: \quad N_{ce} = (0.658^{\lambda_c^2}) N_y \quad (3)$$

$$\text{For } \lambda_c > 1.5: \quad N_{ce} = \left( \frac{0.877}{\lambda_c^2} \right) N_y \quad (4)$$

where,

$$\begin{aligned} \lambda_c &= \text{non - dimensional slenderness used to determine } N_{ce} \\ &= \sqrt{N_y / N_{oc}} \end{aligned}$$

$$\begin{aligned} N_{oc} &= \text{least of the elastic compression member buckling load in flexural,} \\ &\quad \text{torsional and flexural - torsional buckling} \\ &= A f_{oc} \end{aligned}$$

$$\begin{aligned} N_y &= \text{nominal yield capacity of the member in compression} \\ &= A f_y \end{aligned}$$

Nominal axial capacity for local buckling ( $N_{cl}$ ):

$$\text{For } \lambda_l \leq 0.776: \quad N_{cl} = N_{ce} \quad (5)$$

$$\text{For } \lambda_l > 0.776: \quad N_{cl} = \left[ 1 - 0.15 \left( \frac{N_{ol}}{N_{ce}} \right)^{0.4} \right] \left( \frac{N_{ol}}{N_{ce}} \right)^{0.4} N_{ce} \quad (6)$$

where,

$$\lambda_l = \text{non - dimensional slenderness used to determine } N_{cl}$$

$$= \sqrt{N_{ce} / N_{ol}}$$

$$N_{ol} = \text{elastic member local buckling load in compression}$$

$$= Af_{ol}$$

This curve is shown by the solid line (—) in Fig. 17 and is significantly higher than  $N_c$  (EWM) as a result of the fact that  $N_s$ , on which  $N_c$  (EWM) is based, includes some distortional buckling of the edge stiffened elements in Cl 2.4 with a consequent reduction in the  $k$  value (Table 2.4.2) of AS/NZS 4600:2005. The test result for specimens with column length 110 mm was observed to be approximately 15.5 % lower than the predicted value of the strength curve. This unconservative prediction is most likely due to the fact that inelastic local failure occurred on all elements of the specimen as shown in Fig. 11, which is not adequately accounted for by Eq. 6 with a 0.4 exponent.

### 5.3.2 Distortional buckling $N_{cd}$ (DSM)

The equations to predict  $N_{cd}$  (DSM) are as shown:

$$\text{For } \lambda_d \leq 0.561: \quad N_{cd} = N_y \quad (7)$$

$$\text{For } \lambda_d > 0.561: \quad N_{cd} = \left[ 1 - 0.25 \left( \frac{N_{od}}{N_y} \right)^{0.6} \right] \left( \frac{N_{od}}{N_y} \right)^{0.6} N_y \quad (8)$$

where,

$$\lambda_d = \text{non - dimensional slenderness used to determine } N_{cd}$$

$$= \sqrt{N_y / N_{od}}$$

$$N_{od} = \text{elastic distortional compression member buckling load}$$

$$= Af_{od}$$

Two values are shown for this strength, which is based on Cl 7.2.1.4 of AS/NZS 4600:2005. These are for the short (SWD) and long (LWD) half-wavelength distortional buckling. They are shown by dashed-line (---) and dash-dot line (— · —) lines respectively in Fig. 17 and form a cutoff at low slenderness for  $N_{cl}$  (DSM). The elastic distortional buckling stresses ( $f_{od}$ ) used in these calculations were based on the SAFSM values as seen in Table 2 for SWD and LWD.

The strength curve for the SWD was slightly conservative for specimens with column length 600 mm at approximately 38 kN. However the SWD strength curve was unconservative having higher values of approximately 9.5 %, 21.0 % and 29.7 % for specimens with column lengths 1200 mm, 1600 mm and 2000 mm respectively. This was most likely due to the interaction of local and short half-wavelength distortional buckling modes not being accounted for by AS/NZS 4600:2005, or possibly the occurrence of the long half-wavelength distortional modes at 1600 mm and 2000 mm.

It is interesting to observe that since the horizontal lines extend to the  $N_{cl}$  (DSM) line, which is well above the  $N_c$  (EWM) line, then there is a significant region, seen as the shaded area in Fig. 17, of increased design loads in the range of effective length from approximately 750 mm for SWD and 1200 mm for LWD compared with the EWM.

## 6 PROPOSED DESIGN METHODS TO DIRECT STRENGTH METHOD

As described in Section 5.3.1, the Direct Strength Method does not predict the member capacity accurately when the column fails by local buckling only. The design method was unconservative when a column fails in all flange elements. A proposed method is required to account for the local strength curve. At longer length specimens, the design method was significantly unconservative as it does not account for the interactions of local and distortional buckling modes. A proposed method is required to account for the distortional strength curve.

### 6.1 Proposed method for local buckling

When the Direct Strength Method was used to predict the local strength curve, it predicted unconservatively when compared to the test results. This unconservative prediction is most likely due to the fact that inelastic local failure occurred on all elements of the specimen as shown in Fig. 11, which is not adequately accounted for by Eq. 6. Eq. 6 has an exponential of 0.4, which is lower than the 0.5 in the Winter formula for a single element, and most likely assumes that all elements of the section do not fail at the same time. If this is the case, the exponential in Eq. 6 should be 0.5.

The proposed nominal axial capacity for local buckling ( $N_{cl}'$ ):

$$\text{For } \lambda_l \leq 0.673: \quad N_{cl}' = N_{ce} \quad (9)$$

$$\text{For } \lambda_l > 0.673: \quad N_{cl}' = \left[ 1 - 0.22 \left( \frac{N_{ol}}{N_{ce}} \right)^{0.5} \right] \left( \frac{N_{ol}}{N_{ce}} \right)^{0.5} N_{ce} \quad (10)$$

where,

$$\begin{aligned} \lambda_l &= \text{non - dimensional slenderness used to determine } N_{cl}' \\ &= \sqrt{N_{ce} / N_{ol}} \end{aligned}$$

$$\begin{aligned} N_{ol} &= \text{elastic member local buckling load in compression} \\ &= Af_{ol} \end{aligned}$$

The proposed nominal axial capacity for local buckling,  $N_{cl}'$ , is shown as the starred-line (—★—) in Fig. 18. This proposed method predicts the local buckling relatively accurately and can be used to predict the local buckling strength curve for sections that fail in all flange elements. The elastic local buckling stress used was based on the SAFSM value in Table 2.

### 6.2 Proposed method for distortional buckling

The DSM distortional buckling strength curve is very unconservative when compared to the longer length specimens. This is most likely due to the interaction of local and distortional buckling modes and new methods have to account for this behaviour.

### 6.2.1 Method 1

Since the longer length specimens was observed to have failed in the long half-wavelength distortional buckling mode, then the long half-wavelength distortional buckling strength curve can be used to predict for longer length specimens, as previously detailed in Section 5.2.2. The strength curve for method 1 ( $\nabla$ ) is shown in Fig. 18 and is conservative for all specimens up to column length 1600 mm and is slightly unconservative for specimens with column length 2000 mm. This can be made conservative by adjusting the empirical values in Eq. 8. Therefore, sections of the type tested that display more than one distortional buckling mode, the strength curve for the longest half-wavelength mode can be safely used. The elastic distortional buckling stress used was based on the SAFSM value in Table 2 for LWD.

### 6.2.2 Method 2

With the section having more than one distortional buckling mode, it can be observed in Fig. 4 that the long half-wavelength distortional buckling mode has a buckle half-wavelength close to the flexural-torsional mode. Therefore the long half-wavelength distortional buckling mode can be considered as if it was an overall buckling mode.

It should also be noted that the  $N_{cd}$  in Cl 7.2.1.4 of AS/NZS 4600 assumes no interaction of distortional and overall buckling. To observe interaction of short half-wavelength distortional and overall buckling modes,  $N_y$  in Eqs. 7 and 8 is replaced with the overall failure loads,  $N_{ce}$ , and the proposed distortional strength curve is shown as the diamond line ( $\diamond$ ) in Fig. 18.

$$\text{For } \lambda_d \leq 0.561: \quad N_{cd} = N_{ce} \quad (11)$$

$$\text{For } \lambda_d > 0.561: \quad N_{cd} = \left[ 1 - 0.25 \left( \frac{N_{od}}{N_{ce}} \right)^{0.6} \right] \left( \frac{N_{od}}{N_{ce}} \right)^{0.6} N_{ce} \quad (12)$$

This proposed strength curve appears to be more accurate than the AS 4600 DSM curve and EWM curve shown previously in Fig. 17. This proposed strength curve is conservative for short column lengths up to 1200 mm and is slightly unconservative for 1600 mm and 2000 mm column lengths. It can be made more conservative by increasing the exponential value of 0.6 in Eq. 8 to 0.65. The elastic distortional buckling stresses ( $f_{od}$ ) used in these calculations were based on the SAFSM value in Table 2 for SWD.

### 6.2.3 Method 3

A strength curve that considers the interaction of local and distortional buckling modes is necessary. This would include the combination of two different curves, where one accounts for local and short half-wavelength distortional buckling modes while the other accounts for short half-wavelength distortional and overall buckling modes. To account for the interaction of local and short half-wavelength distortional modes, the Kwon and Hancock (1992) strength curve,  $N_{kh}$ , is adopted as the compressive member design strength,  $N_{ce}$  in Eqs. 5 and 6 and is shown below.

$$\text{For } \lambda_d \leq 0.561: \quad N_{kh} = N_y \quad (13)$$

$$\text{For } \lambda_d > 0.561: \quad N_{kh} = \left[ 1 - 0.25 \left( \frac{N_{od}}{N_y} \right)^{0.6} \right] \left( \frac{N_{od}}{N_y} \right)^{0.6} N_y \quad (14)$$

where,

$$\begin{aligned}\lambda_d &= \text{non - dimensional slenderness used to determine } N_{kh} \\ &= \sqrt{N_y / N_{od}}\end{aligned}$$

$$\text{For } \lambda_l \leq 0.776: \quad N_{c\_ld} = N_{hk} \quad (15)$$

$$\text{For } \lambda_l > 0.776: \quad N_{c\_ld} = \left[ 1 - 0.15 \left( \frac{N_{ol}}{N_{kh}} \right)^{0.4} \right] \left( \frac{N_{ol}}{N_{kh}} \right)^{0.4} N_{kh} \quad (16)$$

where,

$$\begin{aligned}\lambda_l &= \text{non - dimensional slenderness used to determine } N_{c\_ld} \\ &= \sqrt{N_{kh} / N_{ol}}\end{aligned}$$

$$\begin{aligned}N_{ol} &= \text{elastic member local buckling load in compression} \\ &= Af_{ol}\end{aligned}$$

The strength curve  $N_{c\_ld}$  is shown as the dash-dot line (—·—) in Fig. 18 and forms a cutoff at lower slenderness at  $N_{cd}$  of the proposed strength curve in method 2. The Kwon and Hancock formula inadvertently picked up the interaction of local and short half-wavelength at shorter column lengths, while at the same time the interaction of distortional and overall buckling modes are also inadvertently picked up as the long half-wavelength distortional buckling mode is very close to the overall mode. This proposed strength curve predicts the test results conservatively when interactions of buckling modes are considered. The elastic buckling stresses  $f_{ol}$  and  $f_{od}$  are based on the SAFSM values in Table 2 for the local and SWD buckling modes respectively.

## 7 CONCLUSIONS

A new innovative stiffened-cross shaped section column was designed using numerical analysis methods such as the semi-analytical finite strip method (SAFSM) and the spline finite strip method (SFSM). Both methods analyse the different buckling behaviours of the column, however SAFSM analyses with simply supported ends whereas SFSM analyses with fixed ends conditions. This stiffened-cross shape section has local buckles at very short half-wavelengths of approximately 30 mm. At intermediate lengths, the section has two different distortional buckling modes, a short half-wavelength distortional mode with a buckle half-wavelength of approximately 230 mm and a long half-wavelength distortional mode with a buckle half-wavelength of approximately 2000 mm. For the thickness used, all three modes had a similar buckling stress over a wide range of lengths.

A series of stiffened-cross shape section columns were manufactured from high strength G550 steel. Tensile coupon tests gave slightly higher than usual values of Young's modulus, which was possibly due to the extensometer measurement method. Compression tests were carried out on the columns to investigate the effects of local and distortional buckling as well as the interactions between the different modes. The Effective Width Method (EWM) and Direct Strength Method (DSM), from the Australian Standards AS/NZS 4600 and North American Specifications, were employed to analyse the nominal capacity of the column and were compared to the test results.

For short column lengths of 110 mm, the column failed with local buckling occurring on all flanges. When compared to the design methods, the nominal capacity using EWM was very conservative whereas with the DSM analysis, the design method was very unconservative. This unconservative prediction was due to the local buckling occurring on all flanges at failure. At intermediate and longer specimen lengths, the EWM and DSM, based on elastic buckling stress of the short half-wavelength distortional mode, were unconservative as the interaction of local and short half-wavelength distortional modes were not accounted for by the design standards.

A design method was proposed to improve the prediction of the local buckling DSM curve and at the same time, three simple design methods were proposed to improve the prediction of the distortional buckling DSM curve by accounting for the interaction of local and distortional buckling modes. Further analytical modelling is required to confirm the range of applicability of these equations. Sections of this type demonstrate the complexity of mode interaction. However, the accurate experimental data allows a better understanding of the applicability of the EWM and DSM equations in existing standards and specifications.

## ACKNOWLEDGEMENTS

This report forms part of an ARC research project entitled “Interaction of local and distortional buckling modes in cold-formed high strength steel” being carried out at the School of Civil Engineering at the University of Sydney. The authors would like to thank the Australian Research Council and BlueScope Steel for the financial support for the project performed at the University of Sydney. The tensile coupons were milled in the William and Agnes Bennet Supersonics Laboratory at the School of Aerospace, Mechanical and Mechatronics. The compression specimens were fabricated by All About Metals, Sydney. The authors would like to thank Mr. Todd Budrodeen for designing and constructing the rig for the experimental testing.

## REFERENCES

American Iron and Steel Institute (AISI), (2001), *North American Specification for the design of cold-formed steel structural members*, Washington, D.C.

American Iron and Steel Institute (AISI), (2004), *Supplement 2004 to the North American Specification for the design of cold-formed steel structural members, 2001 edition*, Washington, D.C.

ASTM A653/A653M-05a, (2000), *Standard Specification for Steel Sheet, Zinc-Coated (Galvanized) or Zinc-Iron Alloy-Coated (Galvannealed) by the Hot-Dip Process*, ASTM International.

ASTM A792/A792M-05, (1999), *Standard Specification for Steel Sheet, 55 % Aluminium-Zinc Alloy-Coated by the Hot-Dip Process*, ASTM International.

ASTM A875/A875M-05, (1999), “Standard Specification for Steel Sheet, Zinc-5% Aluminium Alloy-Coated by the Hot-Dip Process”, ASTM International.

ASTM A1039/A1039M-04, (2004), *Standard Specification for Steel, Sheet, Hot Rolled, Carbon, Commercial and Structural, Produced by the Twin-Roll Casting Process*, ASTM International.

BHP, (1992), *The Making of Iron and Steel*, Seventh Edition, BHP Steel Group, Melbourne.

Cheung, Y. K., (1976), *Finite strip method in structural analysis*, Pergamon Press, Inc. New York, N.Y.

Davies, J.M., (2000), “Recent research advances in cold-formed steel structures”. *Journal of Constructional Steel Research*, v 55, n 1, pp 267-88.

Hancock, G.J., (1998), *Design of cold-formed steel structures (to Australian/New Zealand Stand AS/NZS 4600:1996)*, 3<sup>rd</sup> Ed, Australian Institute of Steel Construction, Sydney, NSW, Australia.

Hancock, G.J., (2003), “Cold-formed steel structures”, *Journal of Constructional Steel Research*, v 59, n 4, pp 473-87.

Kwon Y.B. and Hancock G.J., (1992), “Tests of cold-formed channels with local and distortional buckling”, *Journal of Structural Engineering*, v117, n 7, pp 1786-1803.

Lau, S.C.W. and Hancock, G.J., (1986), “Buckling of thin flat-walled structures by a spline finite strip method”, *Thin-Walled Structures*, v 4, n 4, pp 269-94.

Narayanan, S. and Mahendran, M., (2003) “Ultimate capacity of innovative cold-formed steel column”, *Journal of Constructional Steel Research*, v 59, n 4, pp 489-503.

Papangelis, J.P. and Hancock, G.J., (1995), “Computer analysis of thin-walled structural members”, *Computers & Structures*, v 56, Issue 1, pp 157-76.

Pekoz, T., (1999), "Possible future developments in the design and application of cold-formed steel", *Keynote lecture, 4<sup>th</sup> Int. Conf. Light-weight Steel and Aluminium Structures*. Espoo, Finland.

Rondal, J., (2000), "Cold-formed steel members and structures – general report", *Journal of Constructional Steel Research*, v 55, n 1, pp 155-8.

Rogers, C.A., Hancock, G.J., (1996), "Ductility of G550 sheet steels in tension-elongation measurements and perforated tests", Research Report No. 735, Department of Civil Engineering, University of Sydney, Sydney.

Rogers, C.A., Yang, D. and Hancock, G.J., (2003), "Stability and ductility of thin high strength G550 steel members and connections", *Thin-Walled Structures*, v 41, n 2-3, pp 149-66.

Schafer, B.W., and Pekoz, T., (1998), "Direct strength prediction of cold-formed steel members using numerical elastic buckling solutions", *14<sup>th</sup> International Specialty Conference on Cold-Formed Steel Structures*, St. Louis, MO, USA, pp 69-76.

Standards Australia, (1991), *Methods for tensile testing of metals – AS 1391:1991*, Sydney, NSW, Australia.

Standards Australia, (1993), *Steel Sheet and Strip – Hot-dipped zinc-coated or Aluminium/Zinc-coated, AS 1397:1993*, Sydney, NSW, Australia.

Standards Australia/Standards New Zealand, (1996), *Cold-formed steel structures, AS/NZS 4600: 1996*, Sydney, NSW, Australia.

Standards Australia/Standards New Zealand, (2005), *Cold-formed steel structures, AS/NZS 4600: 2005*, Sydney, NSW, Australia.

Von Karmon, T., Sechler, E.E. and Donnell, L.H., (1932), "The strength of thin plates in compression", *Transactions ASME*, v 54, MP 54-5.

Yang, D. and Hancock, G.J., (2002), "Compression tests of cold-reduced high strength steel stub column", Research Report No. 815, Department of Civil Engineering, University of Sydney, Sydney.

Yang, D. and Hancock, G.J., (2003), "Compression test of cold-reduced high strength steel channel columns failing in the distortional mode", Research Report No. 825, Department of Civil Engineering, University of Sydney, Sydney.

Yang, D. and Hancock, G.J., (2004), "Compression tests of high strength steel channel columns with interaction between local and distortional buckling", *Journal of Structural Engineering*, v 130, n 12, pp 1954-63.

## NOTATIONS

$A$	Cross-sectional area ( $\text{mm}^2$ )
$b$	Width of element (mm)
$b_e$	Effective width of element (mm)
$E$	Young's modulus (GPa)
$f_{od}$	Elastic distortional buckling stress (MPa)
$f_{ol}$	Elastic local buckling stress (MPa)
$f_y$	Yield stress (MPa)
$l_e$	Effective length (mm)
$N_c$	Nominal member compression capacity (kN)
$N_{cd}$	Nominal axial capacity for distortional buckling
$N_{ce}$	Nominal axial capacity for overall failure mode
$N_{cl}$	Nominal axial capacity for local buckling
$N_{cl}'$	Proposed nominal axial capacity for local buckling
$N_{c\_ld}$	Proposed nominal axial capacity for interaction of local and distortional buckling
$N_{kh}$	Nominal axial capacity based on Kwon and Hancock strength equations
$N_l$ & $N_d$	Theoretical local and distortional buckling loads (kN)
$N_{od}$	Elastic distortional buckling load (kN)
$N_{ol}$	Elastic local buckling load (kN)
$N_s$	Nominal section compression capacity (kN)
$N_y$	Squash load (kN)
$t$	Thickness (mm)

# FIGURES

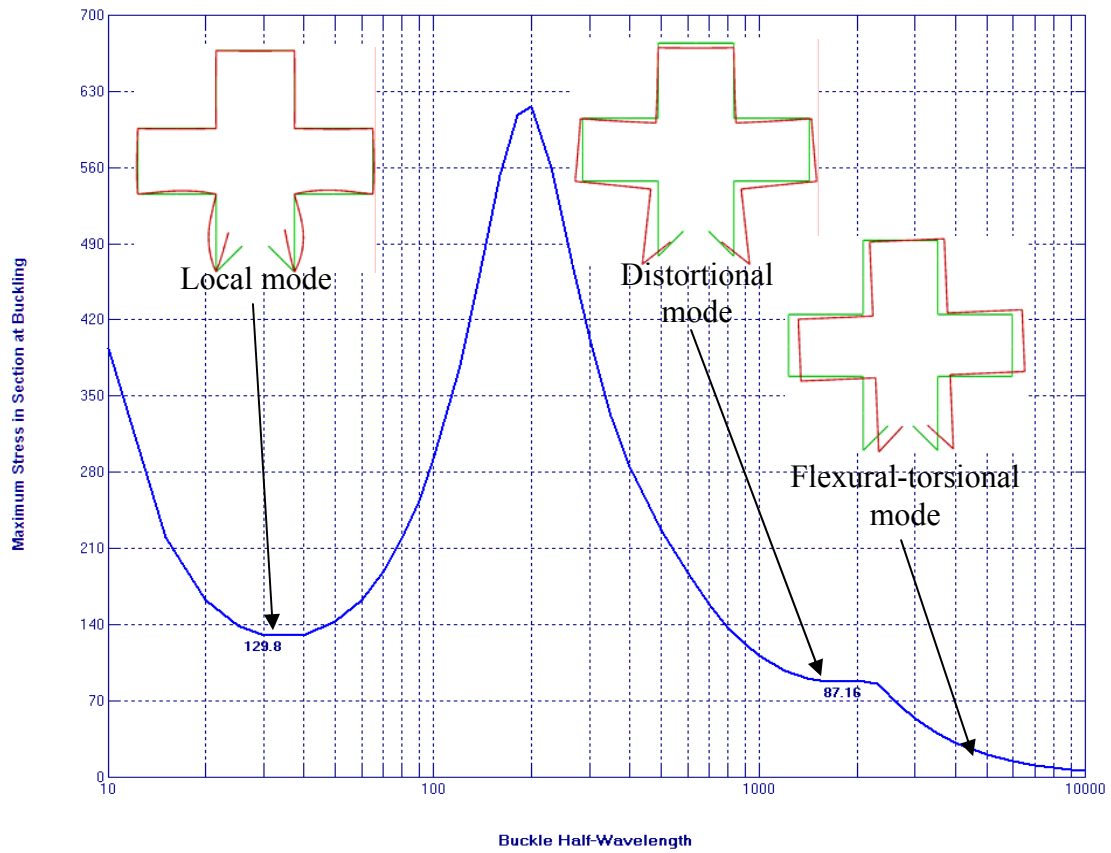


Figure 1 Buckling modes of a cross-shaped section

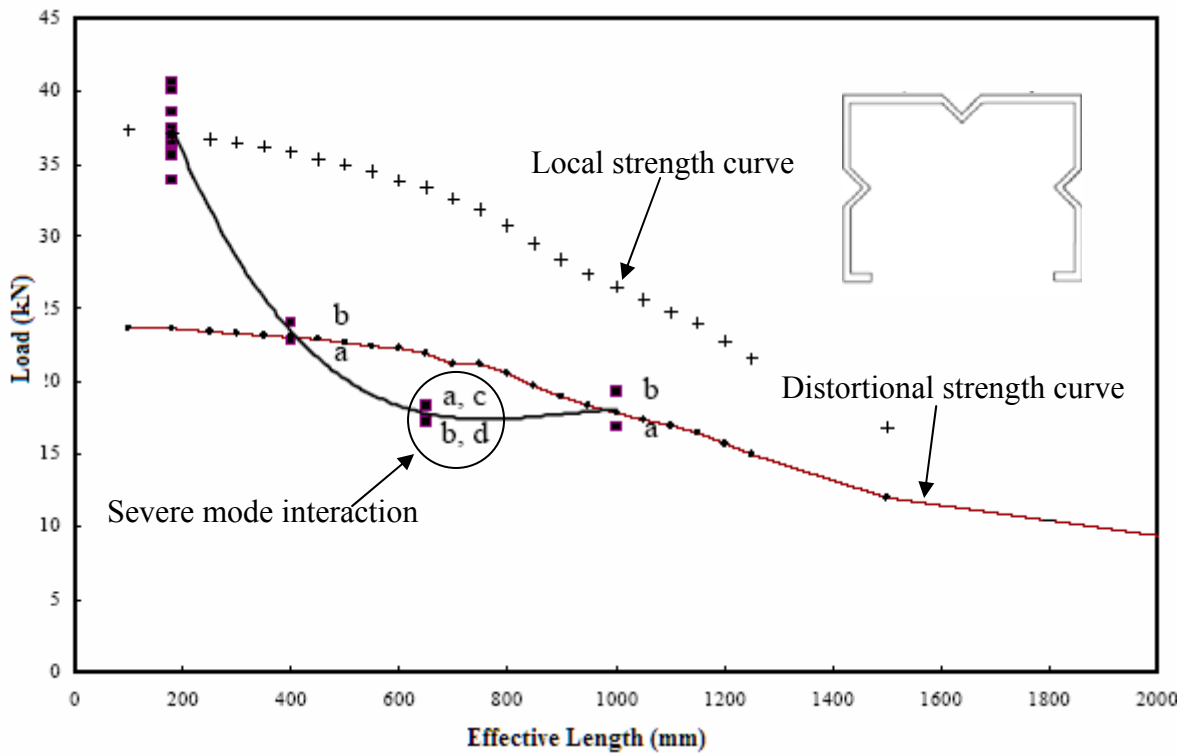
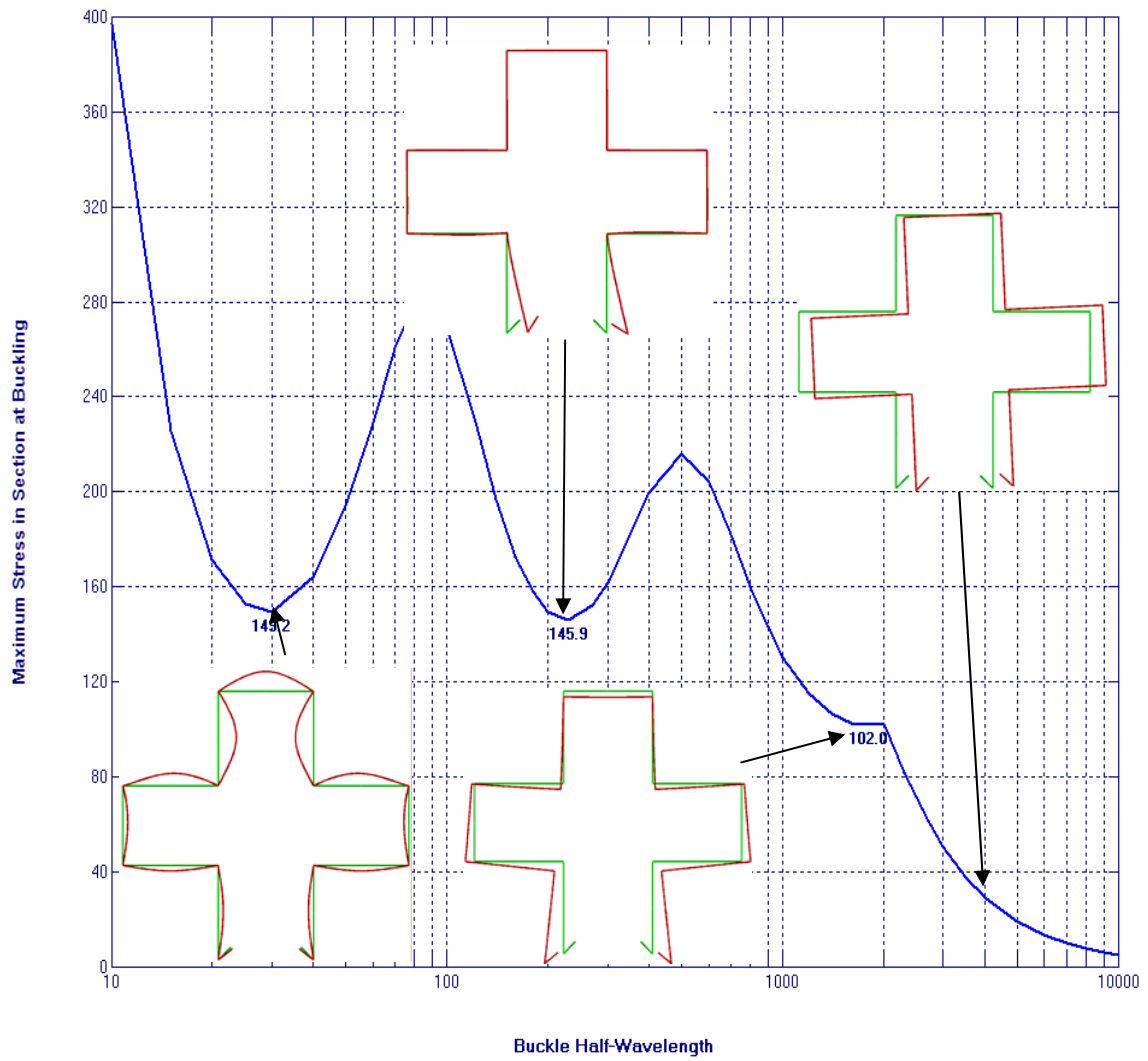


Figure 2 Compression test results from Yang and Hancock (2004)



**Figure 3 Buckling stresses and modes of cross-shaped section**

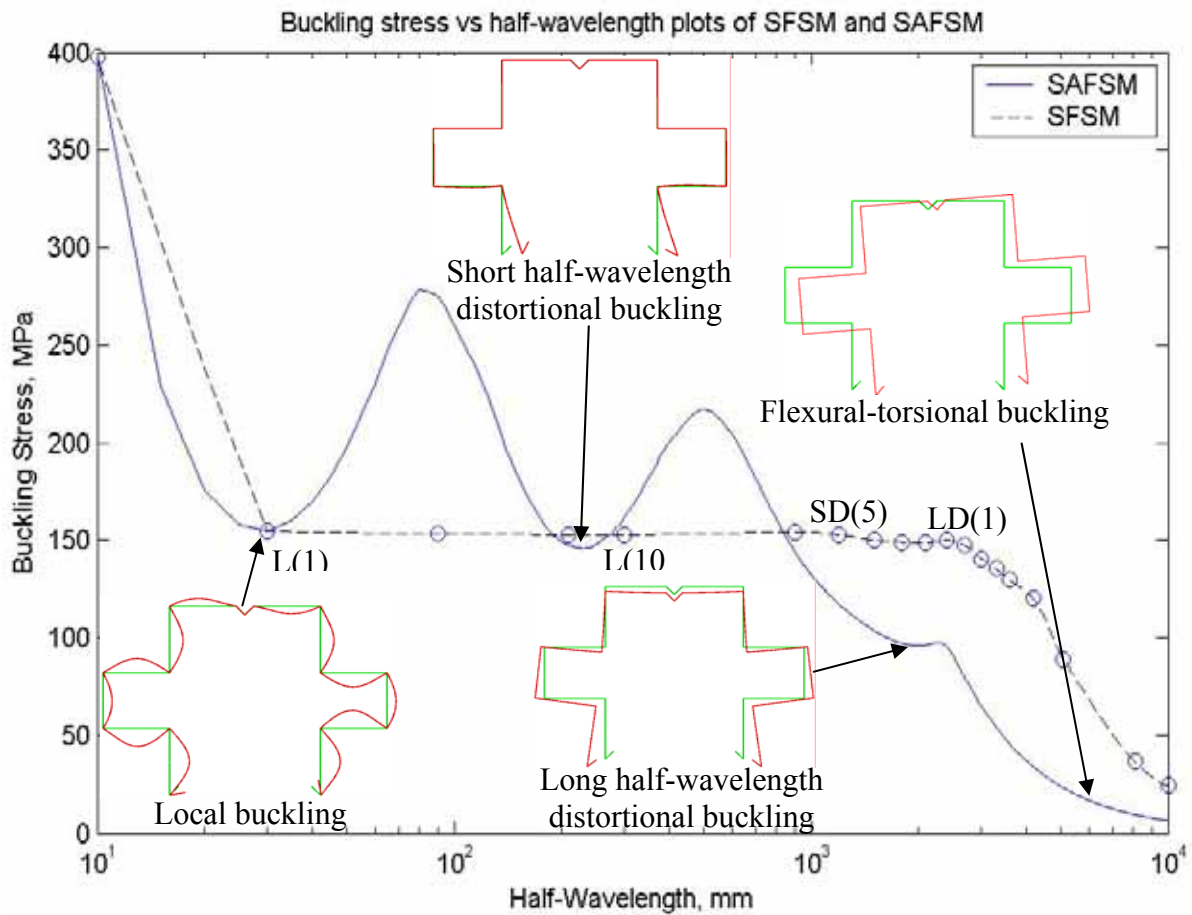


Figure 4 Buckling stresses and modes of an intermediately-stiffened cross-shaped section

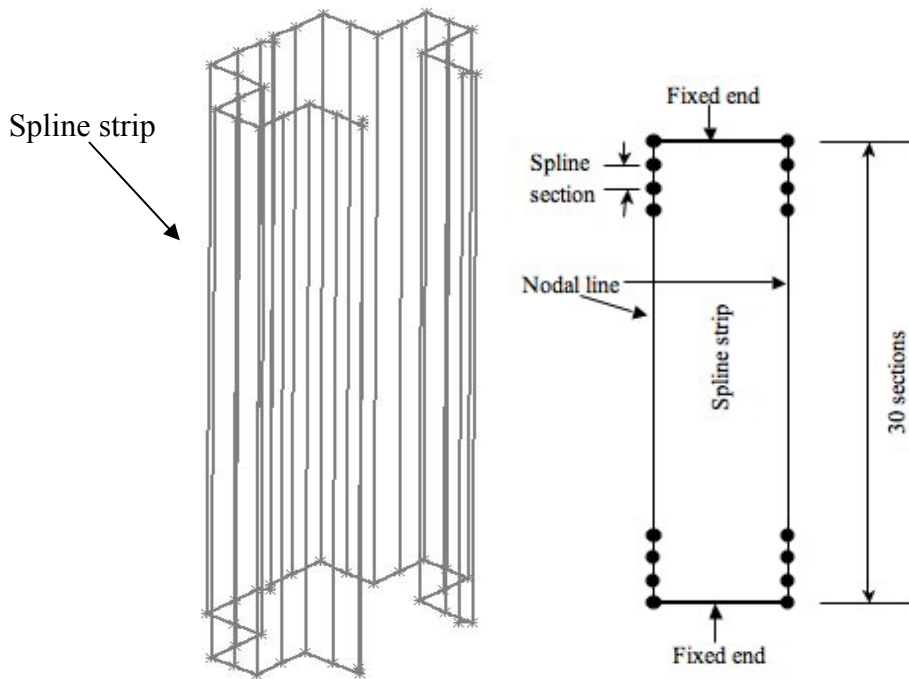
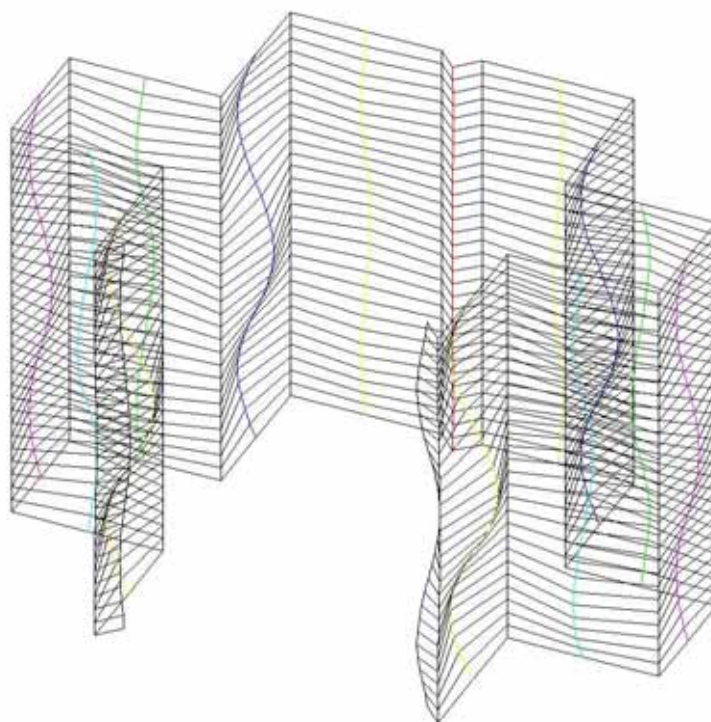
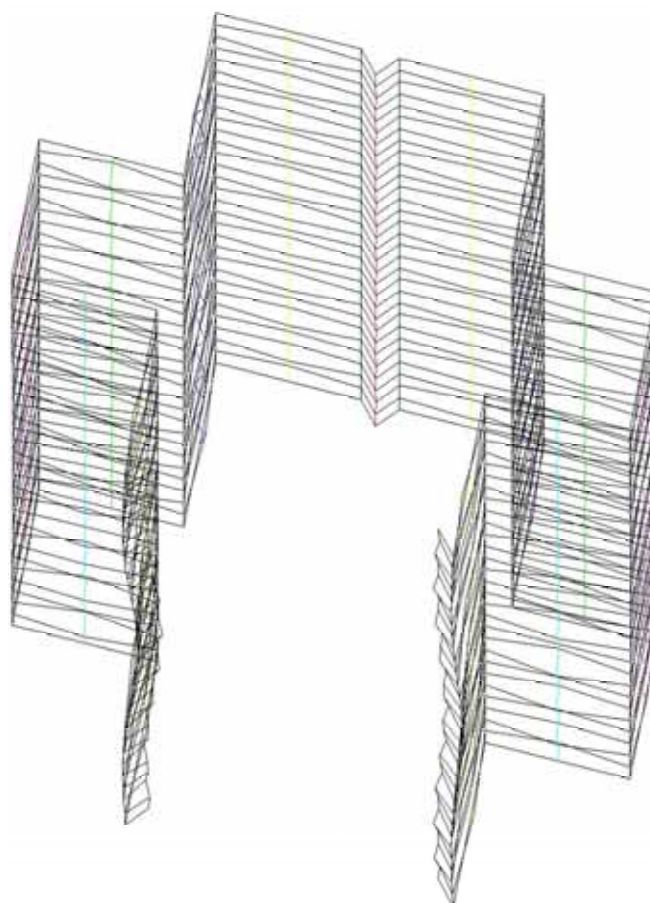


Figure 5 Spline finite strip analysis of section



**Figure 6a Local buckling mode at length 90 mm**



**Figure 6b Local and short half-wavelength distortional buckling modes appearing simultaneously at length 600 mm**

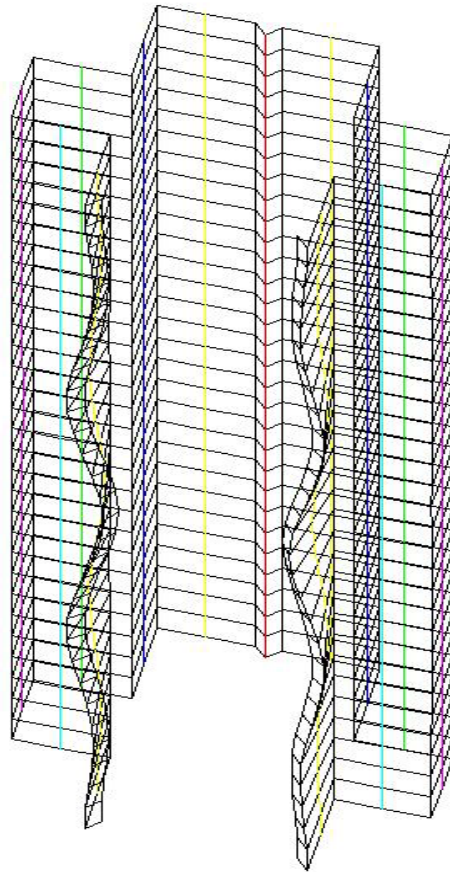


**Figure 6c Short half-wavelength distortional buckling mode at length 1200 mm**

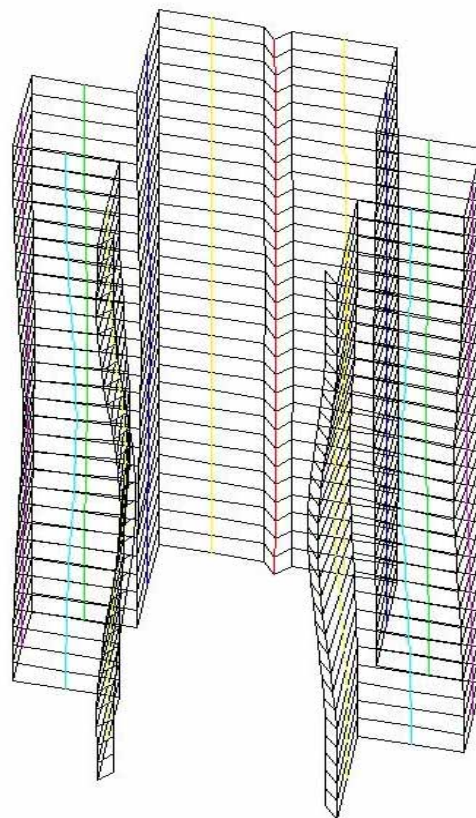


**Figure 6d Long half-wavelength distortional buckling mode at length 2700mm**

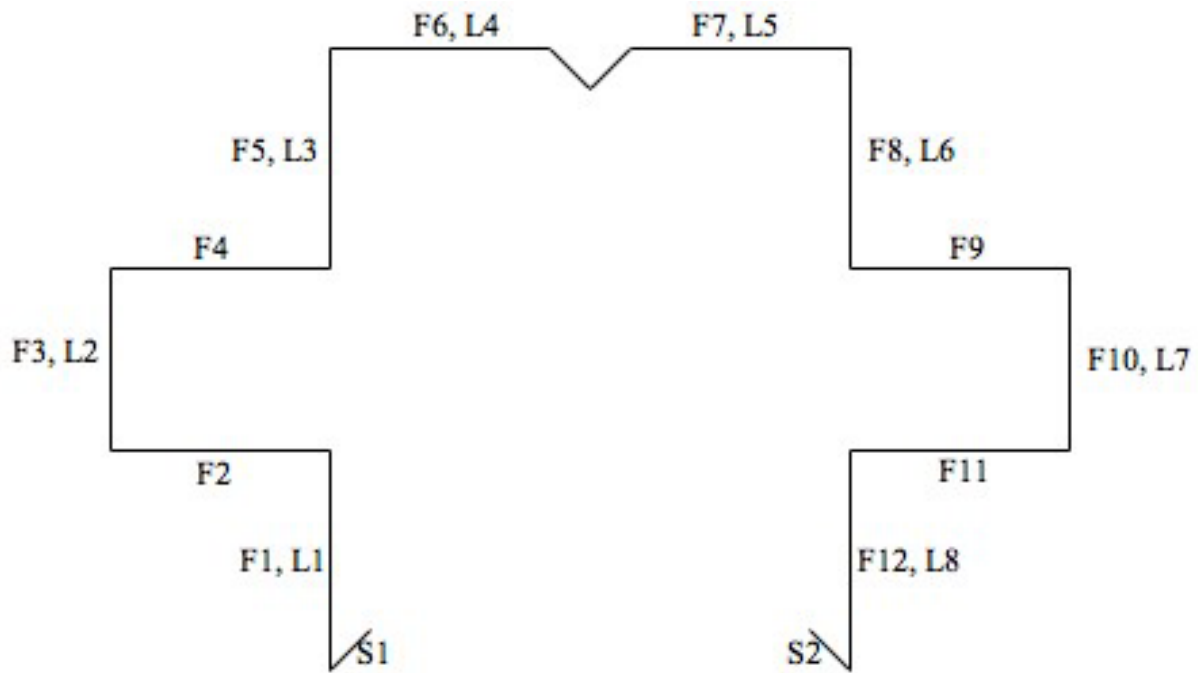


Figure 7 Geometric imperfection measurement positions

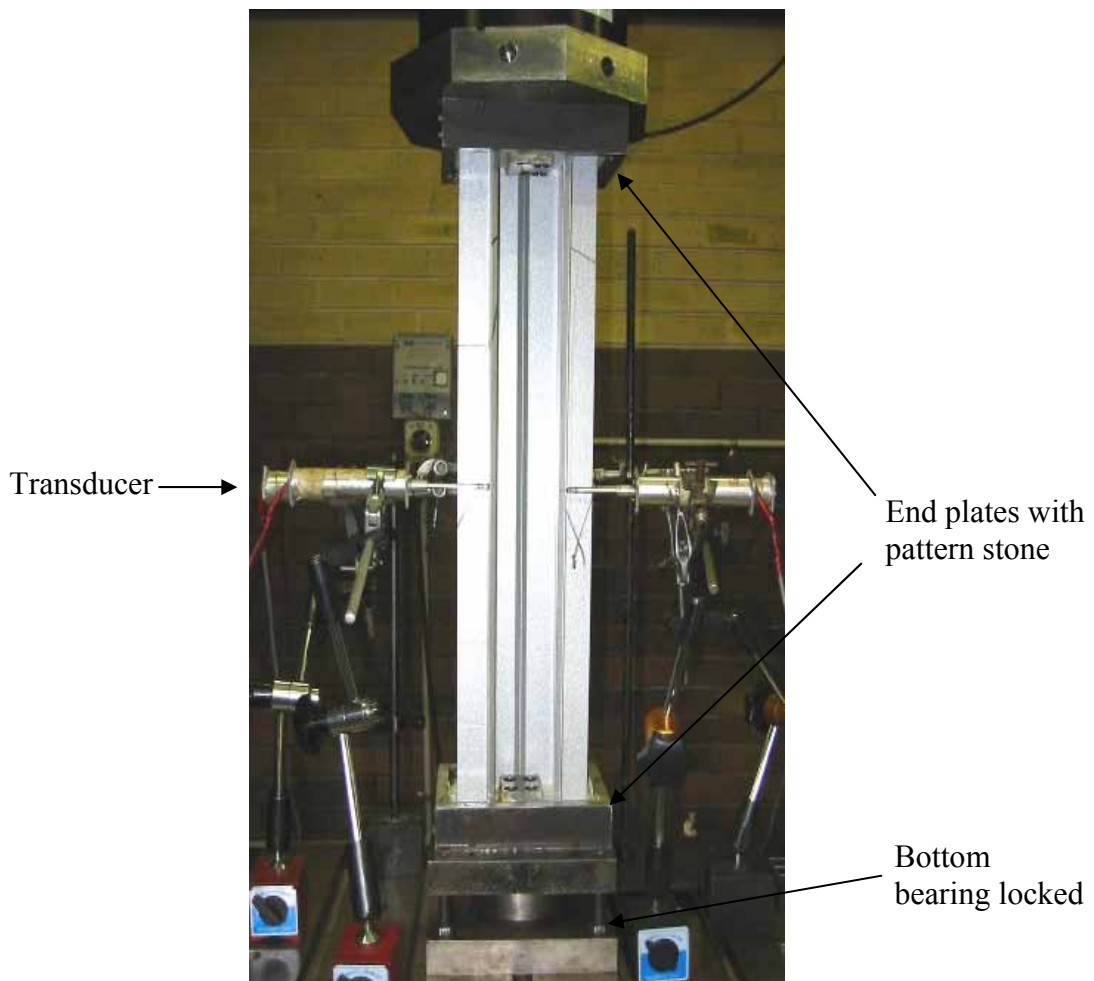


Figure 8 Specimen set-up in test rig

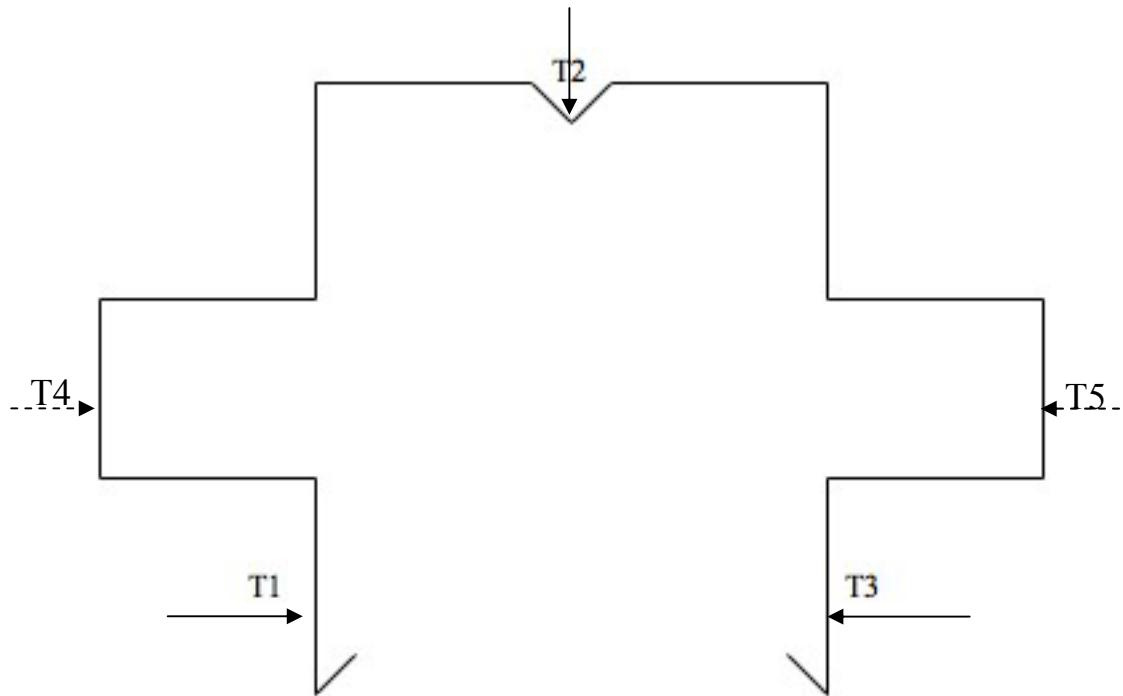


Figure 9 Transducer arrangements at quarter, mid and three-quarter height positions

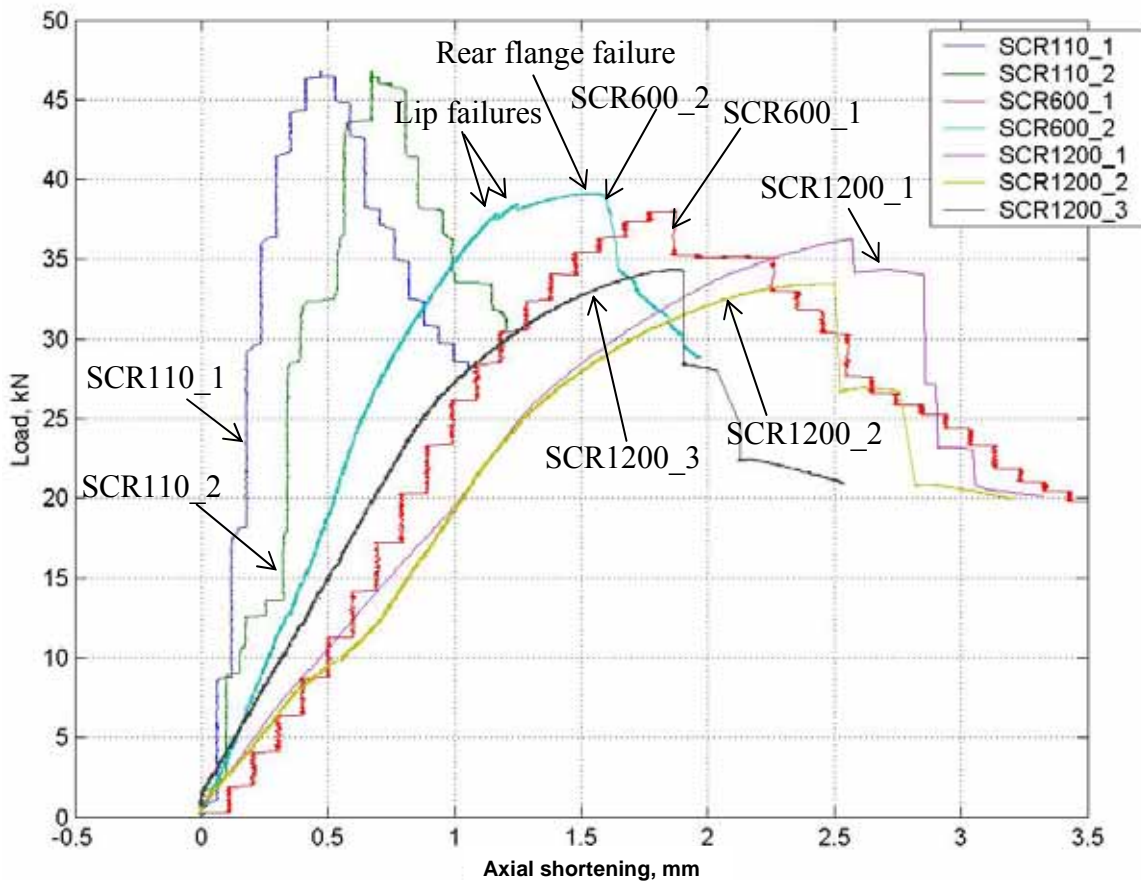


Figure 10a Load versus axial shortening for specimen lengths 110mm, 600mm and 1200mm

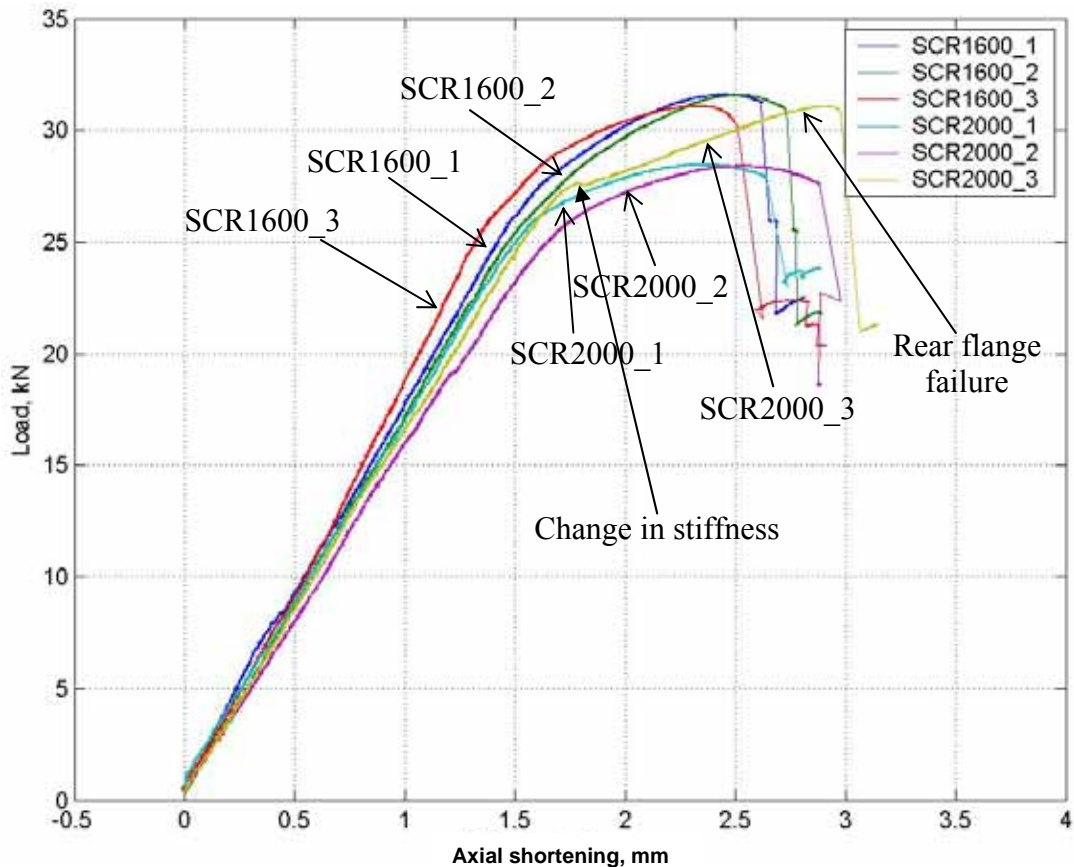


Figure 10b Load versus axial shortening for specimen lengths 1600mm and 2000mm



**Figure 11 Failure mode of SCR110\_2**



**Figure 12a & b Failure modes of SCR600\_1 (left) and SCR600\_2 (right)**

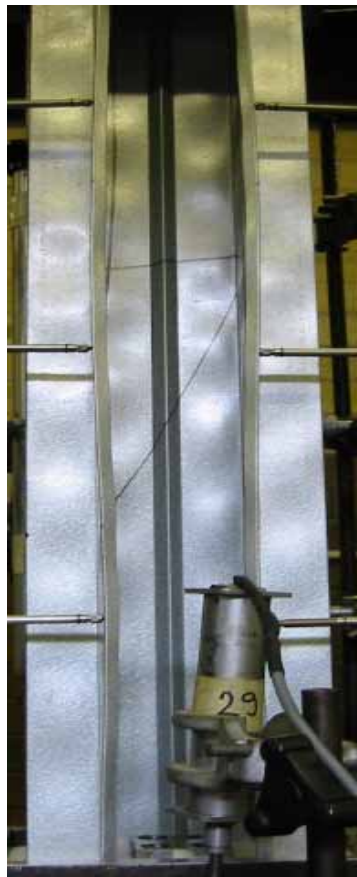


**Figure 12c Interaction of local and short half-wavelength distortional buckling modes (SCR600\_2)**



Figure 13a, b and c Failure modes for SCR1200\_1 (left), SCR1200\_2 (middle) and SCR1200\_3 (right)

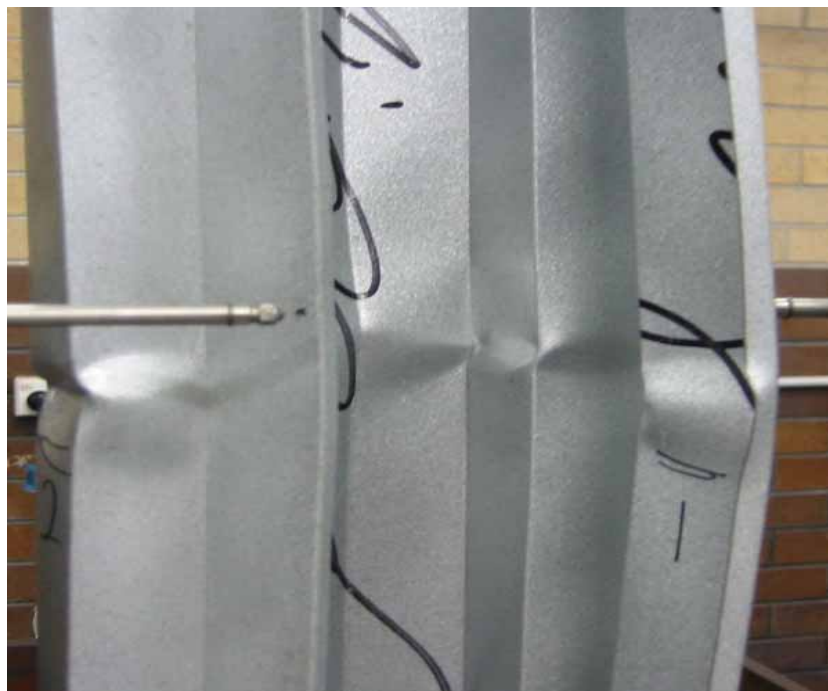


Figure 13d Failure at side and edge-stiffened flange junction of specimen SCR1200\_1



Figure 13e Failure at side flange of specimen SCR1200\_2



Figure 14a, b and c Failure modes of SCR1600\_1 (left), SCR1600\_2 (middle) and SCR1600\_3 (right)

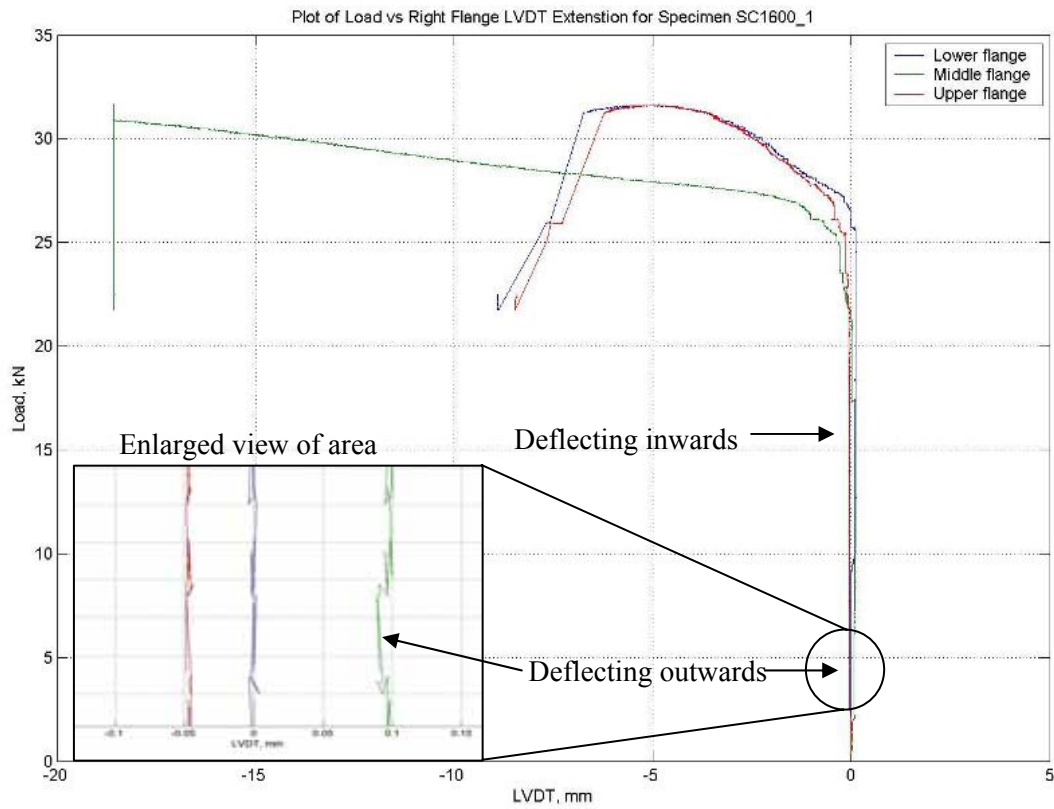


Figure 14d Deflection of the right edge-stiffened flange for SCR1600\_1

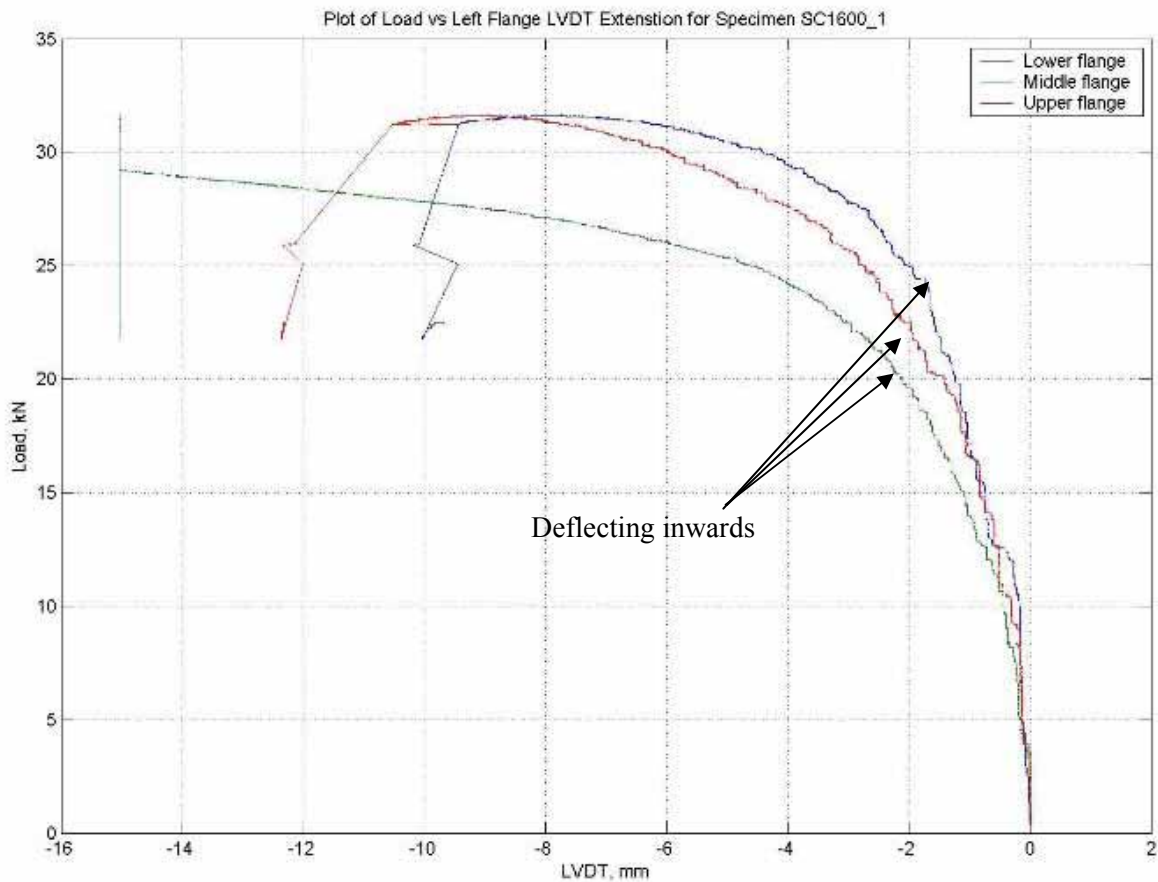


Figure 14e Deflection of the left edge-stiffened flange for SCR1600\_1

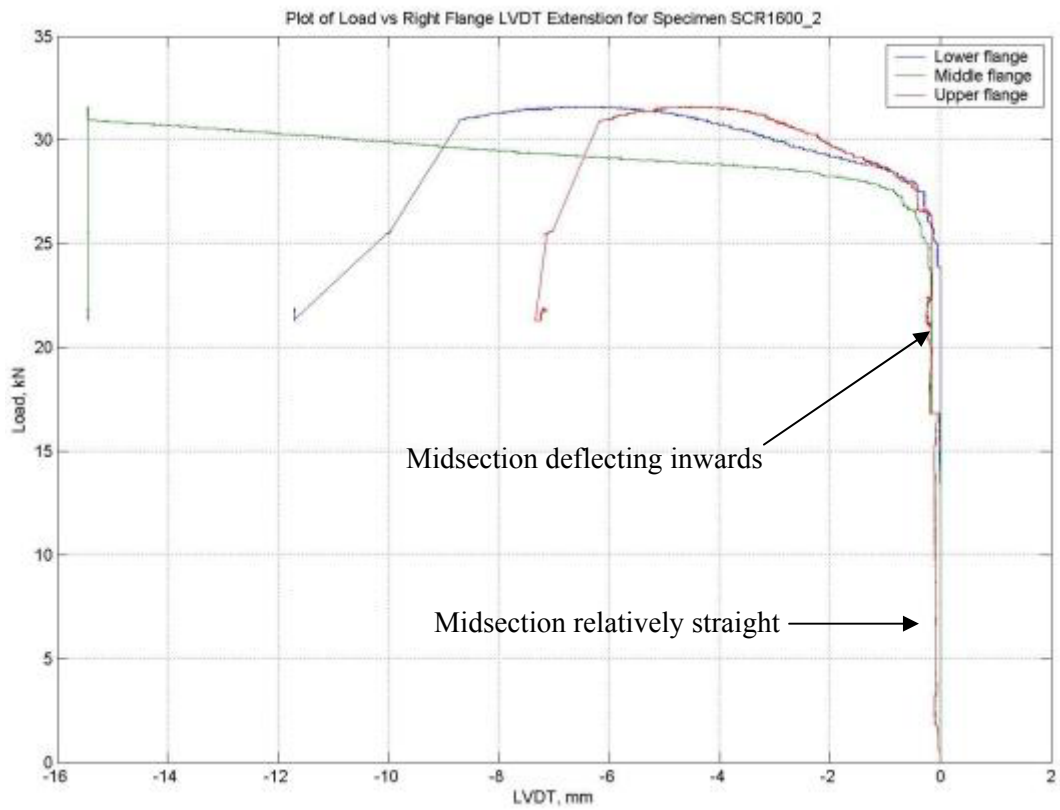


Figure 14f Deflection of the right edge-stiffened flange for SCR1600\_2

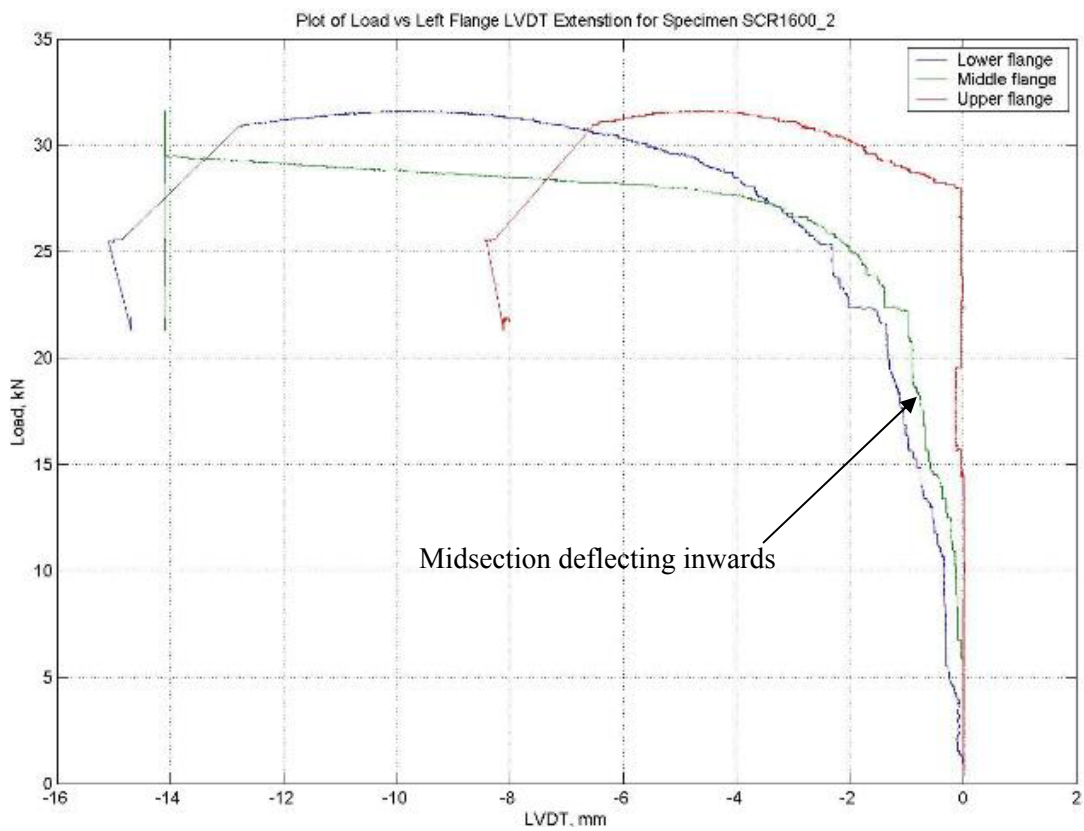


Figure 14g Deflection of the right edge-stiffened flange for SCR1600\_2

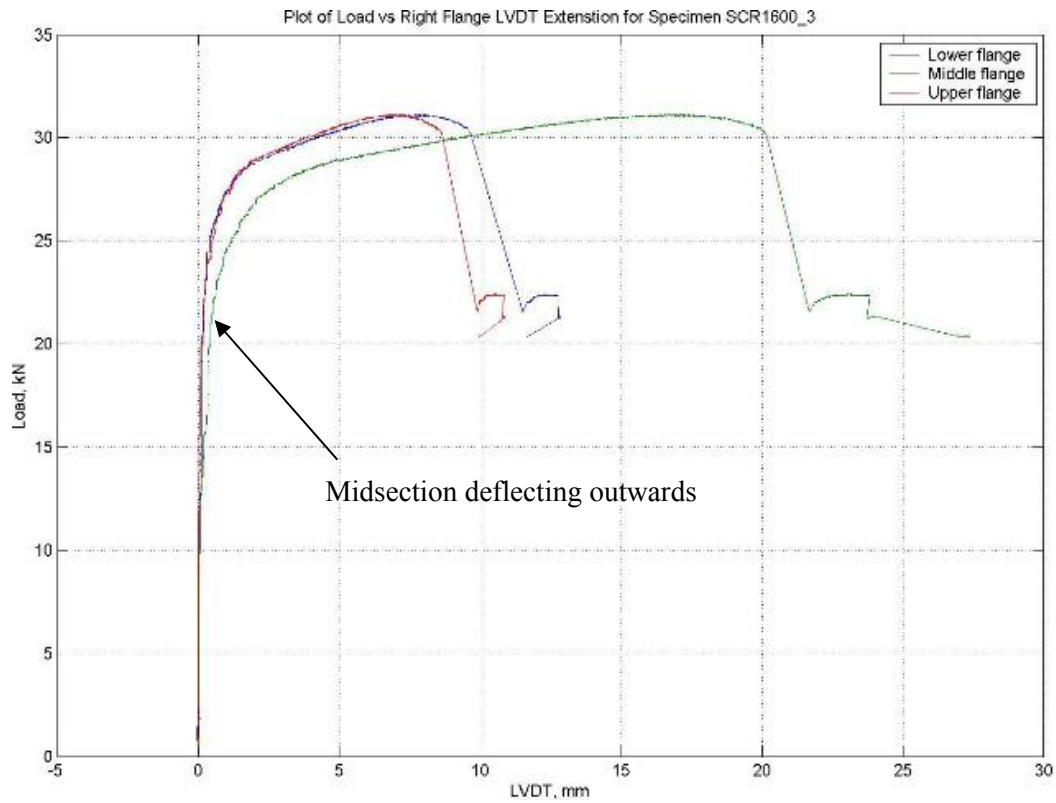


Figure 14h Deflection of the right edge-stiffened flange for SCR1600\_3

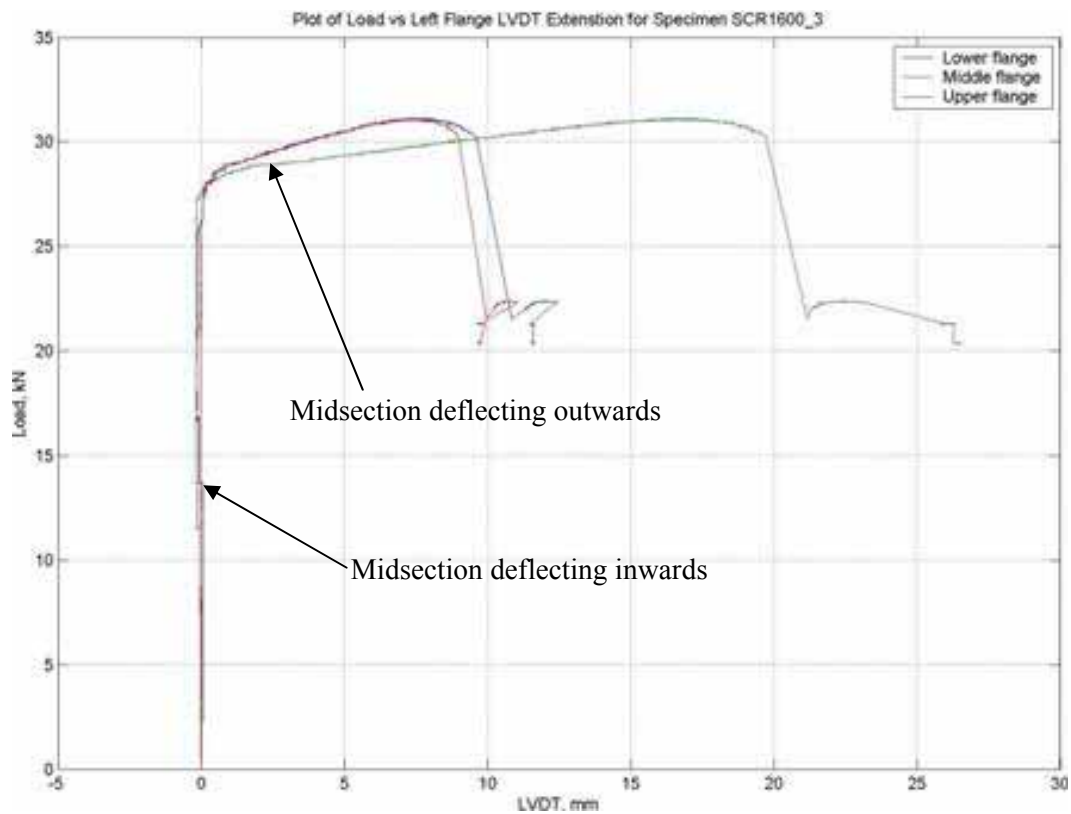


Figure 14i Deflection of the left edge-stiffened flange for SCR1600\_3

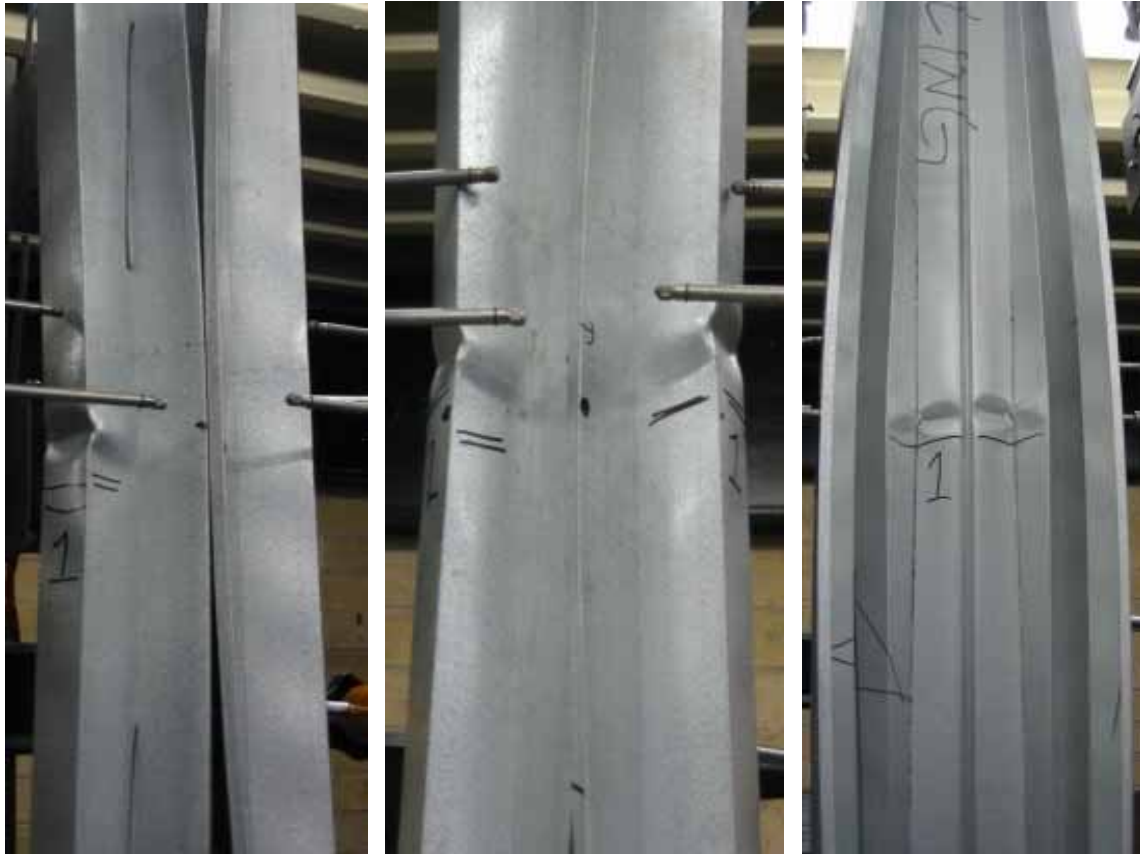


Figure 15a, b and c Failure modes of SCR2000\_1 (left), SCR2000\_2 (middle) and SCR2000\_3 (right)



Figure 15d Interaction of buckling modes of SCR2000\_3

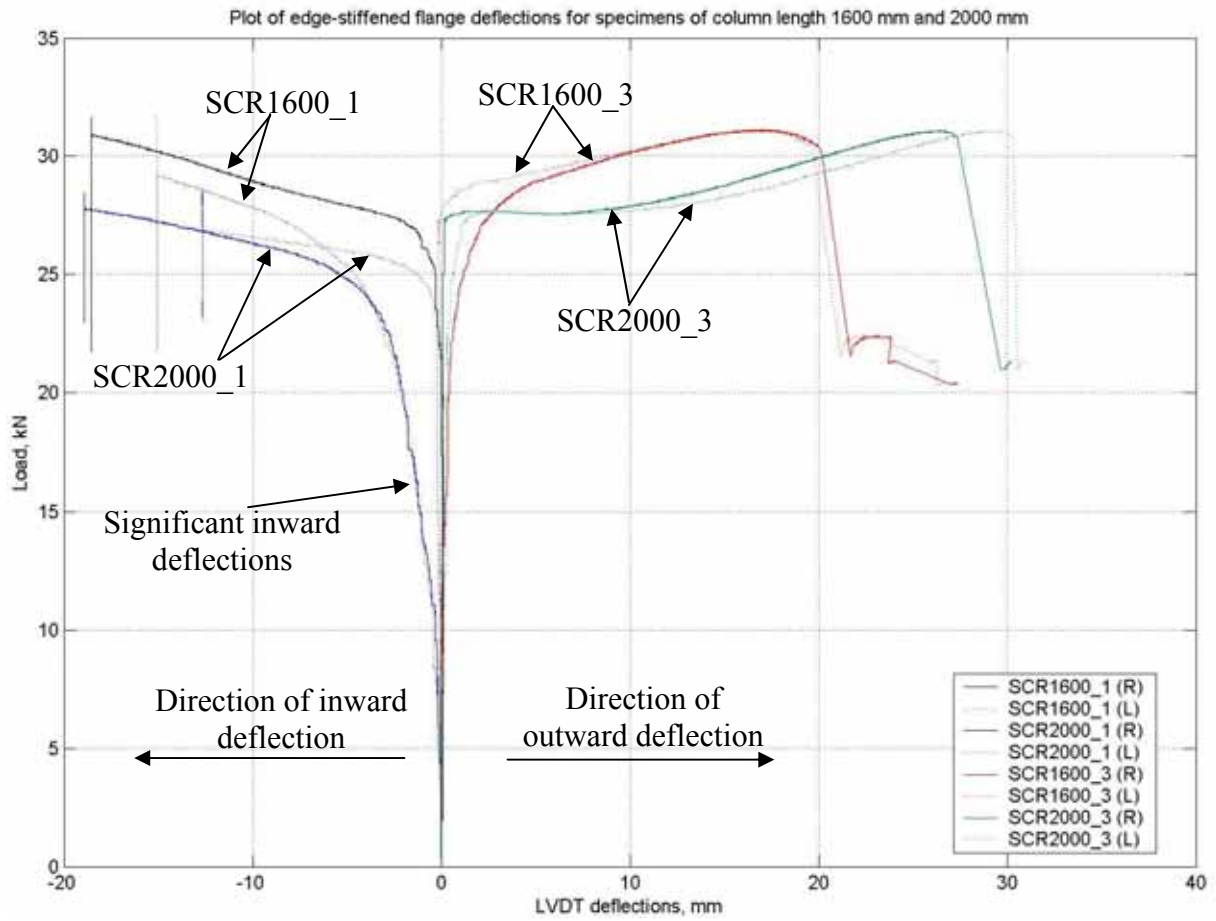


Figure 16 Comparison of specimens with inward and outward deflections of the edge-stiffened flanges

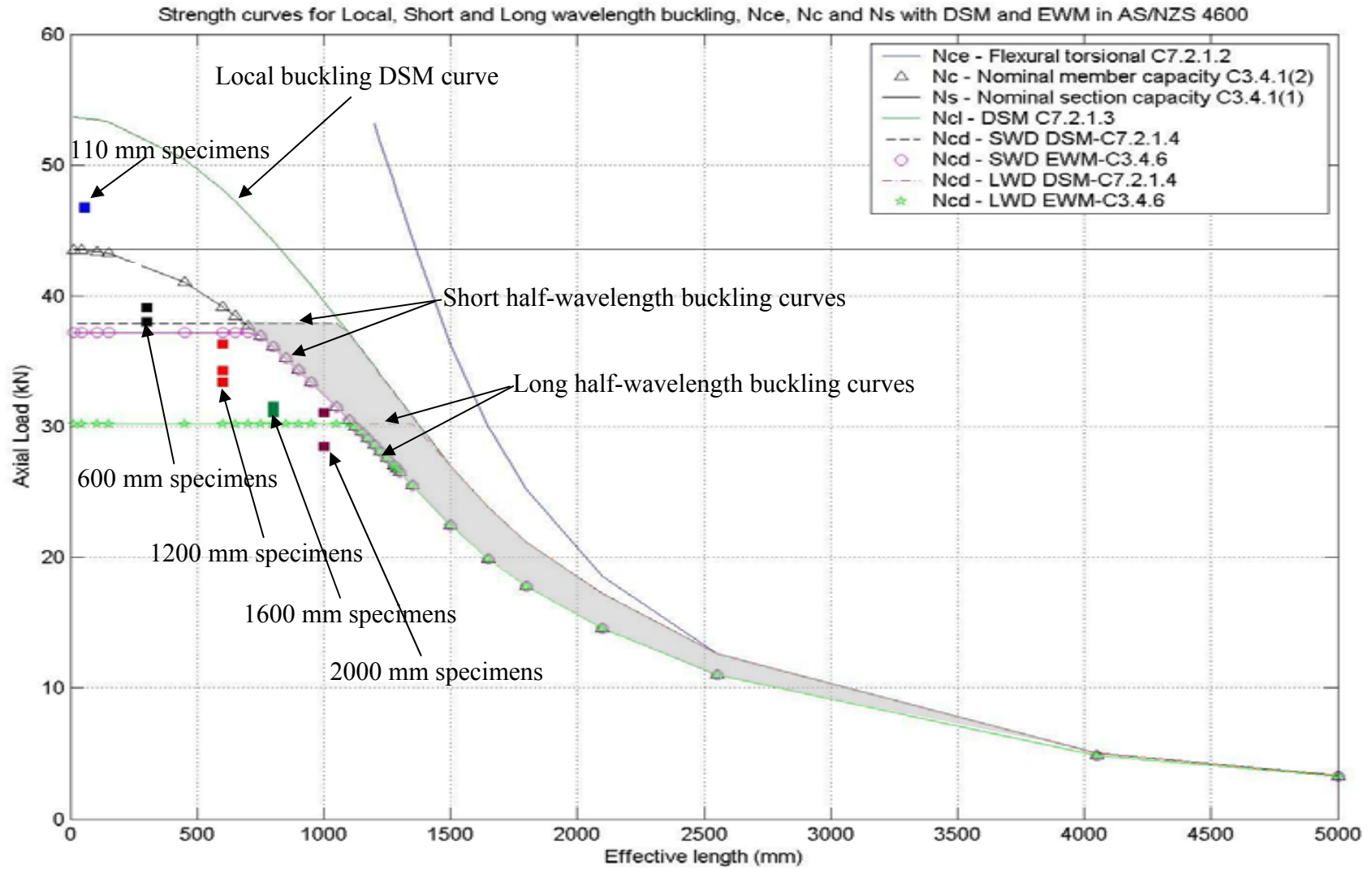


Figure 17 Comparison of design strength curves and test results

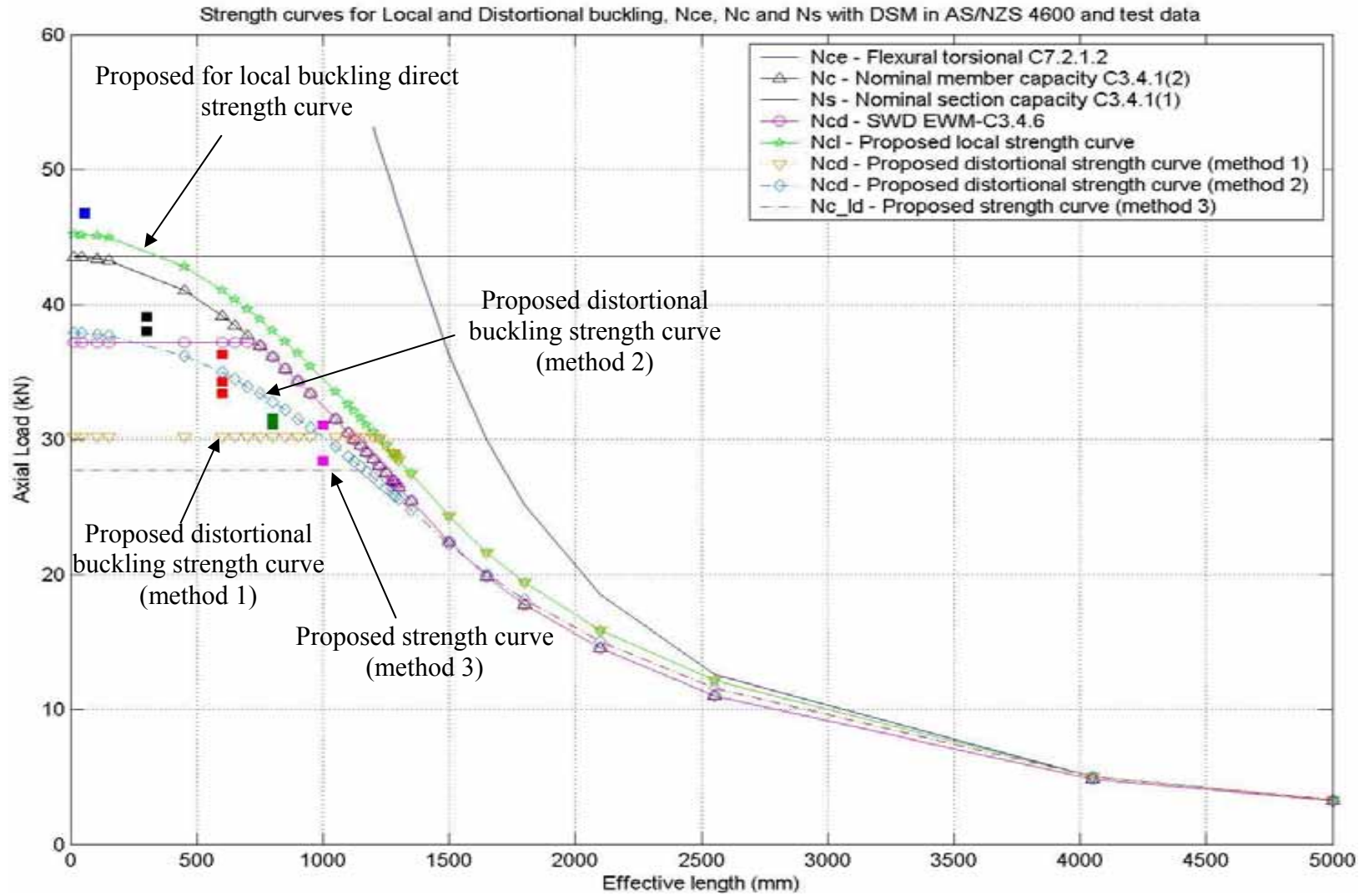


Figure 18 Test results compared with proposed design methods

## TABLES

Lip angle	Local and distortional buckling stresses (MPa)					
	90°		120°		135°	
Lip length (mm)	Local	Distortional (Short, Long)	Local	Distortional (Short, Long)	Local	Distortional (Short, Long)
4.24	154.8	142.0, 98.38	154.6	132.2, 98.35	149.8	81.14, 99.65
5.66	155.4	174.6, 95.01	155.3	167.6, 95.52	154.9	145.9, 95.84
7.07	155.4	229.3, 194.6, 91.89	155.3	229.3, 196.0, 92.65	155.1	175.6, 93.03
8.49	155.0	229.3, 88.93	154.8	229.4, 90.07	154.6	229.4, 199.2, 90.57

Table 1 Buckling stresses at corresponding lip length and angle

Specimen length (mm)	THINWALL (SAFSM)		SFSM	
	Local buckling stress (MPa)	Distortional buckling stress (MPa)	Elastic buckling stress (MPa)	Buckling mode
110	154.9	145.9 (SWD), 95.84 (LWD)	153.3	L(3)
600			153.4	SWD(1) + L(20)
1200			152.3	SWD(3)
1600			149.2	SWD(5)
2000			148.9	SWD(6)

Table 2 Elastic buckling stress for stiffened cross section (SCR)

Specimen	b (mm)	t (mm)	0.2% Proof Stress (MPa)	E (GPa)	% strain
B1_1	12.62	0.40	663.6	230.58	1.1
B1_2	12.50	0.40	694.0	239.93	0.6
B1_3	12.49	0.40	676.5	213.44	2.7
B1_4	12.60	0.40	678.6	211.74	0.6
B1_5	12.62	0.41	651.3	212.14	0.6
B2_1	12.54	0.40	-	237.78	0.3
B2_2	12.54	0.40	-	227.41	0.3
B2_3	12.55	0.41	-	238.72	0.3
B2_4	12.59	0.40	-	238.97	0.3
B2_5	12.50	0.40	-	229.88	0.3
<b>Mean</b>	<b>12.55</b>	<b>0.40</b>	<b>672.8</b>	<b>228.06</b>	

Table 3 Results of tensile coupon tests

Specimen	Maximum imperfection readings							
	L1 (mm)	L2 (mm)	L3 (mm)	L4 (mm)	L5 (mm)	L6 (mm)	L7 (mm)	L8 (mm)
SCR600_1	-0.3	0.2	0.18	0.35	0.4	0.2	-0.15	0.3
SCR600_2	0.2	0.18	0.65	0.58	-0.33	-0.28	-0.31	-0.18
SCR1200_1	0.18	-0.3	-0.2	-0.2	-0.25	0.2	0.32	-0.25
SCR1200_2	0.56	0.68	0.5	-1.3	-1.06	-0.48	-0.25	-0.55
SCR1200_3	0.22	0.31	0.74	-0.38	-0.42	0.6	0.17	0.19
SCR1600_1	0.59	0.41	0.34	1.21	1.0	0.35	0.55	0.54
SCR1600_2	0.75	0.59	0.28	0.8	0.75	0.2	0.18	0.37
SCR1600_3	0.24	0.51	-1.1	0.4	0.21	0.19	0.37	0.3
SCR2000_1	0.71	0.58	0.55	0.69	0.51	0.26	0.4	0.29
SCR2000_2	1.02	0.99	-0.55	0.86	0.80	0.51	0.58	0.49
SCR2000_3	-0.48	0.34	-1.2	0.39	0.58	-0.99	0.87	0.52

Table 4 Maximum imperfection readings of specimens

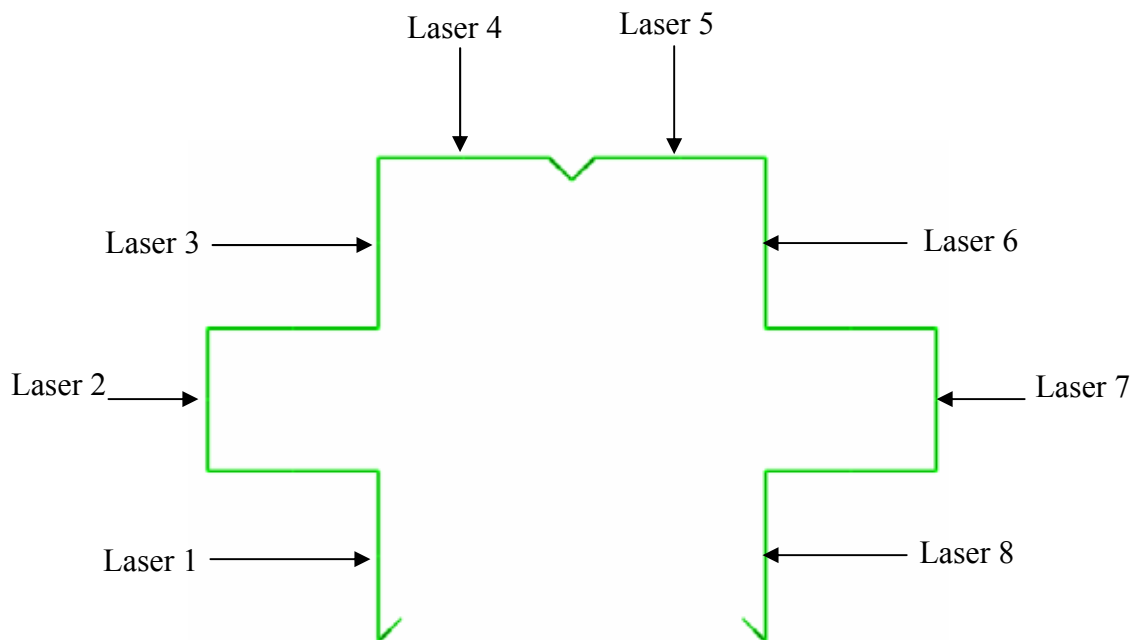
Specimen	Area (mm <sup>2</sup> )	P <sub>u</sub> (kN)	F <sub>u</sub> (MPa)	N <sub>i</sub> (kN)	N <sub>d</sub> (kN)
SCR110_1	158.3	46.8	295.64	24.2	24.27
SCR110_2	158.0	46.7	295.57	24.2	24.22
SCR110_3	158.0	43.5*	275.32	24.2	24.22
SCR600_1	158.0	38.0	240.51	24.2	24.24
SCR600_2	157.4	39.1	248.41	24.2	24.15
SCR600_3	157.8	-	-	-	-
SCR1200_1	157.8	36.3	230.04	24.2	24.03
SCR1200_2	157.7	33.4	211.79	24.2	24.02
SCR1200_3	157.6	34.3	217.64	24.2	24.00
SCR1600_1	157.9	31.6	200.13	24.2	23.56
SCR1600_2	157.7	31.6	200.38	24.2	23.53
SCR1600_3	157.7	31.1	197.21	24.2	23.53
SCR2000_1	157.7	28.4	180.09	24.2	23.48
SCR2000_2	158.2	28.4	179.52	24.2	23.56
SCR2000_3	156.3	31.1	198.98	24.2	23.27

**Table 5 Summary of results for stiffened-cross sections (SCR)**

## APPENDIX A

### Geometric and imperfection measurements

Appendix A contains the measured geometric imperfections for the intermediately-stiffened cross shaped section specimens. This includes the measured geometries of each of the specimens, with the flanges and lips labelled 'F' and 'S' respectively. The imperfection measurements for each specimen are also included and the locations of the measurements are indicated by the arrows on the figure provided.



All measurements are in millimetres

Specimen No.	F1	F2	F3	F4	F5	F6	F7	F8	F9	F10	F11	F12	S1	S2
SCR110_1 (top)	31.92	30.3	24.69	30.61	30.67	29.65	29.55	31.19	30.73	24.93	30.03	32.13	6.85	6.89
SCR110_1 (bottom)	32.16	30.13	25	30.78	31.71	28.95	30.3	31.53	29.95	24.66	30.73	31.92	6.79	6.74
SCR110_1 (avg)	32.04	30.215	24.845	30.695	31.19	29.3	29.925	31.36	30.34	24.795	30.38	32.025	6.82	6.815
SCR110_2 (top)	31.93	30.22	24.71	30.67	31.25	28.9	29.56	31.58	30.69	24.93	30.14	32.18	6.8	6.89
SCR110_2 (bottom)	32.17	29.82	25.07	30.63	30.78	28.9	29.49	31.2	30.48	24.66	30.25	31.85	6.92	6.79
SCR110_2 (avg)	32.05	30.02	24.89	30.65	31.015	28.9	29.525	31.39	30.585	24.795	30.195	32.015	6.86	6.84
SCR110_3 (top)	31.92	30.18	24.74	30.67	31.35	28.95	29.6	31.06	30.69	25.16	30.17	32.18	6.98	6.84
SCR110_3 (bottom)	32.23	29.91	25.05	30.71	30.87	28.9	29.88	31.52	30.12	24.86	30.56	31.9	6.87	6.91
SCR110_3 (avg)	32.075	30.045	24.895	30.69	31.11	28.925	29.74	31.29	30.405	25.01	30.365	32.04	6.925	6.875

Table A-1 Geometric measurements of specimens SCR110\_1, SCR110\_2 and SCR110\_3

Specimen No.	F1	F2	F3	F4	F5	F6	F7	F8	F9	F10	F11	F12	S1	S2
SCR600_1 (top)	31.76	30.46	24.39	30.96	29.96	30.71	30.43	29.52	30.43	24.8	30.69	32.04	6.84	6.42
SCR600_1 (bottom)	31.96	30.32	24.6	30.59	30.38	30.17	29.61	30.5	30.37	24.54	30.76	31.85	6.65	6.2
SCR600_1 (avg)	31.86	30.39	24.495	30.775	30.17	30.44	30.02	30.01	30.4	24.67	30.725	31.945	6.745	6.31
SCR600_2 (top)	31.92	30.64	24.36	29.97	30.02	29.82	29.42	31.17	30.86	24.68	29.91	31.81	6.8	6.75
SCR600_2 (bottom)	31.9	30.66	24.43	29.97	29.87	29.38	29.67	31.04	30.8	24.38	30.45	31.91	6.81	6.72
SCR600_2 (avg)	31.91	30.65	24.395	29.97	29.945	29.6	29.545	31.105	30.83	24.53	30.18	31.86	6.805	6.735
SCR600_3 (top)	31.85	30.63	24.58	30.63	29.6	31.04	29.23	30.51	30.15	24.71	30.35	32.05	6.78	6.54
SCR600_3 (bottom)	32.09	30.27	24.62	30.74	29.92	30.56	29.86	29.98	30.12	24.44	30.86	31.89	6.82	6.6
SCR600_3 (avg)	31.97	30.45	24.6	30.685	29.76	30.8	29.545	30.245	30.135	24.575	30.605	31.97	6.8	6.57

Table A-2 Geometric measurements of specimens SCR600\_1, SCR600\_2 and SCR600\_3

All measurements are in millimetres

Specimen No.	F1	F2	F3	F4	F5	F6	F7	F8	F9	F10	F11	F12	S1	S2
SCR1200_1 (top)	31.85	29.7	24.67	30.52	30.2	30.45	31.15	30.29	30.18	24.69	30.6	31.86	6.75	6.92
SCR1200_1 (bottom)	31.87	29.69	24.56	30.64	30.73	30	30.23	30.18	30.6	24.54	29.98	31.84	6.92	6.82
SCR1200_1 (avg)	31.86	29.695	24.615	30.58	30.465	30.225	30.69	30.235	30.39	24.615	30.29	31.85	6.835	6.87
SCR1200_2 (top)	31.82	29.72	24.6	30.27	29.58	30.68	30.5	30.67	30.38	24.35	30.55	31.63	6.74	6.96
SCR1200_2 (bottom)	31.67	29.37	24.4	30.31	31.77	30.02	31	29.9	30.96	24.48	29.73	31.77	6.97	6.72
SCR1200_2 (avg)	31.745	29.545	24.5	30.29	30.675	30.35	30.75	30.285	30.67	24.415	30.14	31.7	6.855	6.84
SCR1200_3 (top)	31.88	29.65	24.4	30.43	29.46	31.75	30.18	29.65	29.95	24.45	30.82	31.8	7.07	6.9
SCR1200_3 (bottom)	31.69	30.18	24.35	30.45	29.65	31.8	30.28	29.85	30.38	24.1	30.85	31.77	6.82	6.78
SCR1200_3 (avg)	31.785	29.915	24.375	30.44	29.555	31.775	30.23	29.75	30.165	24.275	30.835	31.785	6.945	6.84

Table A-3 Geometric measurements of specimens SCR1200\_1, SCR1200\_2 and SCR1200\_3

Specimen No.	F1	F2	F3	F4	F5	F6	F7	F8	F9	F10	F11	F12	S1	S2
SCR1600_1 (top)	31.94	30.76	24.42	30.28	30.43	29.93	30.74	29.9	30.72	24.5	30.28	31.95	6.89	6.94
SCR1600_1 (bottom)	31.96	30.54	24.8	30.22	29.71	30.79	29.62	30.78	29.51	23.78	31.61	32.17	7.32	6.01
SCR1600_1 (avg)	31.95	30.65	24.61	30.25	30.07	30.36	30.18	30.34	30.115	24.14	30.945	32.06	7.105	6.475
SCR1600_2 (top)	31.83	31.01	24.3	30.37	30.49	30.09	31.13	28.8	30.39	24.83	30.15	31.99	6.92	6.67
SCR1600_2 (bottom)	31.82	29.69	25.44	30.42	28.75	31.4	29.7	31.17	30.47	23.77	31.32	32	6.52	6.53
SCR1600_2 (avg)	31.825	30.35	24.87	30.395	29.62	30.745	30.415	29.985	30.43	24.3	30.735	31.995	6.72	6.6
SCR1600_3 (top)	32.05	31.06	24.41	30.16	30.23	30.97	30.1	30.08	30.48	24.76	29.86	31.71	6.61	6.65
SCR1600_3 (bottom)	31.95	30.76	24.37	30.24	30.07	30.59	29.15	30.97	30.47	23.65	31.47	31.9	6.6	6.38
SCR1600_3 (avg)	32	30.91	24.39	30.2	30.15	30.78	29.625	30.525	30.475	24.205	30.665	31.805	6.605	6.515

Table A-4 Geometric measurements of specimens SCR1600\_1, SCR1600\_2 and SCR1600\_3

All measurements are in millimetres

Specimen No.	F1	F2	F3	F4	F5	F6	F7	F8	F9	F10	F11	F12	S1	S2
SCR2000_1 (top)	32.33	30.38	24.4	29.98	30.13	30.83	31	29.84	30.13	24.31	30.82	32.1	6.61	6.42
SCR2000_1 (bottom)	32.48	29.92	24.79	30.98	29.74	30.27	28.9	31.43	30.2	23.63	31.64	32.26	6.61	5.68
SCR2000_1 (avg)	32.405	30.15	24.595	30.48	29.935	30.55	29.95	30.635	30.165	23.97	31.23	32.18	6.61	6.05
SCR2000_2 (top)	32.16	31.1	23.8	30.74	30.99	30	31.25	29.06	30.61	24.91	30.36	32.14	6.79	6.68
SCR2000_2 (bottom)	32.1	30.05	25.56	30.52	28.67	30.7	28.86	32.61	29.97	23.1	32.02	31.98	6.79	6.66
SCR2000_2 (avg)	32.13	30.575	24.68	30.63	29.83	30.35	30.055	30.835	30.29	24.005	31.19	32.06	6.79	6.67
SCR2000_3 (top)	31.87	30.63	24.96	30.27	29.76	28.86	28.73	30	30.85	24.94	30.64	31.62	6.39	6.12
SCR2000_3 (bottom)	31.69	30.32	25.08	30.23	30.32	28.81	28.84	30.51	29.92	24.94	30.76	31.83	6.13	5.88
SCR2000_3 (avg)	31.78	30.475	25.02	30.25	30.04	28.835	28.785	30.255	30.385	24.94	30.7	31.725	6.26	6

Table A-5 Geometric measurements of specimens SCR2000\_1, SCR2000\_2 and SCR2000\_3

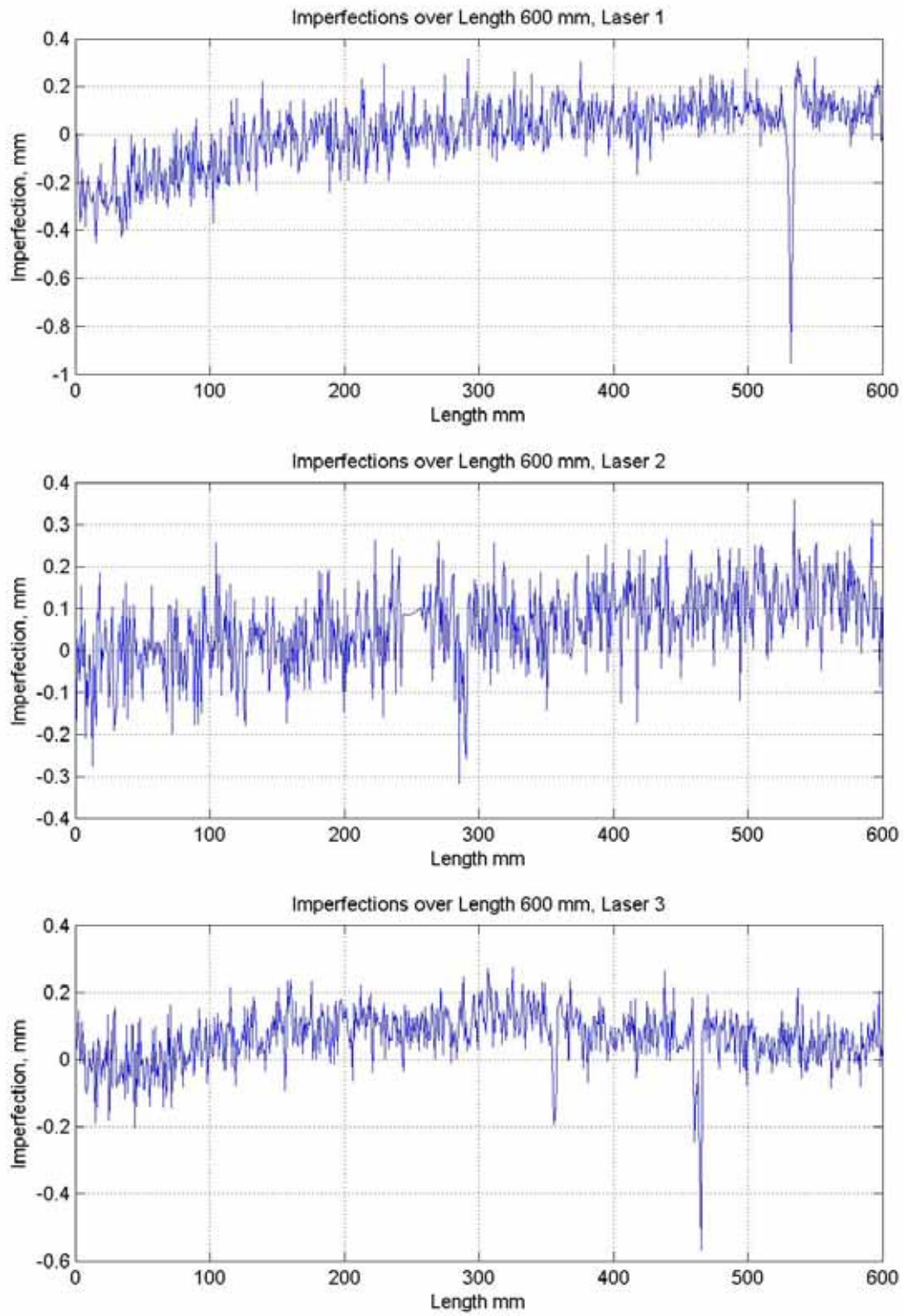


Figure A - 1 Imperfection measurements for specimen SCR600\_1

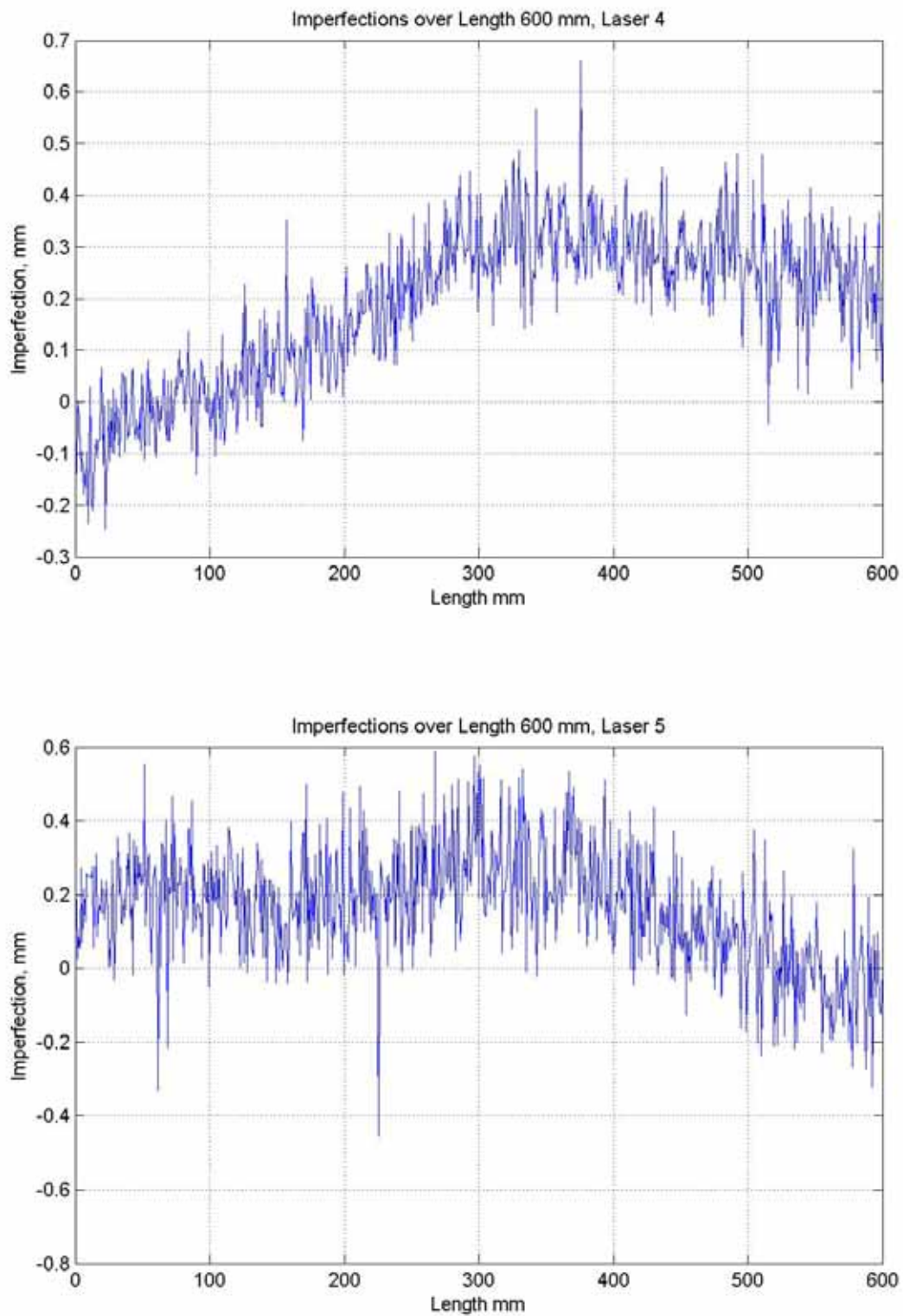


Figure A - 2 Imperfection measurements for specimen SCR600\_1

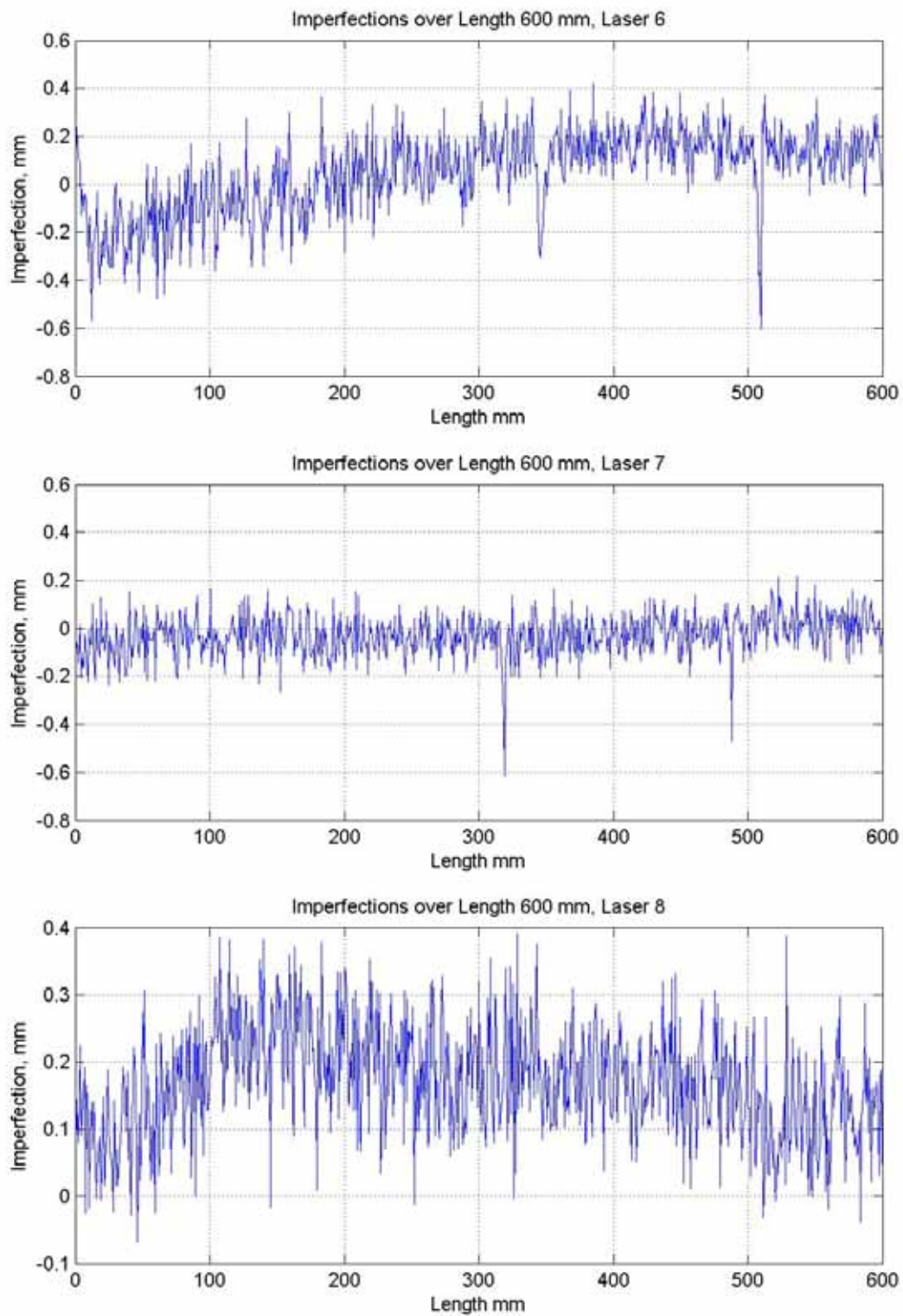


Figure A - 3 Imperfection measurements for specimen SCR600\_1

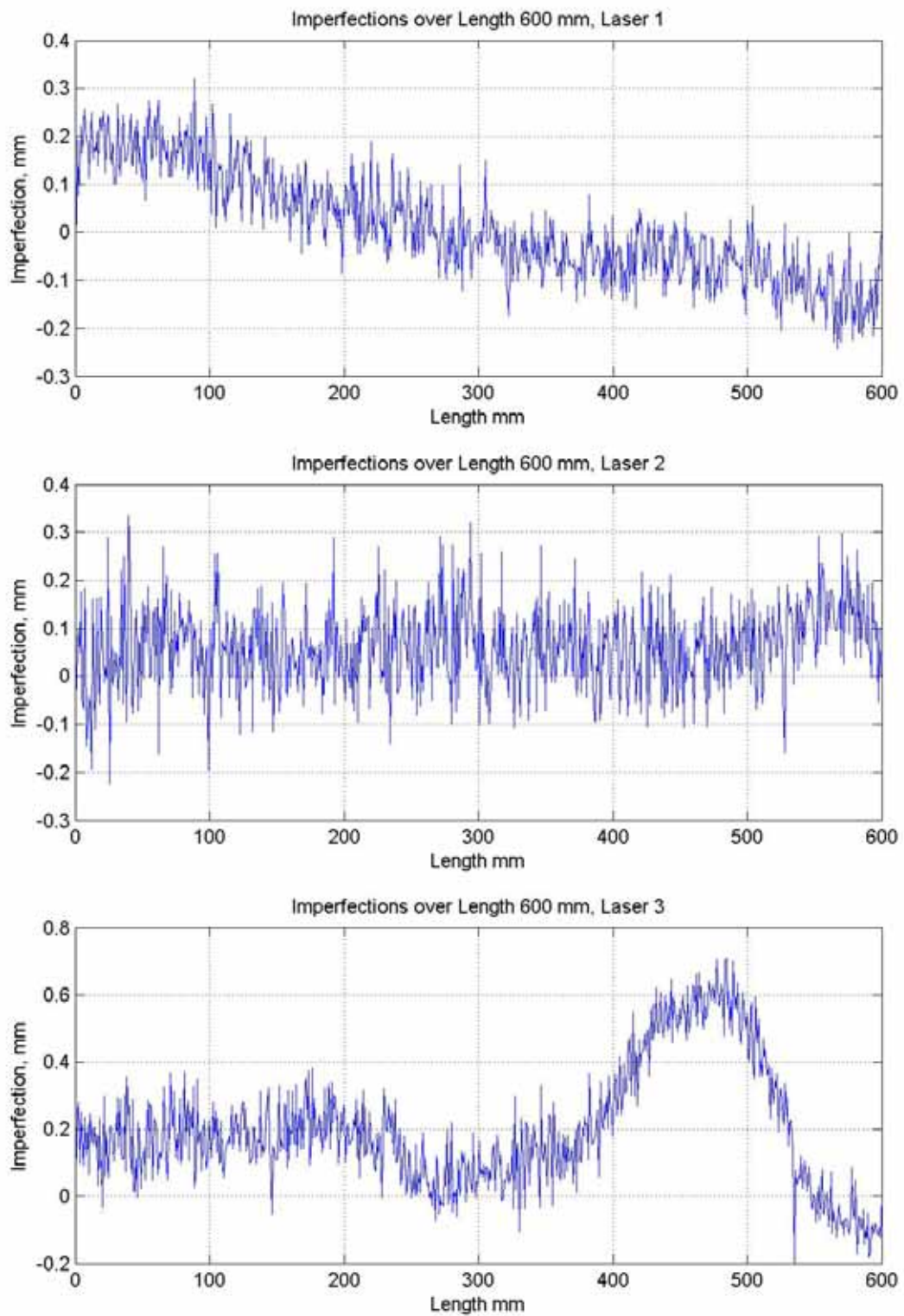


Figure A - 4 Imperfection measurements for specimen SCR600\_2

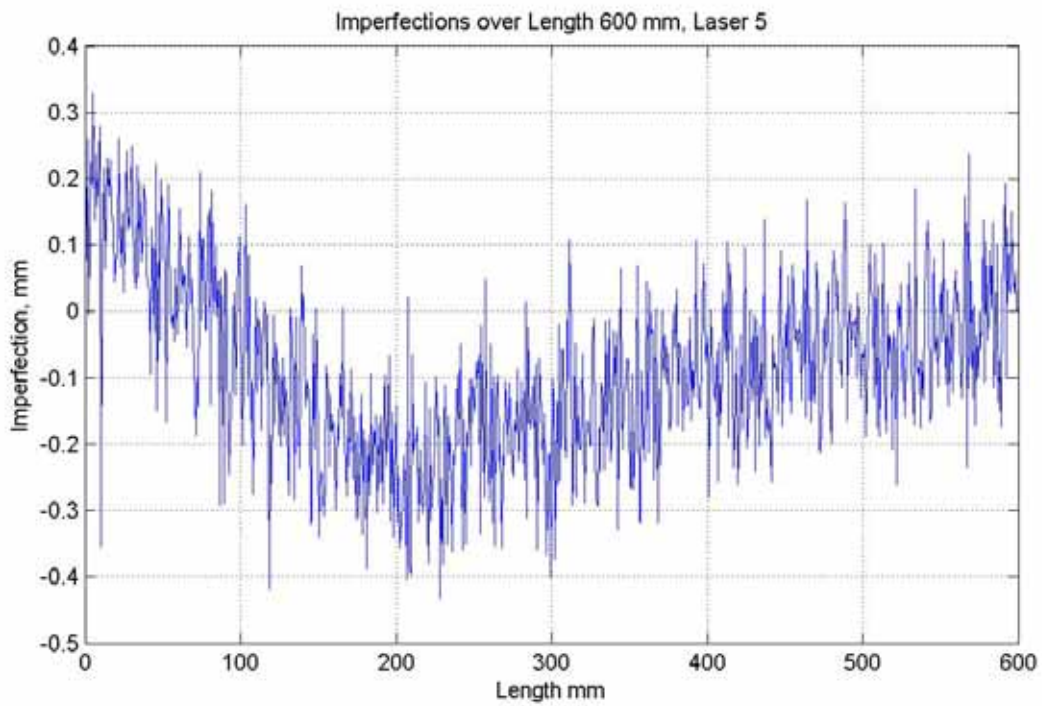
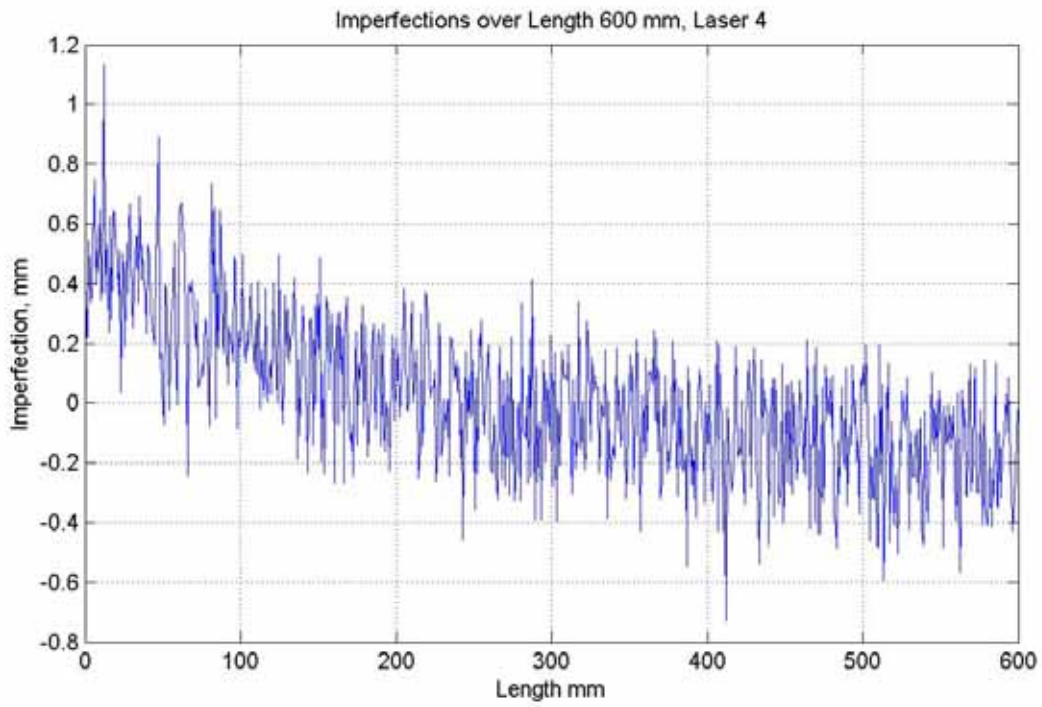


Figure A - 5 Imperfection measurements for specimen SCR600\_2

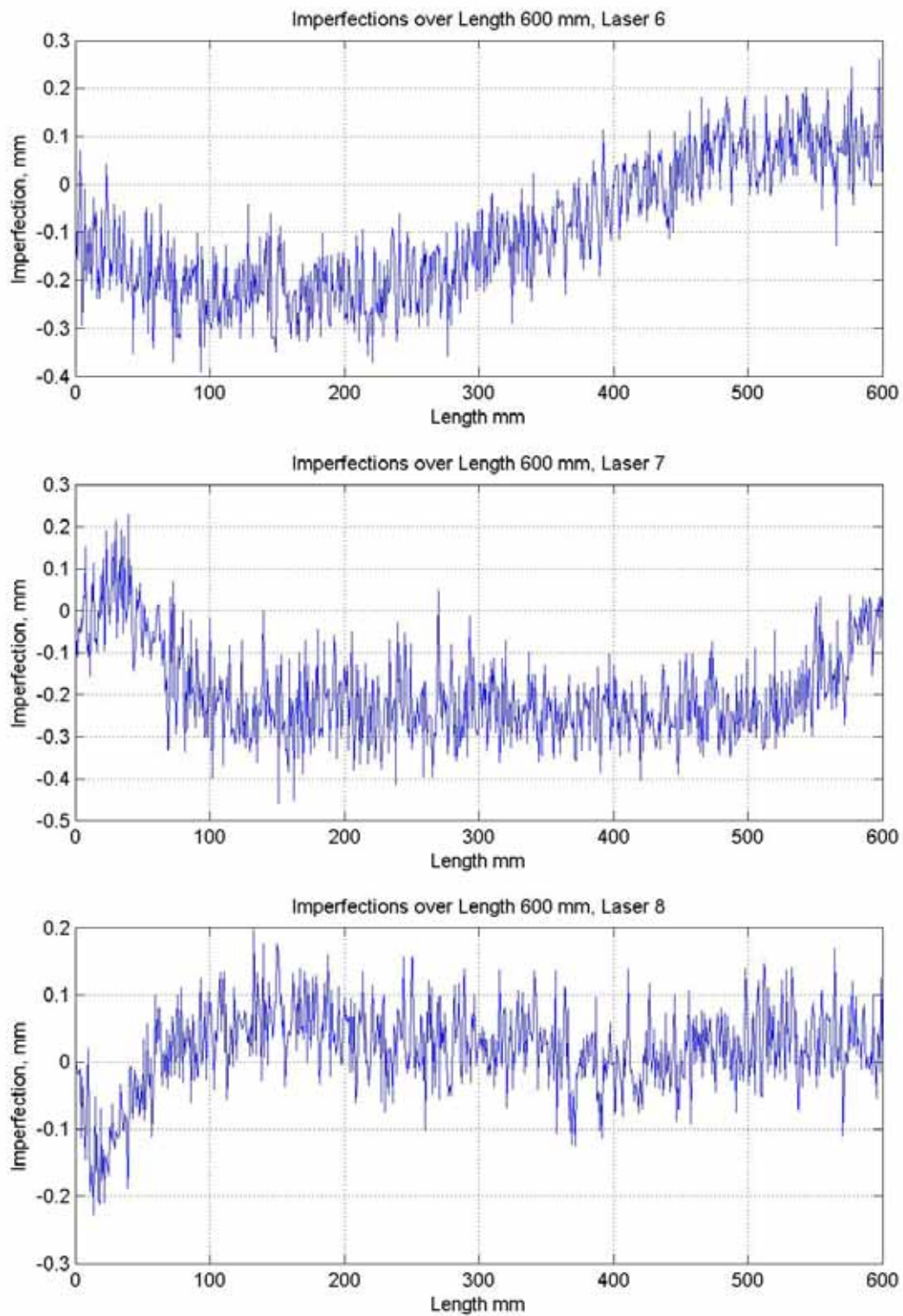


Figure A - 6 Imperfection measurements for specimen SCR600\_2

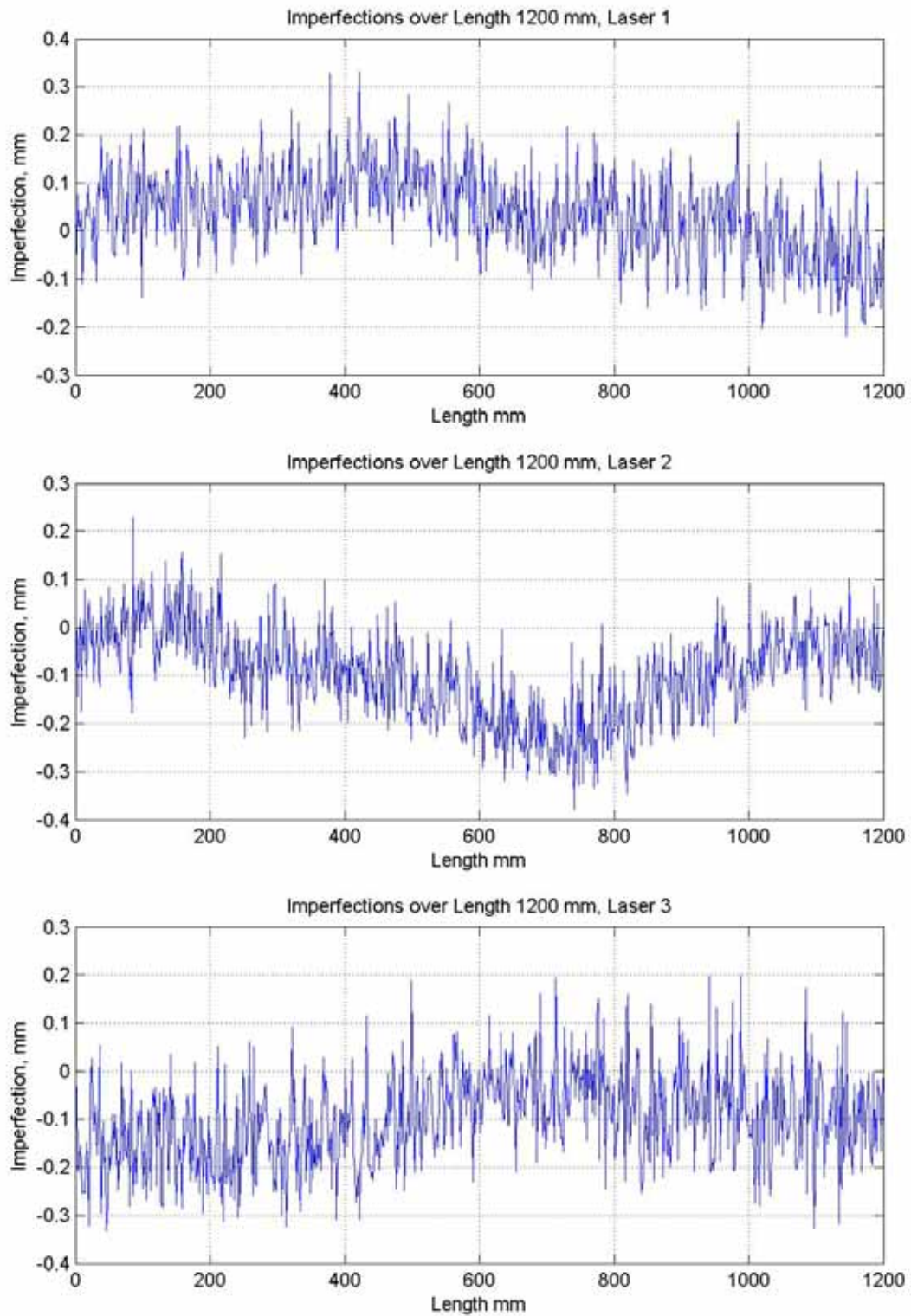


Figure A - 7 Imperfection measurements for specimen SCR1200\_1

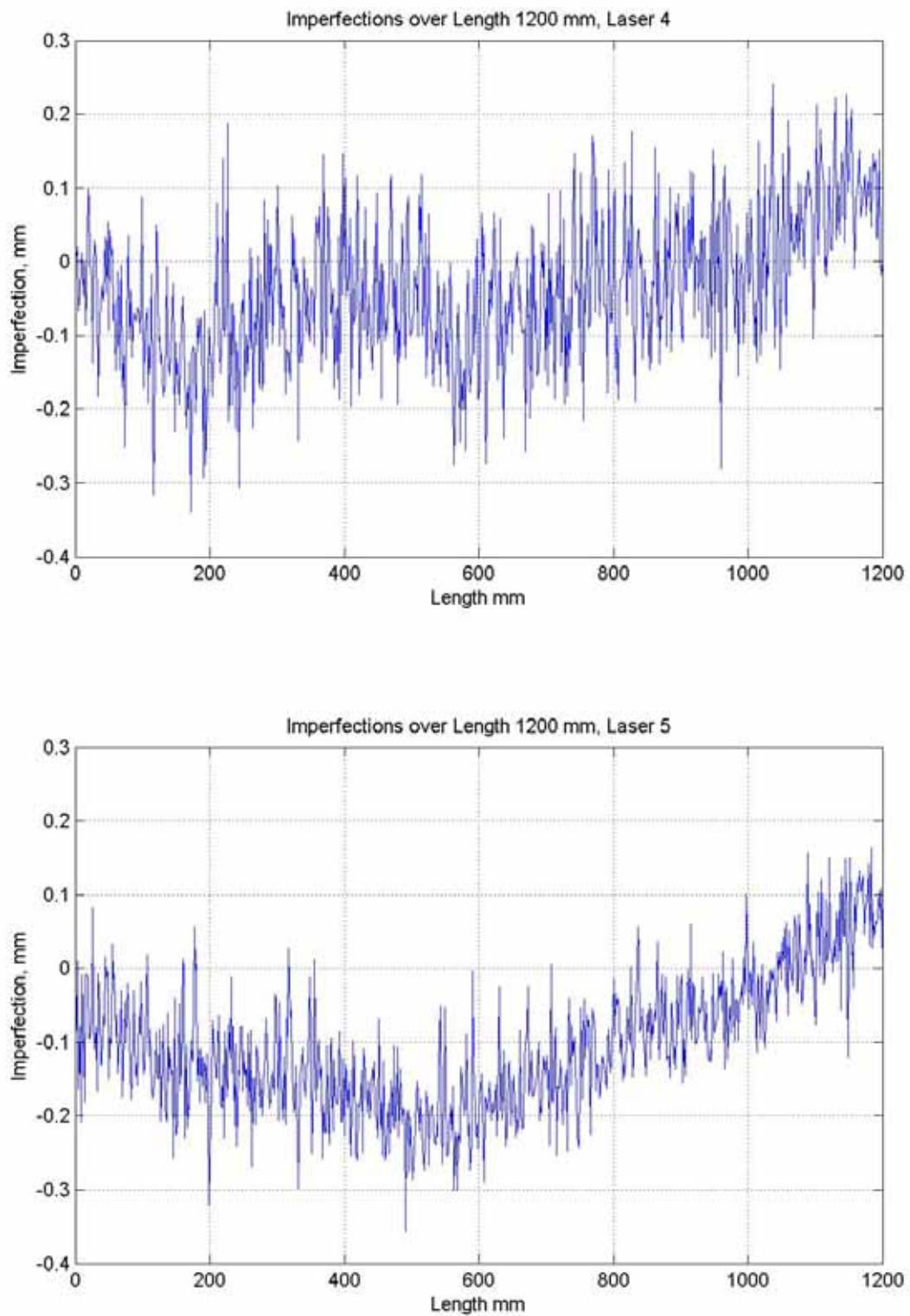


Figure A - 8 Imperfection measurements for specimen SCR1200\_1

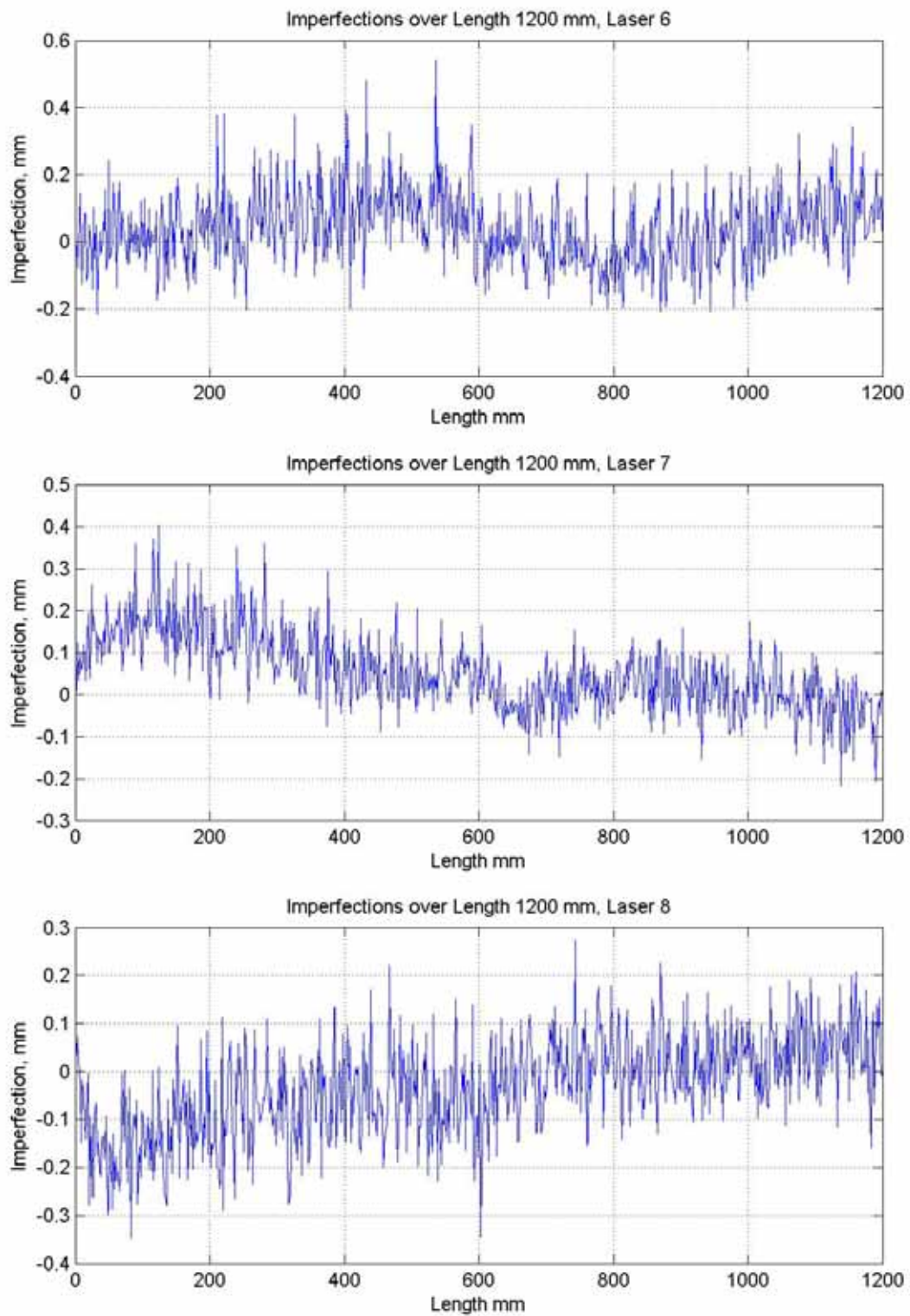


Figure A - 9 Imperfection measurements for specimen SCR1200\_1

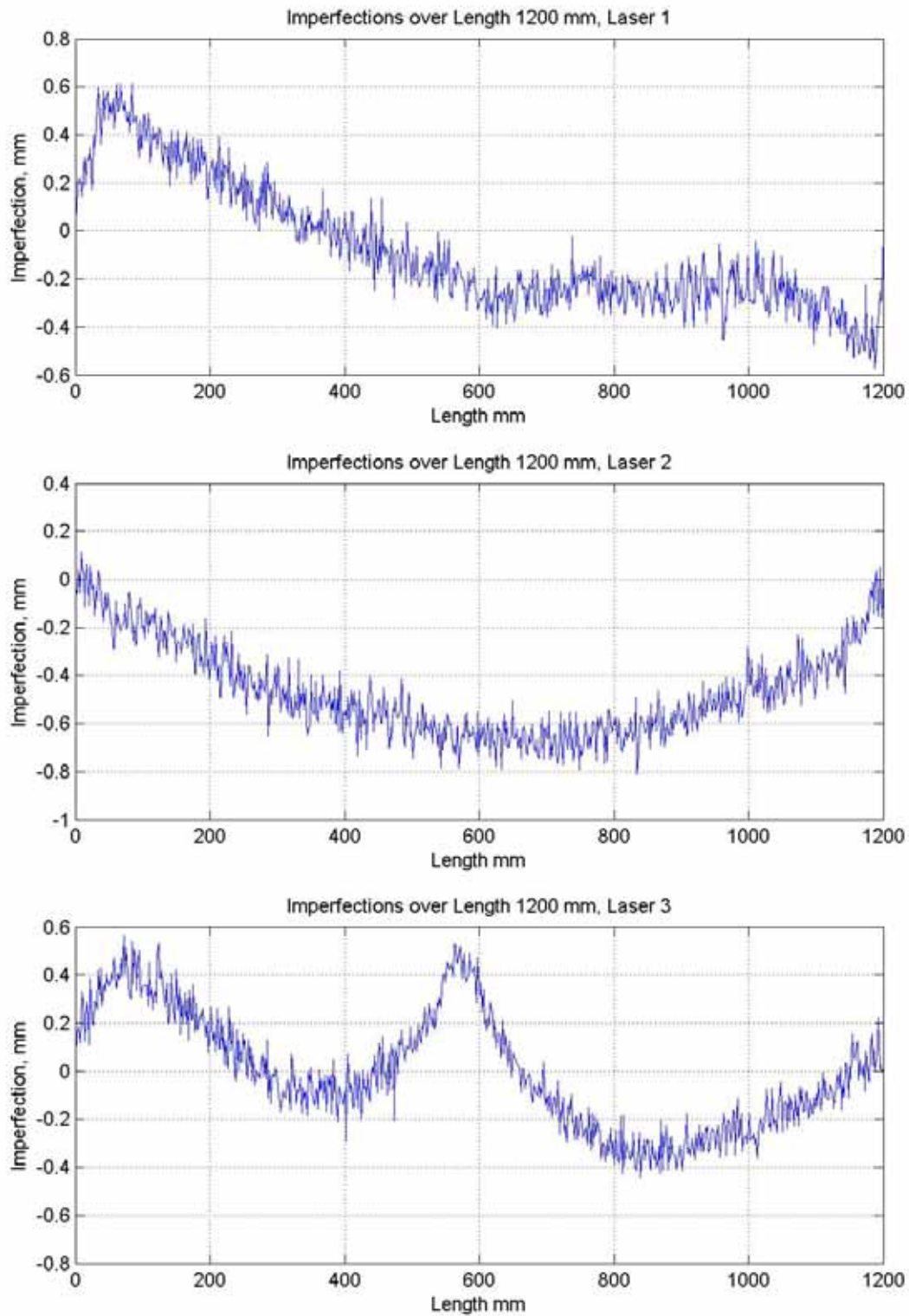


Figure A - 10 Imperfection measurements for specimen SCR1200\_2

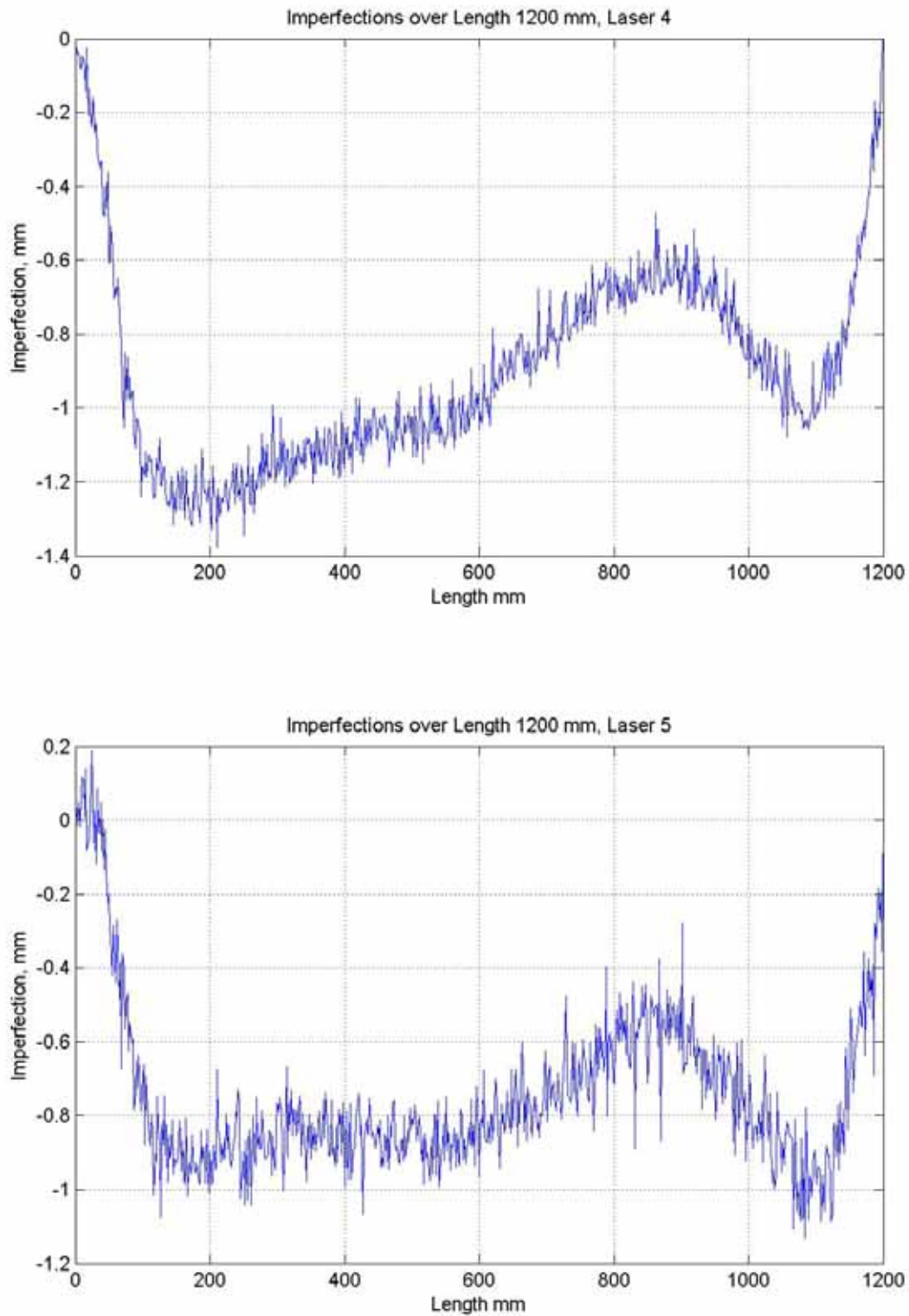


Figure A - 11 Imperfection measurements for specimen SCR1200\_2

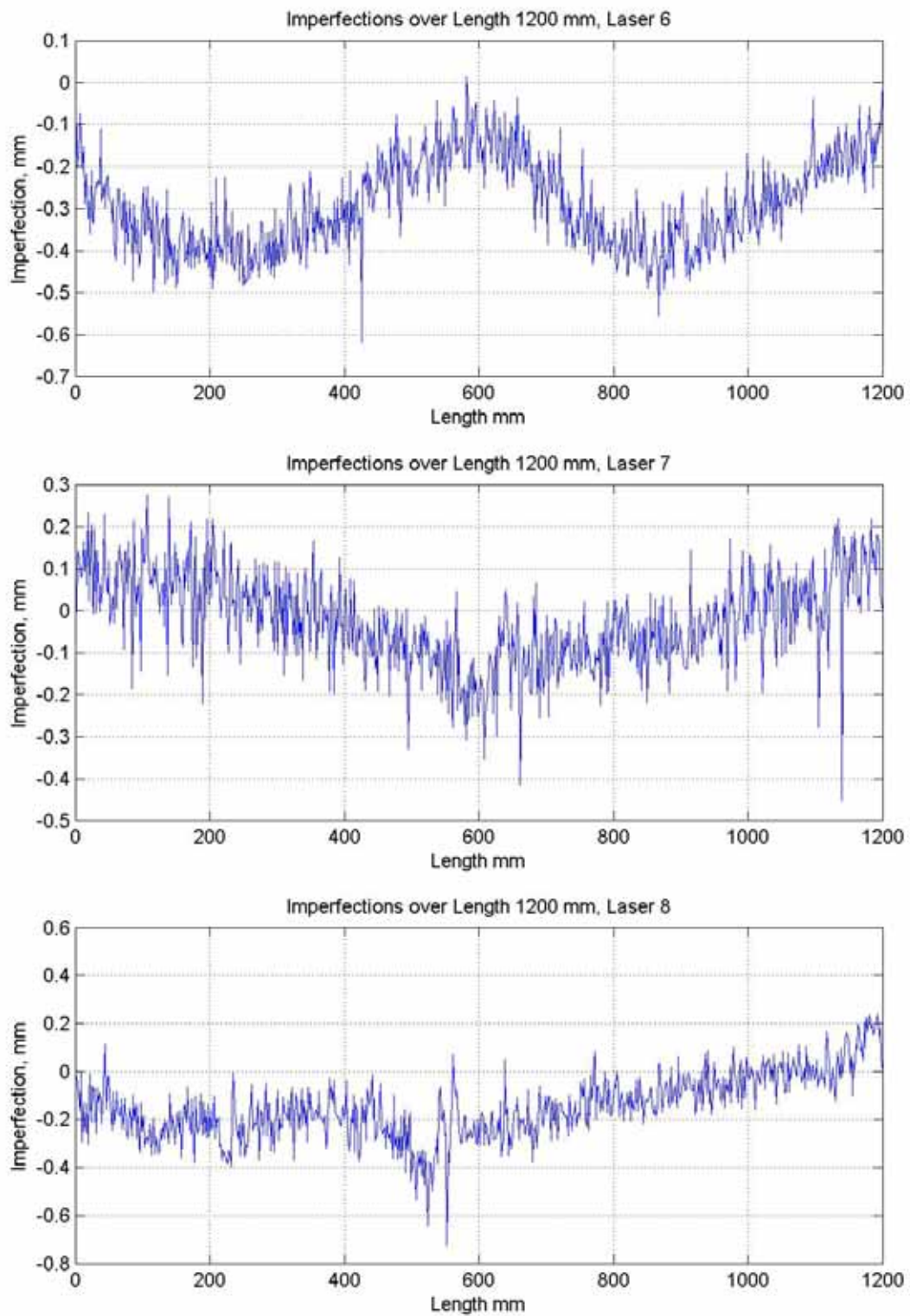


Figure A - 12 Imperfection measurements for specimen SCR1200\_2

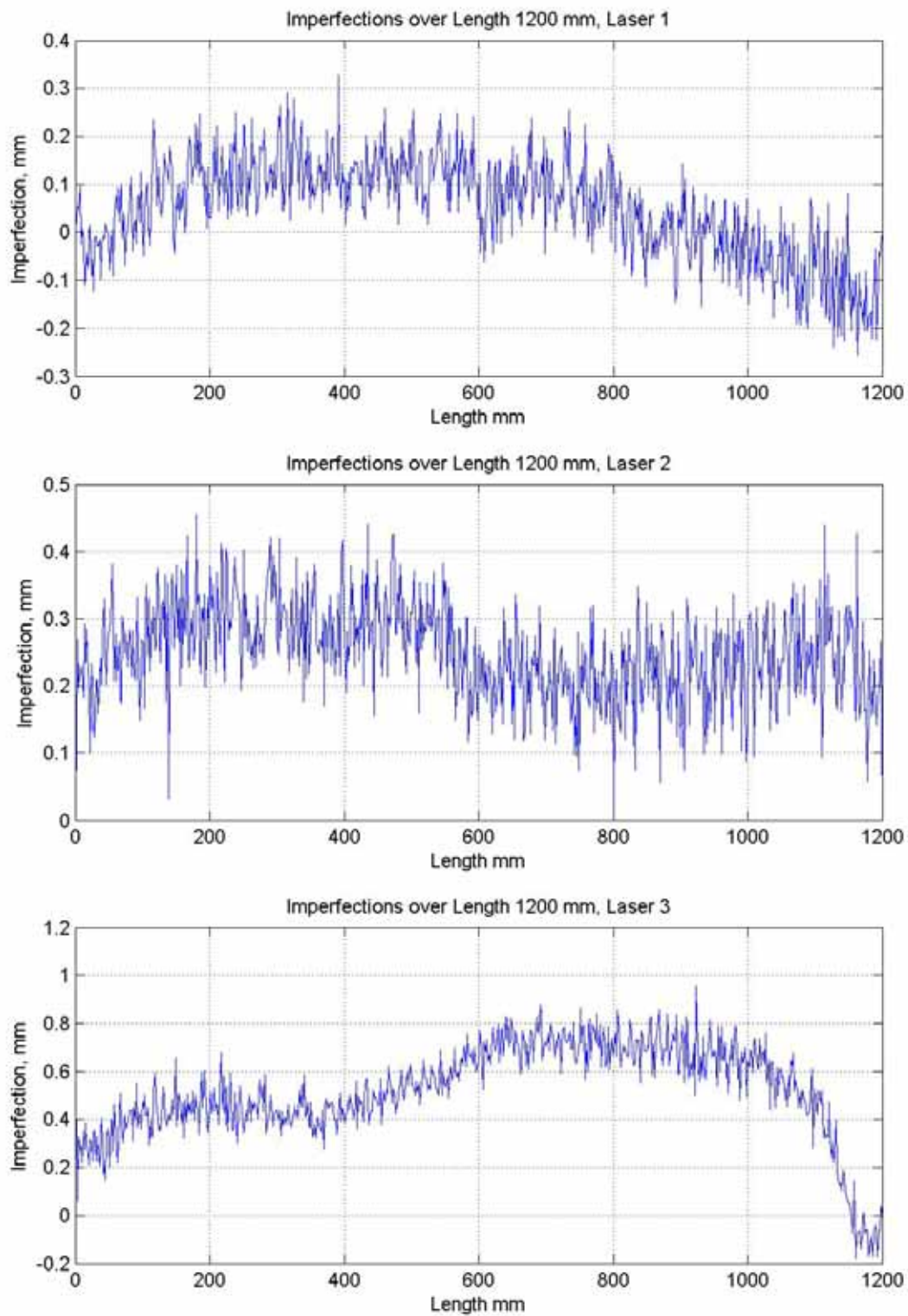


Figure A - 13 Imperfection measurements for specimen SCR1200\_3

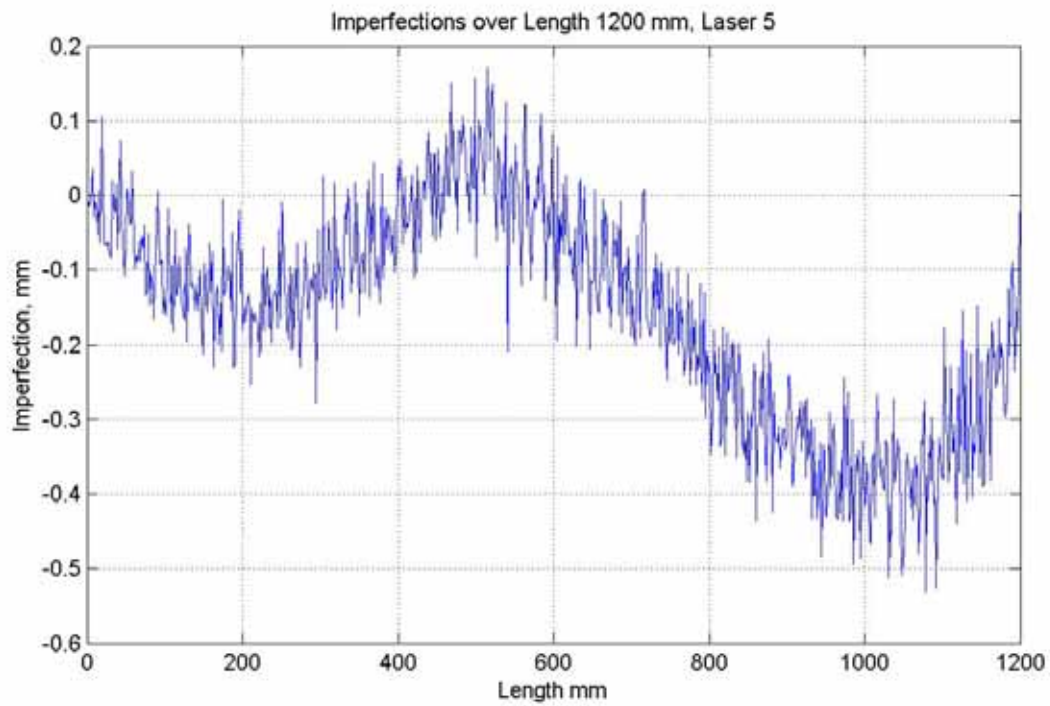
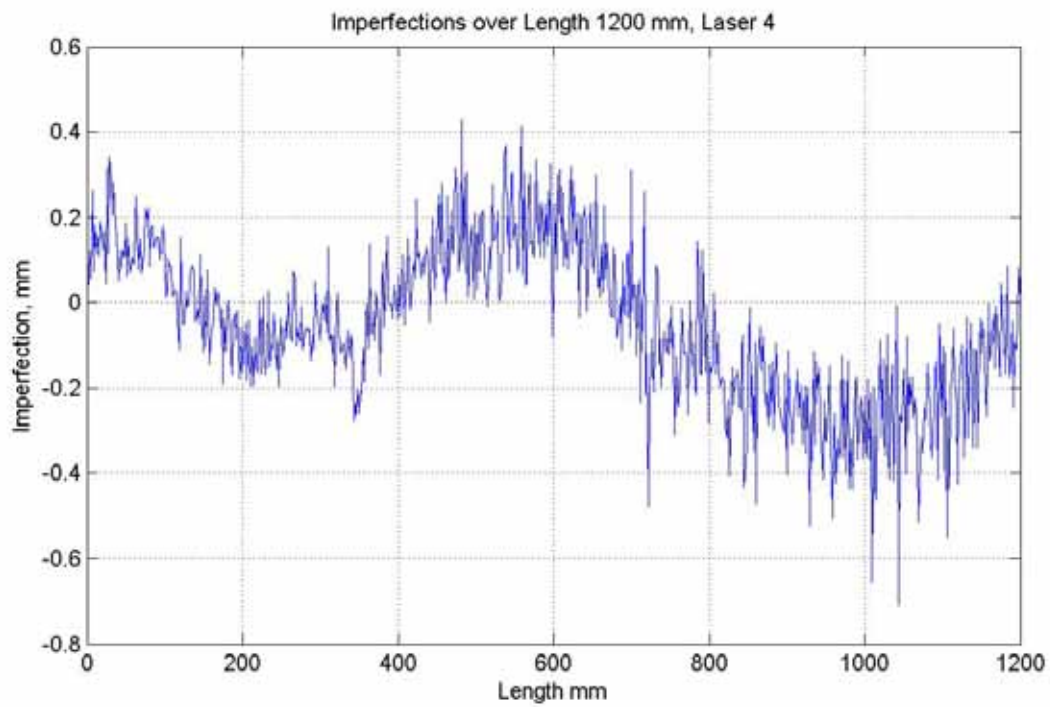


Figure A - 14 Imperfection measurements for specimen SCR1200\_3

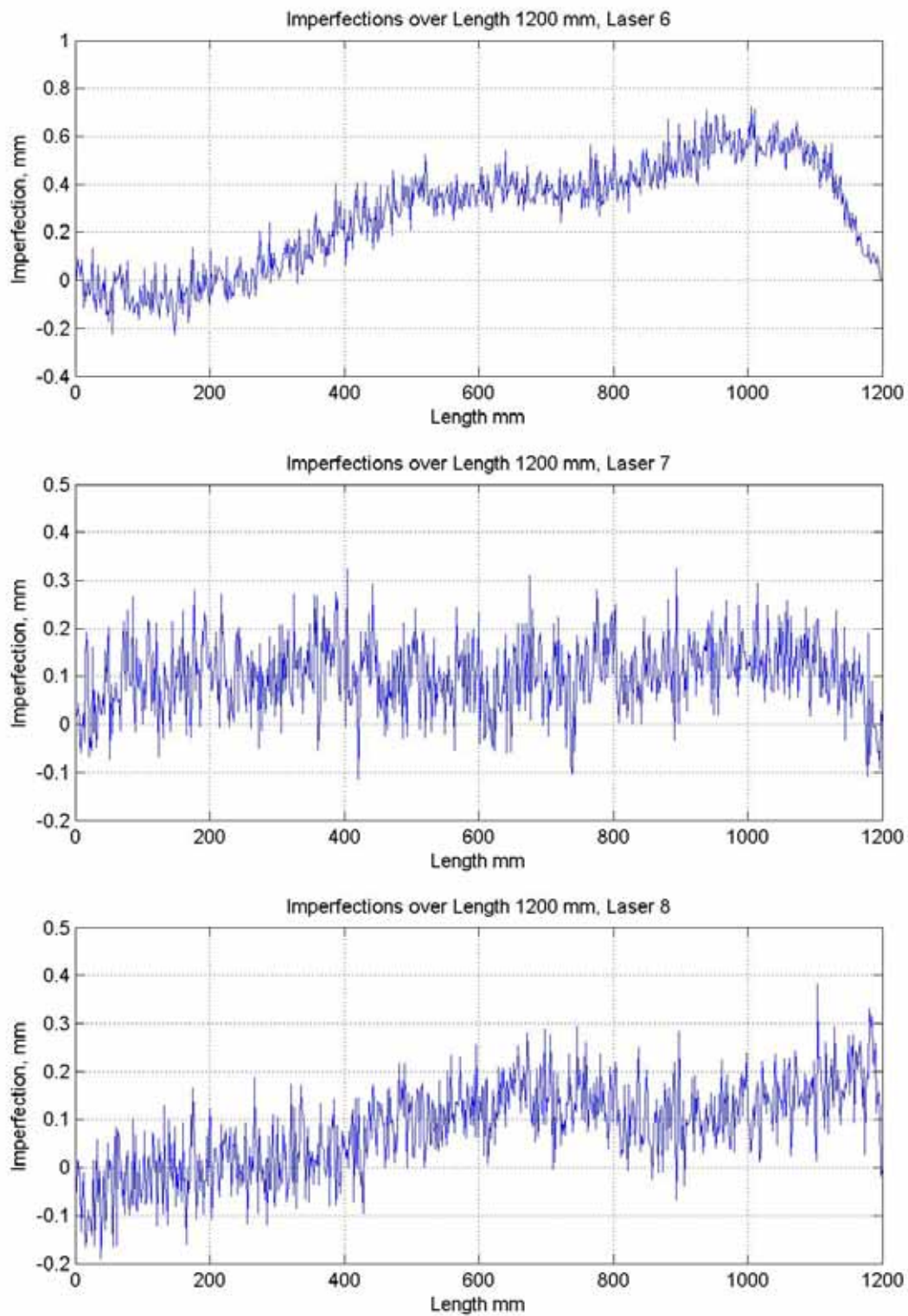


Figure A - 15 Imperfection measurements for specimen SCR1200\_3

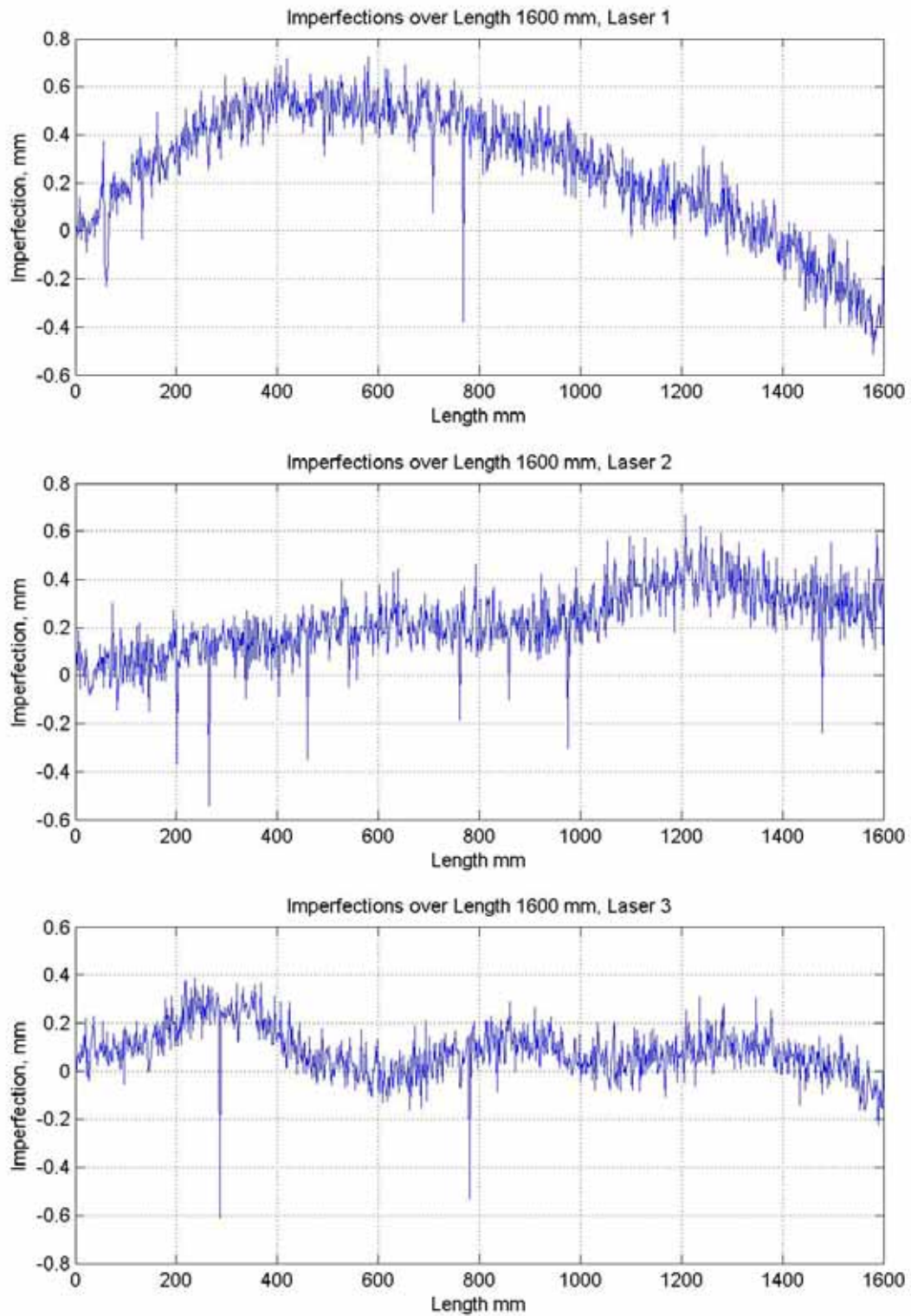


Figure A - 16 Imperfection measurements for specimen SCR1600\_1

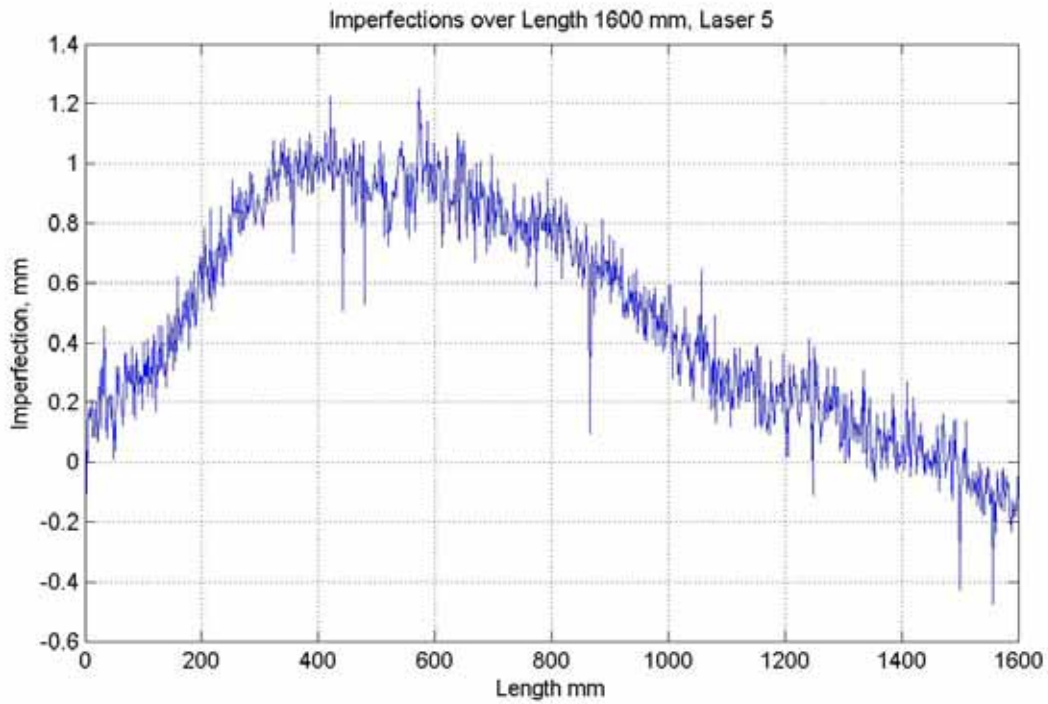
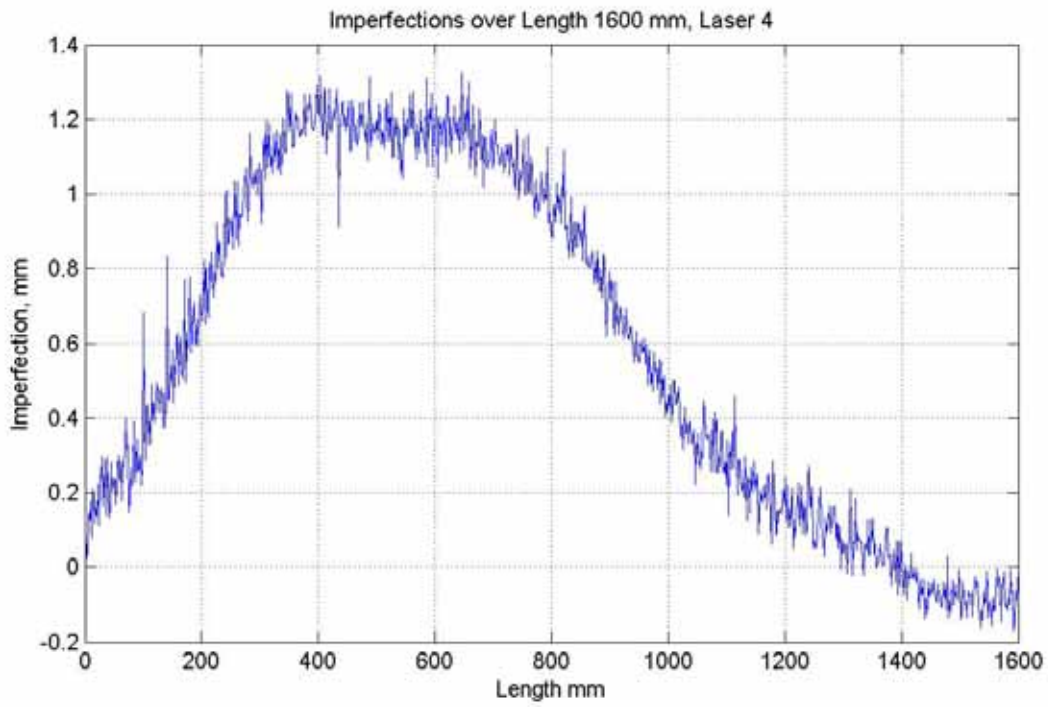


Figure A - 17 Imperfection measurements for specimen SCR1600\_1

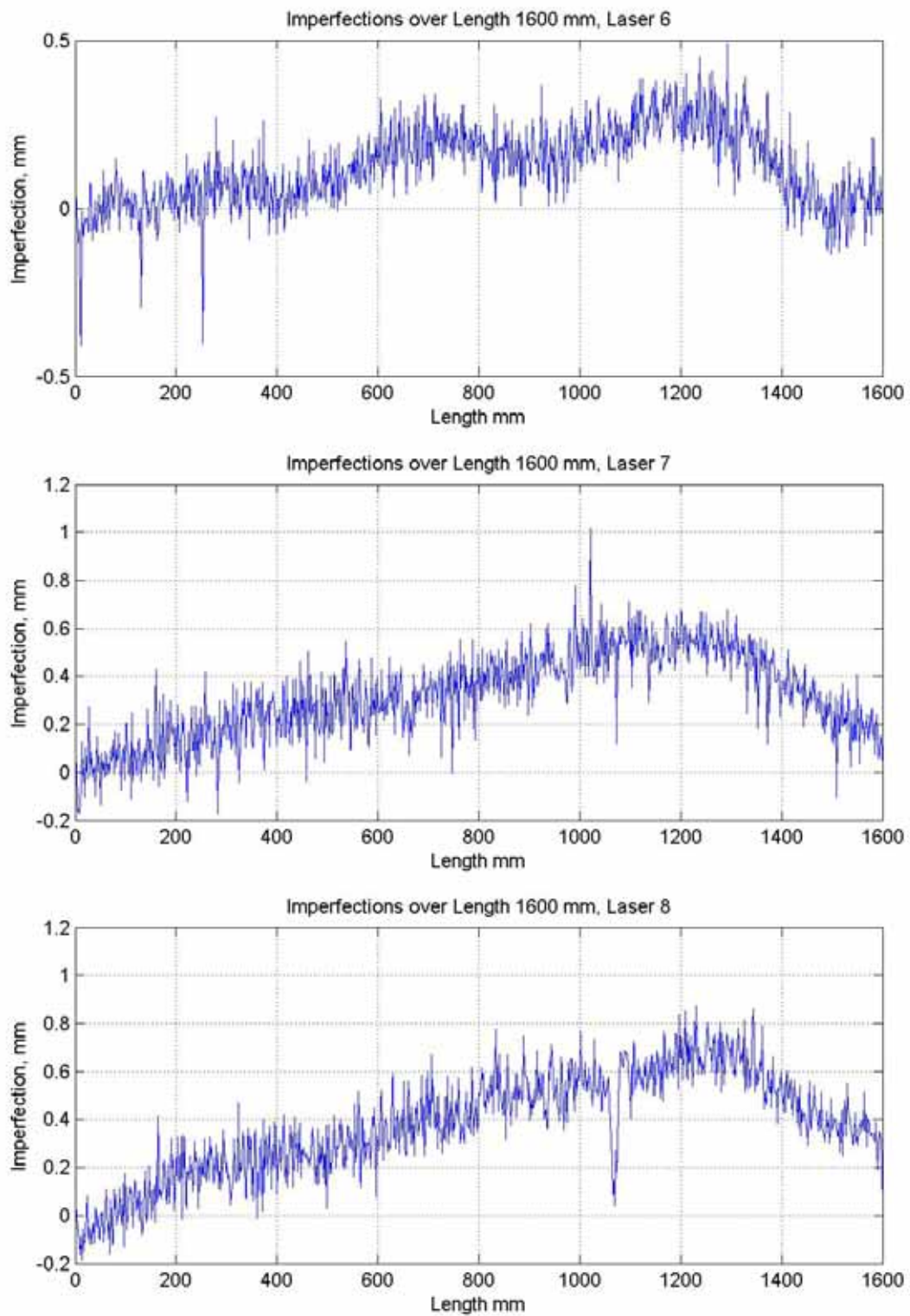


Figure A - 18 Imperfection measurements for specimen SCR1600\_1

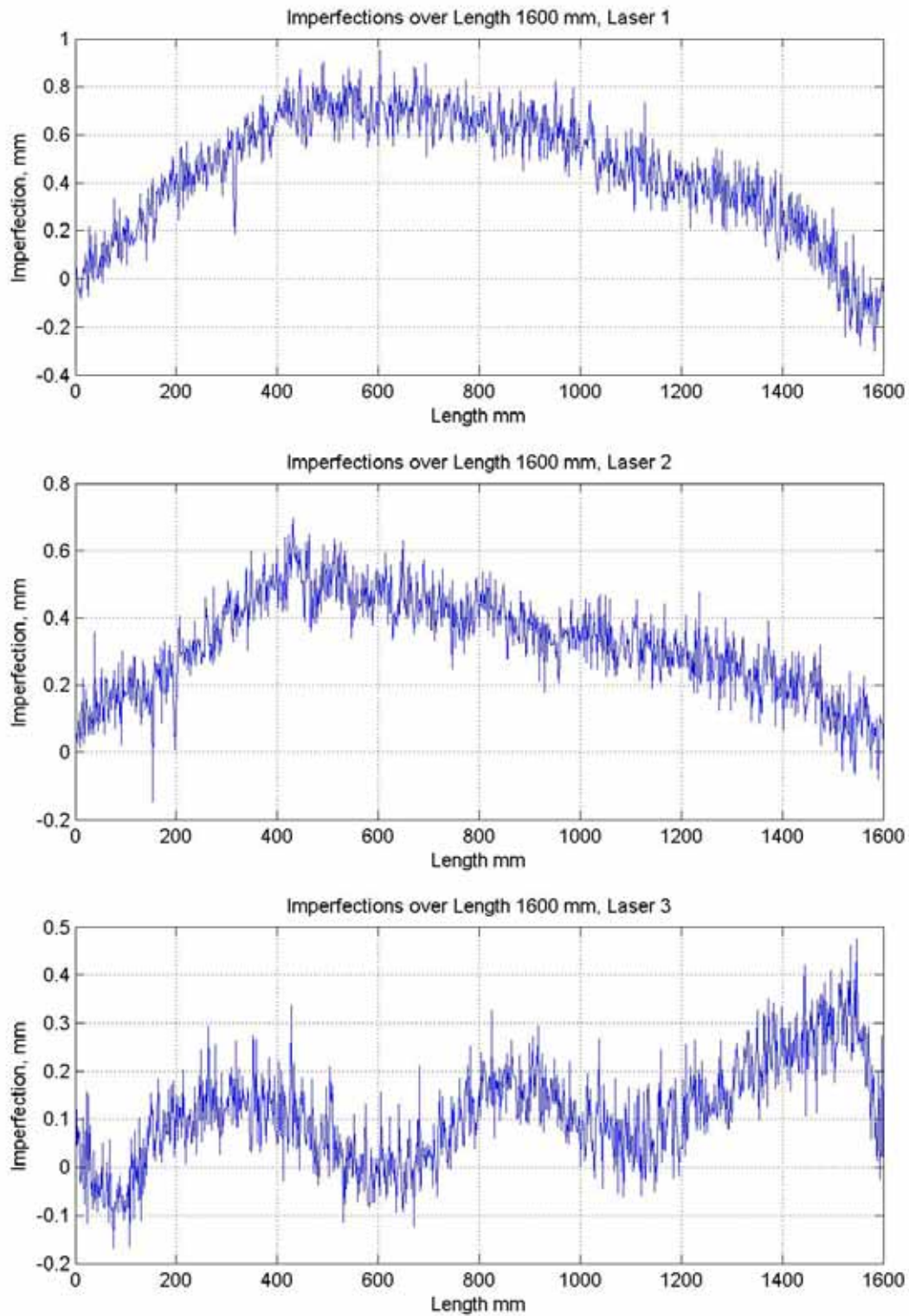


Figure A - 19 Imperfection measurements for specimen SCR1600\_2

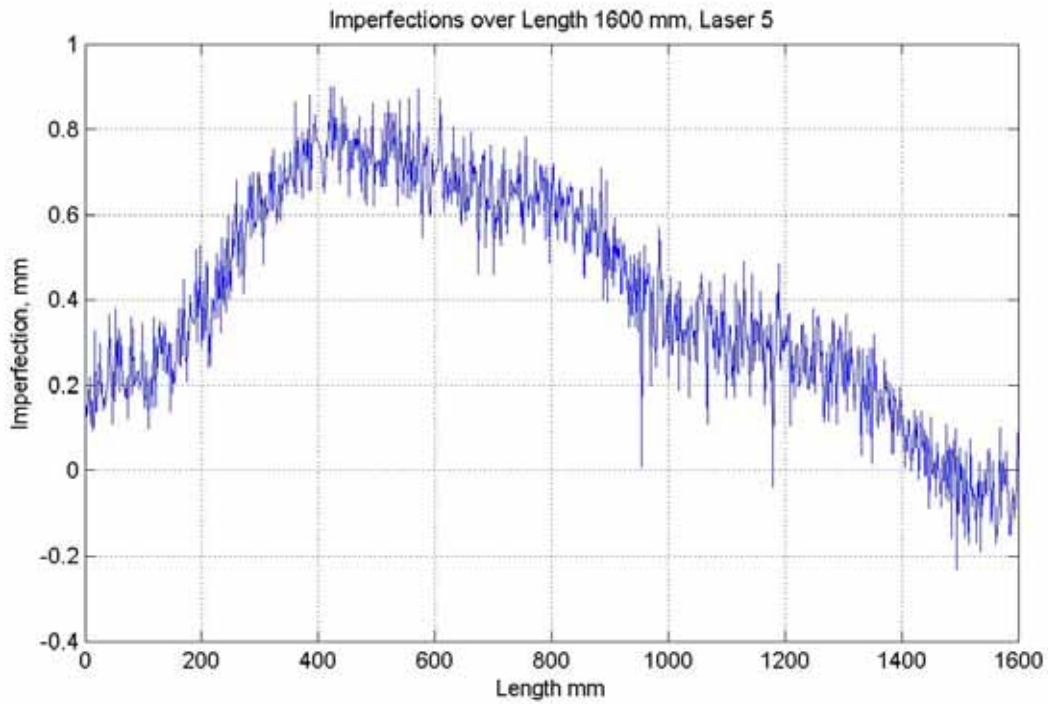
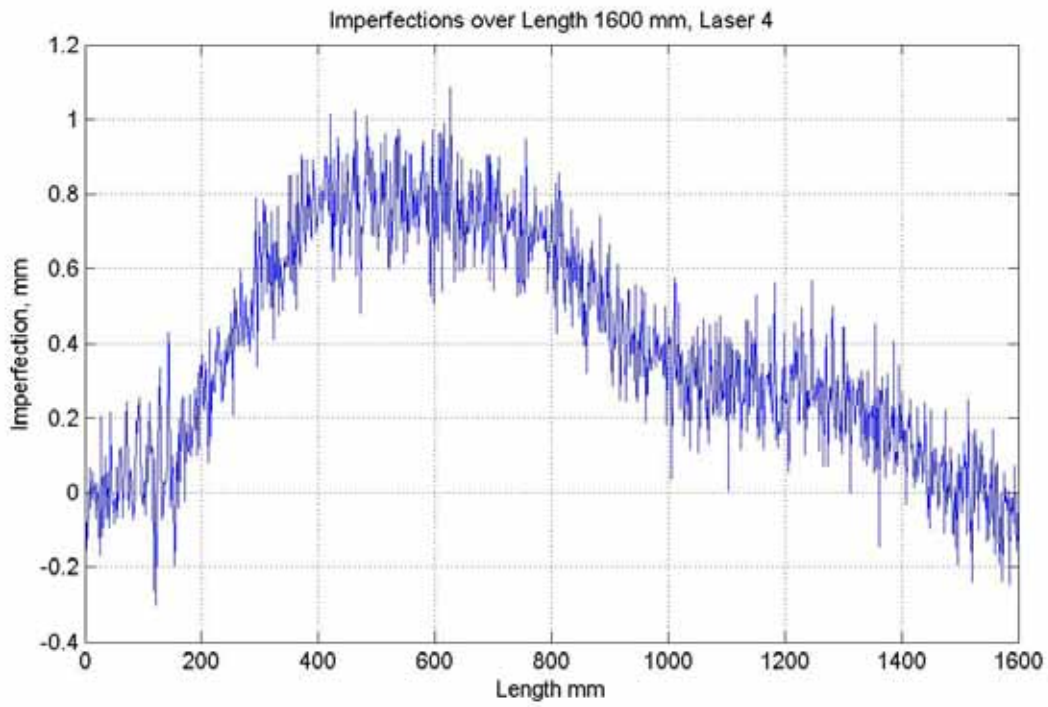


Figure A - 20 Imperfection measurements for specimen SCR1600\_2

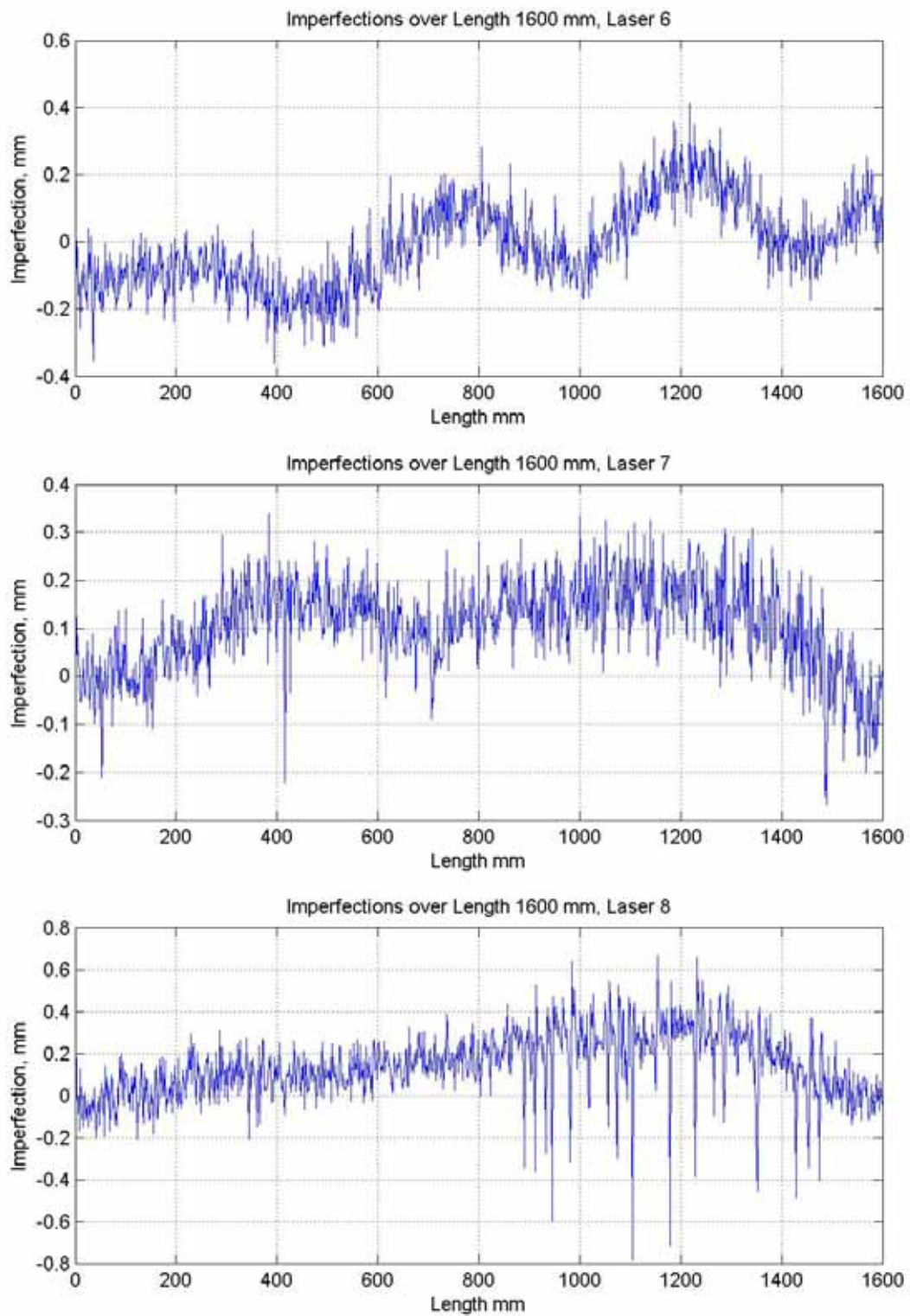


Figure A - 21 Imperfection measurements for specimen SCR1600\_2

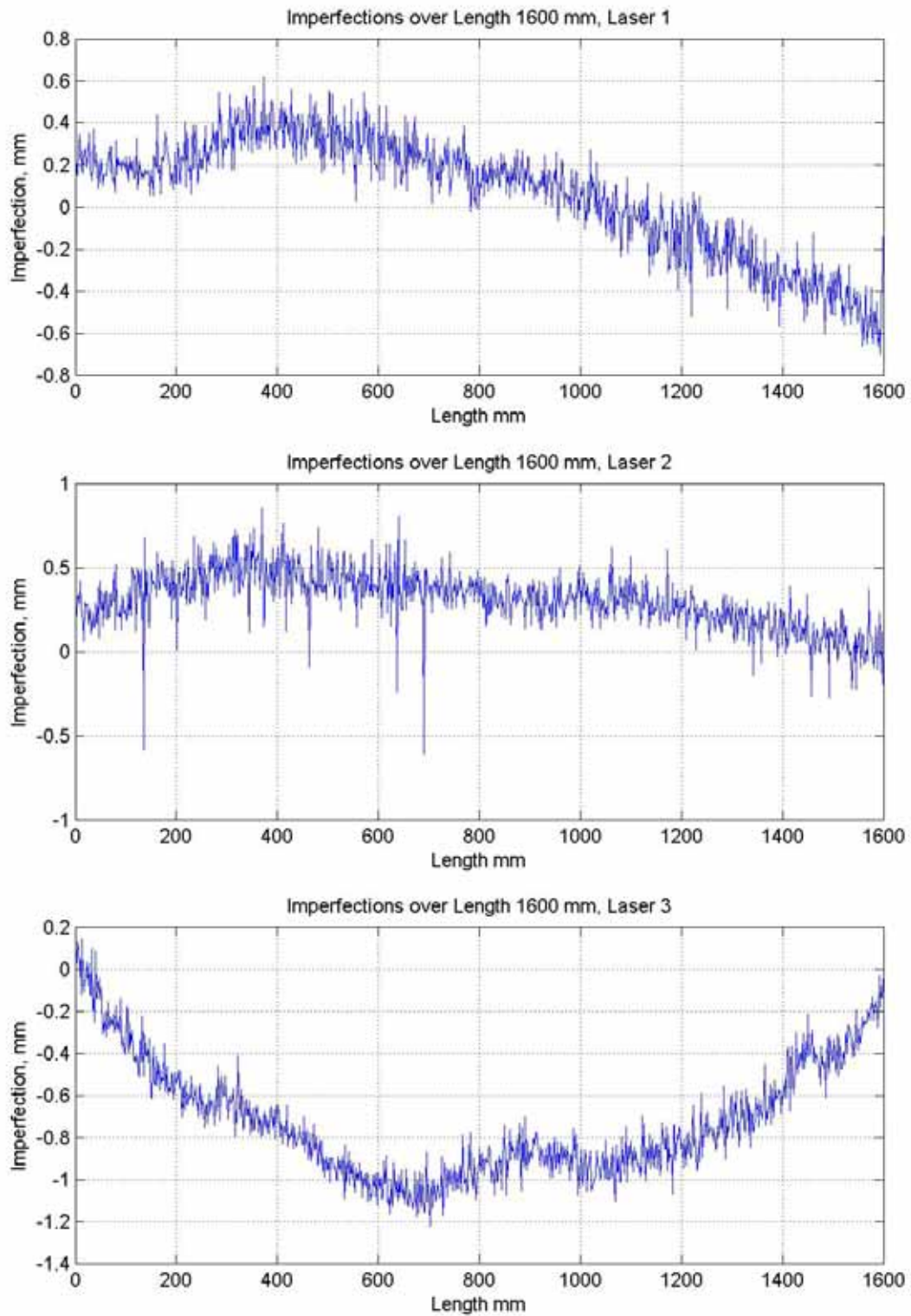


Figure A - 22 Imperfection measurements for specimen SCR1600\_3

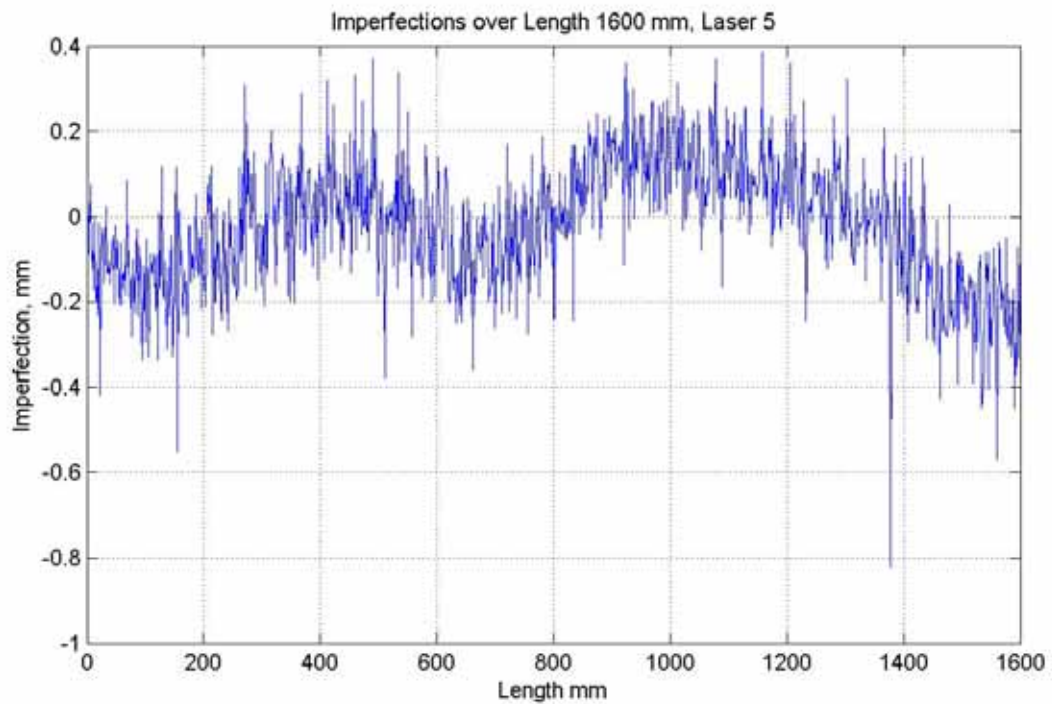
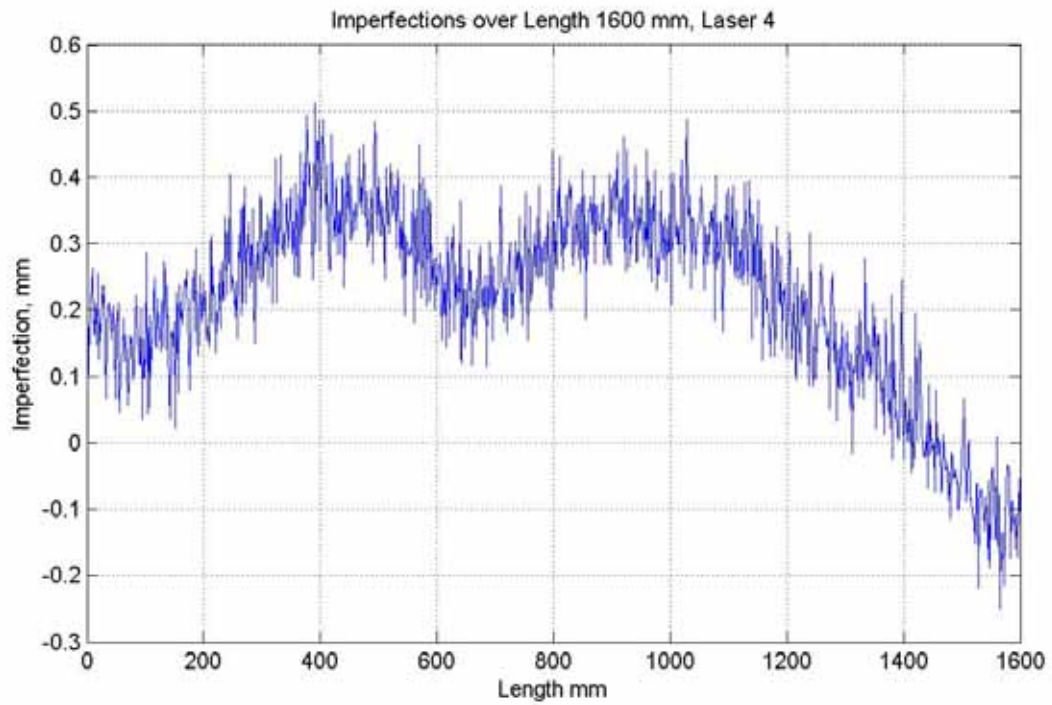


Figure A - 23 Imperfection measurements for specimen SCR1600\_3

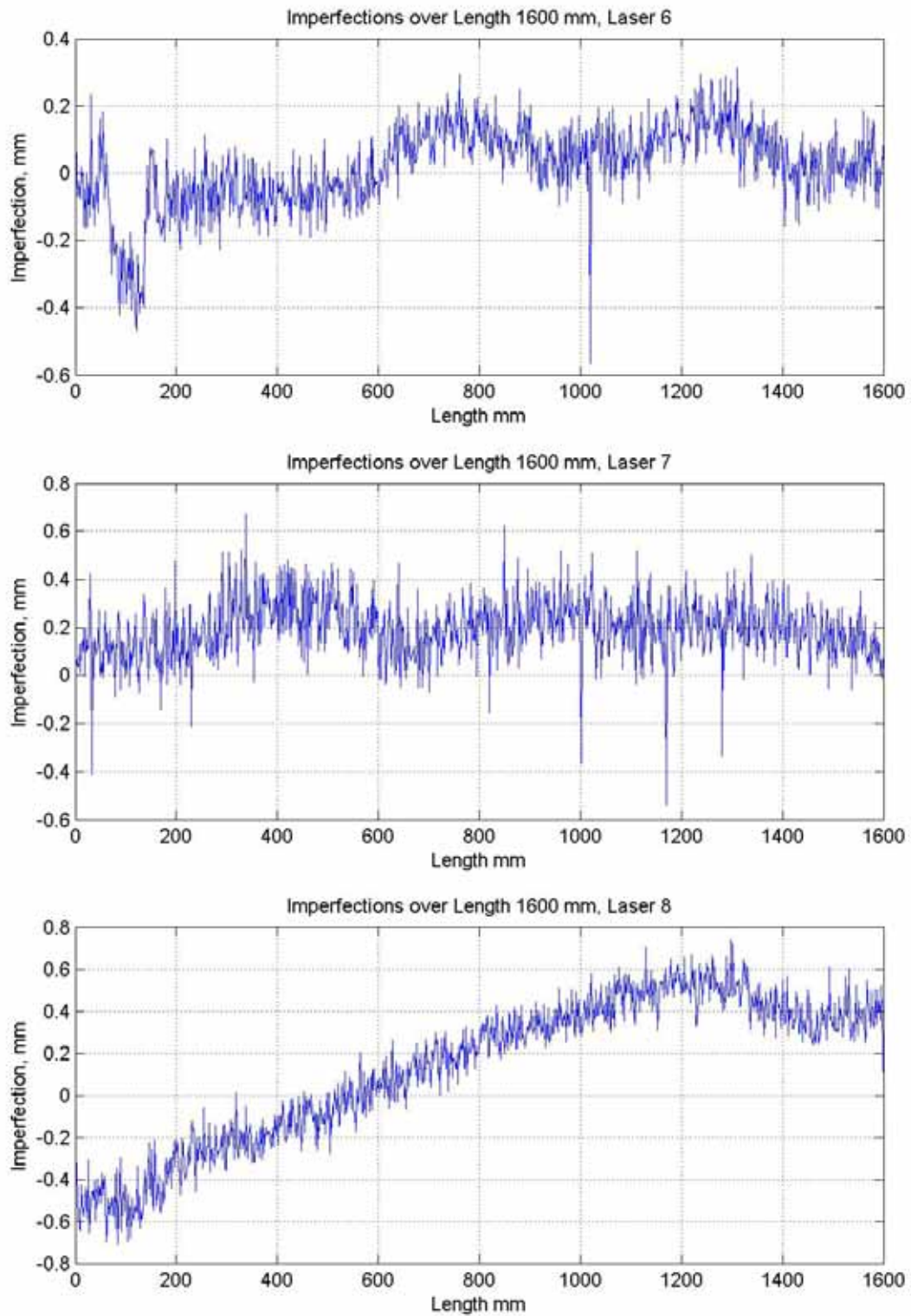


Figure A - 24 Imperfection measurements for specimen SCR1600\_3

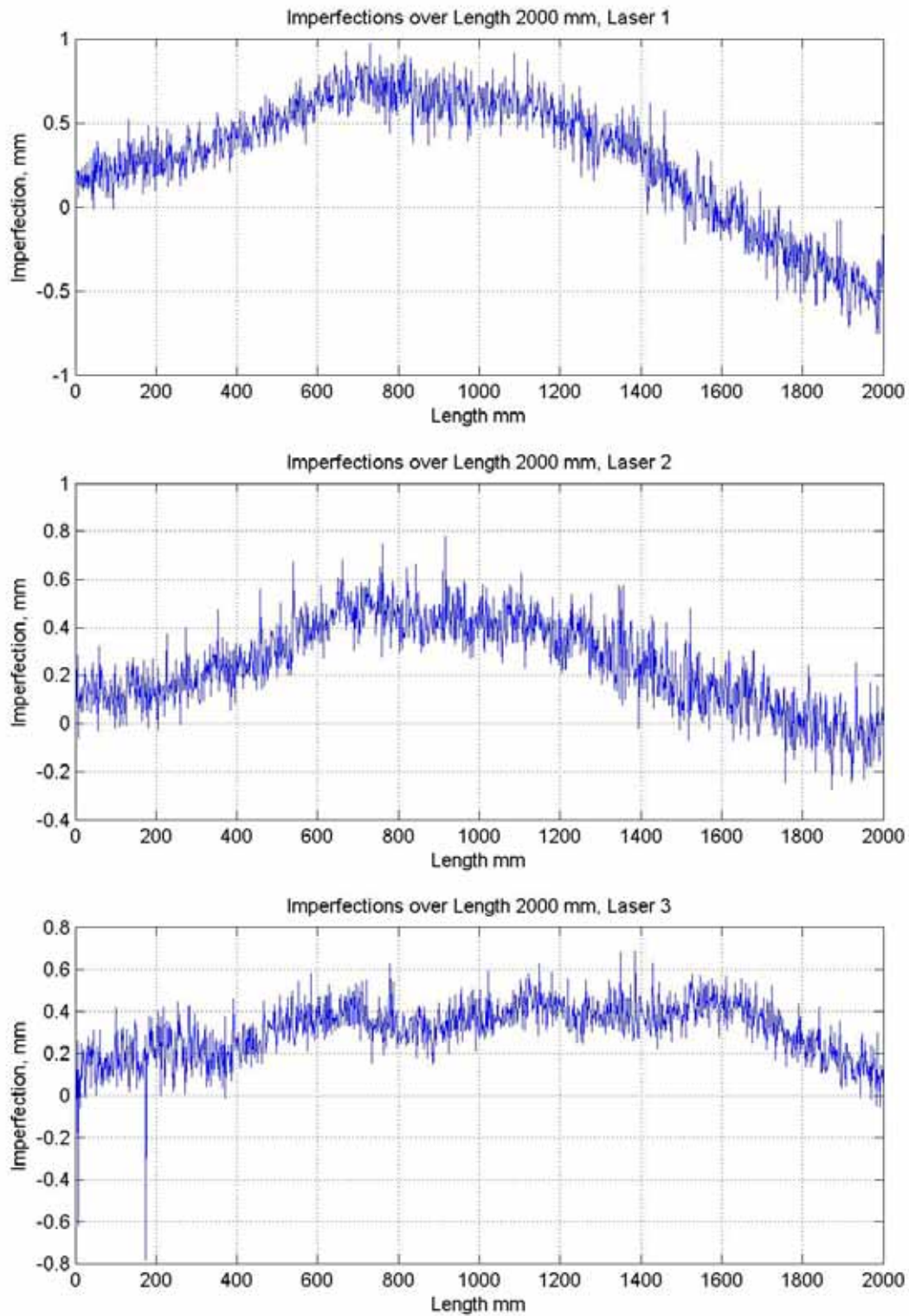


Figure A - 25 Imperfection measurements for specimen SCR2000\_1

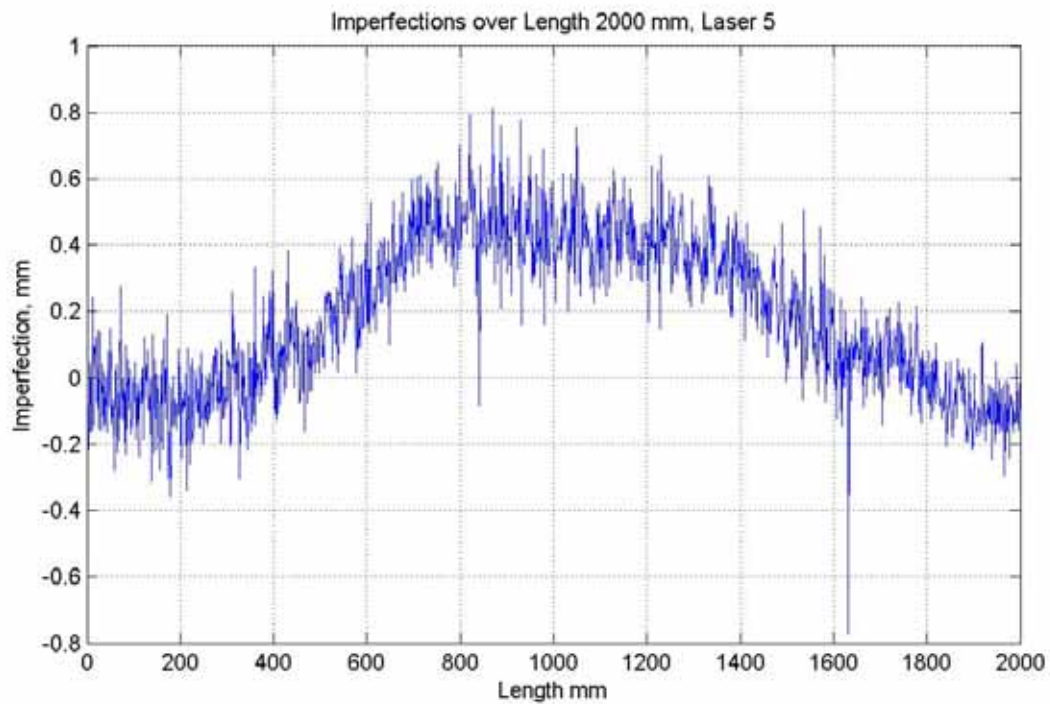
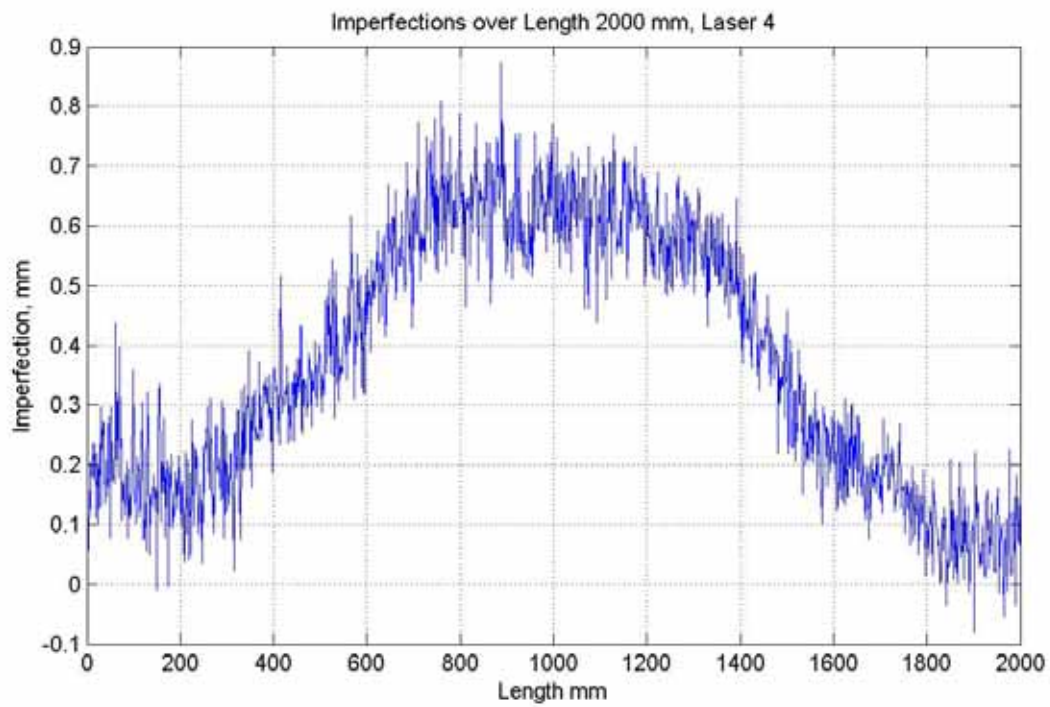


Figure A - 26 Imperfection measurements for specimen SCR2000\_1

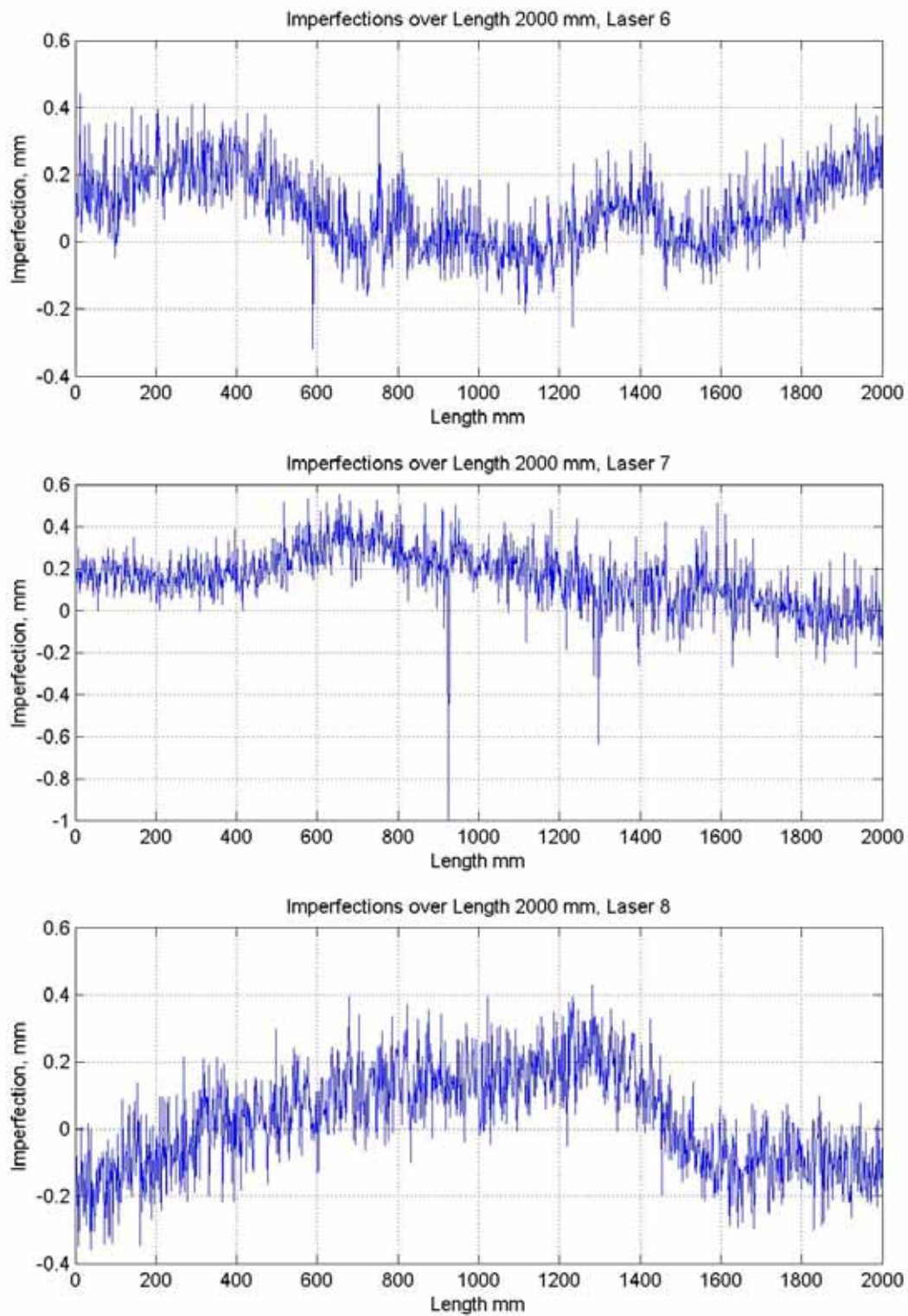


Figure A - 27 Imperfection measurements for specimen SCR2000\_1

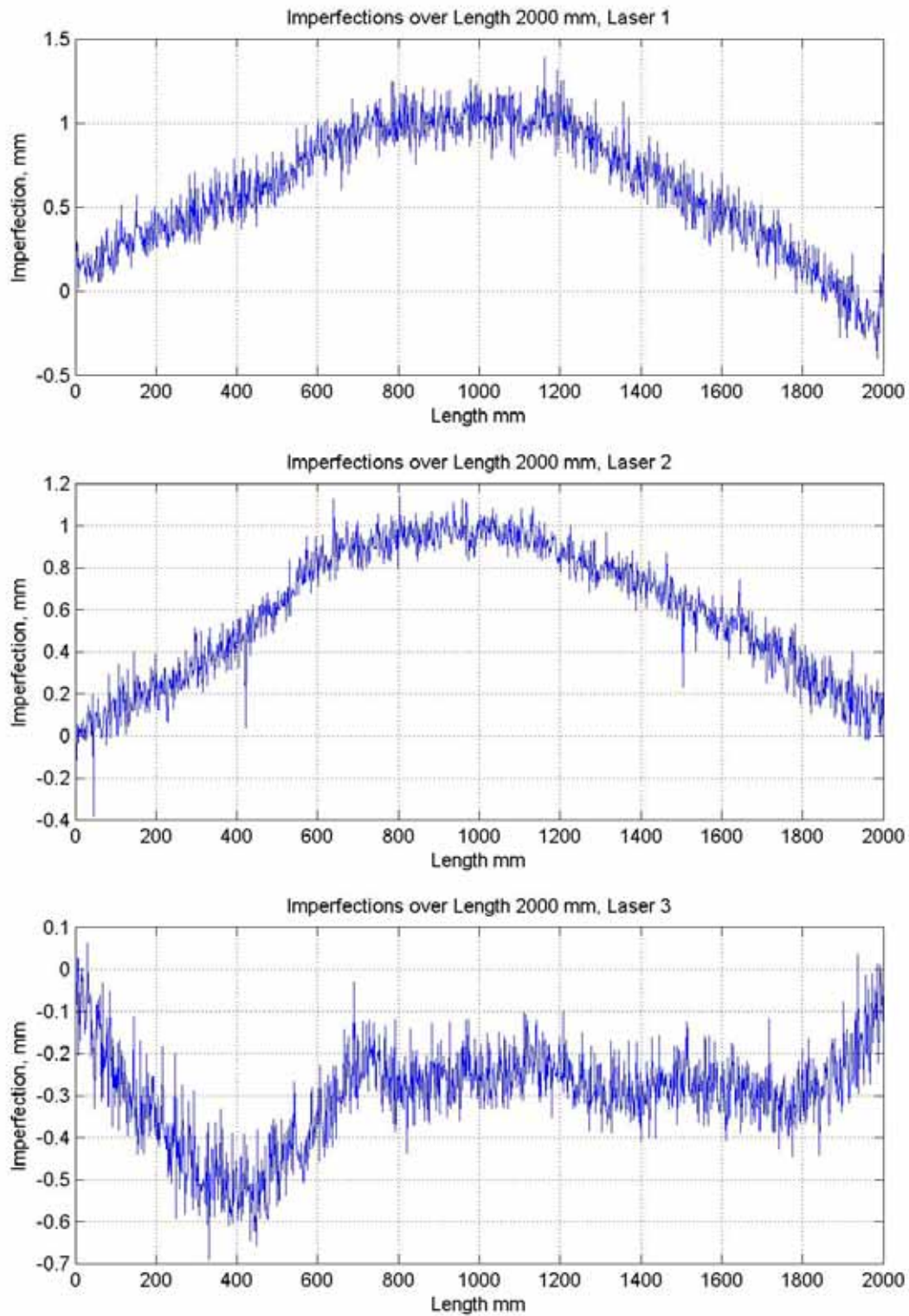


Figure A - 28 Imperfection measurements for specimen SCR2000\_2

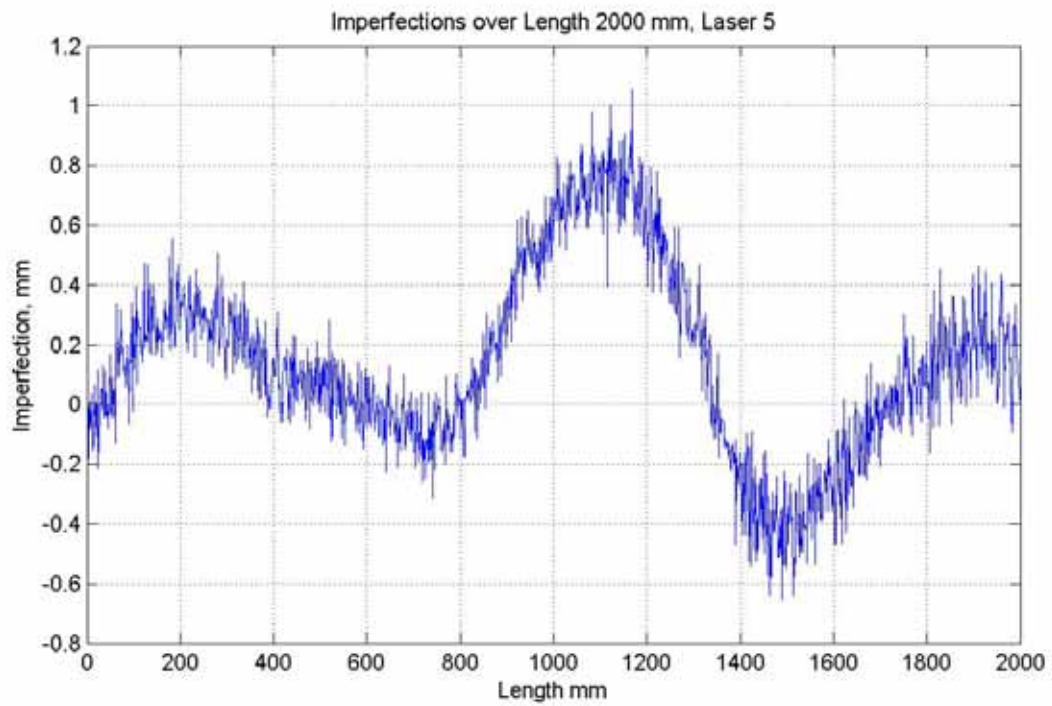
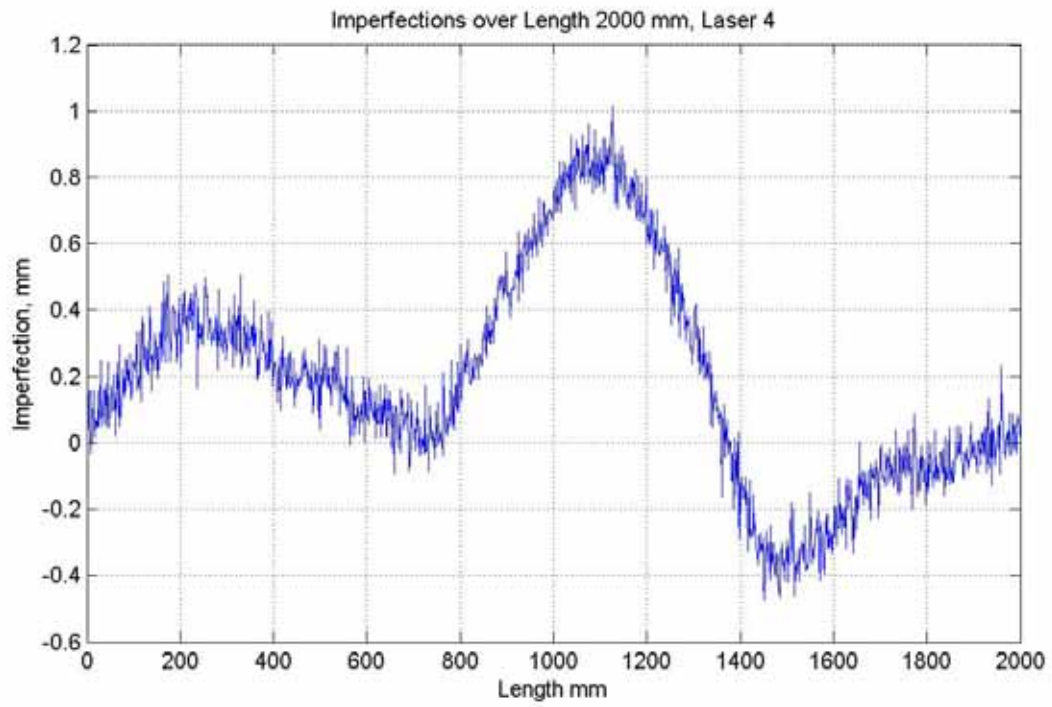


Figure A - 29 Imperfection measurements for specimen SCR2000\_2

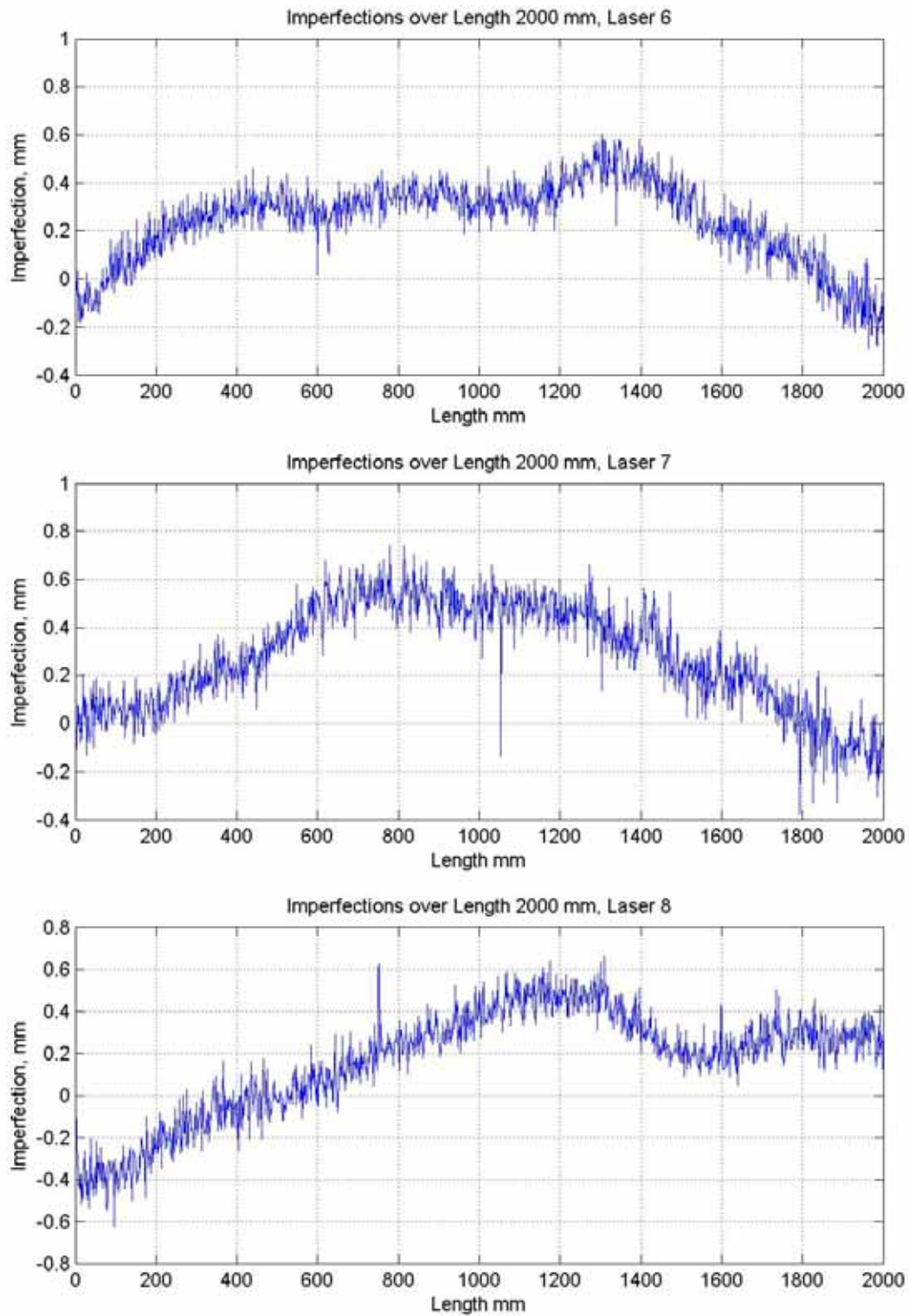


Figure A - 30 Imperfection measurements for specimen SCR2000\_2

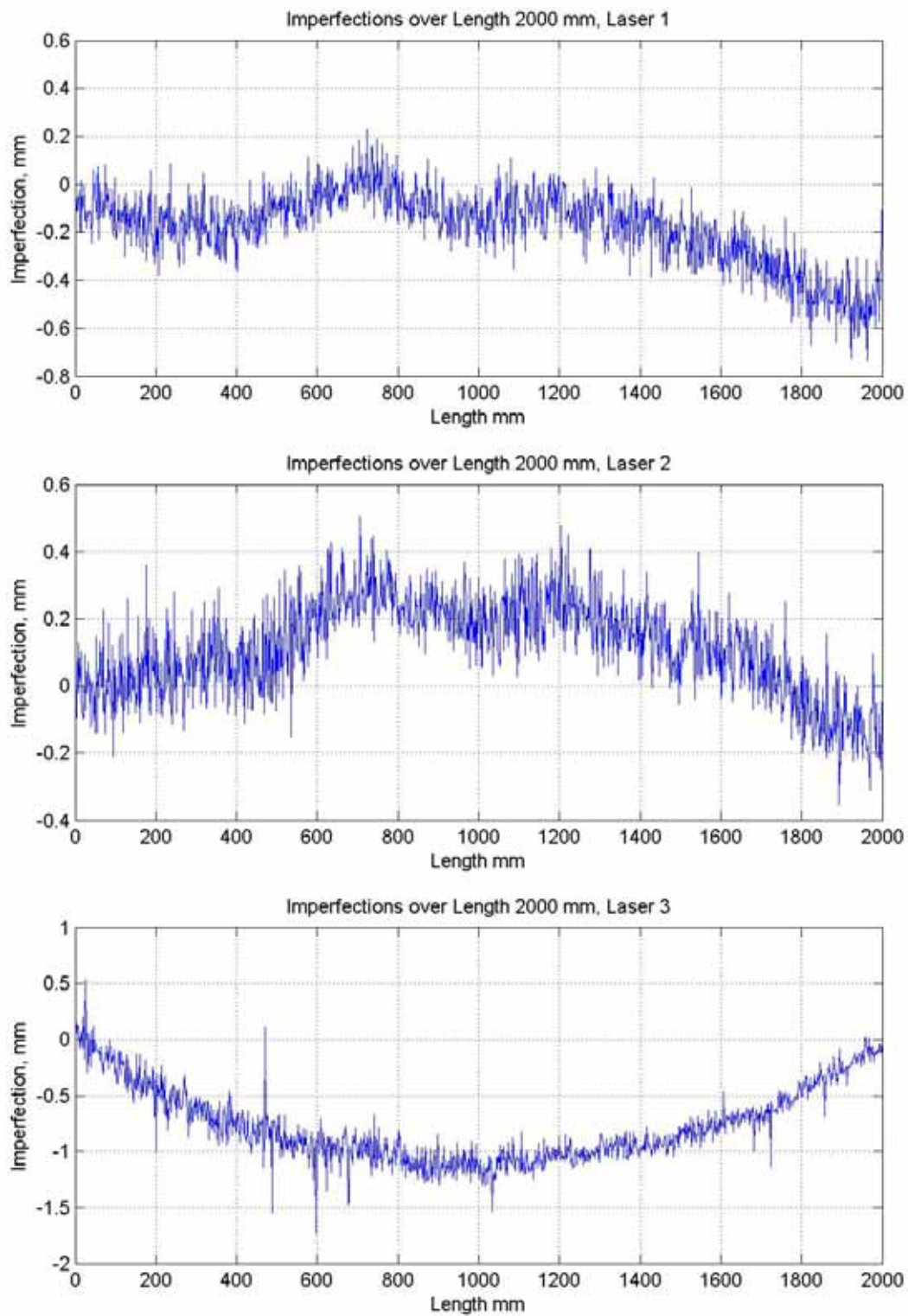


Figure A - 31 Imperfection measurements for specimen SCR2000\_3

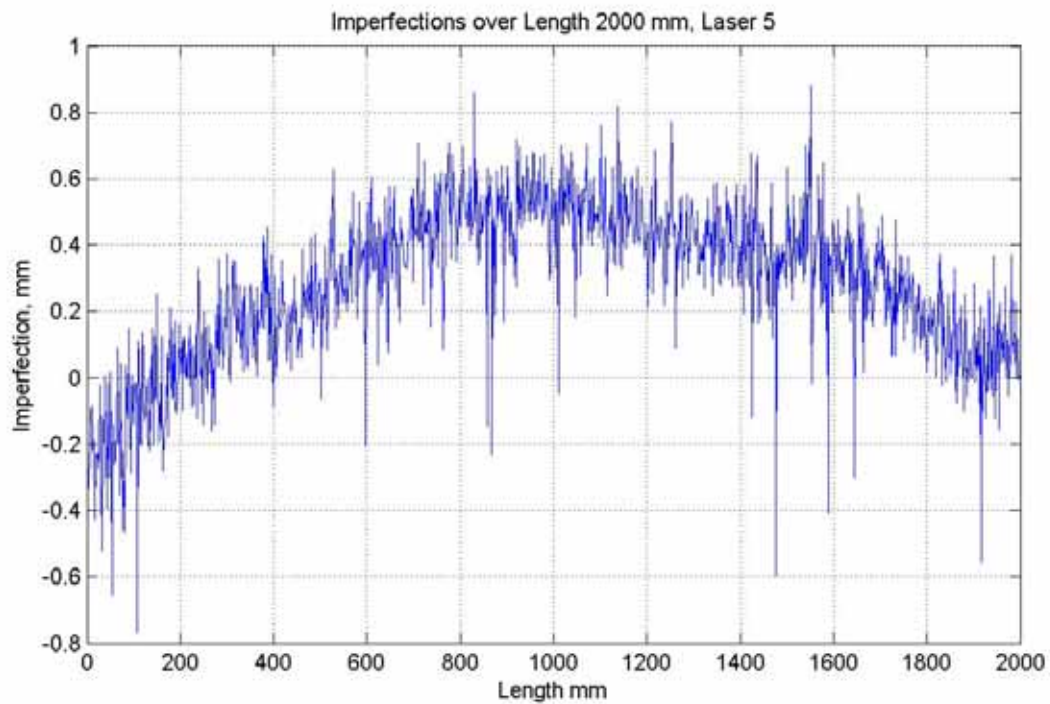
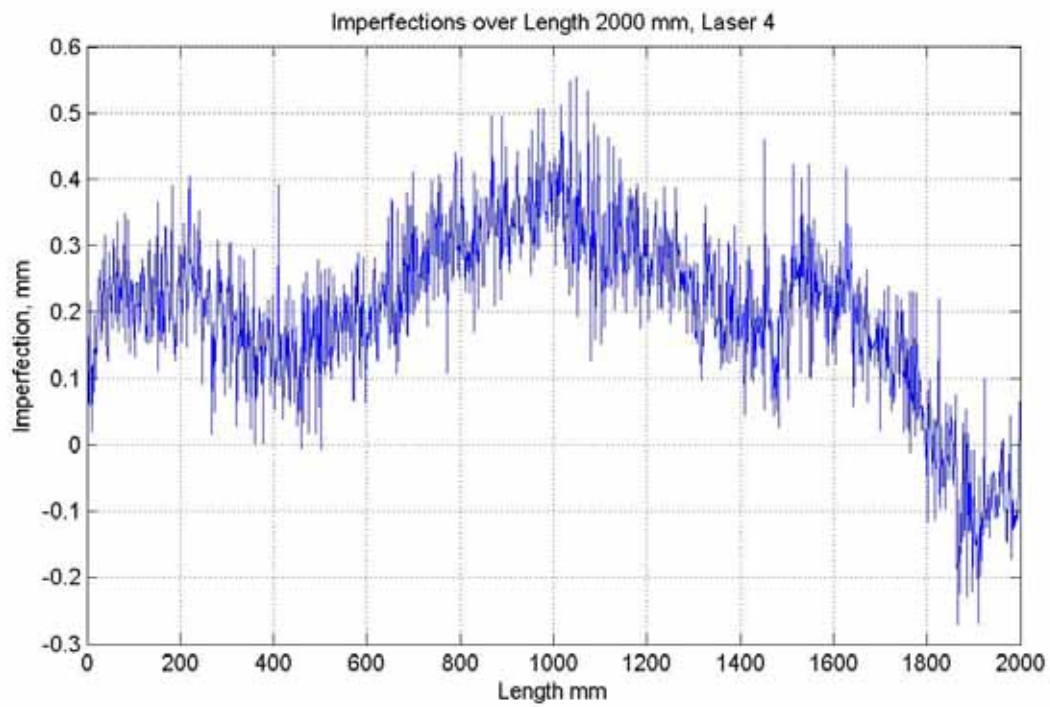


Figure A - 32 Imperfection measurements for specimen SCR2000\_3

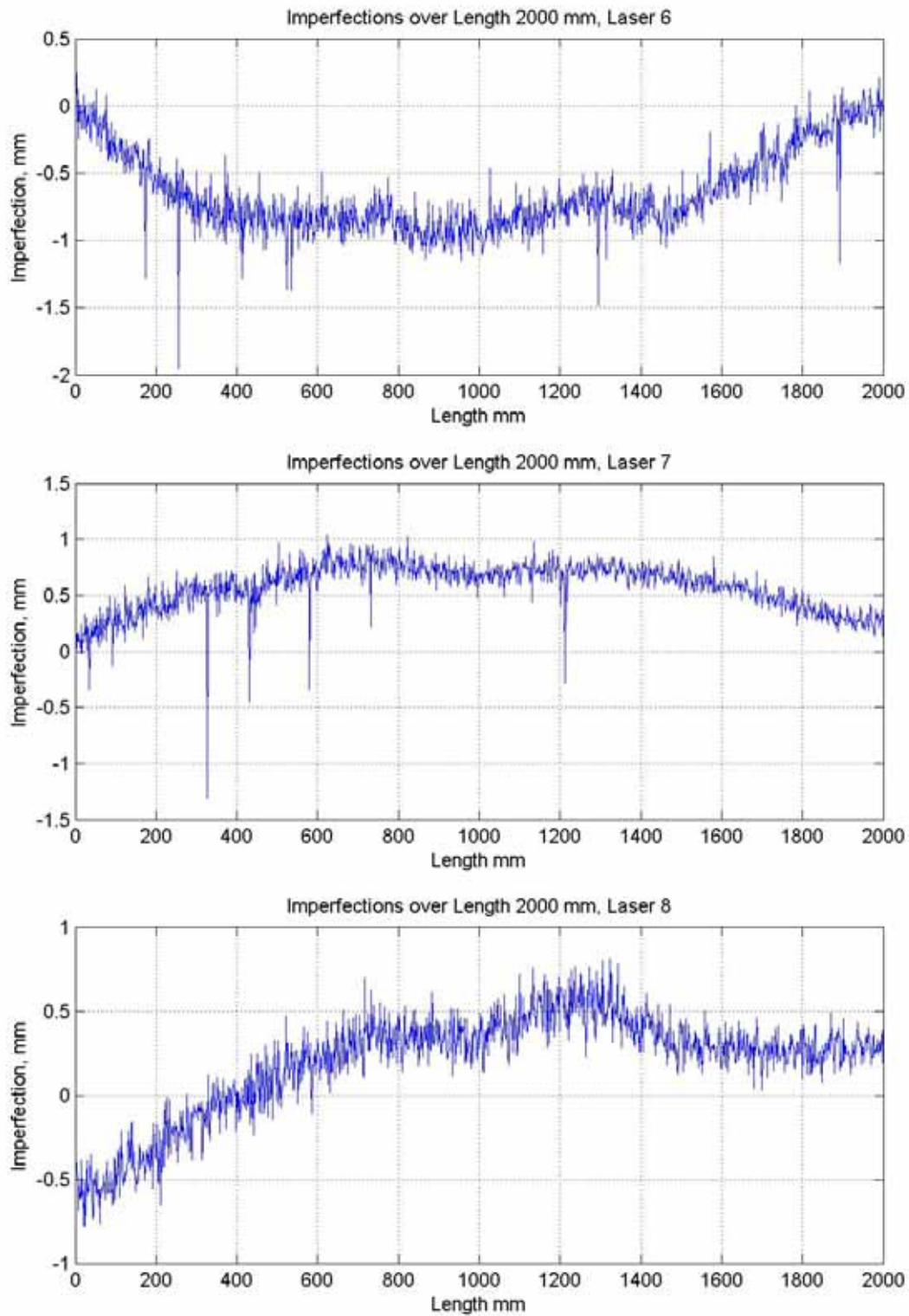
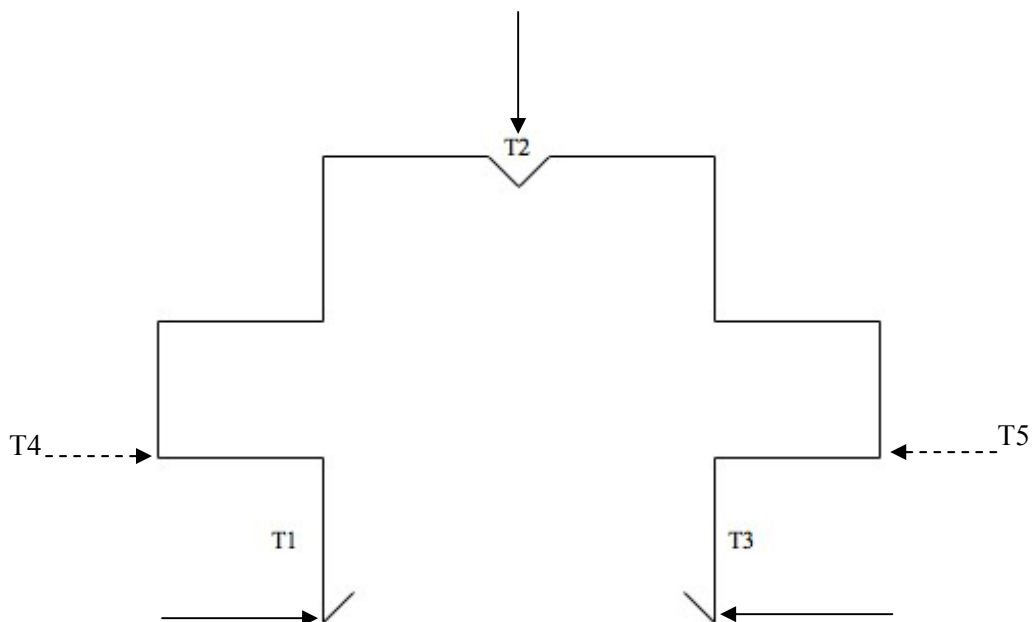


Figure A - 33 Imperfection measurements for specimen SCR2000\_3

## APPENDIX B

### Experimental graphs

Appendix B shows the graphs that detail the LVDT measurements taken during the compression tests. There are generally four graphs per specimen. The first graph shows the load versus axis shortening and is followed by the load versus lateral displacements of the right and left flanges and web. The positions of the transducers are on both stiffened flanges as well as on the stiffened rear flange. Some of the specimens had two additional LVDT transducers along the side flanges. They are generally positioned at the quarter, mid and three-quarter height of the specimen.



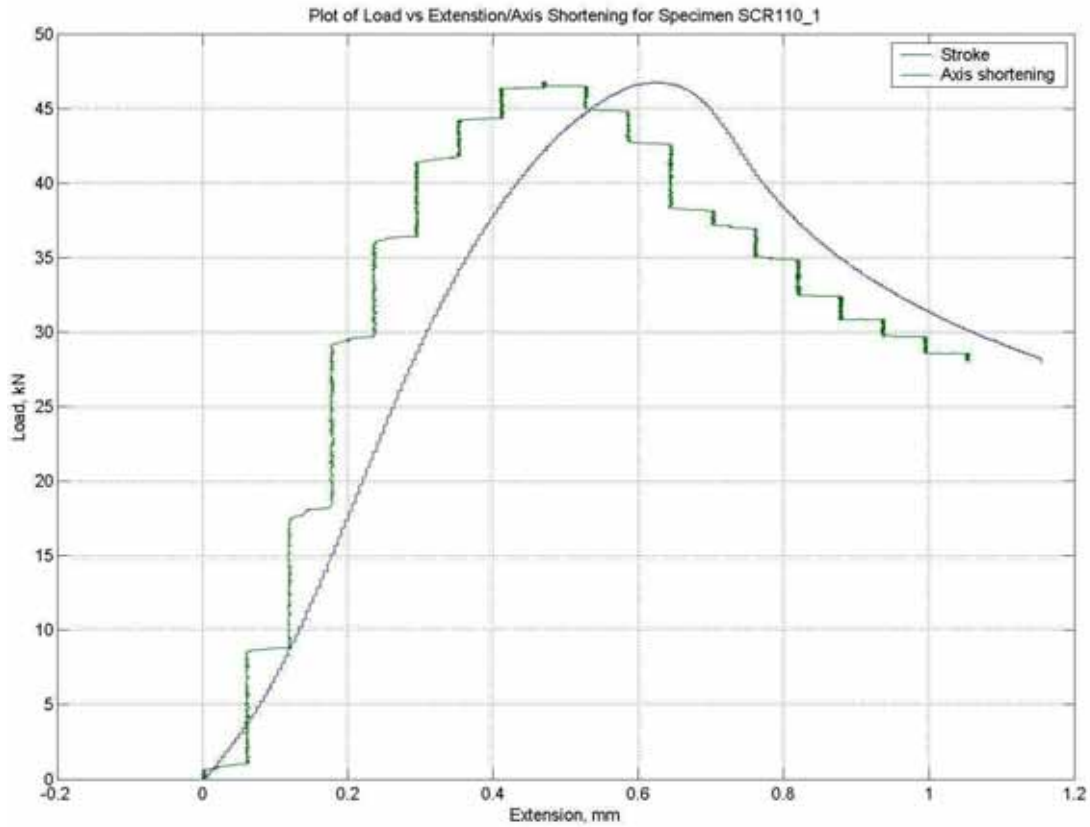


Figure B - 1 Load vs displacement curve for specimen SCR110\_1

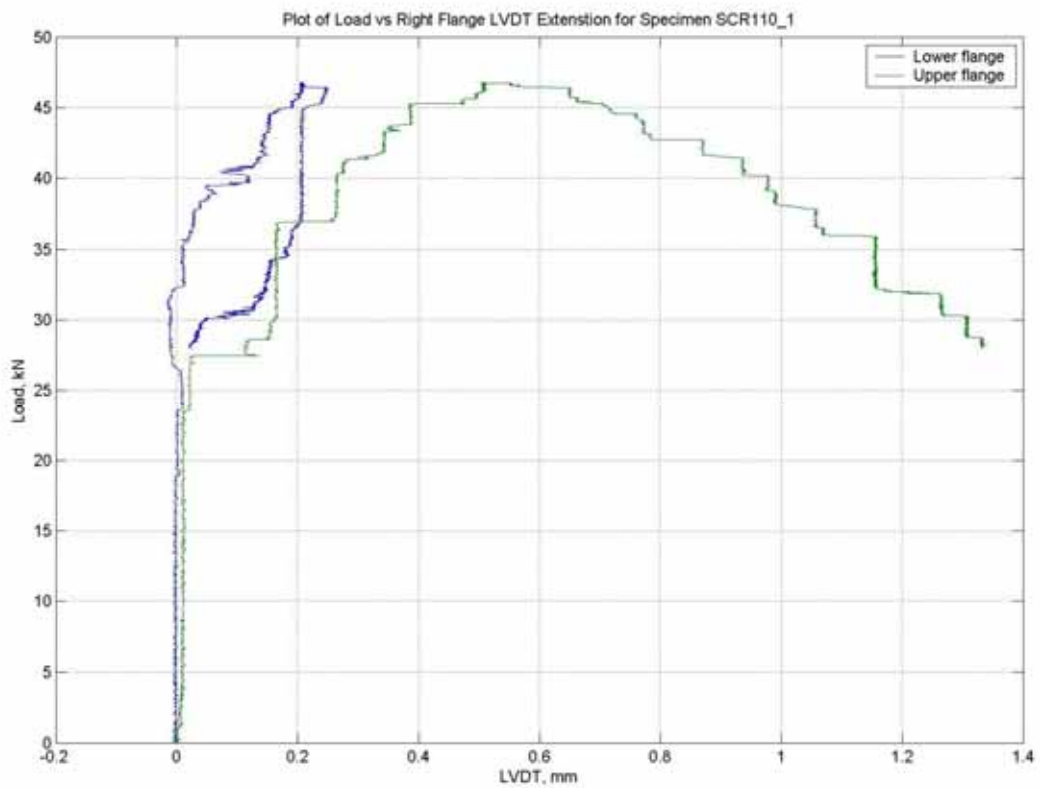


Figure B - 2 Load vs Right flange displacement for specimen SCR110\_1

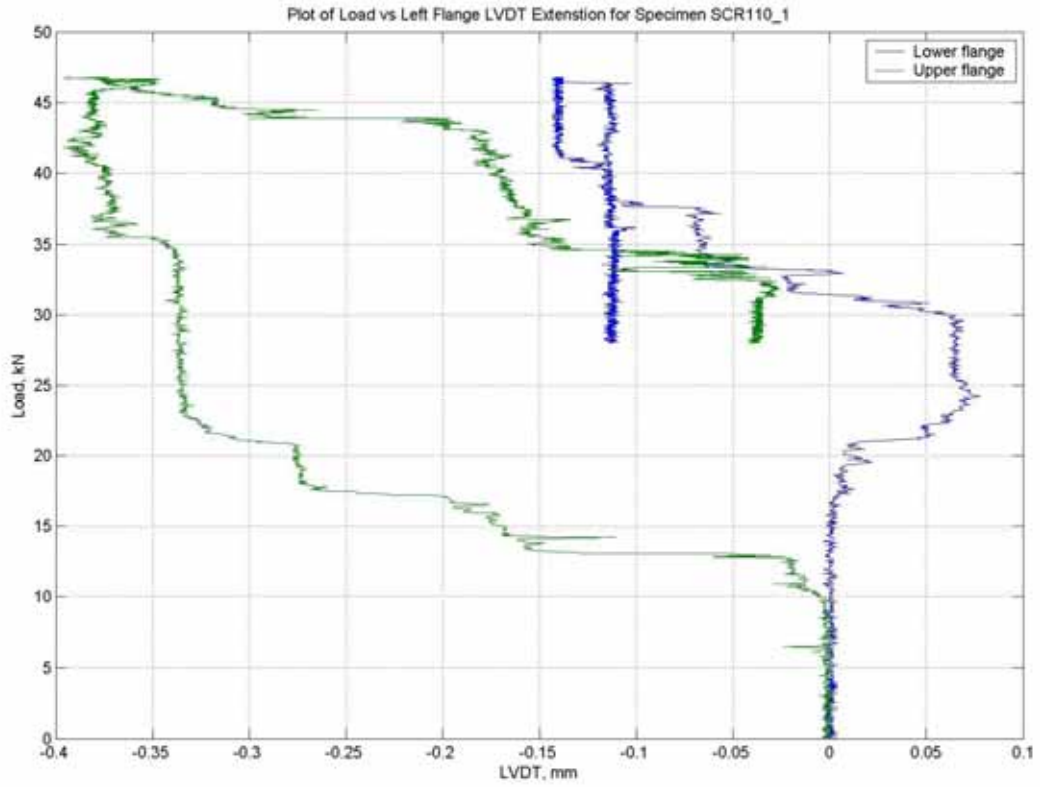


Figure B - 3 Load vs left flange displacement for specimen SCR110\_1

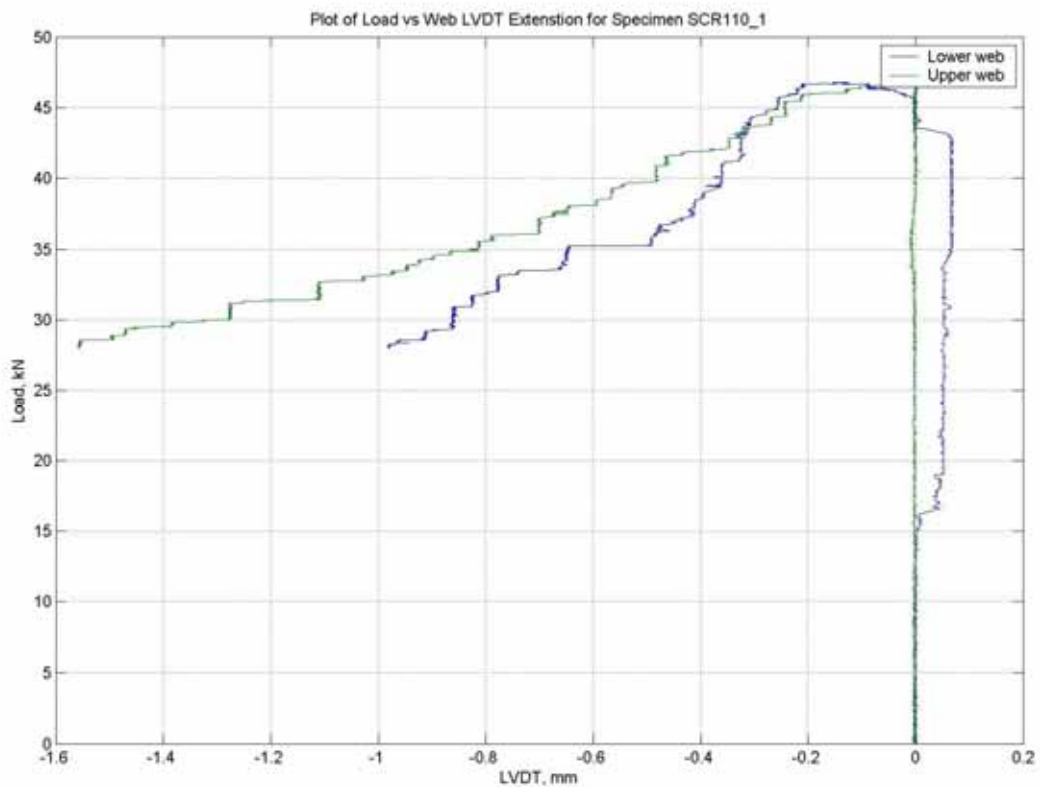


Figure B - 4 Load vs web displacement for specimen SCR110\_1

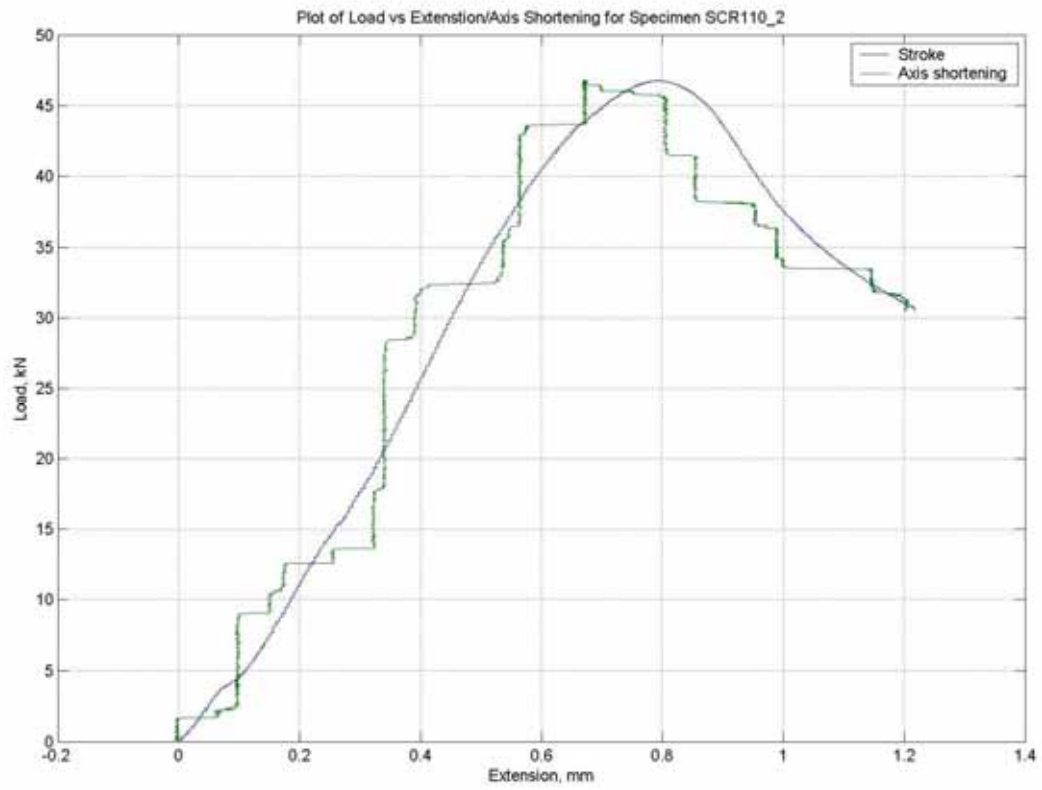


Figure B - 5 Load vs displacement for specimen SCR110\_2

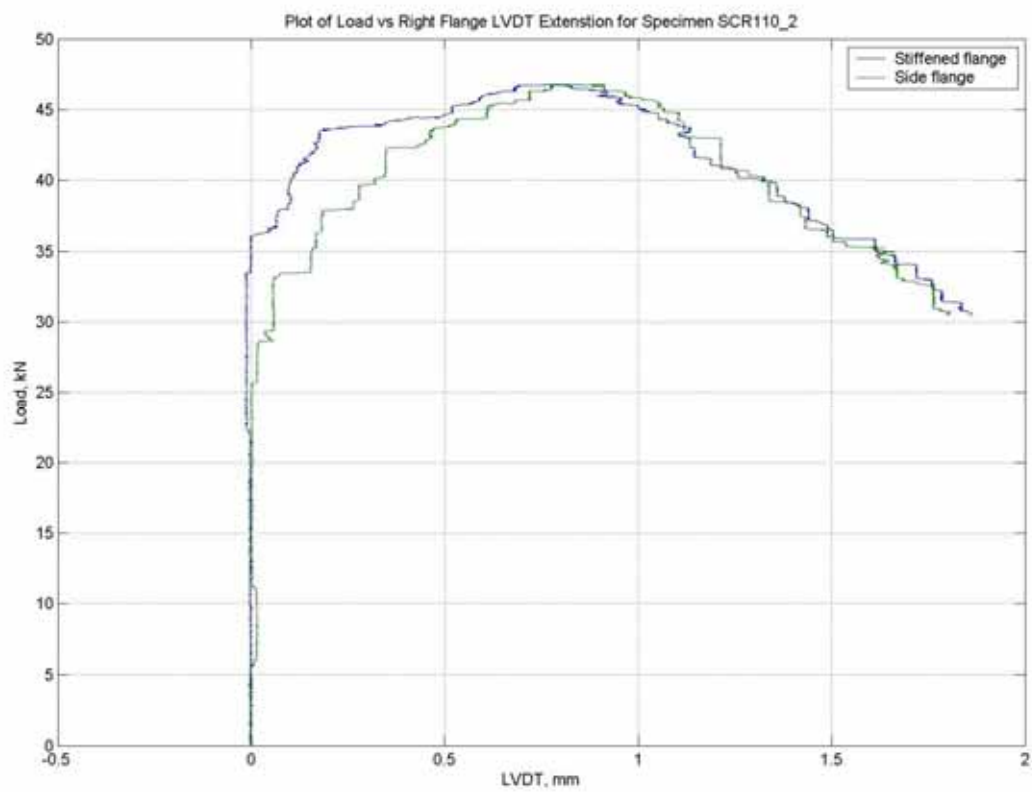


Figure B - 6 Load vs right flange displacement for specimen SCR110\_2

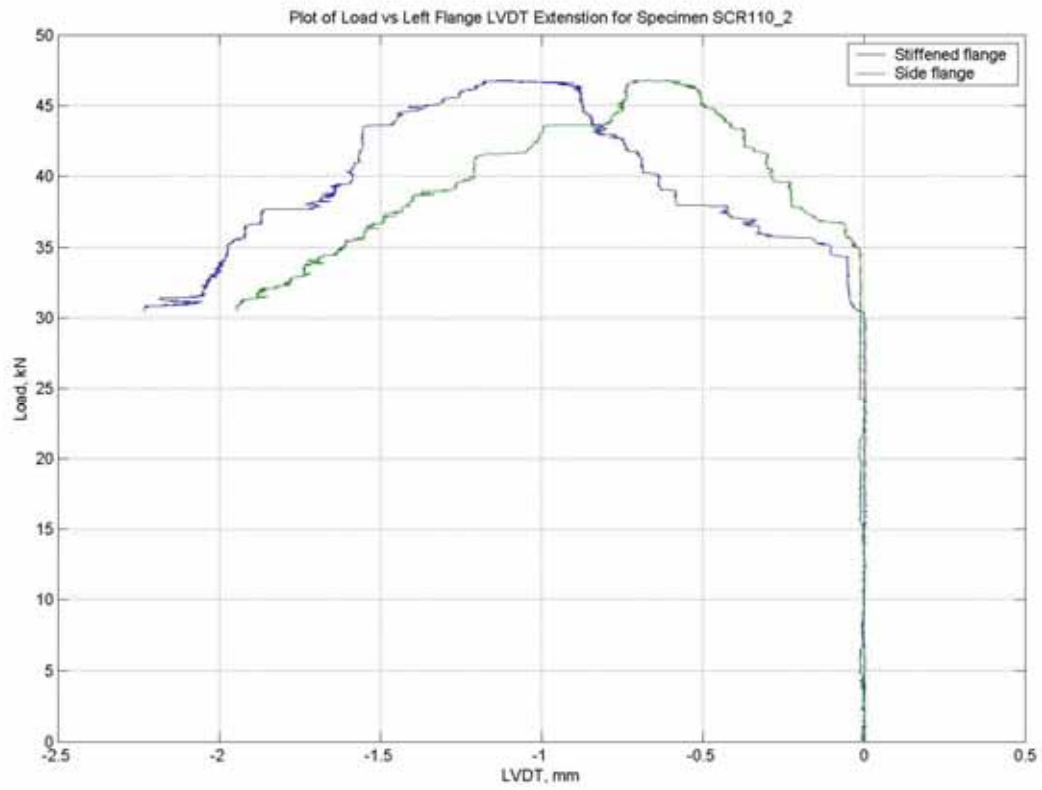


Figure B - 7 Load vs left flange displacement for specimen SCR110\_2

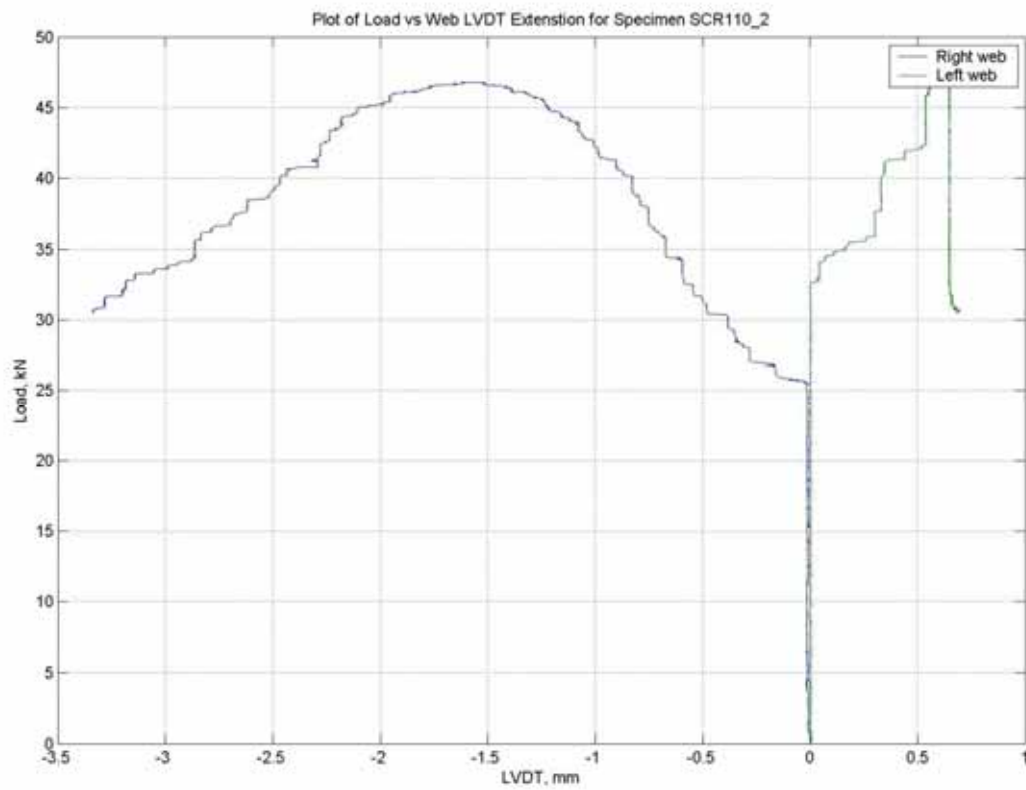


Figure B - 8 Load vs web displacement for specimen SCR110\_2

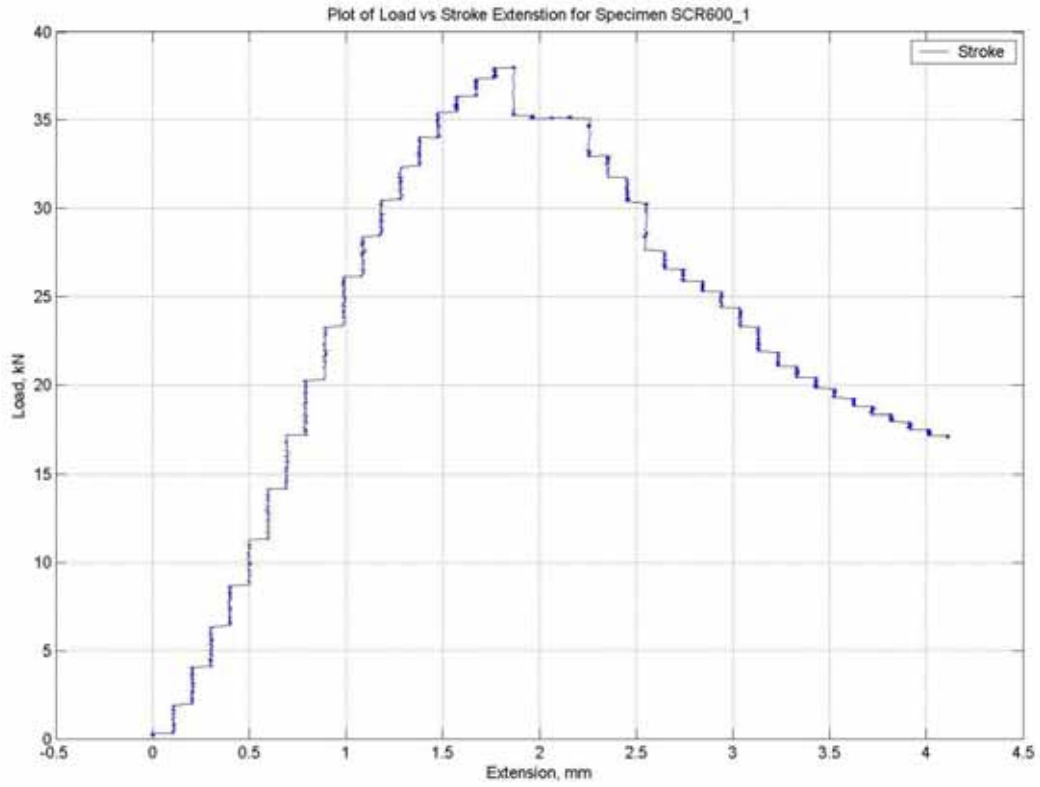


Figure B - 9 Load vs displacement for specimen SCR600\_1

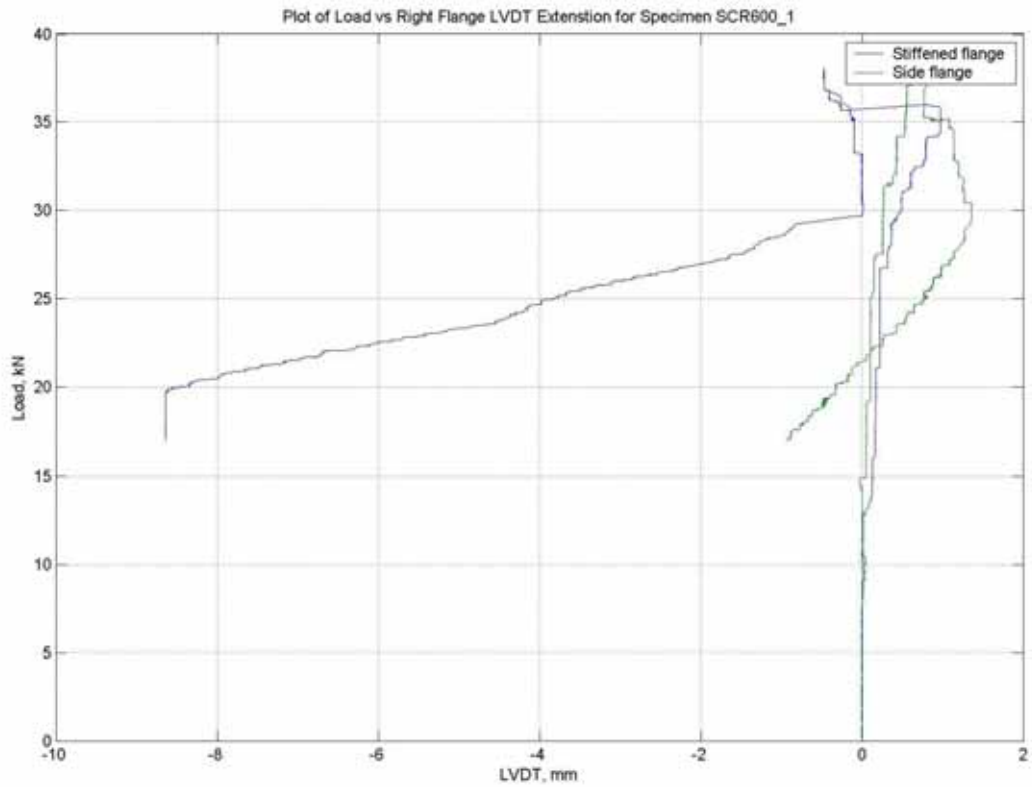


Figure B - 10 Load vs right flange displacement for specimen SCR600\_1

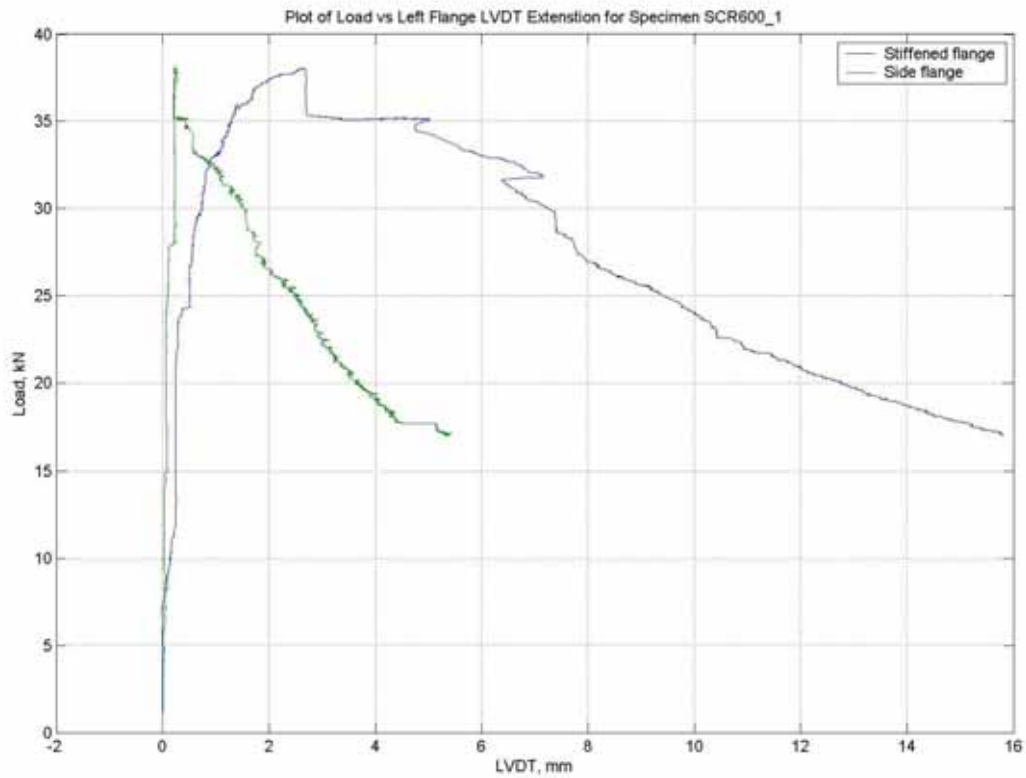


Figure B - 11 Load vs left flange displacement for specimen SCR600\_1

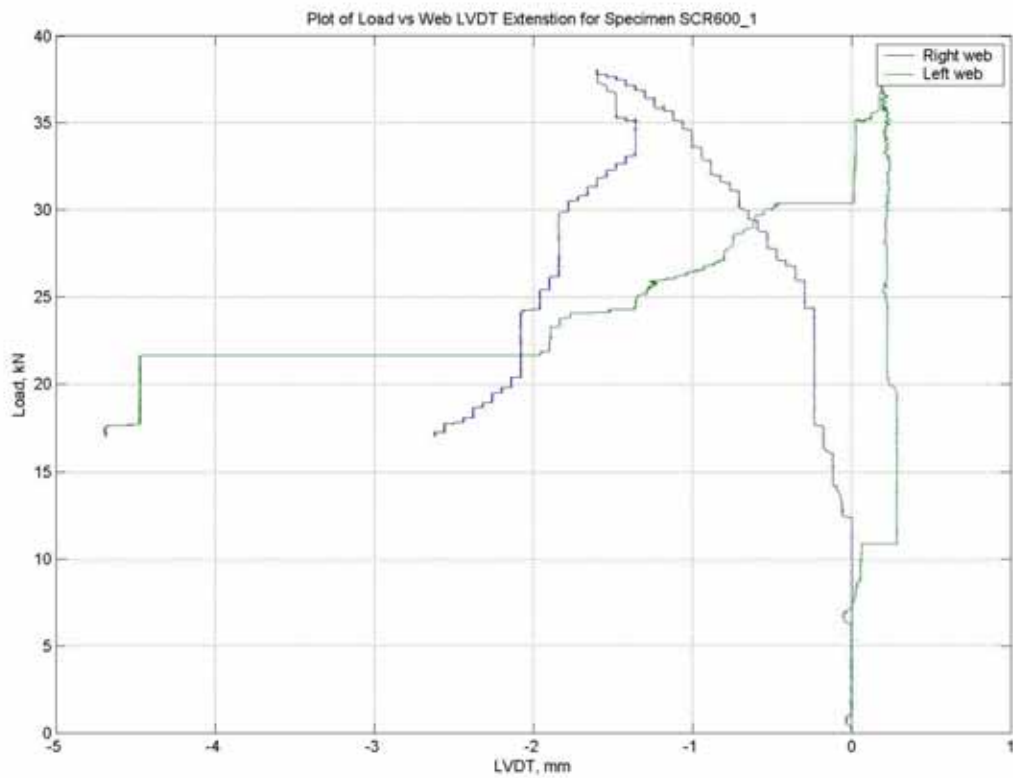


Figure B - 12 Load vs web displacement for specimen SCR600\_1

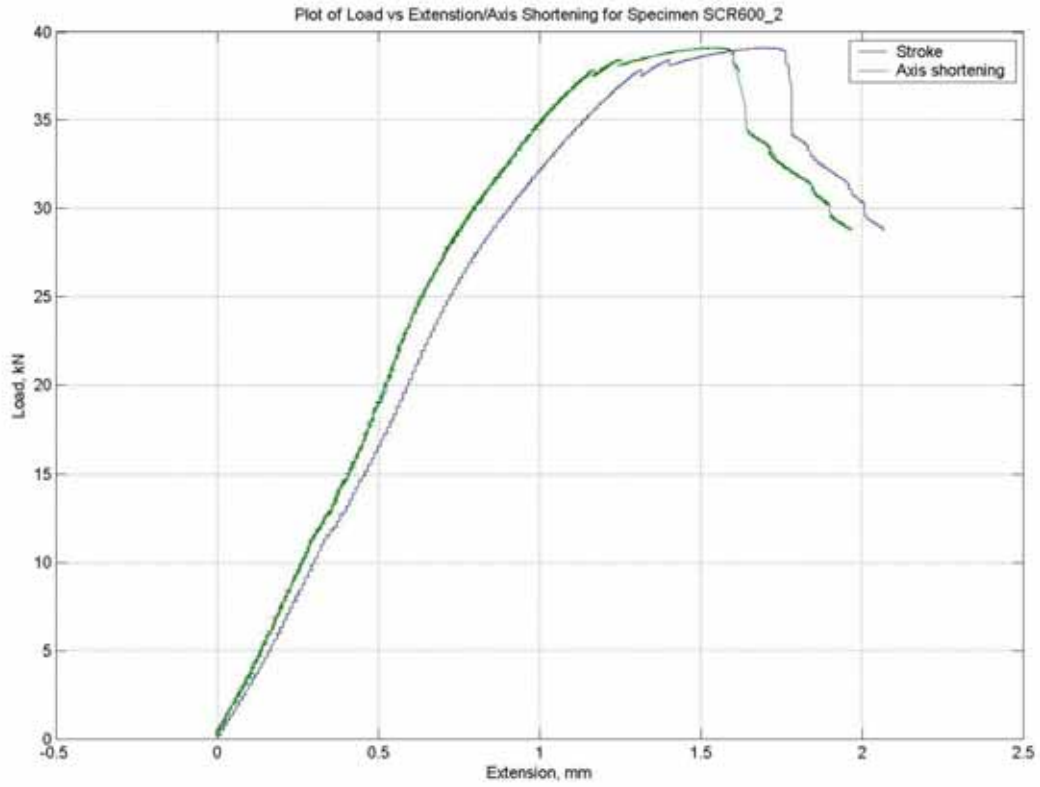


Figure B - 13 Load vs displacement for specimen SCR600\_2

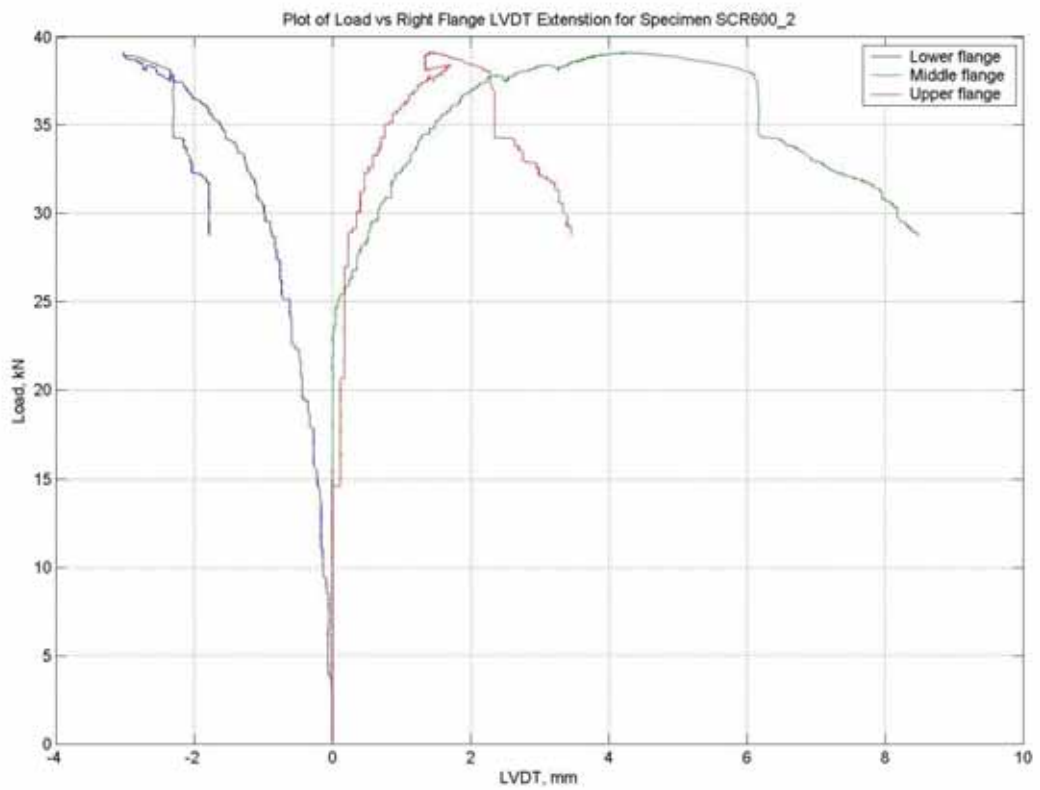


Figure B - 14 Load vs right flange displacement for specimen SCR600\_2

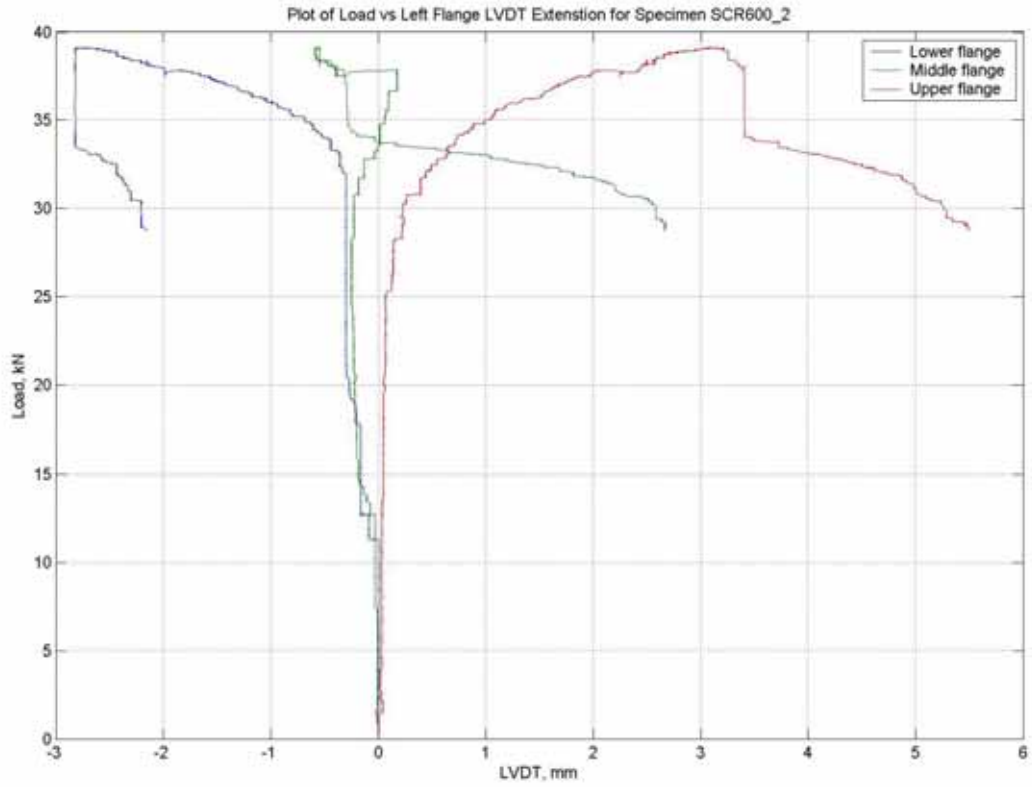


Figure B - 15 Load vs left displacement for specimen SCR600\_2

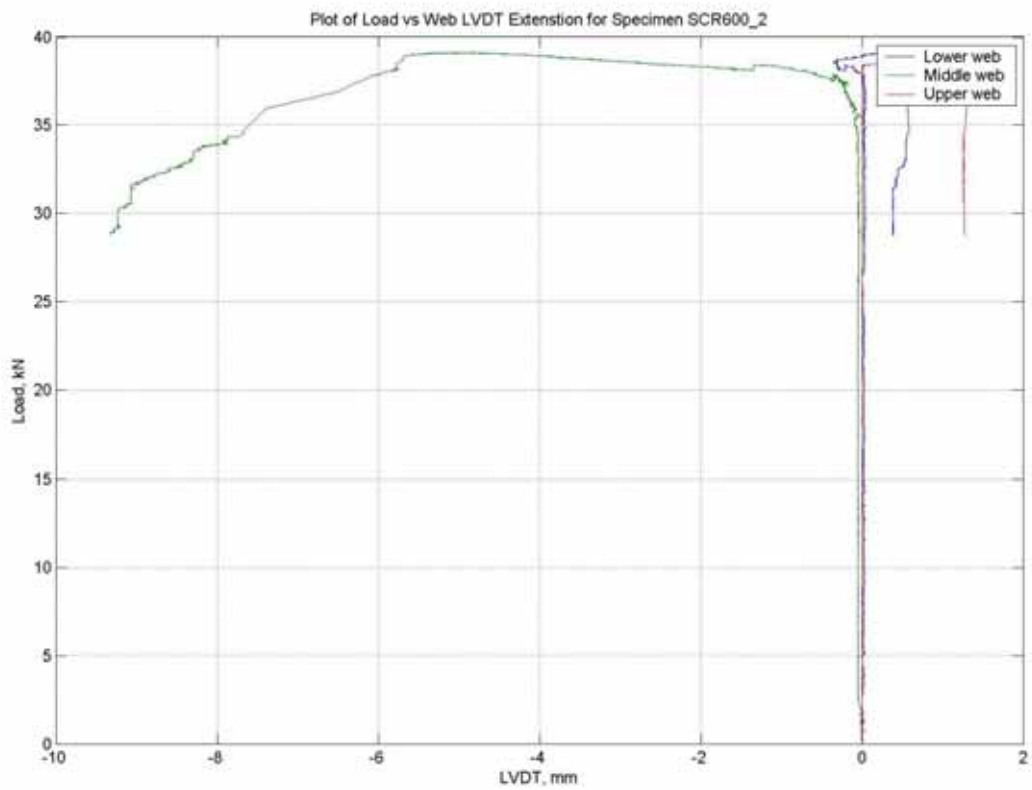


Figure B - 16 Load vs web displacement for specimen SCR600\_2

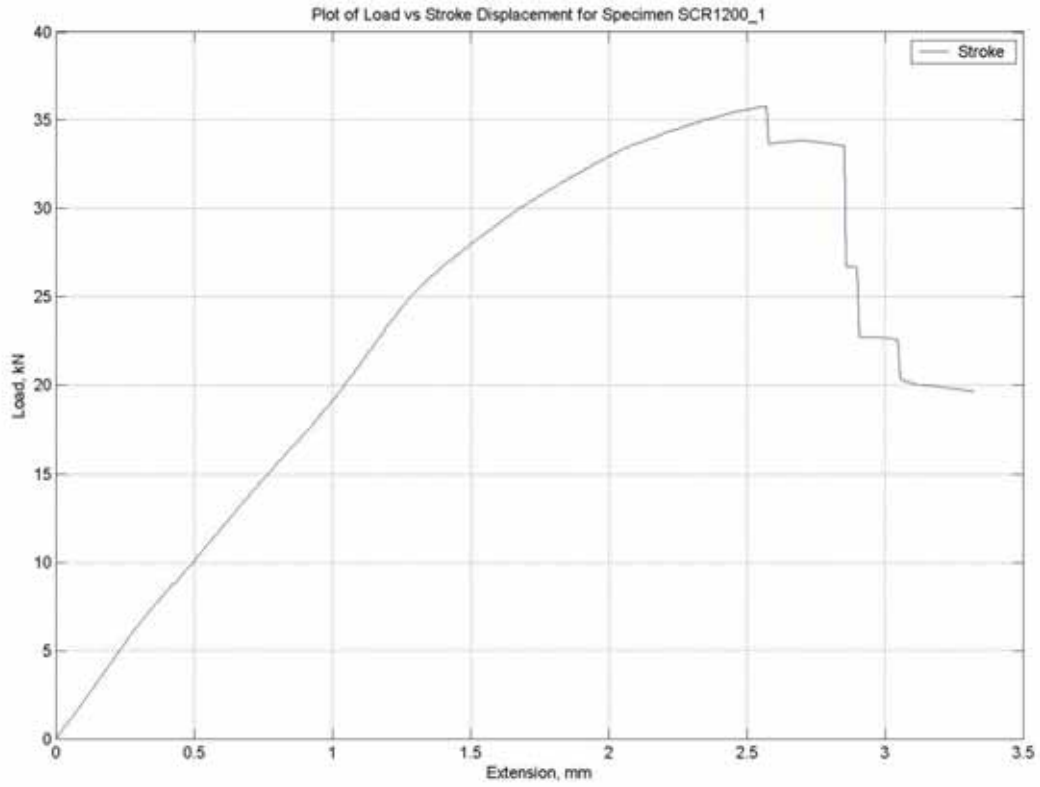


Figure B - 17 Load vs displacement for specimen SCR1200\_1

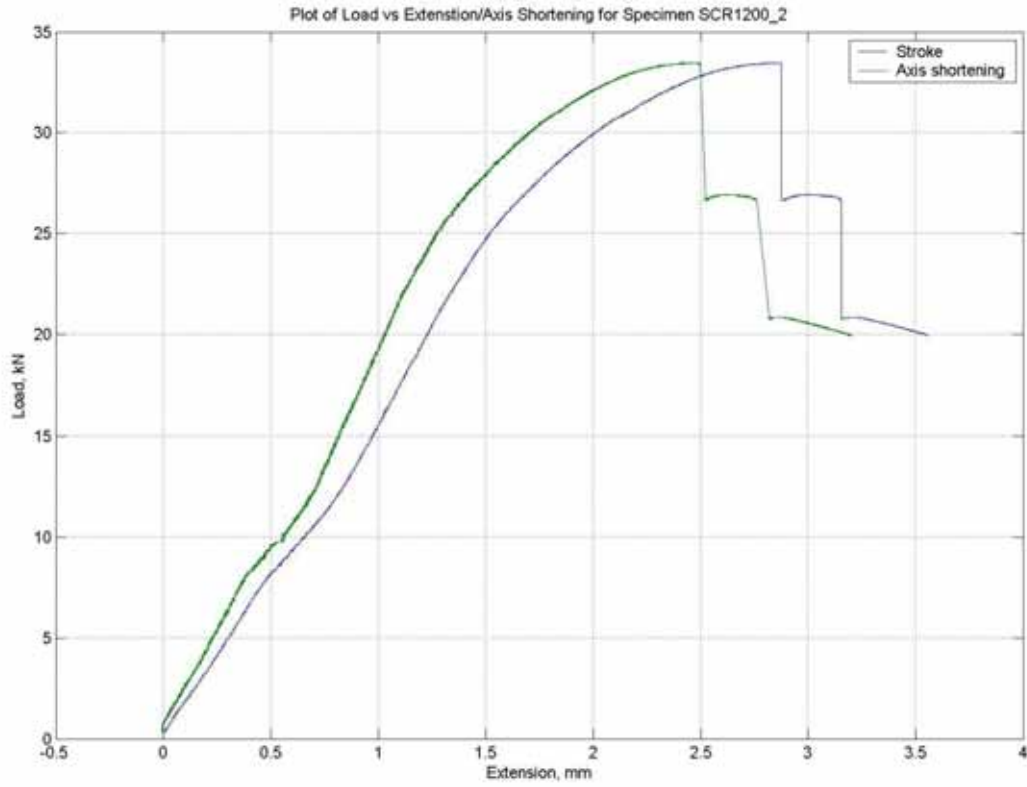


Figure B - 18 Load vs displacement for specimen SCR1200\_2

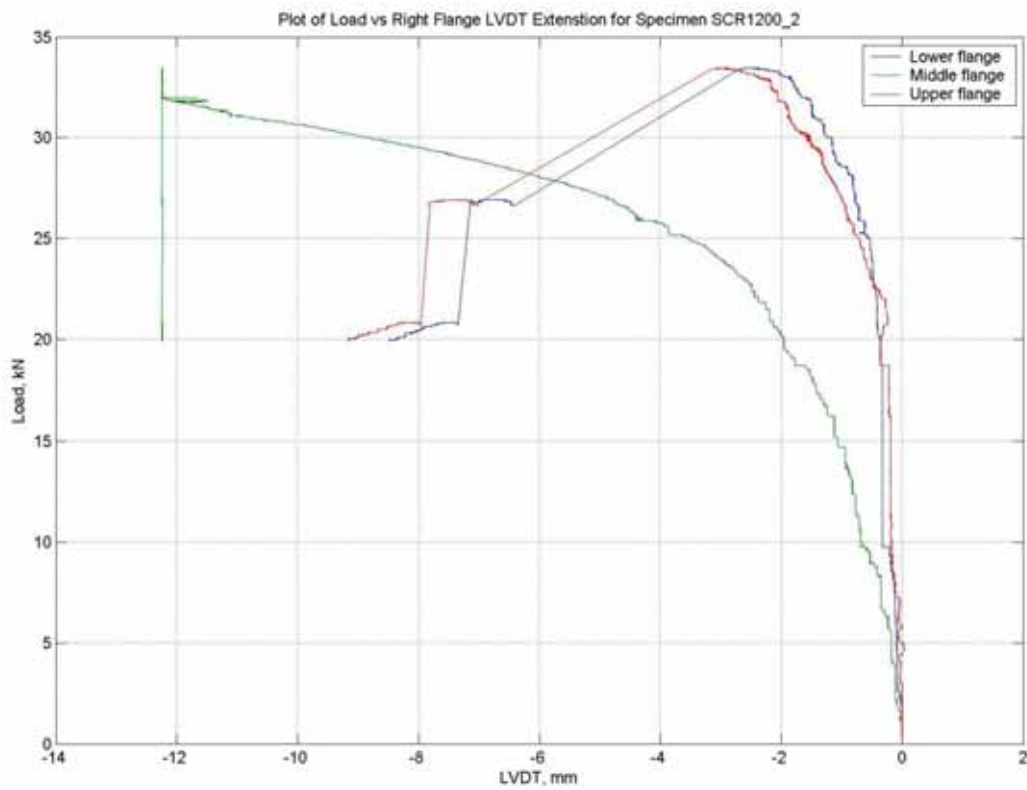


Figure B - 19 Load vs right flange displacement for specimen SCR1200\_2

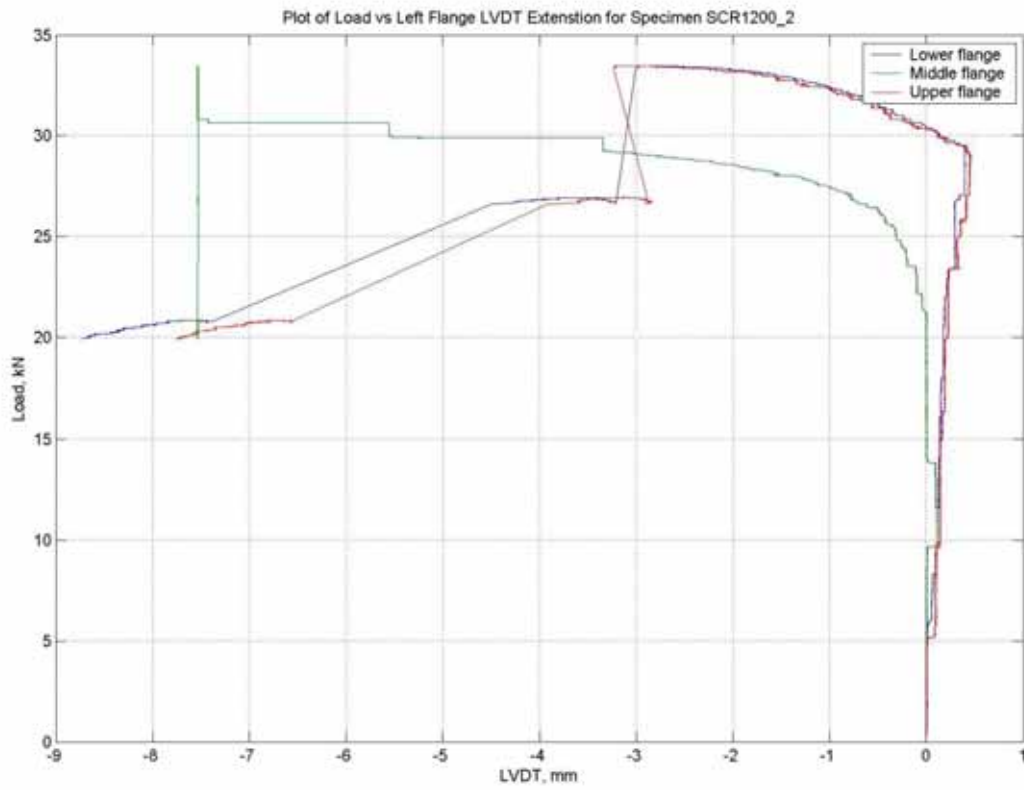


Figure B - 20 Load vs left flange displacement for specimen SCR1200\_2

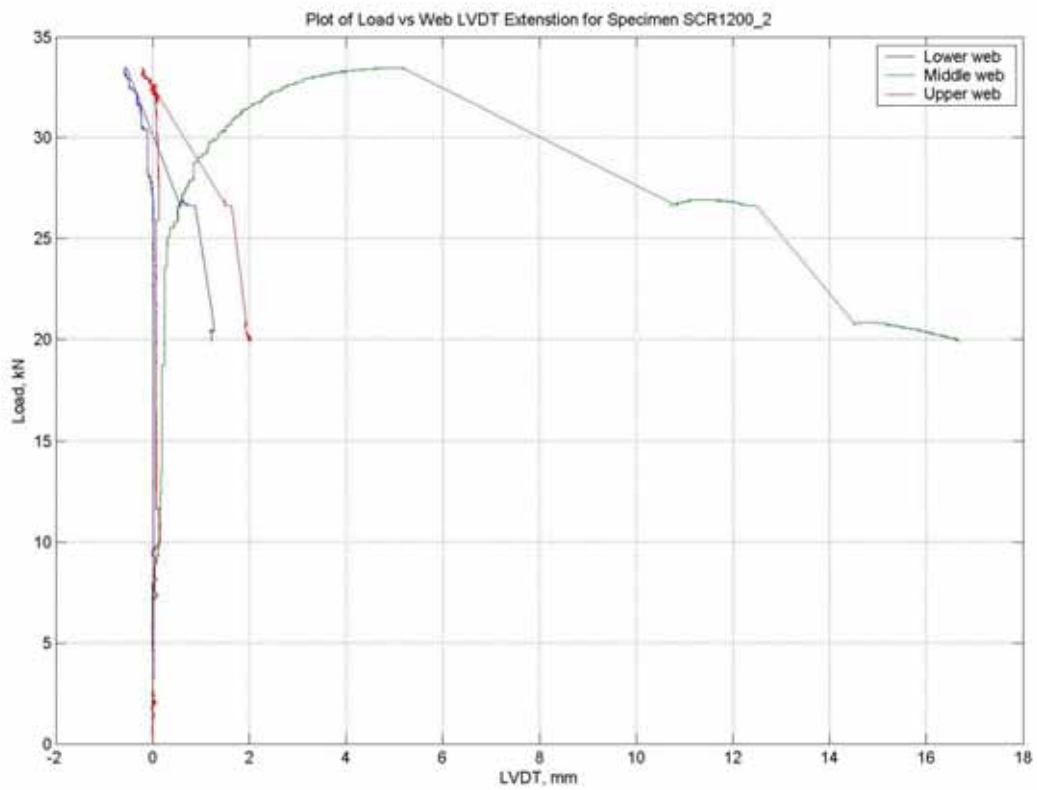


Figure B - 21 Load vs web displacement for specimen SCR1200\_2

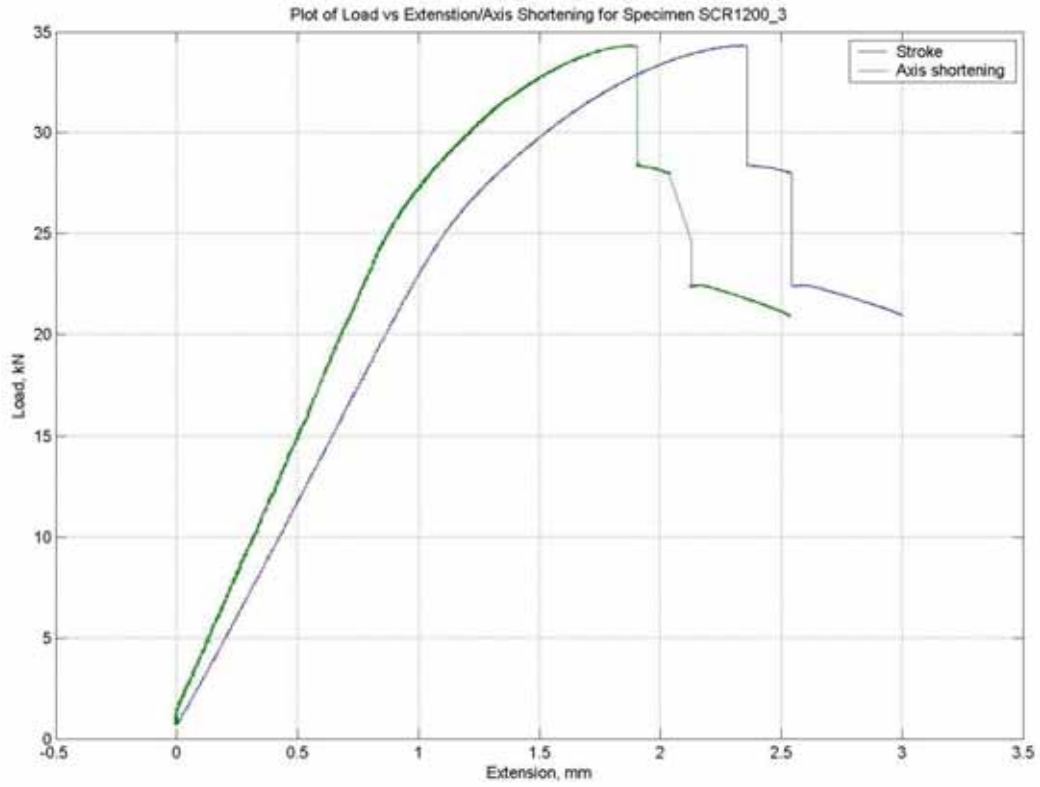


Figure B - 22 Load vs displacement for specimen SCR1200\_3

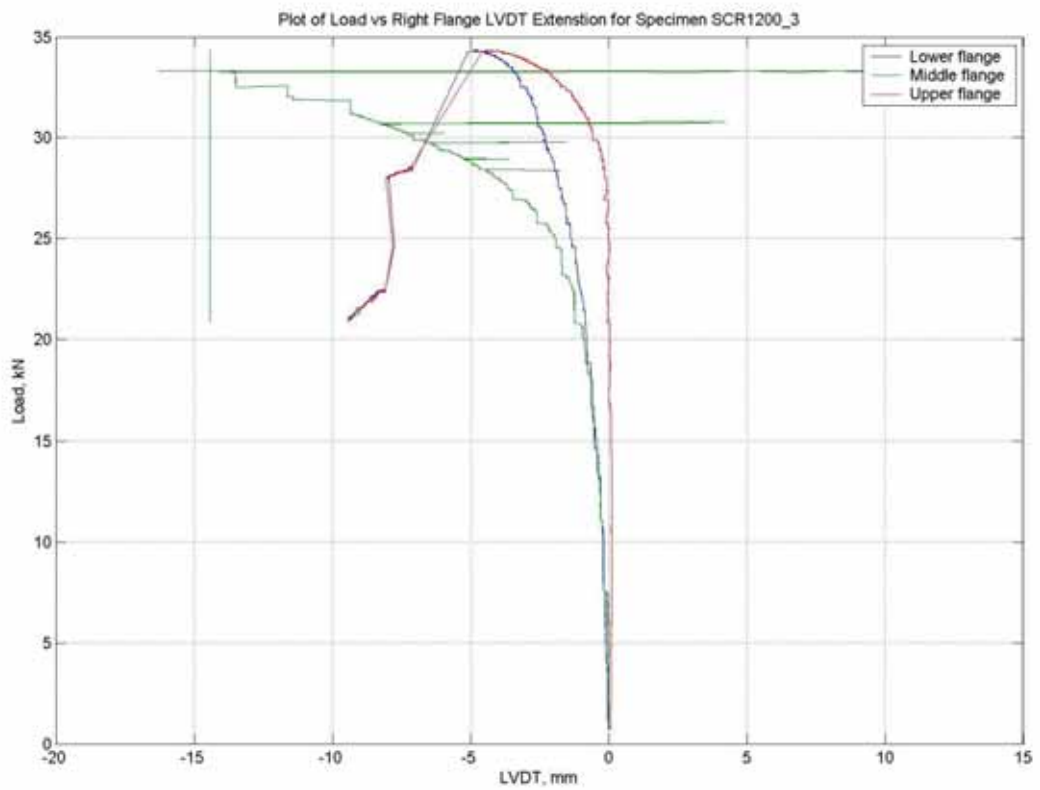


Figure B - 23 Load vs right flange displacement for specimen SCR1200\_3

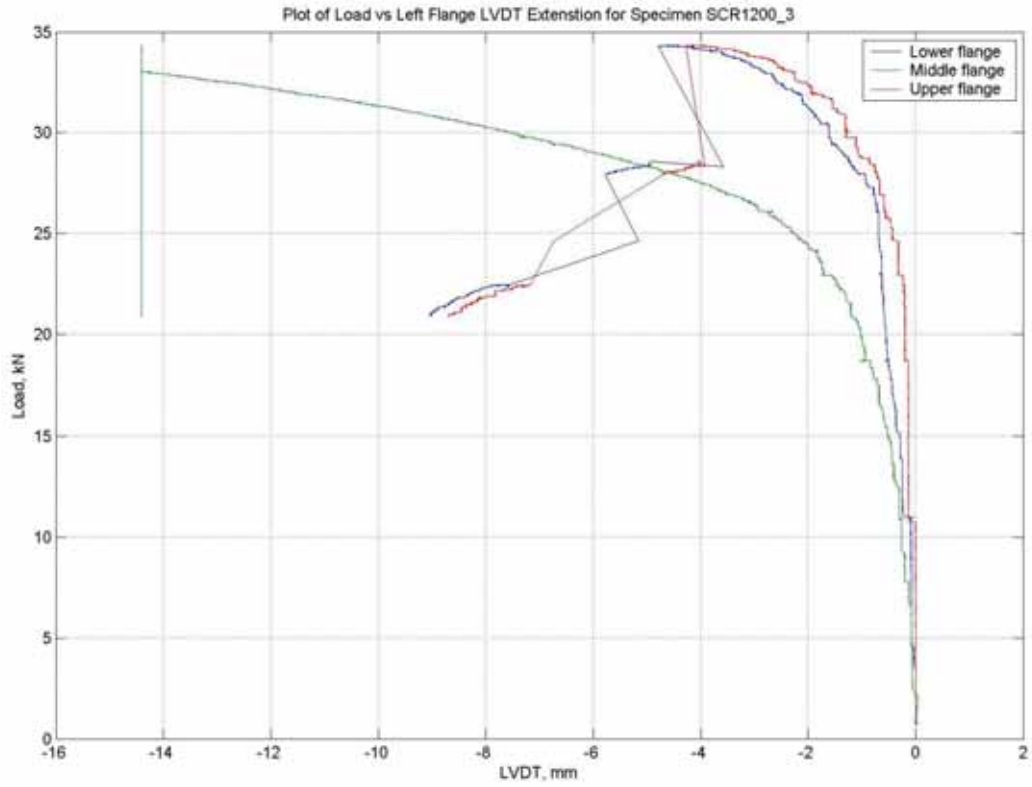


Figure B - 24 Load vs left flange displacement for specimen SCR1200\_3

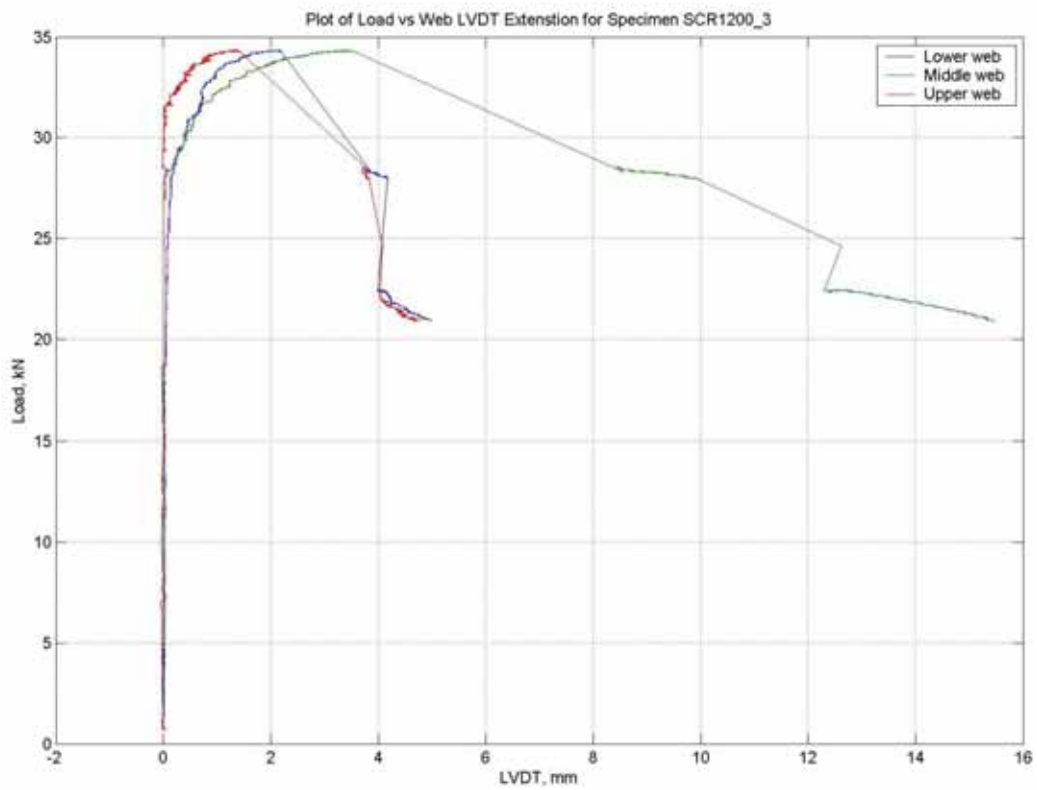


Figure B - 25 Load vs web displacement for specimen SCR1200\_3

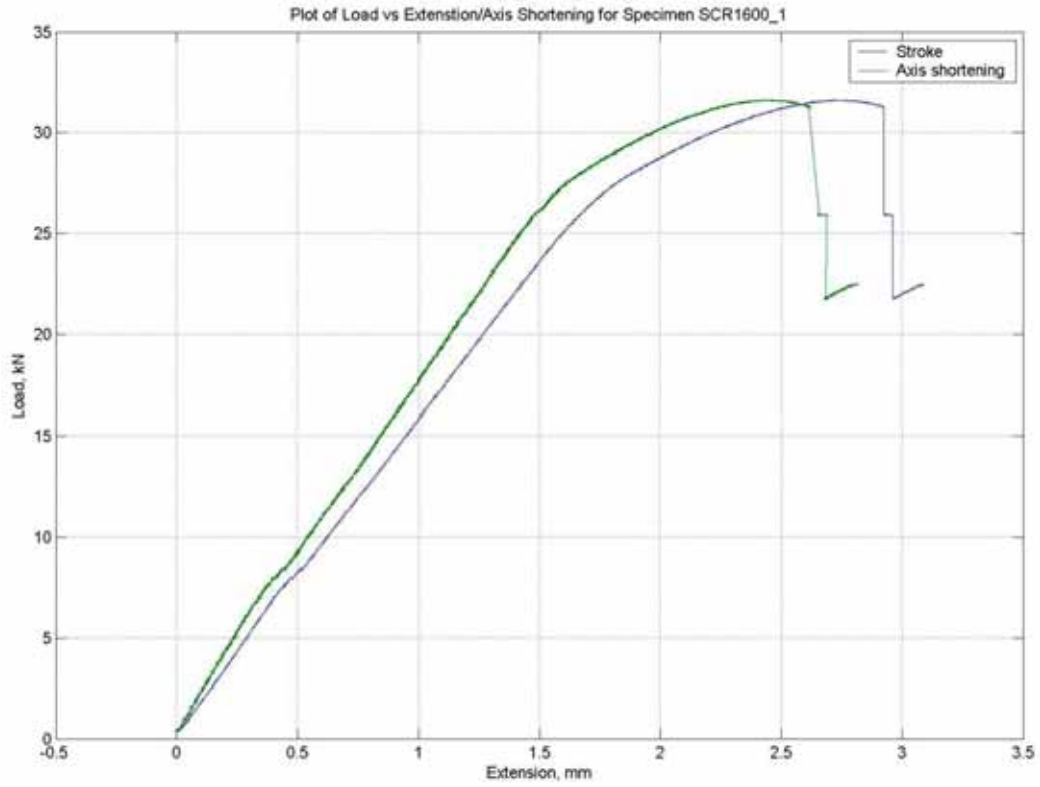


Figure B - 26 Load vs displacement for specimen SCR1600\_1

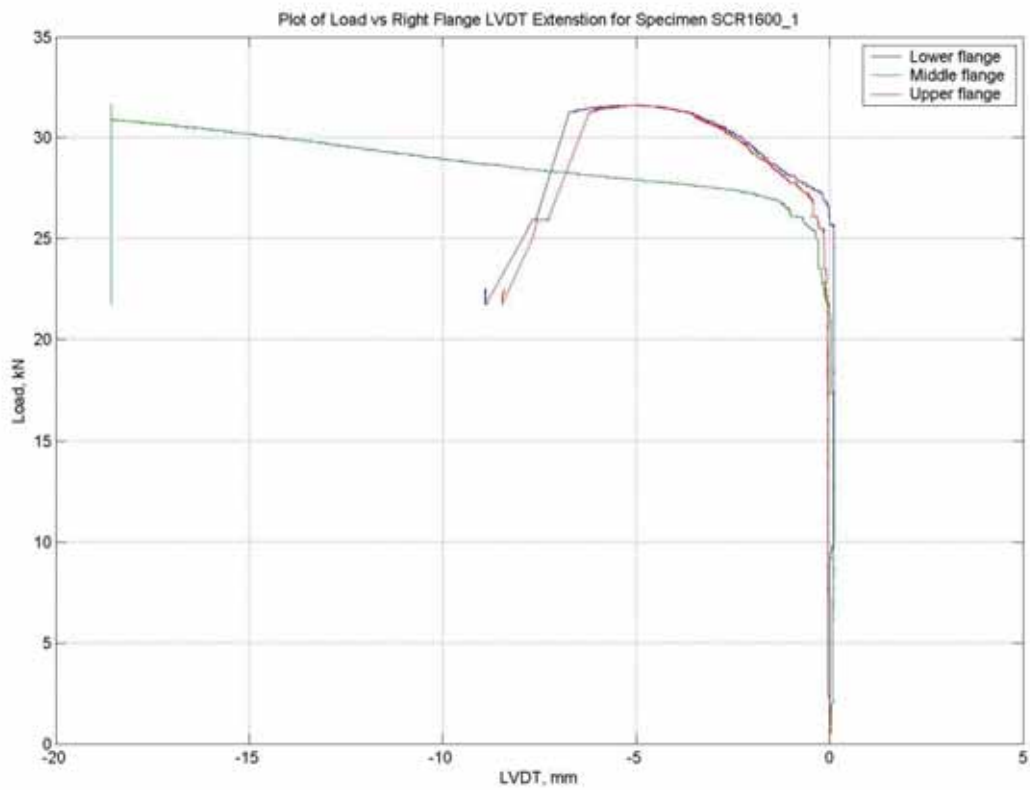


Figure B - 27 Load vs right flange displacement for specimen SCR1600\_1

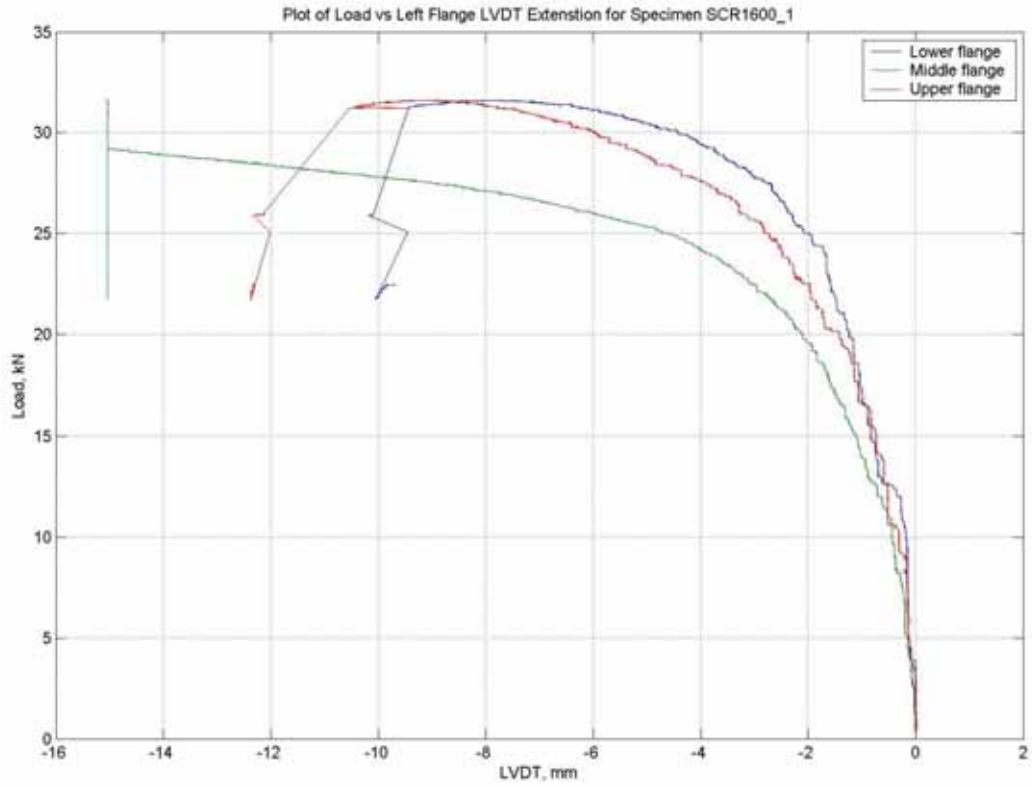


Figure B - 28 Load vs left flange displacement for specimen SCR1600\_1

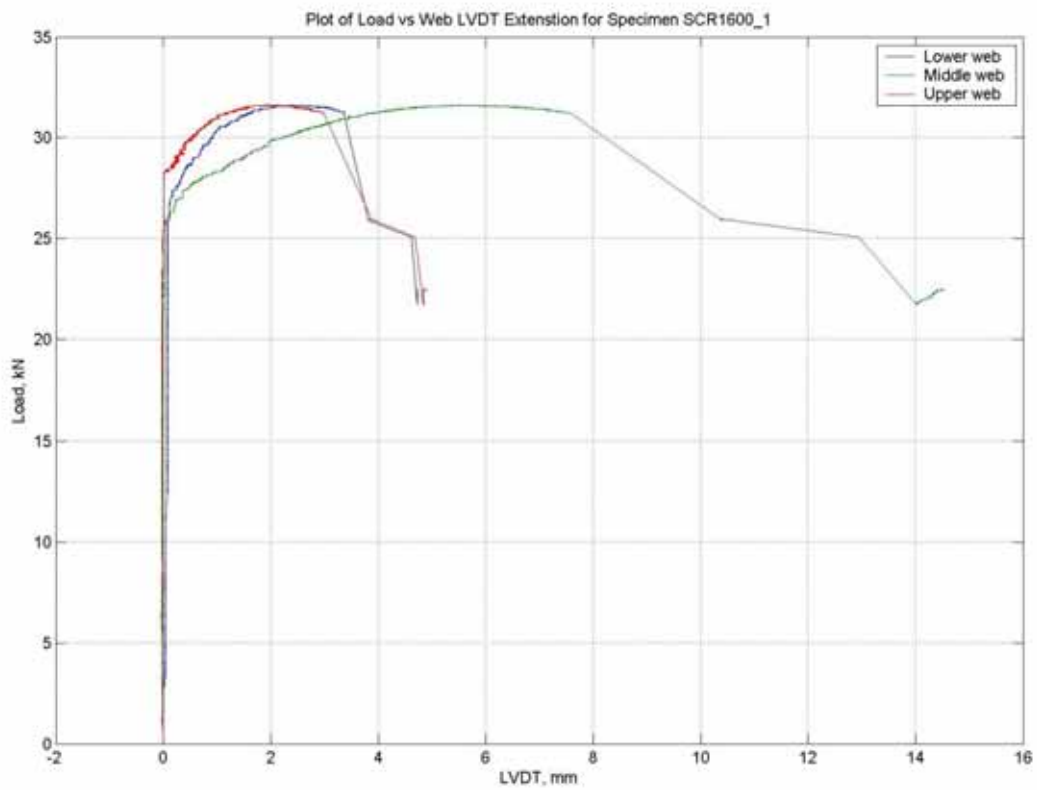


Figure B - 29 Load vs web displacement for specimen SCR1600\_1

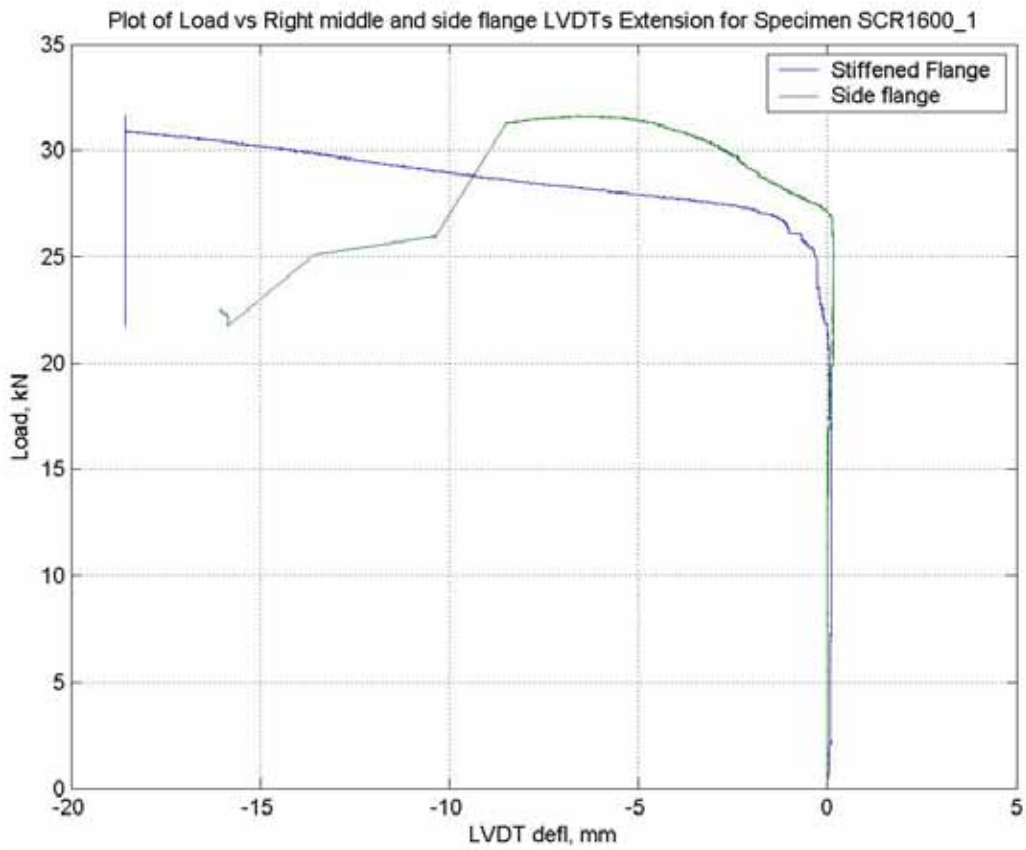


Figure B - 30 Load vs right stiffened and side flanges displacement for specimen SCR1600\_1

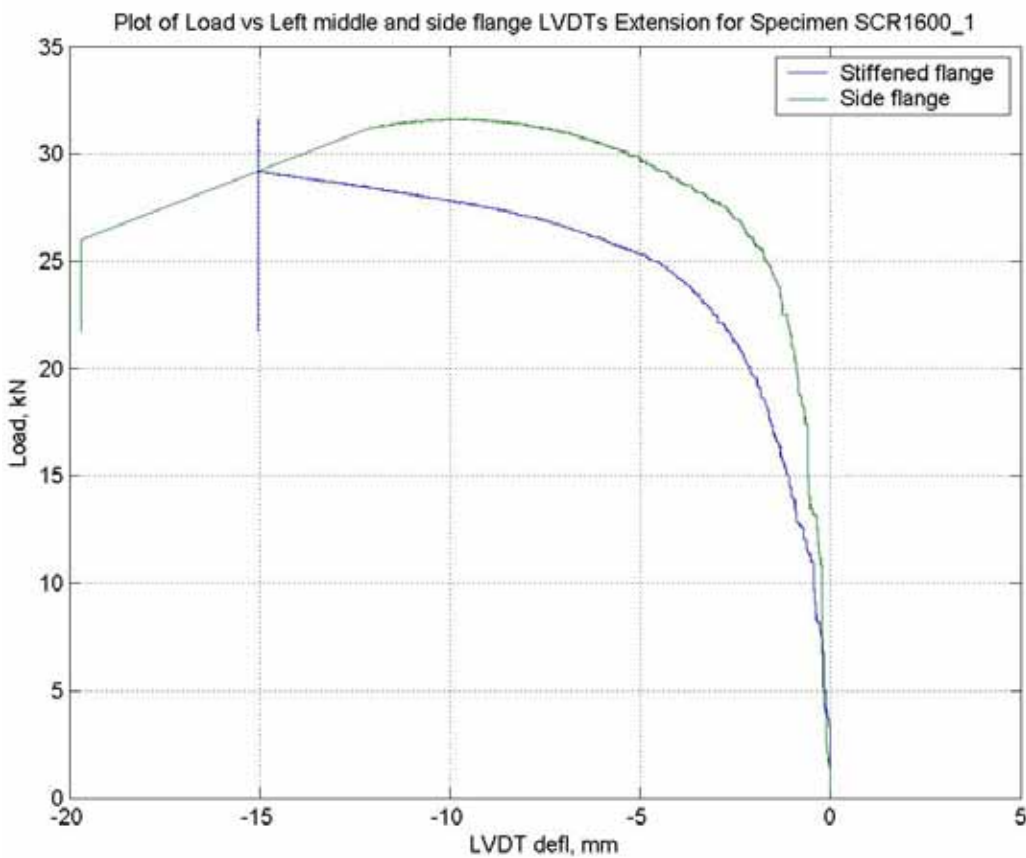


Figure B - 31 Load vs left stiffened and side flanges displacement for specimen SCR1600\_1

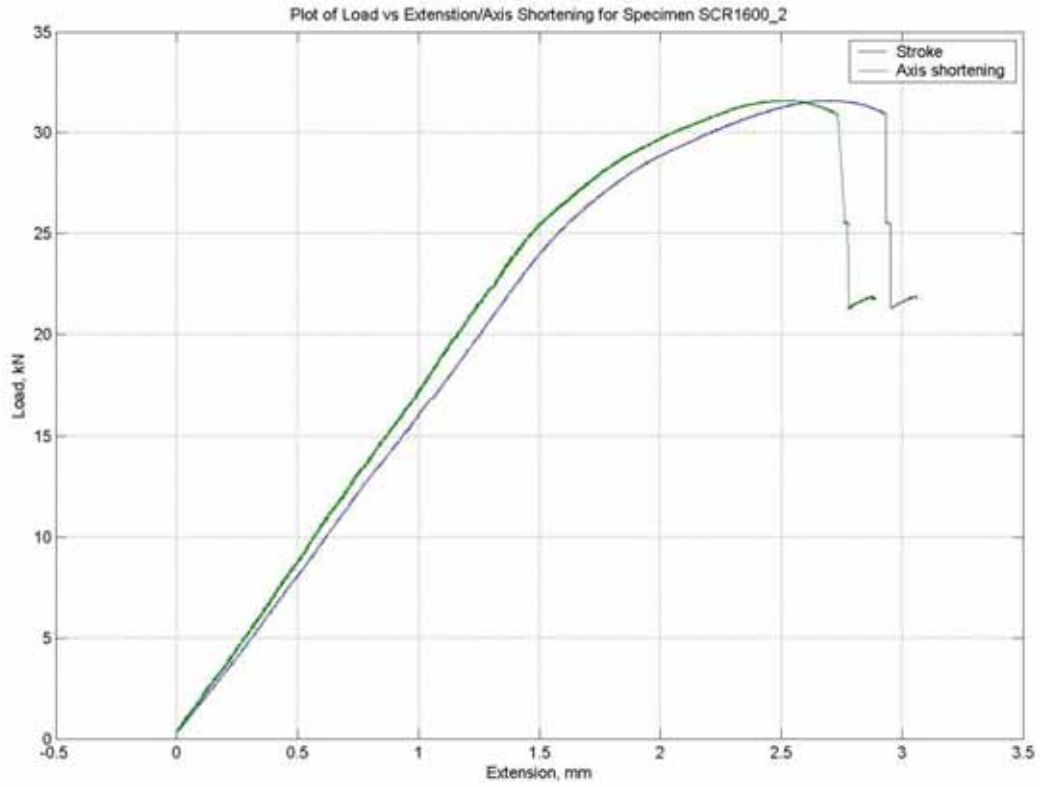


Figure B - 32 Load vs displacement for specimen SCR1600\_2

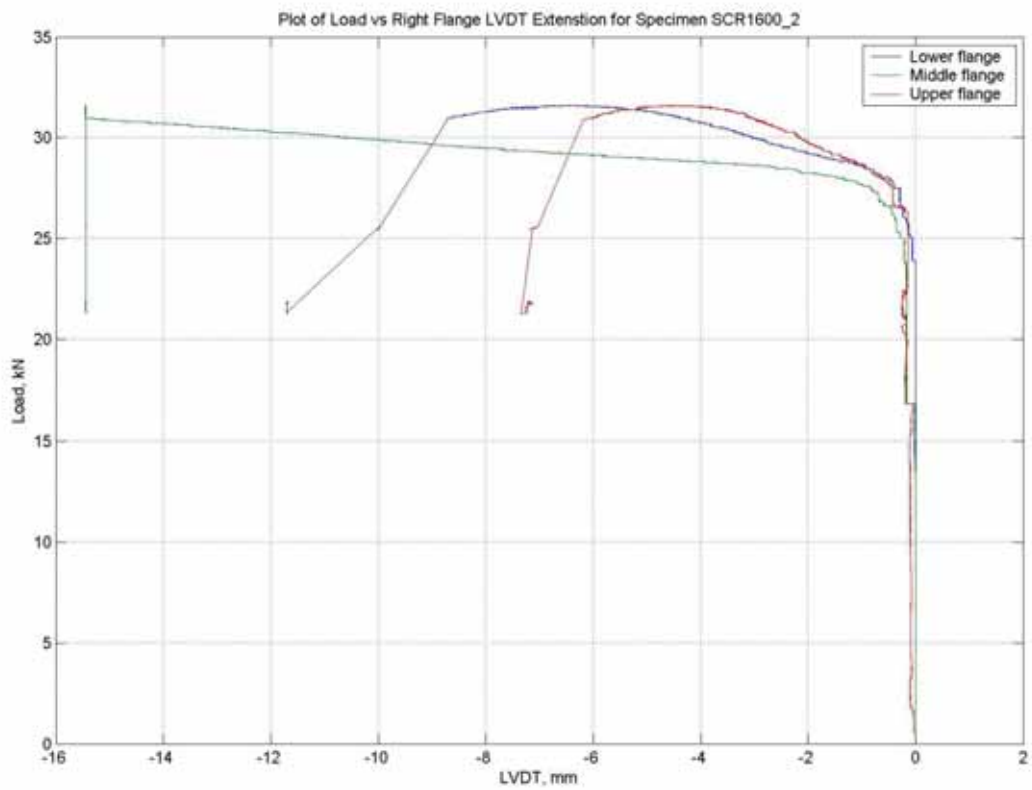


Figure B - 33 Load vs right flange displacement for specimen SCR1600\_2

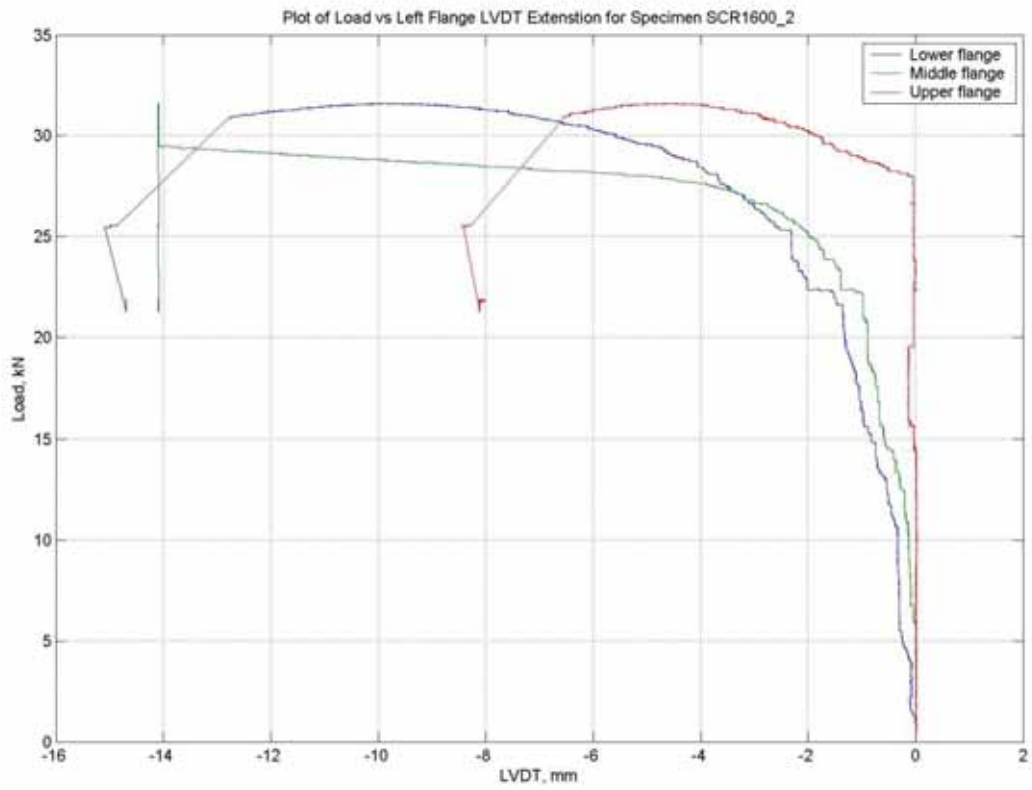


Figure B - 34 Load vs left flange displacement for specimen SCR1600\_2

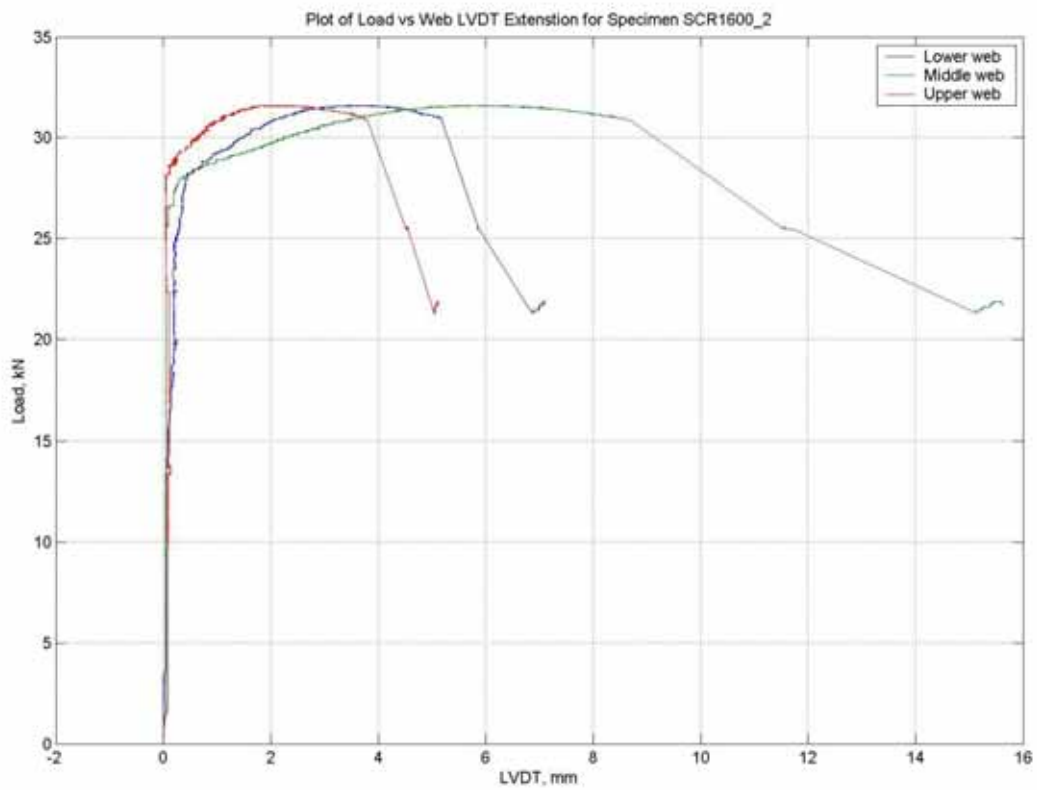


Figure B - 35 Load vs web displacement for specimen SCR1600\_2

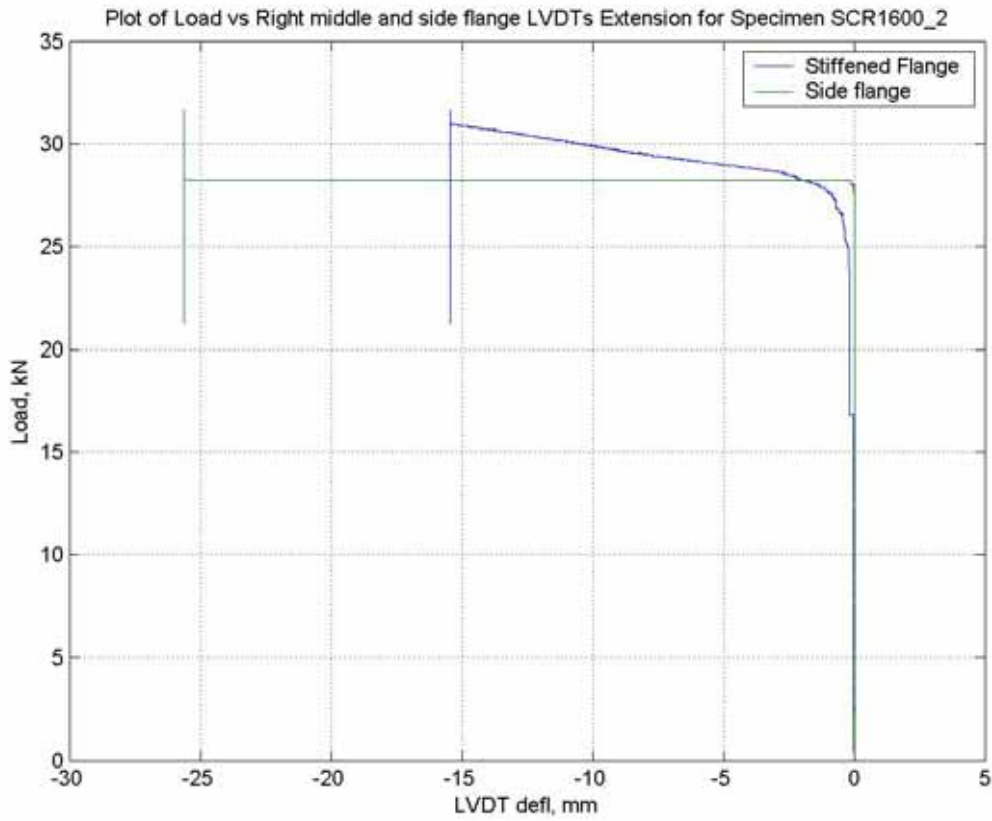


Figure B - 36 Load vs right stiffened and side flanges displacement for specimen SCR1600\_2

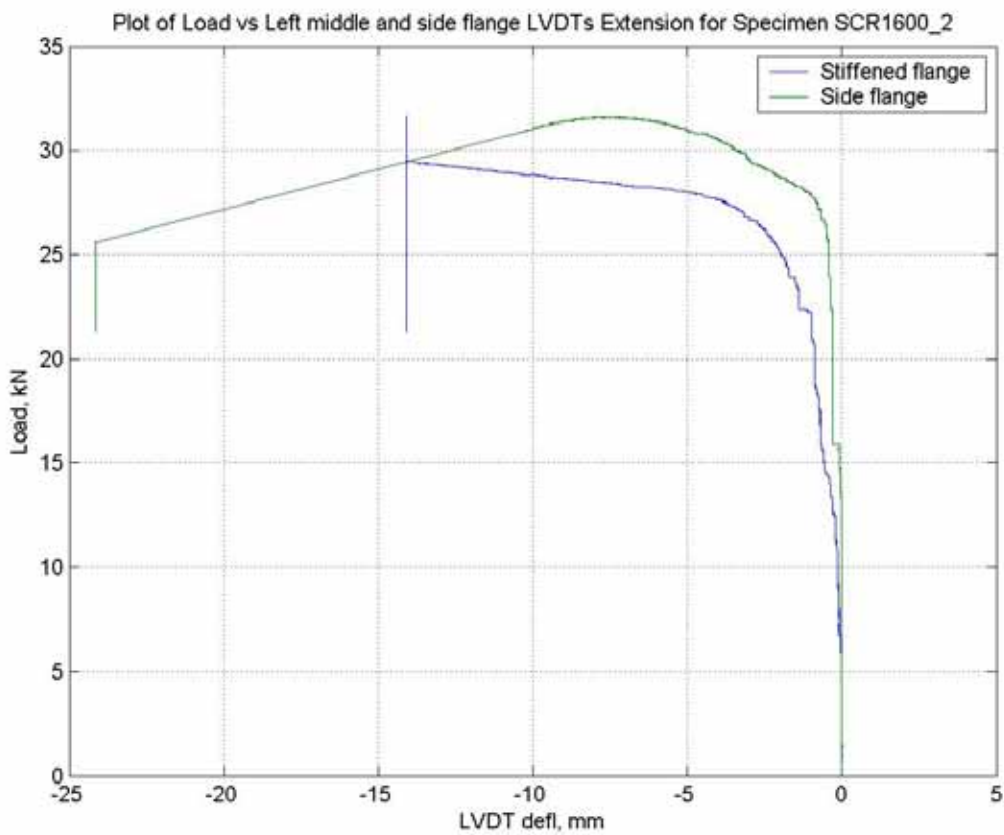


Figure B - 37 Load vs left stiffened and side flanges displacement for specimen SCR1600\_2

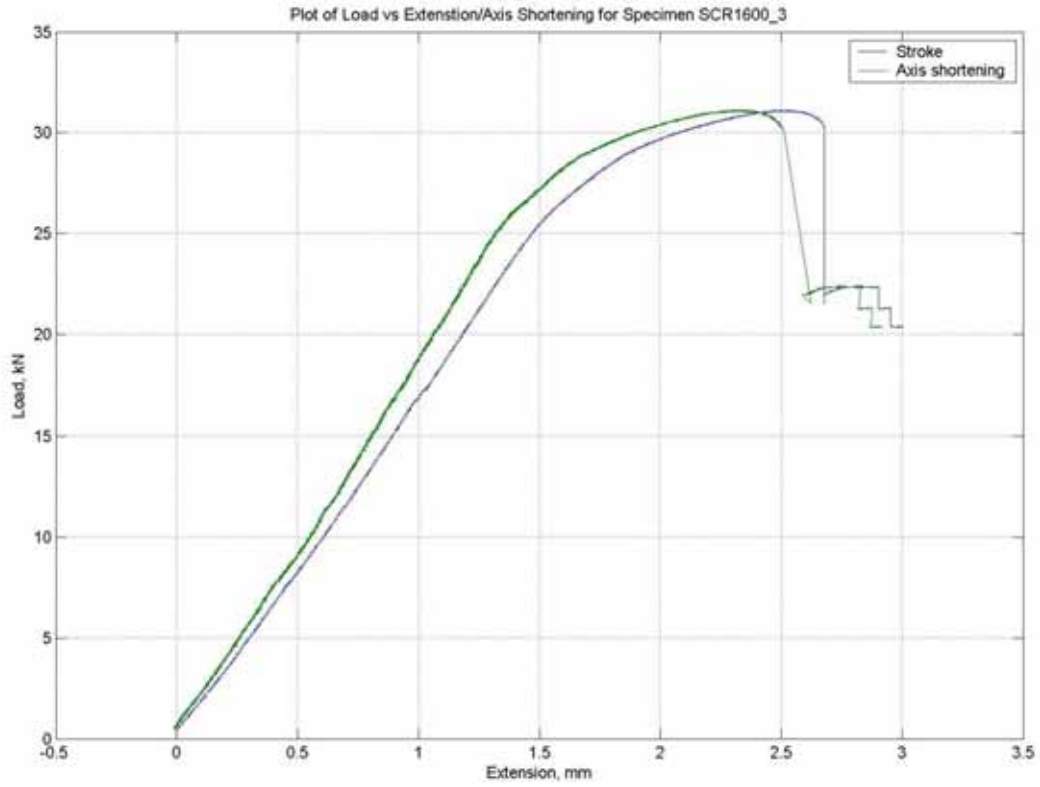


Figure B - 38 Load vs displacement for specimen SCR1600\_3

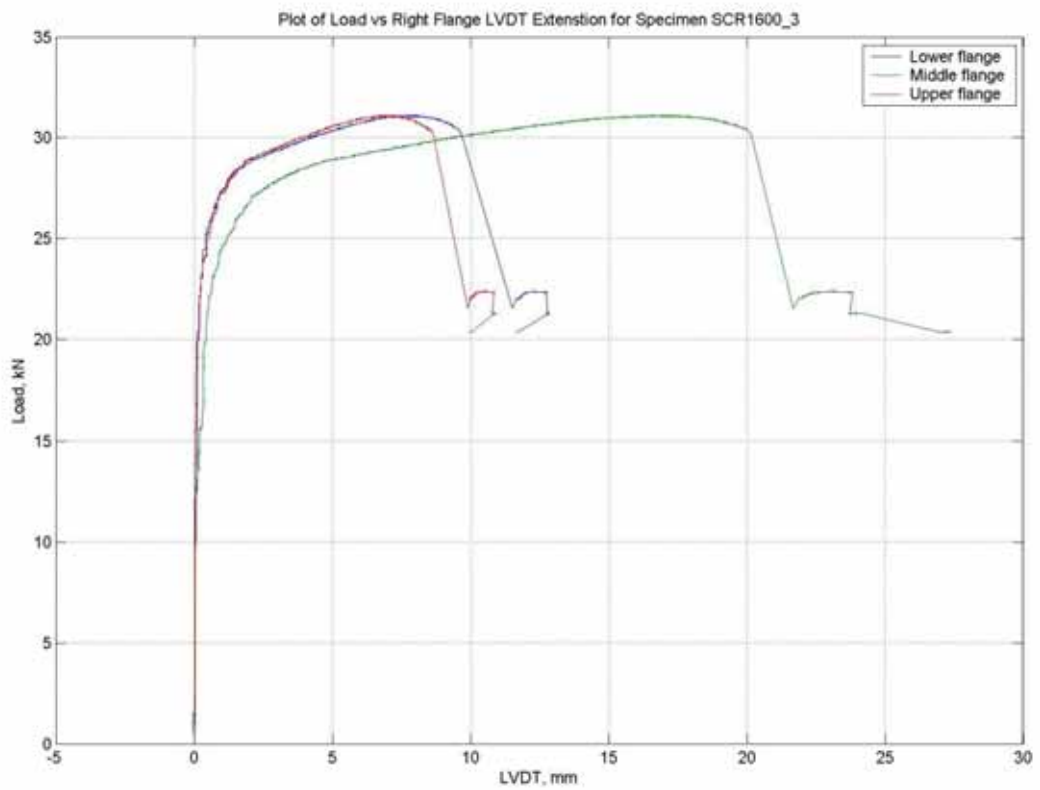


Figure B - 39 Load vs right flange displacement for specimen SCR1600\_3

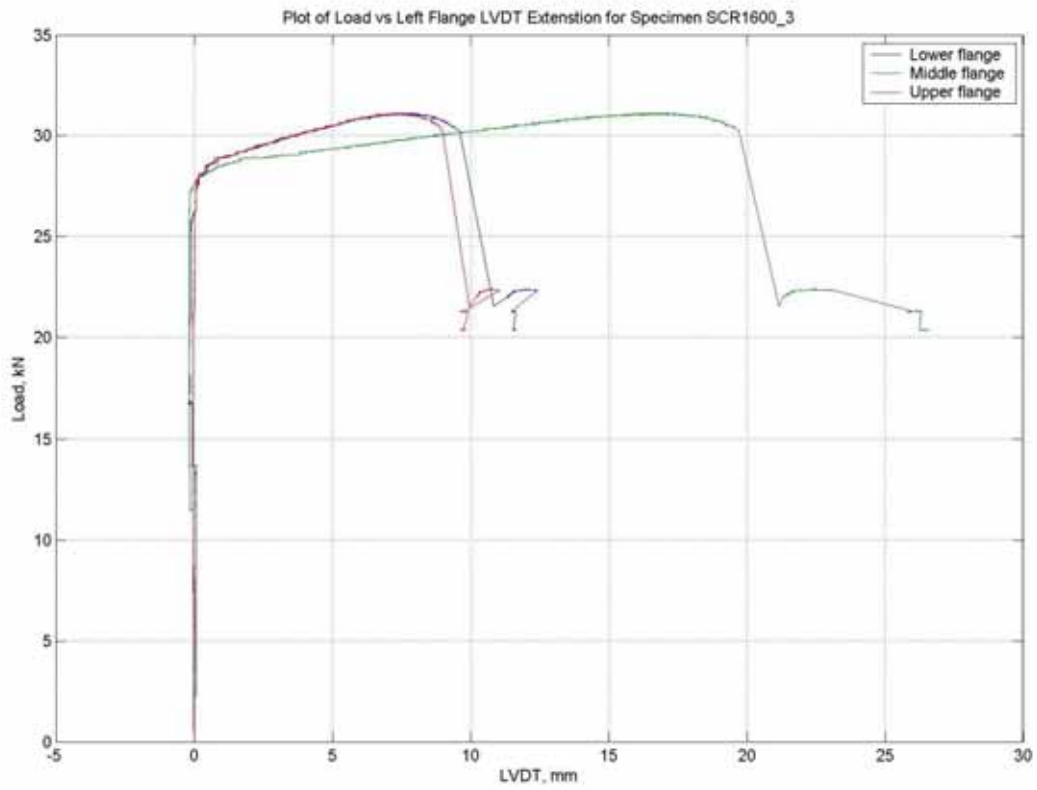


Figure B - 40 Load vs left flange displacement for specimen SCR1600\_3

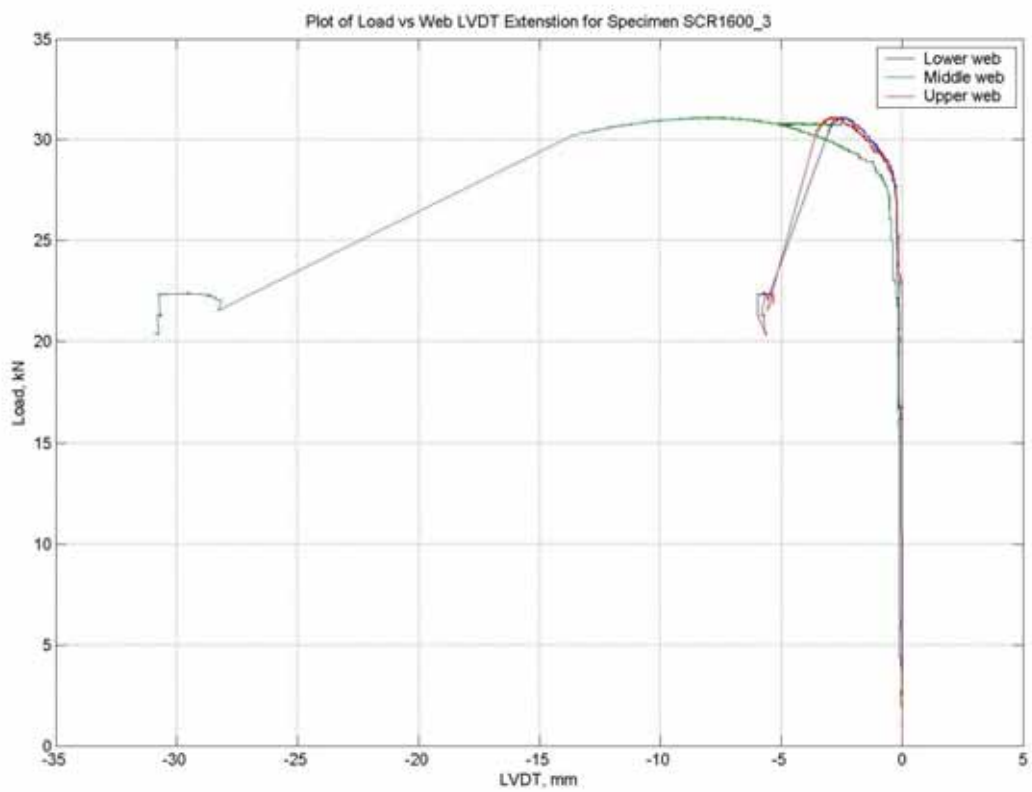


Figure B - 41 Load vs web displacement for specimen SCR1600\_3

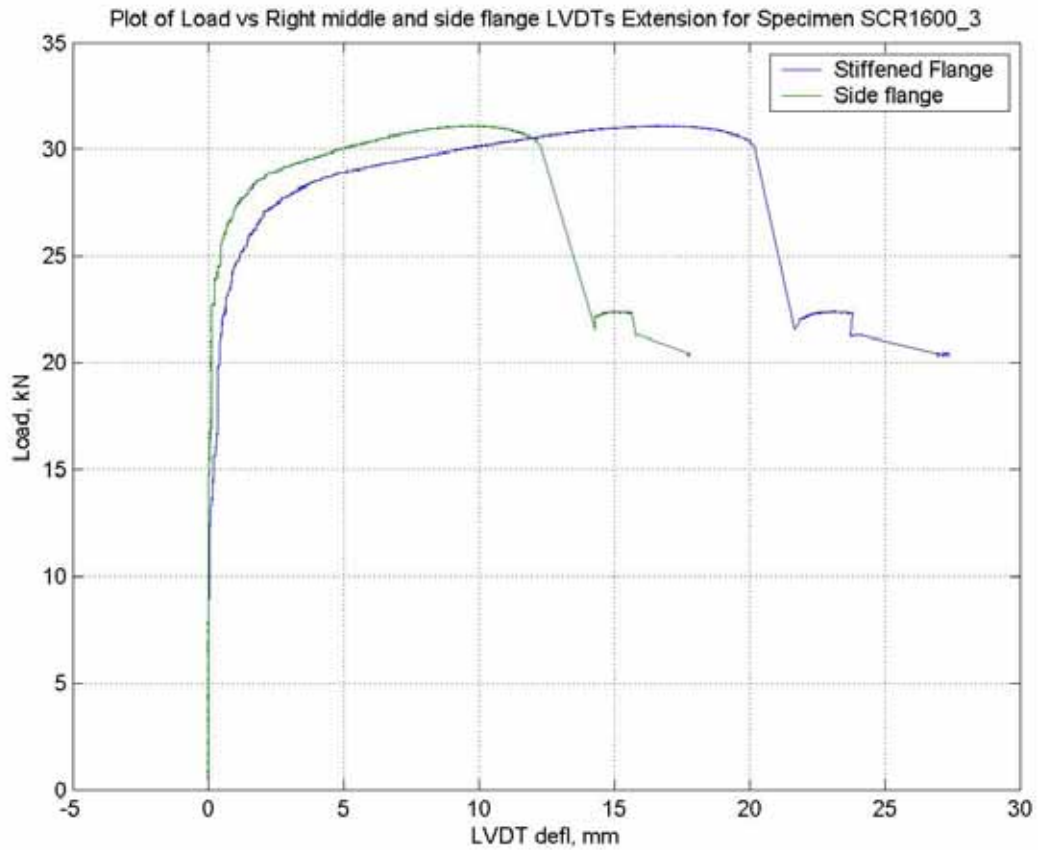


Figure B - 42 Load vs right stiffened and side flanges displacement for specimen SCR1600\_3

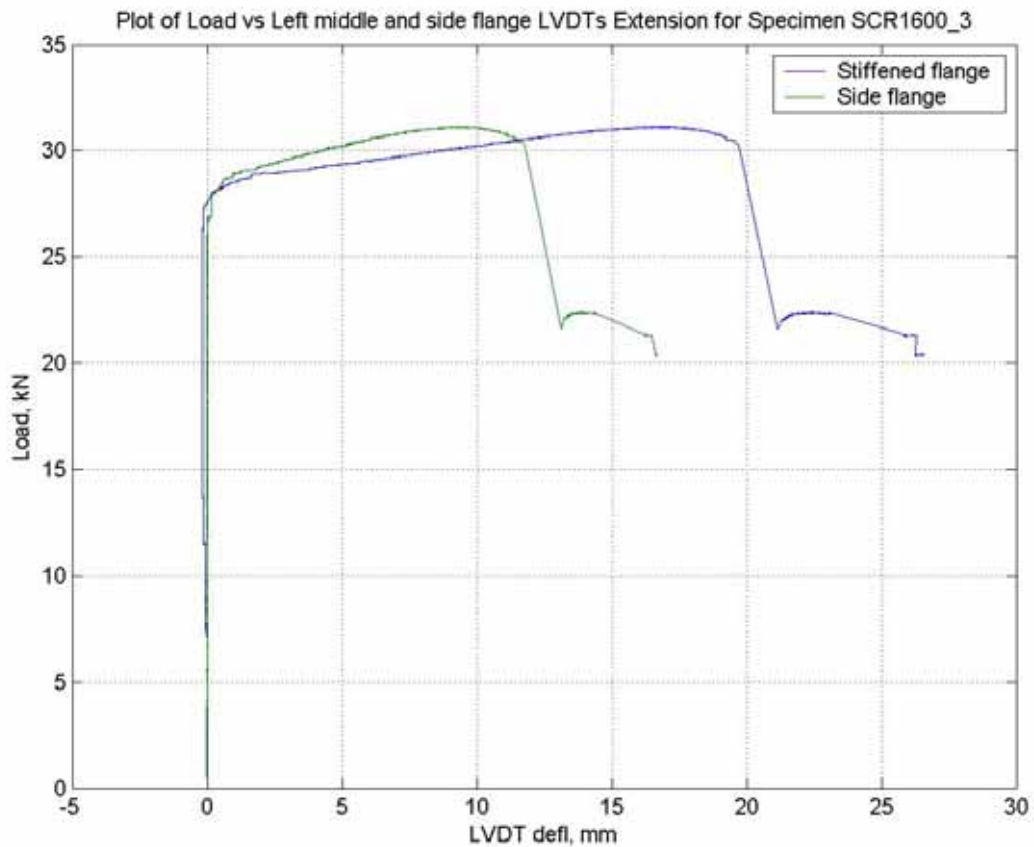


Figure B - 43 Load vs left stiffened and side flanges displacement for specimen SCR1600\_3

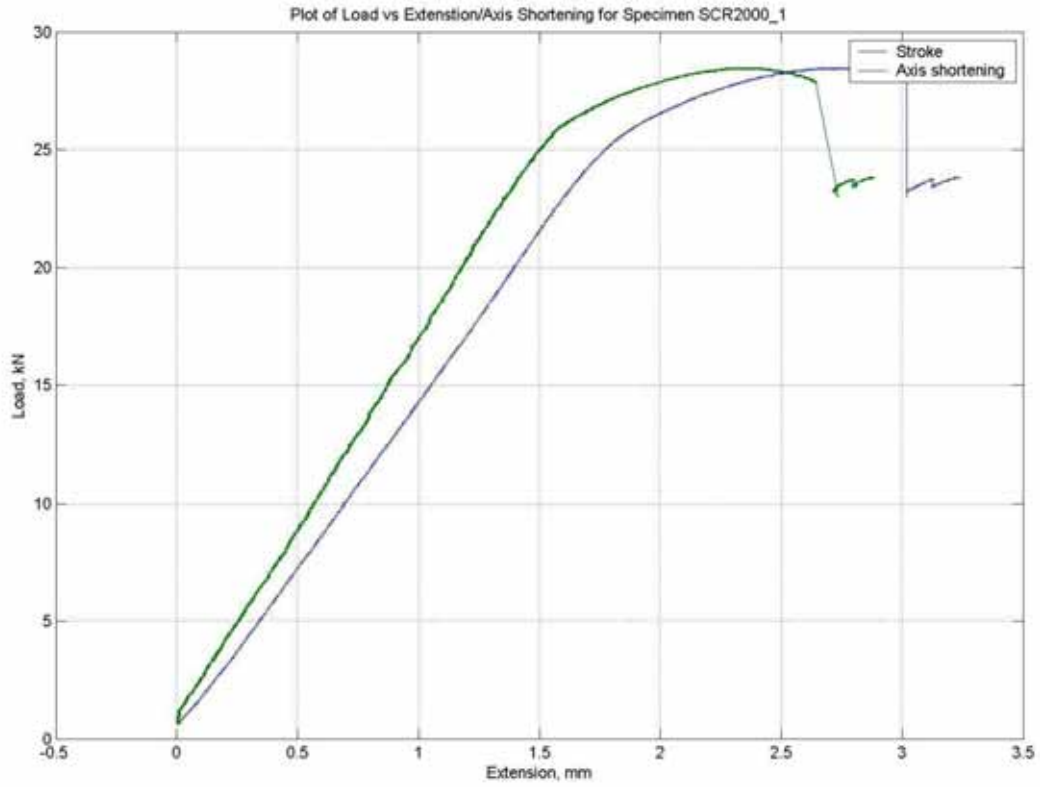


Figure B - 44 Load vs displacement for specimen SCR2000\_1

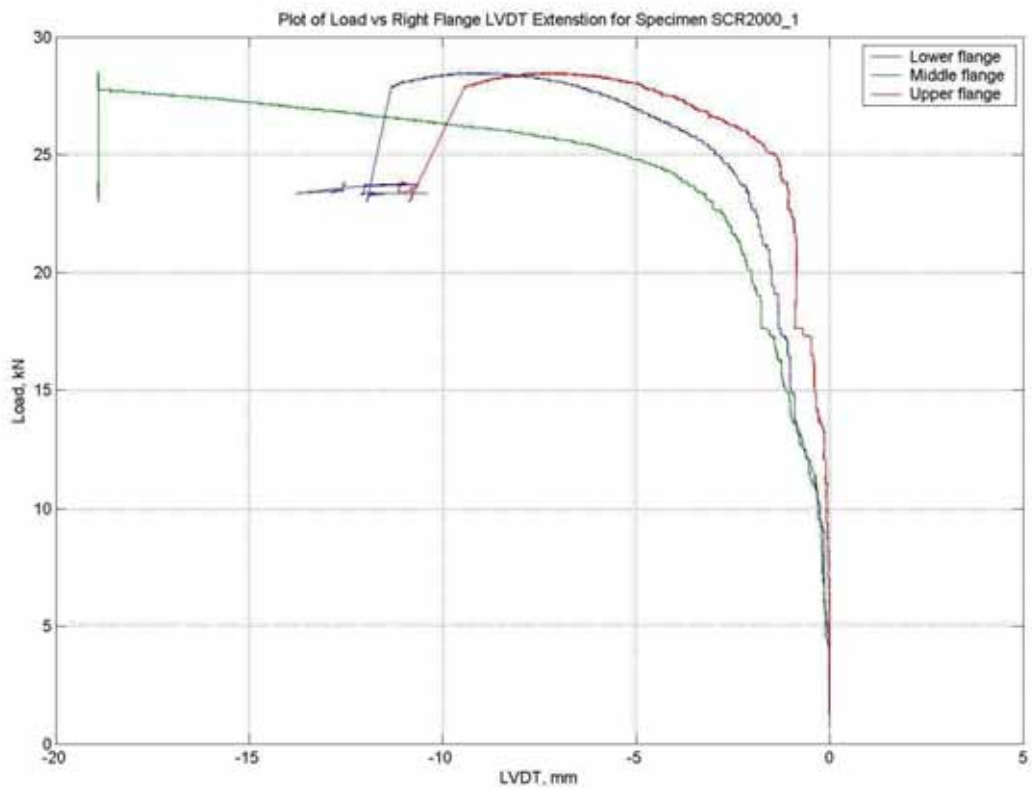


Figure B - 45 Load vs right flange displacement for specimen SCR2000\_1

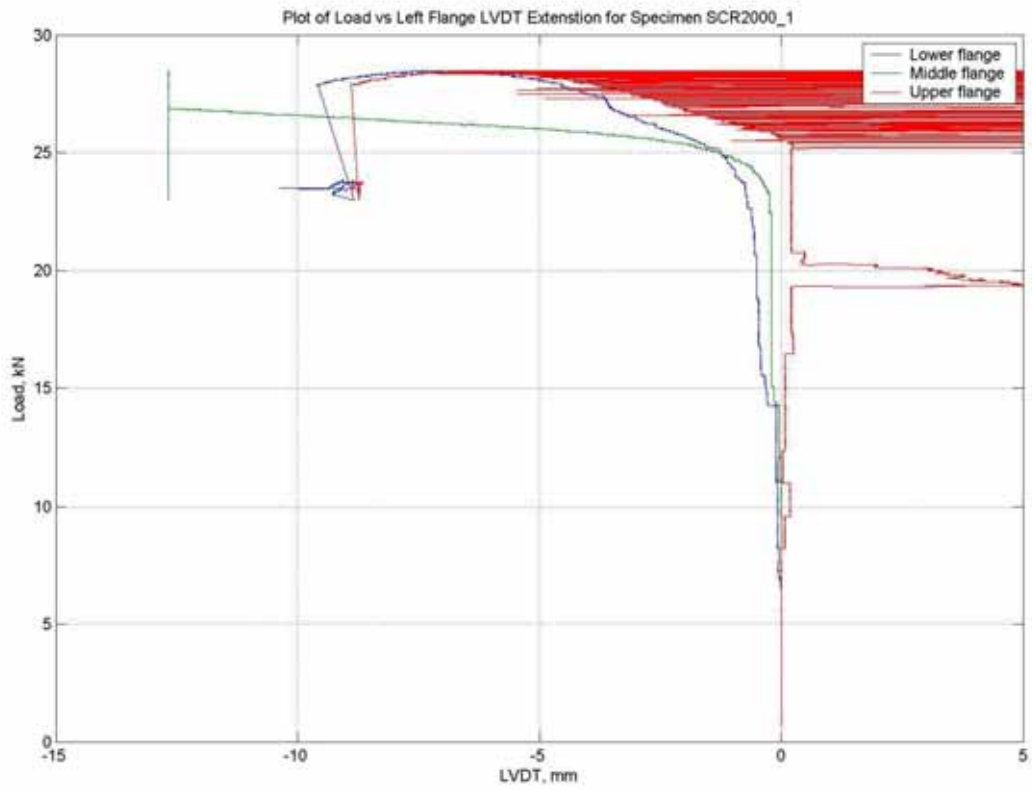


Figure B - 46 Load vs left flange displacement for specimen SCR2000\_1

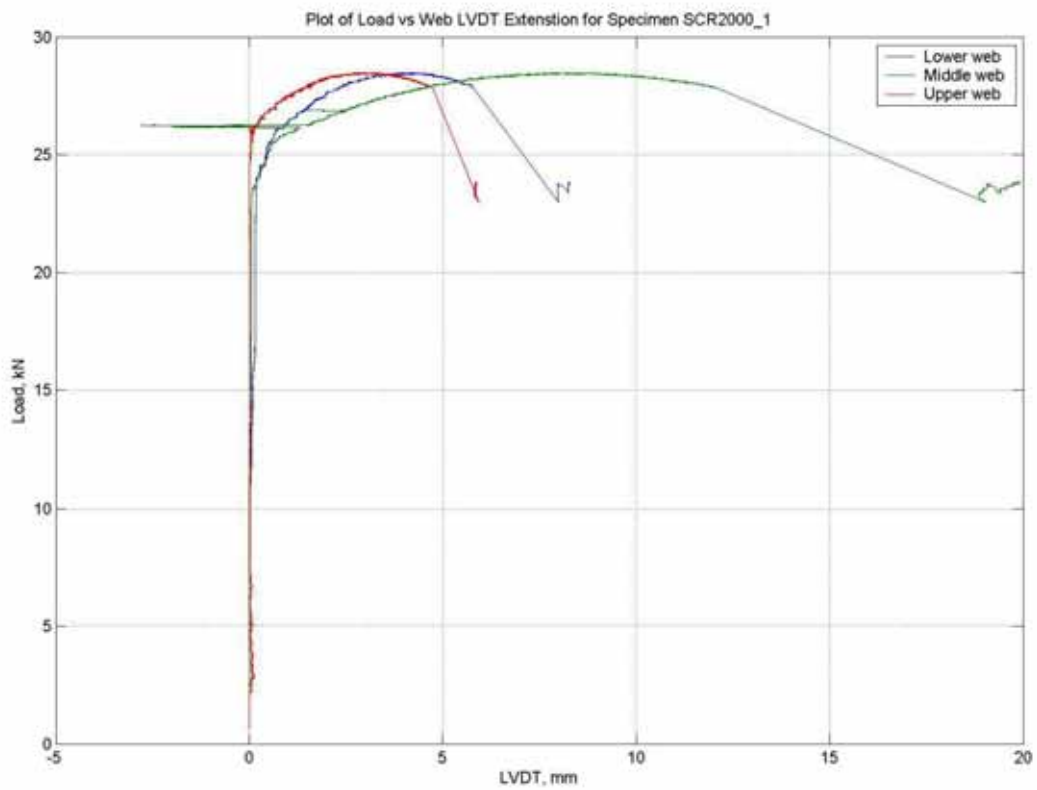


Figure B - 47 Load vs web displacement for specimen SCR2000\_1

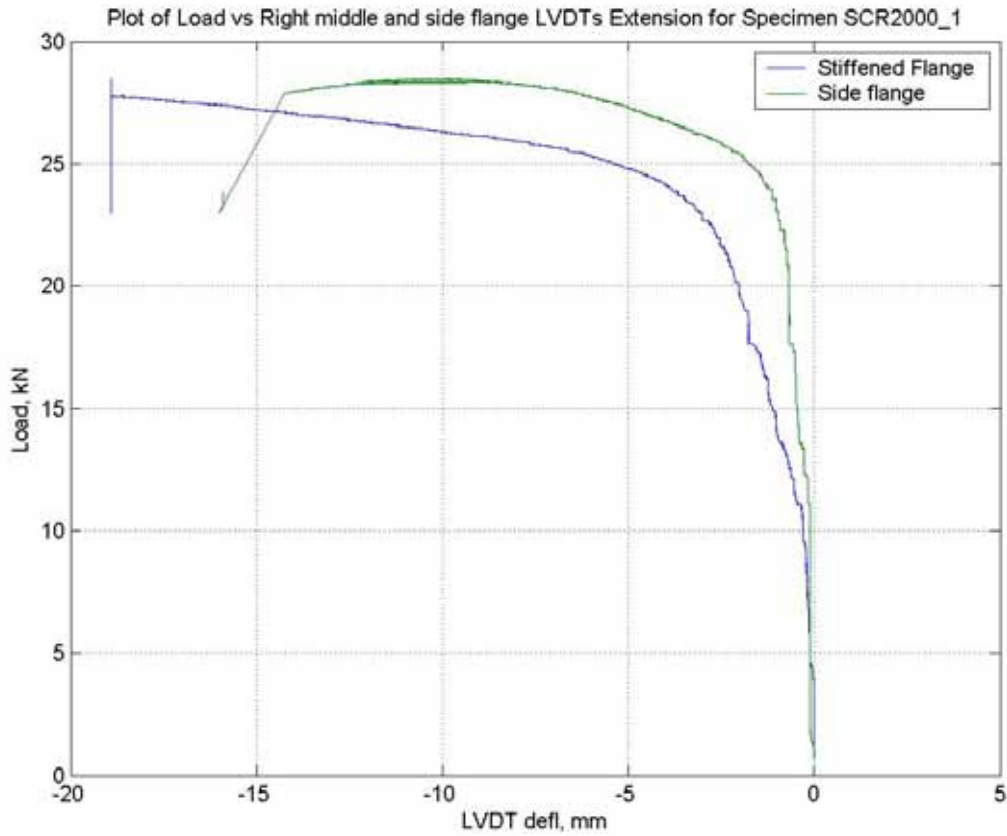


Figure B - 48 Load vs right stiffened and side flanges displacement for specimen SCR2000\_1

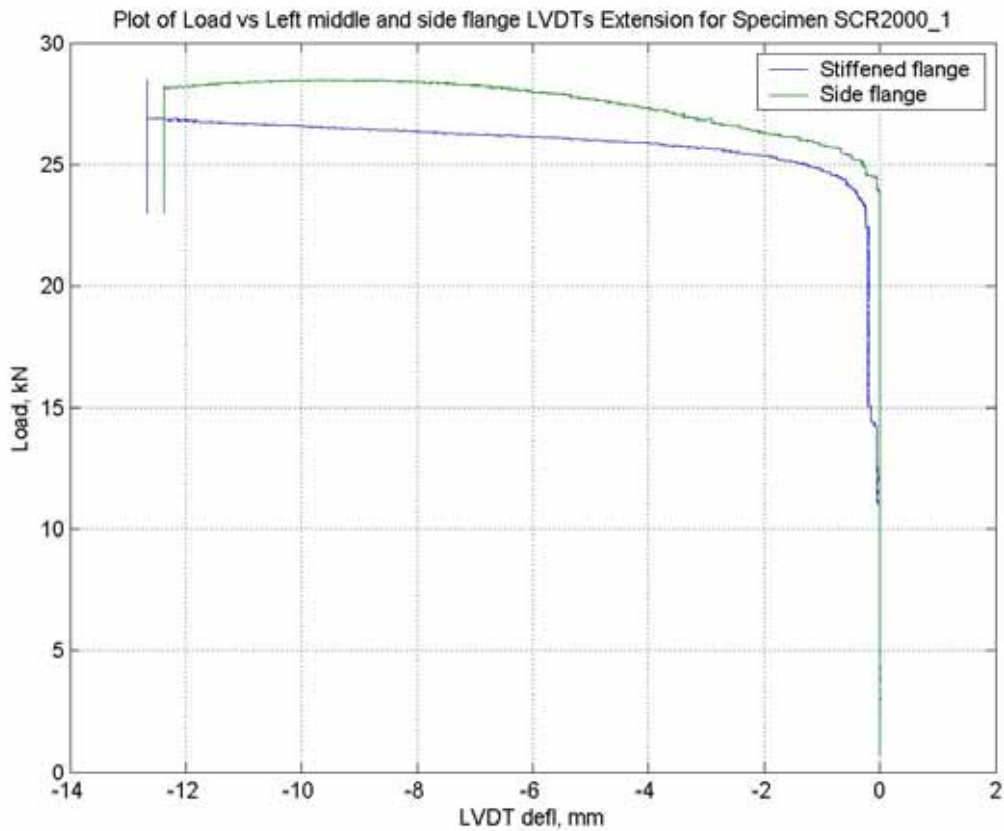


Figure B - 49 Load vs left stiffened and side flanges displacement for specimen SCR2000\_1

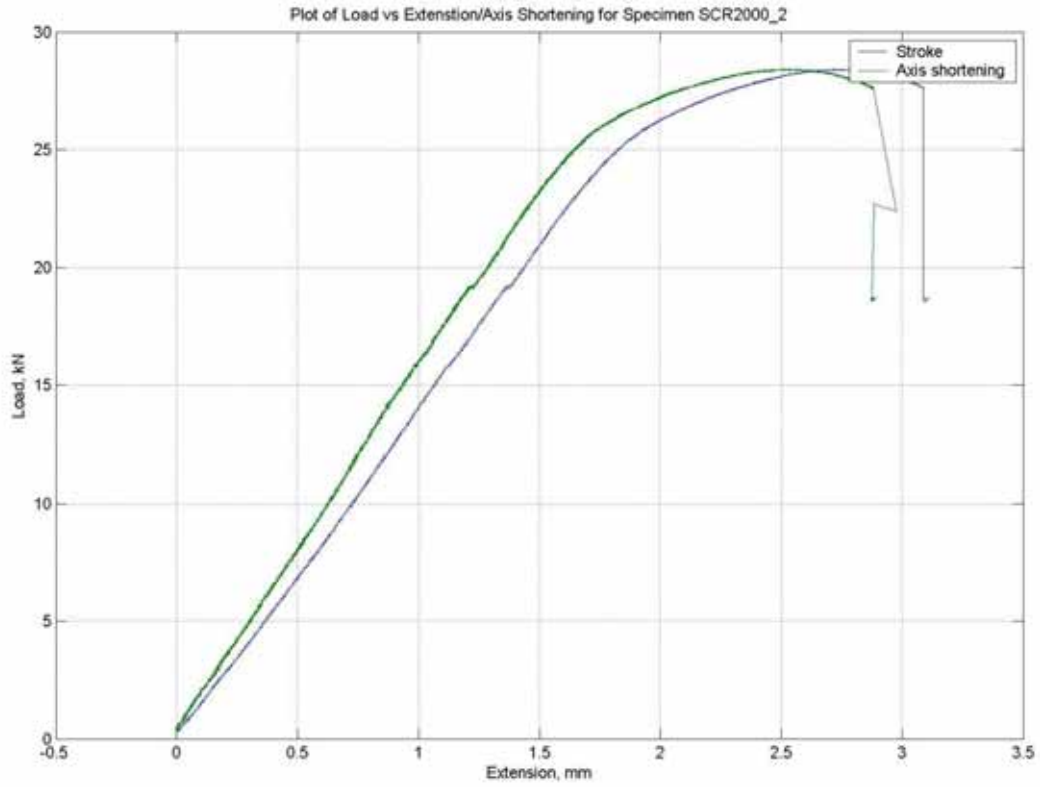


Figure B - 50 Load vs displacement for specimen SCR2000\_2

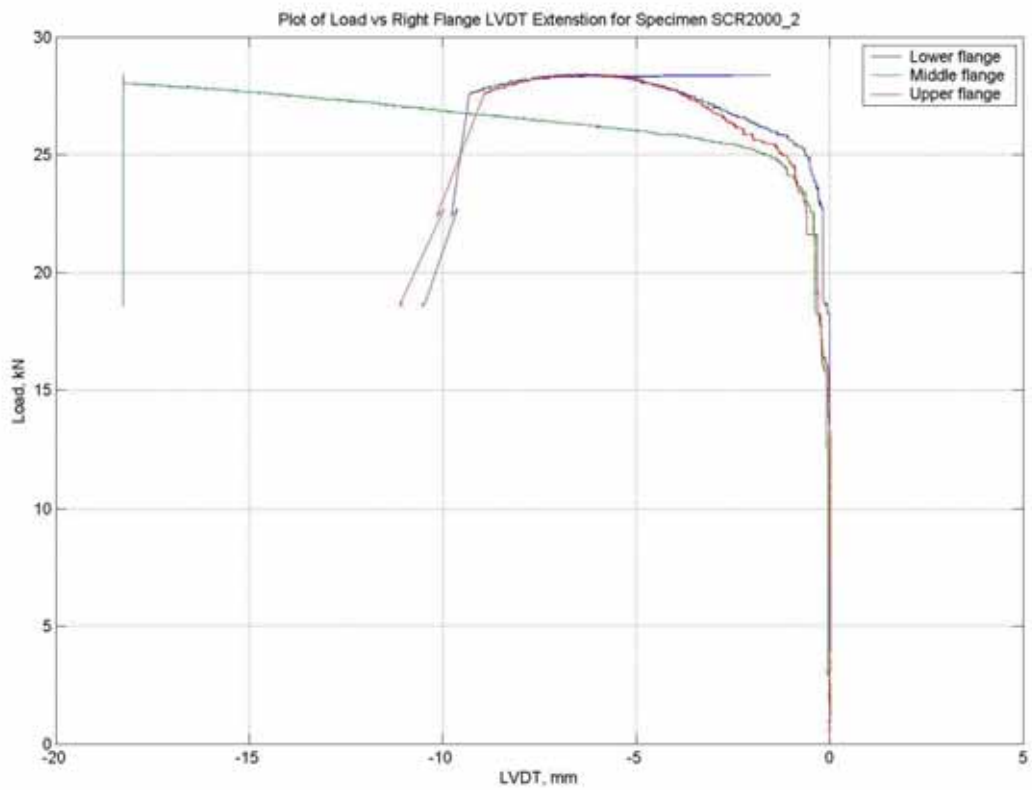


Figure B - 51 Load vs right flange displacement for specimen SCR2000\_2

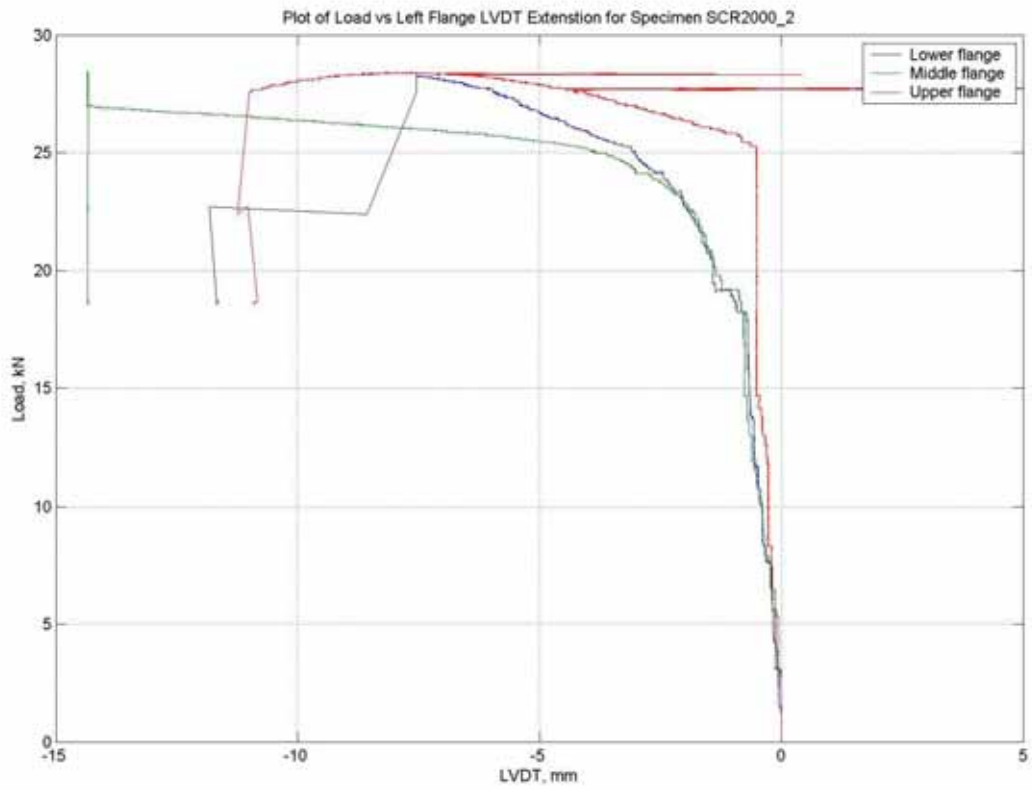


Figure B - 52 Load vs left flange displacement for specimen SCR2000\_2

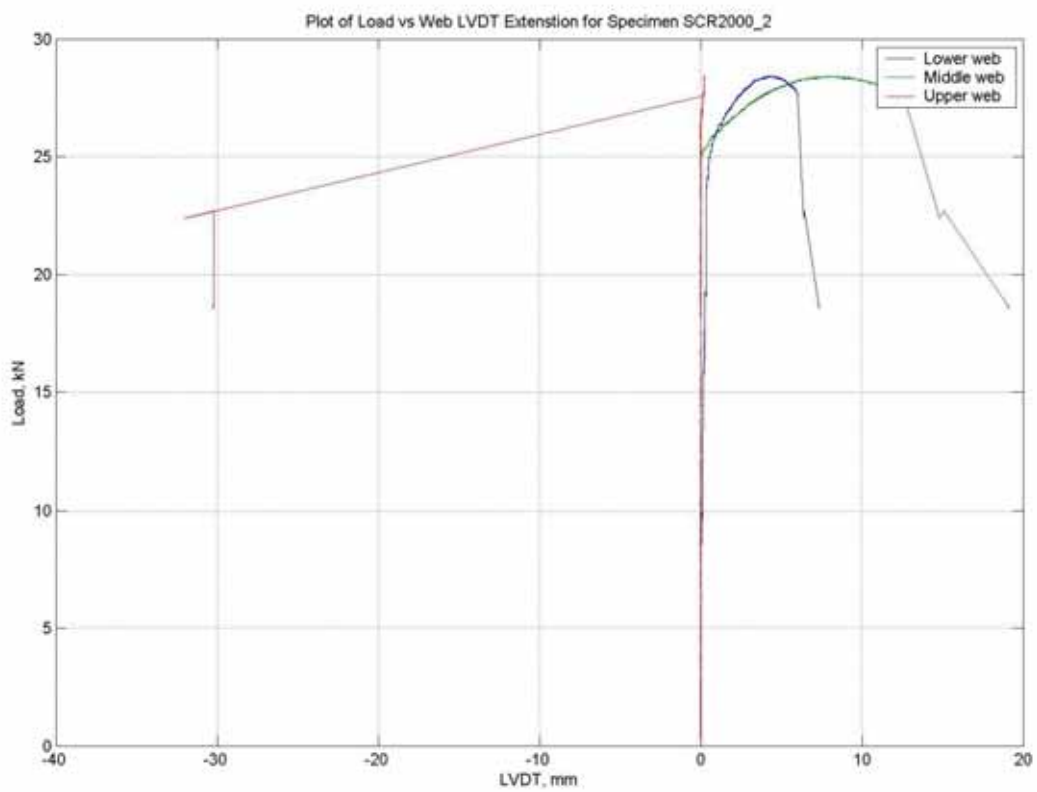


Figure B - 53 Load vs web displacement for specimen SCR2000\_2

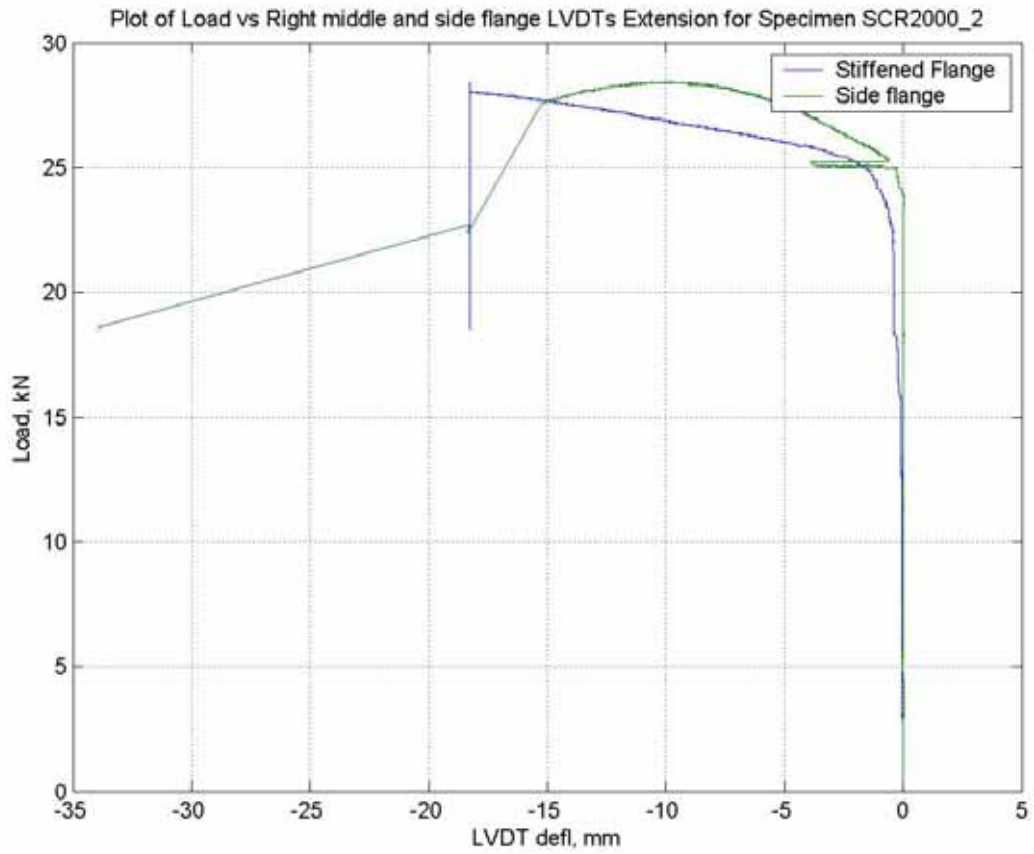


Figure B - 54 Load vs right stiffened and side flanges displacement for specimen SCR2000\_2

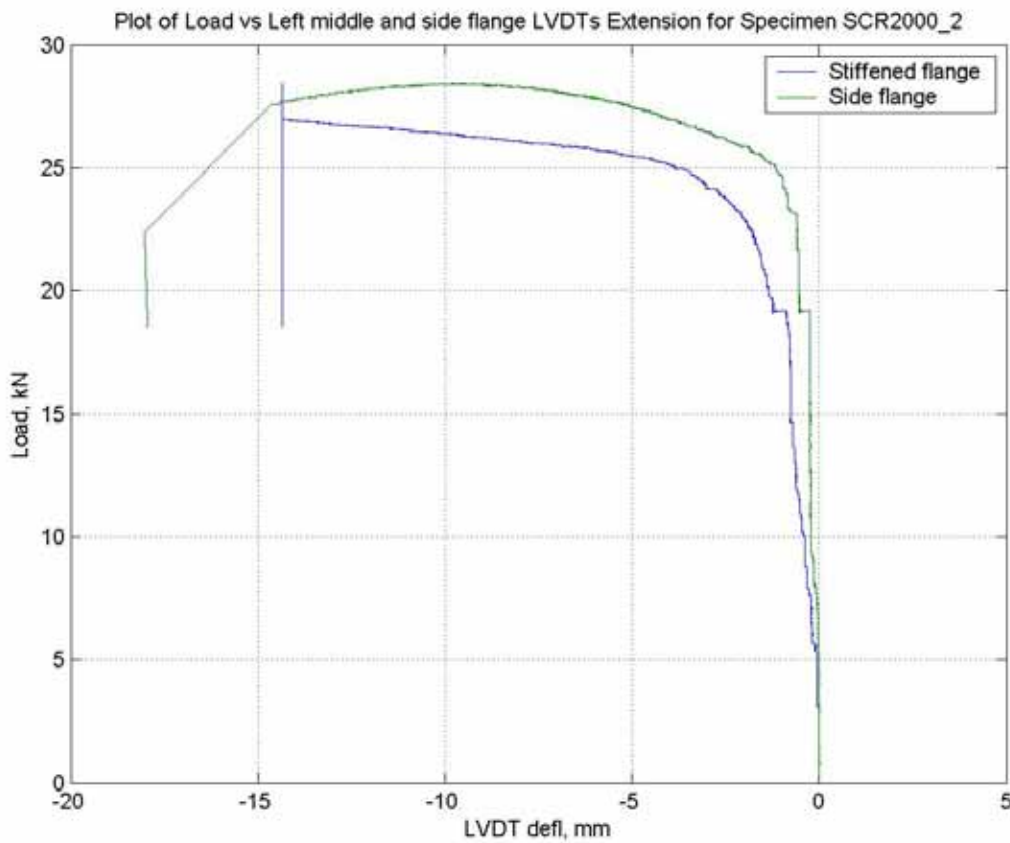


Figure B - 55 Load vs left stiffened and side flanges displacement for specimen SCR2000\_2

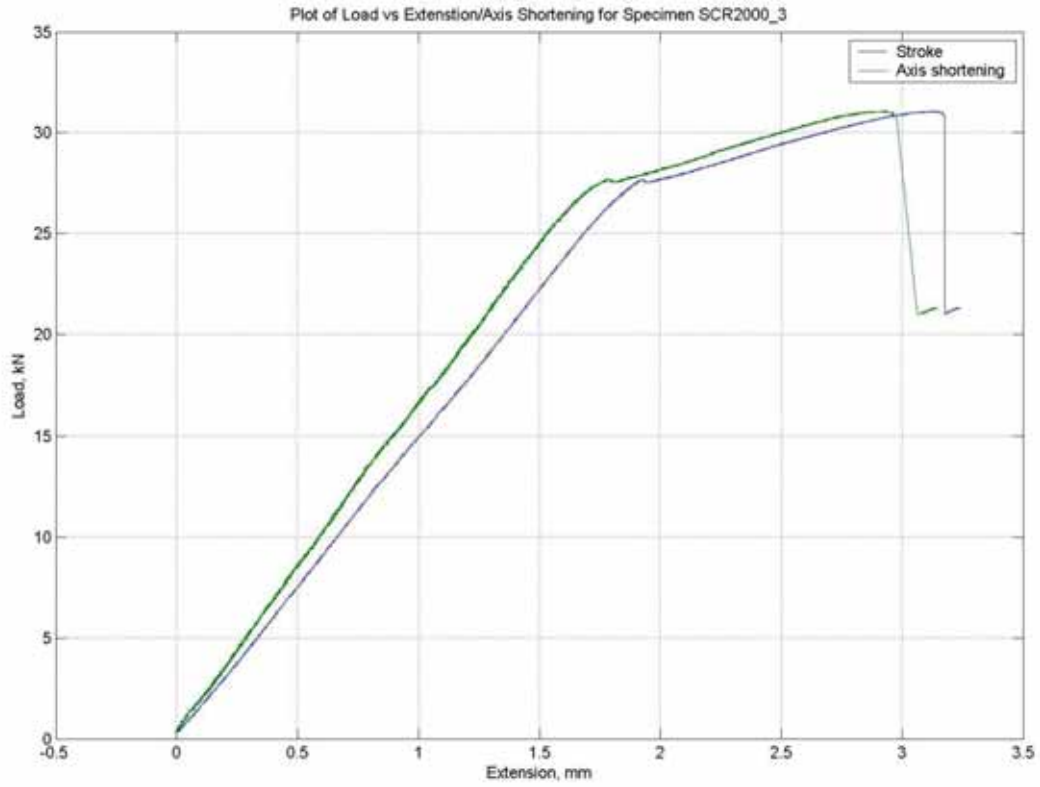


Figure B - 56 Load vs displacement for specimen SCR2000\_3

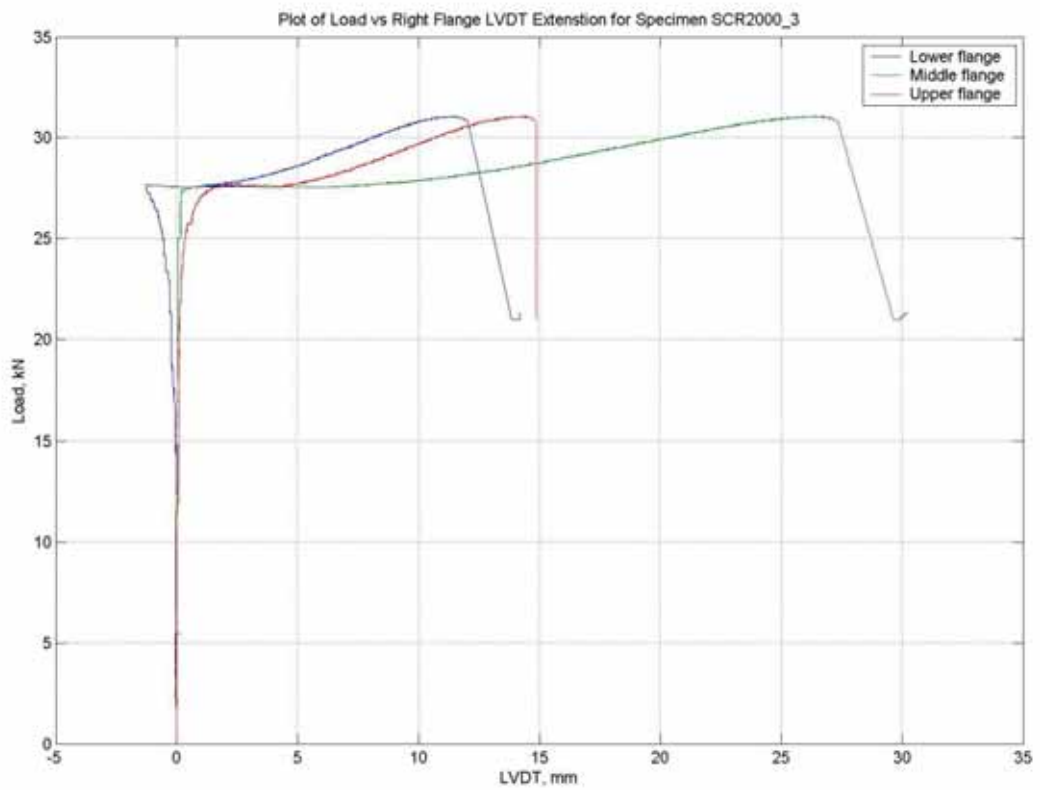


Figure B - 57 Load vs right flange displacement for specimen SCR2000\_3

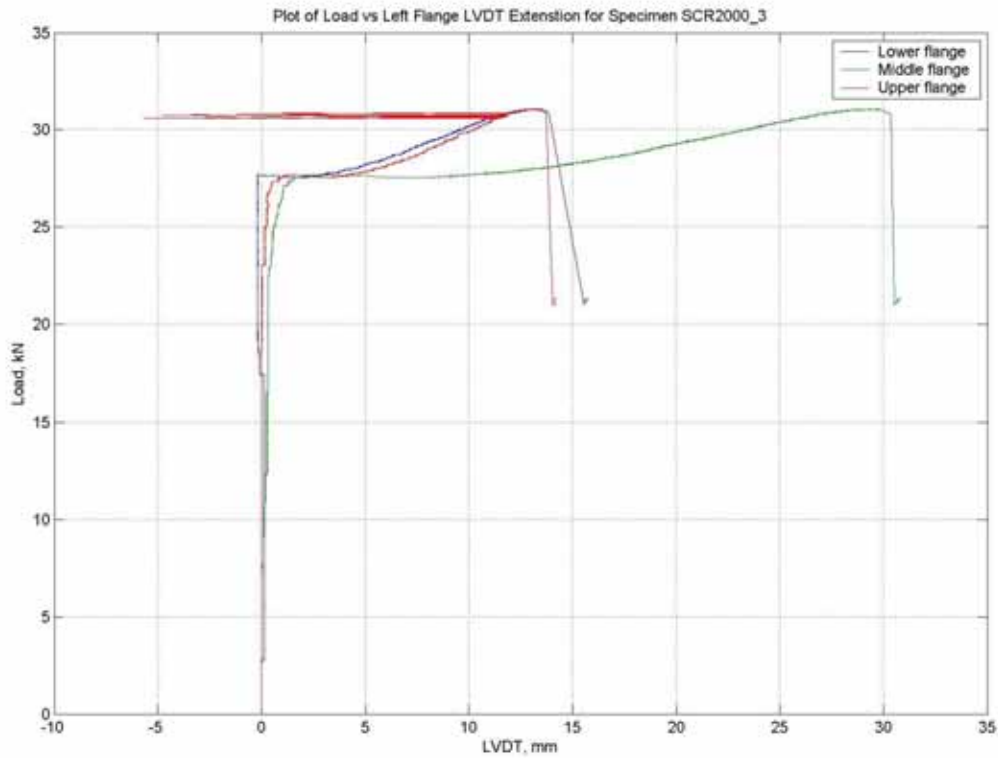


Figure B - 58 Load vs left flange displacement for specimen SCR2000\_3

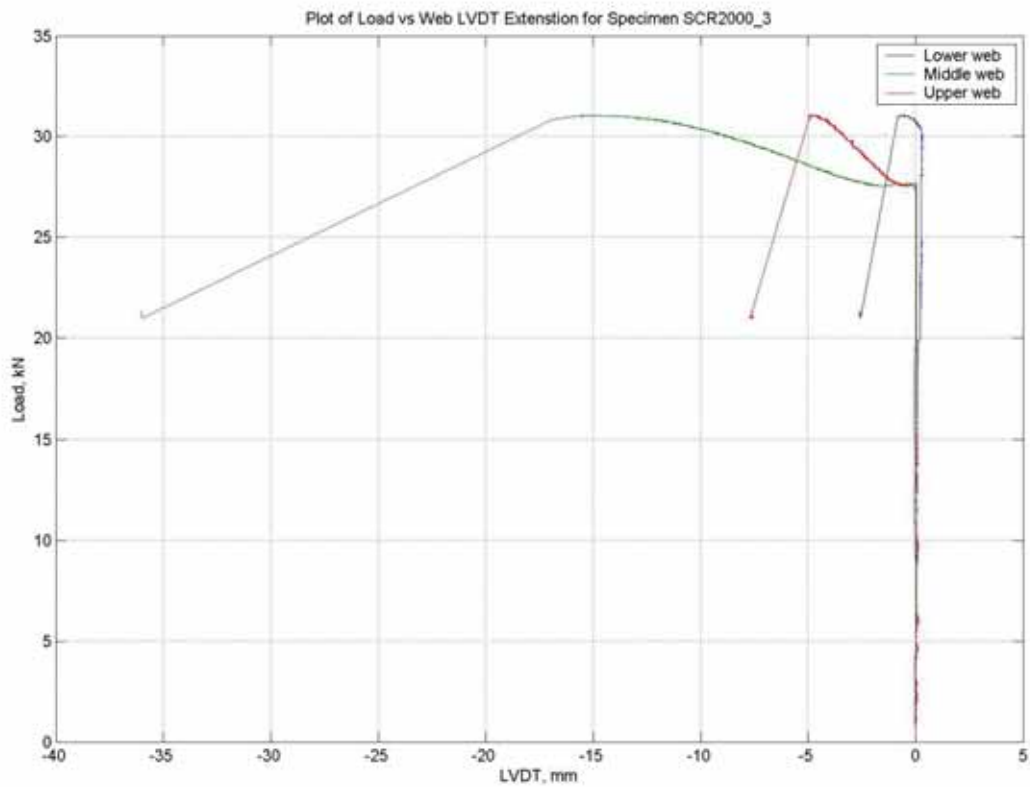


Figure B - 59 Load vs web displacement for specimen SCR2000\_3

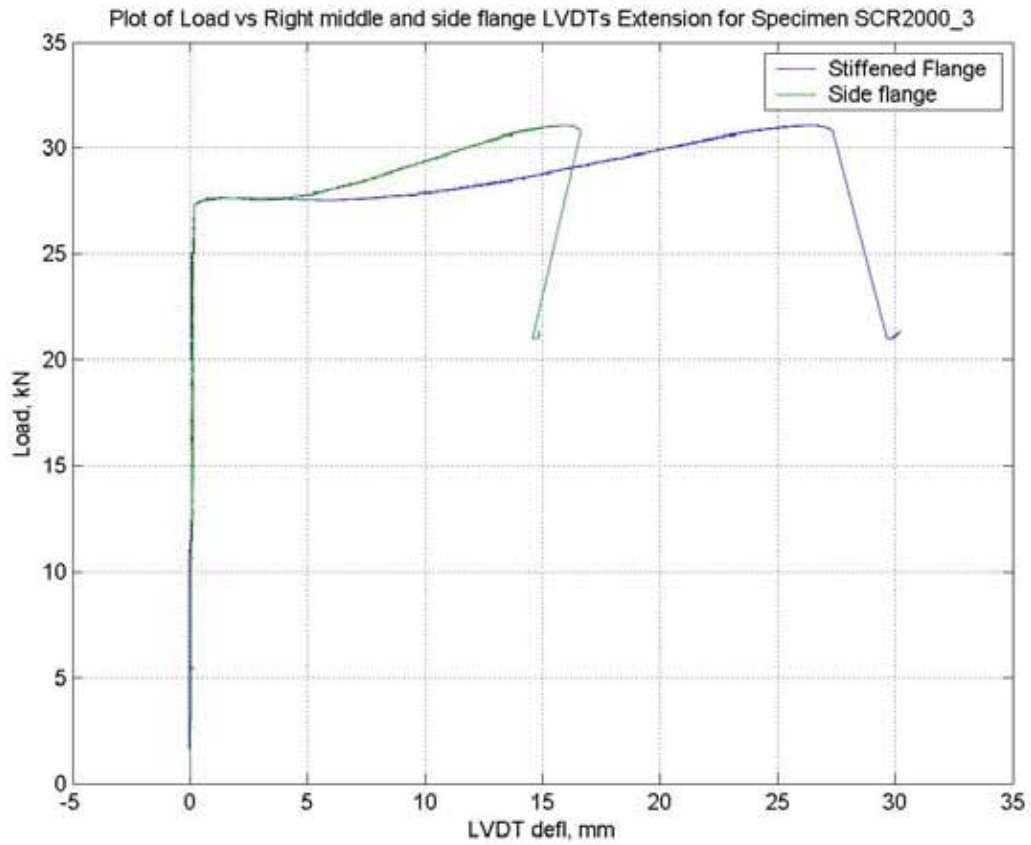


Figure B - 60 Load vs right stiffened and side flanges displacement for specimen SCR2000\_3

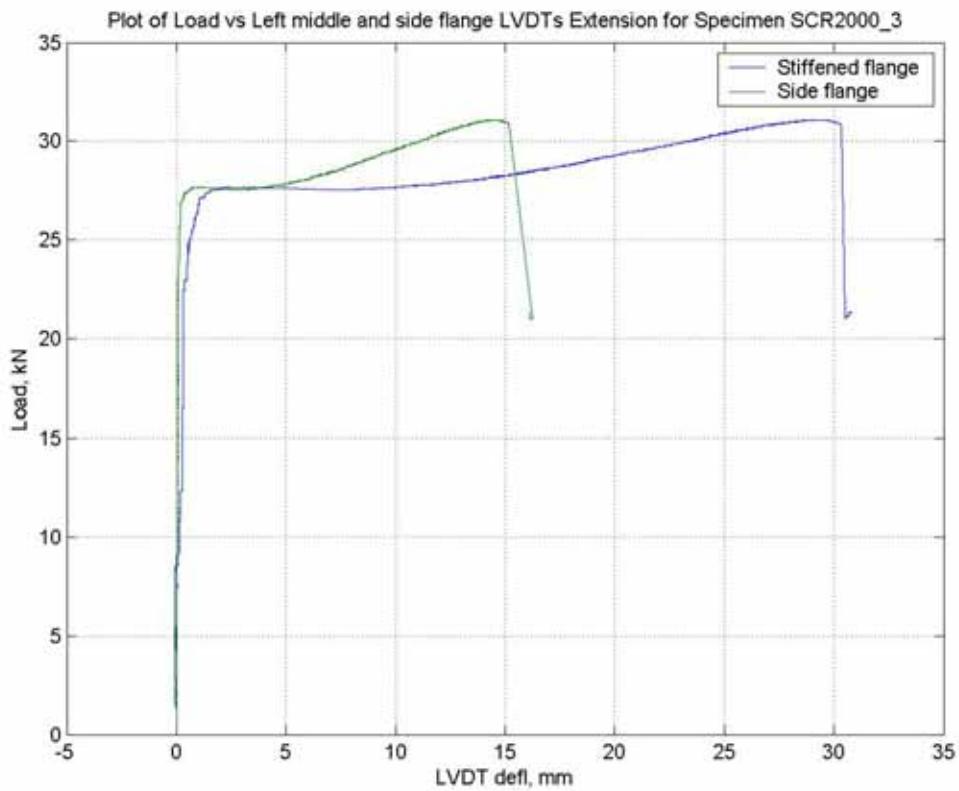


Figure B - 61 Load vs left stiffened and side flanges displacement for specimen SCR2000\_3